Aspects of (pseudo) Nambu-Goldstone Bosons in Physics Beyond the Standard Model

Soumen Kumar Manna

A thesis
submitted for the degree of

Doctor of Philosophy

Supervisor

Prof. Arunansu Sil

Department of Physics
Indian Institute of Technology Guwahati
Guwahati - 781039, Assam, India

Aspects of (pseudo) Nambu-Goldstone Bosons in Physics Beyond the Standard Model

A thesis submitted by

Soumen Kumar Manna

to

Indian Institute of Technology Guwahati
in partial fulfillment of the requirements
for the award of the degree of
Doctor of Philosophy in Physics

Supervisor

Prof. Arunansu Sil

Department of Physics
Indian Institute of Technology Guwahati
Guwahati - 781039, Assam, India

To my family...

" We are trying to prove ourselves wrong
as quickly as possible, because only in
that way can we find progress."

-Richard P. Feynman

Declaration

Soumen Kumar Manna
Roll No. 196121028
Department of Physics
IIT Guwahati
Guwahati, India

I hereby declare that works presented in the thesis entitled "**Aspects of (pseudo) Nambu-Goldstone Bosons in Physics Beyond the Standard Model**" has been carried out by me under the supervision of Prof. Arunansu Sil at the Department of Physics, Indian Institute of Technology Guwahati, India. The thesis has not been submitted anywhere else for any degree. Works presented in the thesis are all my own unless referenced to the contrary in the thesis.

Soumen kumar Manna

Soumen Kumar Manna

Date: 09/05/2025

Certificate

Prof. Arunansu Sil
Professor
Department of Physics
Indian Institute of Technology Guwahati
Guwahati, India
email:asil@iitg.ac.in

It is certified that the work contained in the thesis entitled "**Aspects of (pseudo) Nambu-Goldstone Bosons in Physics Beyond the Standard Model**" by Mr. Soumen Kumar Manna (Roll No - 196121028), a Ph.D. student in the Department of Physics, Indian Institute of Technology Guwahati is carried out under my supervision and has not been submitted elsewhere for the award of any other degree.

Prof. Arunansu Sil

Date : 09/05/2025

Acknowledgements

As I come to the end of this PhD journey, I carry with me a blend of experiences, which includes moments of joy and excitements, at the same time, moments of challenges, struggle, and a steady process of learning. Looking back, it's hard to believe how far this path has taken me – from a simple curiosity at the start to the completion of the thesis, has only been possible due to the encouragement, guidance and support of many people to whom I owe my deepest thanks.

First and foremost, I would like to express my heartfelt gratitude to my supervisor, Prof. Arunansu Sil, for his unwavering guidance and support throughout my PhD journey. His deep expertise, reasoning abilities, clarity of thought and positive outlook served as a source of motivation at every step. He always gave me the right push when I needed it, helping me to move forward with confidence. He was always approachable for discussions and was always generous with his time and attention. The insightful and thought-provoking scientific discussions we shared have deeply influenced my way of thinking. It has truly been an honour to work with him, and I am deeply grateful for everything I have gained under his mentorship.

I am grateful to my doctoral committee members – Prof. Subhaditya Bhattacharya, Prof. Debaprasad Maity and Dr. Debasish Borah for their insightful comments, suggestions and constructive feedback. I would like to convey a special note of thanks to Prof. Soumitra Nandi, under whom I did my MSc project, which introduced me to the world of high energy physics research. I remain grateful to Arunansu Sir, Subhaditya Sir, and Debu Sir for their lucid way of teaching Quantum field theory and Particle physics during the time of my MSc and PhD coursework, which laid the foundation for much of my research.

I sincerely thank the current and former Heads of the Department of Physics, Prof. Bosanta Ranjan Boruah, Prof. Perumal Alagarsamy and Prof. Subhradip Ghosh for providing me with all the facilities for my research. I also extend my gratitude to all the faculty members from whom I have learned during my MSc and PhD coursework, as well as the technical staff and non-teaching members of the department for their assistance over the years.

I am heartily thankful to my seniors-cum-collaborators, Dr. Rishav Roshan and Dr. Arghyajit Datta, for their continuous support, generosity with time, thoughtful academic discussions, and countless informal conversations that helped me adapt to PhD life. I also thank Dr. Sahabub Jahedi for our collaborations and many helpful academic and non-academic exchanges. I am grateful to my other collaborators, Prof. Stephen F. King and Prof. Subhaditya Bhattacharya. I am also thankful to Dr. Felix Yu, Dr. Miguel Escudero Abenza and Prof. Marco Cirelli for many discussions and the opportunities to visit Johannes Gutenberg University, Mainz, CERN and LPTHE, Paris, respectively. I also appreciate all the anonymous peer reviewers whose critical comments helped strengthen my publications.

I would like to take this opportunity to thank my other seniors in the high energy physics and cosmology community – Dr. Biswajit Karmakar, Dr. Abhijit Kumar Saha, Dr. Purusottam Ghosh, Dr. Basabendu Barman, Dr. Dibyendu Nanda, Dr. Rajesh Karmakar, Dr.

Devabrat Mahanta, Dr. Suruj Jyoti Das, Dr. Pritam Das, Dr. Riajul Haque and others, whose work and insights have been valuable resources during my PhD journey. I am also thankful to my other group members, Dipendu, Rajat and Rohan for their various lively discussions. I also thankful to my enthusiastic juniors like Indrajit, Niloy, Amit, Nayan, Ayan, Rajesh, Subhasis, Disha, Subhankar, Sourav and Abhik for their cheerful energy and discussions. I am also grateful to the HEP and Gravity journal clubs for numerous discussions on the latest trends of research.

I am lucky to have made many wonderful friends during my PhD. I thank Amalika, Swarup, Amit, Dipankar, Alolika, Sonali, Gargi, Ashirbad, Chinmoy, Shantanu, Lipika, Seshadri, Banashree, Shafeeque, Samik, Pooja, Himangshu, Mijanur, Saraswati, Rajendra and others, for turning my time at IITG into a delightful and memorable experience. Also, I have shared some great moments with seniors like Arghya da, Rajesh da, Surojit da, Rony da, Samit da, Pronoy da, Rakesh da, Sayan da, Sanket da, Sourav da, Monu Da and others. The conversations during the post-dinner walks on the campus with many of them and with my colourful hostel mates like Swarup, Amit, Avishek, Subhrojyoti, Abhijeet made everyday life flavourful. A heartfelt thanks to Amalika, especially, for staying by my side throughout the ups and downs of this journey with all her support, warmth, and encouragement.

I must acknowledge the serenity of the IIT Guwahati campus – the surrounding hills, lakes and greenery, which has always been a quiet and constant source of peace and motivation. I also acknowledge the efforts of hostel mess workers, cleaning staff, and the familiar food joints beyond the mess for making life easier and more comfortable.

Last but certainly not least, I extend my deepest love and gratitude my parents and my sister for their unconditional love, endless support, unwavering encouragement, and belief in me. Without their collective hard work and sacrifices, none of this would have been possible.

Thank you all.

Abstract

This thesis explores the phenomenology of two prominent pseudo-Nambu-Goldstone bosons, the Majoron and the Axion-like Particles (ALPs), as an effective and minimal way to address some of the most profound puzzles in particle physics and cosmology, such as the nature of dark matter, the origin of neutrino masses, and the existence of matter-antimatter asymmetry of the Universe. These light and feebly interacting particles naturally emerge from the spontaneous breaking of approximate global symmetries, establishing themselves not only theoretically appealing, but also highly relevant for experimental searches. We first explore Majorons, the pseudo-Nambu-Goldstone bosons associated to global lepton number symmetry breaking, as a viable freeze-in dark matter, where dimension-5 lepton number violating terms play the central role not only in producing the dark matter Majoron over a broader mass range (in keV-GeV), but also in facilitating high-scale resonant leptogenesis via right-handed neutrino mass splitting. In the next part, we turn our attention to ALPs, a generalization of the QCD axion, which was originally introduced to resolve the strong CP problem in the Standard Model. Although ALPs do not necessarily solve the strong CP problem, they offer a much wider parameter space to explore, as their mass and decay constant are independent parameters, in contrast to the QCD axion. In this context, we first examine their evolution as coherently oscillating dark matter via the well-known misalignment mechanism in presence of a Standard Model Higgs boson-assisted global symmetry breaking interaction, which results into a significantly enhanced allowed parameter space, and further achieve low-scale spontaneous leptogenesis, driven by ALP-induced CPT violation and an inert Higgs doublet assisted lepton number breaking interaction. Lastly, we explore an ALP-portal fermionic dark matter scenario at electron-positron colliders, emphasizing on the distinctive mono-photon plus missing energy signature. Across these studies, explicit symmetry breaking operators play a crucial role in solving some of the open problems of particle physics and cosmology, while preserving the models theoretically economical.

Publications included in the thesis :

1. Majorons revisited: Light dark matter as a FIMP: **Soumen Kumar Manna** and Arunansu Sil; Phys.Rev.D 108 (2023) 7, 075026 [arXiv: 2212.08404 (hep-ph)].

2. Effects of electroweak symmetry breaking on axionlike particles as dark matter: **Soumen Kumar Manna** and Arunansu Sil; Phys.Rev.D 109 (2024) 9, 095036, [arXiv: 2311.05125 (hep-ph)].

3. Spontaneous leptogenesis with sub-GeV axionlike particles: Arghyajit Datta, **Soumen Kumar Manna** and Arunansu Sil; Phys.Rev.D 110 (2024) 9, 095035, [arXiv: 2405.07003 (hep-ph)].

4. Leptogenesis with Majoron Dark Matter: Stephen F. King, **Soumen Kumar Manna**, Rishav Roshan and Arunansu Sil; Phys.Rev.D 111 (2025) 9, 095008, [arXiv: 2412.14121 (hep-ph)].

5. Probing the SM-ALP effective couplings at a future electron-positron collider: Subhaditya Bhattacharya, Sahabub Jahedi, **Soumen Kumar Manna** and Arunansu Sil; [arXiv: 2505.00478 (hep-ph)].

Other Publications/Proceedings:

1. Impact of First-order Electroweak Phase Transition on QCD Axion: Dipendu Bhandari, **Soumen Kumar Manna** and Arunansu Sil; [arXiv: 2507.05353 (hep-ph)].

2. Light Majorons as Freeze-in Dark Matter: **Soumen Kumar Manna** and Arunansu Sil; DOI: 10.1007/978-981-97-7441-8_24, Springer Proc. Phys. 361 (2025), International Conference on Future Prospects in Neutrino and Astroparticle Physics 2024.

Contents

Chapter 1

Introduction

1.1 A Glimpse into the Standard Model

The Standard Model (SM) [1–7] of particle physics is our well-established framework for understanding the fundamental building blocks of the Universe and their interactions. It unifies three of nature's fundamental forces, the strong, weak and electromagnetic interactions, into a single mathematical framework based on quantum fields and symmetry principles. At its core, the SM is built on gauge invariance, which connects elementary particles with their interactions and introduces gauge bosons as the force carriers. The SM is built upon the gauge group $\mathcal{G}_{\rm SM} = SU(3)_C \times SU(2)_L \times U(1)_Y$, which defines its fundamental forces. Here, $SU(3)_C$ governs the strong interaction, with C denoting the color charge, while $SU(2)_L \times U(1)_Y$ unifies the weak and electromagnetic forces into the electroweak theory, where L signifies left-handed chirality and Y represents weak hypercharge. The particle spectrum of the SM comprises the following: (a) spin-$\frac{1}{2}$ fermion fields, including *quarks* and *leptons*, are classified into left-handed (LH) and right-handed (RH) states based on their transformations under the $SU(2)_L$ gauge group, (b) spin-1 fields, represented by the four gauge bosons ($W_\mu^{i=1,2,3}$ and B_μ), which mediate the electroweak interactions, and eight gluon fields ($G_\mu^{a=1,2,\ldots,8}$), which mediate the strong interactions, and (c) the spin-0 scalar field, the Higgs boson (H), which is crucial for generating the masses of all other fields. The transformation properties of these fields under $\mathcal{G}_{\rm SM}$ are tabulated in Tab. 1.1.

While the left handed spin-$\frac{1}{2}$ fermion fields (*quarks* and *leptons*) transform as doublets under the weak isospin $SU(2)_L$ symmetry, represented as Q_{L_α} and ℓ_{L_α} in Tab 1.1, the right handed counterparts ($u_{R_\alpha},\ d_{R_\alpha},\ e_{R_\alpha}$) remain singlet under the same gauge group. Both quarks and leptons exist in three generations (indicated by α), called 'flavors', differing only in their masses. The three quark generations are given by:

$$Q_{L_\alpha} \equiv \begin{pmatrix} u \\ d \end{pmatrix}_L ; \begin{pmatrix} c \\ s \end{pmatrix}_L ; \begin{pmatrix} t \\ b \end{pmatrix}_L , \quad u_{R_\alpha} \equiv u_R;\ c_R;\ t_R, \quad d_{R_\alpha} \equiv d_R;\ s_R;\ b_R.$$

Here, the left handed quark doublets, Q_{L_α}, consist of left handed up-type and down-type quarks, while u_{R_α} and d_{R_α} represent the right handed up-type and down-type quarks, re-

Spin	Fields	Field Notation	$\mathcal{G}_{\rm SM} \equiv SU(3)_c \times SU(2)_L \times U(1)_Y$
$\frac{1}{2}$	Quarks	$Q_{L_\alpha} = \begin{pmatrix} u_{L_\alpha} \\ d_{L_\alpha} \end{pmatrix}$	(3, 2, 1/6)
		u_{R_α}, d_{R_α}	(3, 1, 2/3), (3, 1, $-1/3$)
	Leptons	$\ell_{L_\alpha} = \begin{pmatrix} \nu_{\ell_{L_\alpha}} \\ \ell_{L_\alpha} \end{pmatrix}$	(1, 2 ,$-1/2$)
		e_{R_α}	(1, 1, -1)
1	Gauge Bosons	G^a_μ	(8, 1, 0)
		W^i_μ, B_μ	(1, 3, 0), (1, 1, 0)
0	Scalar	$H = \begin{pmatrix} H^+ \\ H^0 \end{pmatrix}$	(1, 2, 1/2)

Table 1.1: The particle content of the Standard Model and their charge assignments under the gauge group $\mathcal{G}_{\rm SM}$.

spectively. The up-type quarks include u (up), c (charm) and t (top) quarks, whereas the down-type quarks consist of d (down), s (strange) and b (bottom) quarks. Additionally, these quark fields carry $SU(3)_C$ color charges, as they participate in the strong interaction. Similarly, the leptonic sector is structured as

$$\ell_{L_\alpha} \equiv \begin{pmatrix} \nu_e \\ e^- \end{pmatrix}_L ; \begin{pmatrix} \nu_\mu \\ \mu^- \end{pmatrix}_L ; \begin{pmatrix} \nu_\tau \\ \tau^- \end{pmatrix}_L , \quad e_{R_\alpha} \equiv e_R;\ \mu_R;\ \tau_R,$$

where the left handed neutrinos and charged leptons are grouped into $SU(2)_L$ doublets, ℓ_{L_α}, while right handed charged leptons, e_{R_α}, are singlet. Here, the three generations correspond to the three lepton flavor states, denoted by $\alpha = e^-,\ \mu^-,\ \tau^-$. Unlike quarks, leptons do not carry any $SU(3)_C$ charges and do not take part in strong interactions. Also, in the SM, right-handed neutrinos are not present.

These quarks and leptons interact through fundamental forces, each governed by a quantum field theory where interactions are mediated by spin-1 force carriers, known as gauge bosons. For instance, the strong interaction is carried by eight gauge bosons, known as gluons ($G^{a=1,2...8}_\mu$), corresponding to the eight generators of the $SU(3)_C$ symmetry ($3^2-1=8$). Similarly, the *electroweak* sector, governed by $SU(2)_L \otimes U(1)_Y$ gauge group, comprises of four gauge bosons: $W^{1,2,3}_\mu$ and B_μ.

The final key ingredient in defining a theory like the SM is understanding the symmetry of the vacuum, or more precisely, the structure of Spontaneous Symmetry Breaking (SSB) within the gauge group. In the SM (defined by $\mathcal{G}_{\rm SM}$), spontaneous symmetry breaking requires the introduction of a scalar $SU(2)_L$ doublet, denoted as Higgs $H = (\phi^+ \ \ \phi^0)^T$. The SSB of $\mathcal{G}_{\rm SM}$ occurs via the vacuum expectation value (*vev*) of H, leading to a reduction of the gauge symmetry as follows:

$$\mathcal{G}_{\rm SM} = SU(3)_C \times SU(2)_L \times U(1)_Y \ \rightarrow \ SU(3)_C \times U(1)_Q,$$

where Q is the electric charge. This mechanism not only explains the origin of particle

masses but also led to the prediction of the Higgs boson, which was later discovered in 2012 at the Large Hadron Collider (LHC) [8,9] with a mass of 125.09 ± 0.24 GeV [10], marking the completion of the SM particle content.

1.1.1 The SM Lagrangian

Taking all fields and symmetries into account, the most general SM Lagrangian is constructed, keeping the theory invariant under the $SU(3)_C \times SU(2)_L \times U(1)_Y$ gauge group and containing only operators up to dimension four to maintain renormalizability[1]. The SM Lagrangian can be expressed in terms of the following four components:

$$-\mathcal{L}_{\rm SM} = \mathcal{L}_{\rm Gauge} + \mathcal{L}_{\rm Fermion} + \mathcal{L}_{\rm Scalar} + \mathcal{L}_{\rm Yukawa}, \tag{1.1}$$

where,

I. $\mathcal{L}_{\rm Gauge}$ describes the pure gauge Lagrangian which involves the $SU(3)_C$, $SU(2)_L$ and $U(1)_Y$ gauge bosons, expressed as

$$\mathcal{L}_{\rm Gauge} = -\frac{1}{4} G^a_{\mu\nu} G^{\mu\nu}_a - \frac{1}{4} W^i_{\mu\nu} W^{\mu\nu}_i - \frac{1}{4} B_{\mu\nu} B^{\mu\nu}, \tag{1.2}$$

with $G^a_{\mu\nu}$, $W^i_{\mu\nu}$ and $B_{\mu\nu}$ representing the field strength tensors associated with the gauge groups $SU(3)_C$, $SU(2)_L$ and $U(1)_Y$, respectively, and defined as

$$G^a_{\mu\nu} = \partial_\mu G^a_\nu - \partial_\nu G^a_\mu - g_s\, f^{abc}\, G^b_\mu G^c_\nu, \tag{1.3a}$$
$$W^i_{\mu\nu} = \partial_\mu W^i_\nu - \partial_\nu W^i_\mu - g_2\, \epsilon^{ijk}\, W^j_\mu W^k_\nu, \tag{1.3b}$$
$$B_{\mu\nu} = \partial_\mu B_\nu - \partial_\nu B_\mu. \tag{1.3c}$$

Here f^{abc} (ϵ^{ijk}) represent the structure constants, while $g_s(g_2)$ denote gauge couplings correspond to $SU(3)_c$ ($SU(2)_L$), respectively. The indices i and a range over 1,2,3 and 1,2,...,8, respectively.

II. $\mathcal{L}_{\rm Fermion}$ includes the kinetic terms for fermion fields, consisting of quarks and leptons. For a generic fermionic field $\Psi = \Psi_L + \Psi_R$, where, $\Psi_L = \frac{1-\gamma_5}{2}\Psi$ and $\Psi_R = \frac{1+\gamma_5}{2}\Psi$, the kinetic terms are defined as

$$\mathcal{L}_{\rm Fermion} = -\left(\overline{\Psi}_L i\gamma^\mu \mathcal{D}_\mu \Psi_L + \overline{\Psi}_R i\gamma^\mu \mathcal{D}_\mu \Psi_R\right), \tag{1.4}$$

where, $\mathcal{D}_\mu$ denotes the covariant derivative and is expressed as

$$\mathcal{D}_\mu = \partial_\mu - i g_s \frac{\lambda^a}{2} G^a_\mu - i g_2 \frac{\tau^i}{2} W^i_\mu - i g_1 Y B_\mu, \tag{1.5}$$

where g_1 represents the gauge coupling corresponds to $U(1)_Y$ symmetry, while Y denotes the generator of the same $U(1)_Y$ group. The generators of $SU(3)_c$ are given by

[1]Terms arising from higher-dimensional operators (with dimensions greater than four) are suppressed at low energies by inverse powers of a high-energy scale, making them negligible within the energy regime where the Standard Model remains applicable.

$\frac{\lambda^a}{2}$ $(a = 1, ..., 8)$, where λ^a are the Gell-Mann matrices, while those of $SU(2)_L$ are $\frac{\tau^i}{2}$ $(i = 1, 2, 3)$, with τ^i being the Pauli spin matrices. The hypercharges corresponding to different particles are listed in Table 1.1. Gauge invariance dictates the form of the fermionic kinetic terms, which in turn determine their interactions with gauge bosons. These interactions are governed by the same gauge couplings defined in the $\mathcal{L}_{\text{Gauge}}$ sector.

III. $\mathcal{L}_{\text{Scalar}}$ defines the scalar part of the Lagrangian as follows:

$$\mathcal{L}_{\text{Scalar}} = (\mathcal{D}_\mu H)^\dagger (\mathcal{D}^\mu H) - V(H), \tag{1.6}$$

where, $V(H)$ is the Higgs potential, given by

$$V(H) \quad = \quad \mu_H^2 (H^\dagger H) + \lambda_H (H^\dagger H)^2. \tag{1.7}$$

Here μ_H^2 and λ_H denote the quadratic and quartic couplings of the SM Higgs, respectively. The covariant derivative $\mathcal{D}_\mu$, as defined in Eq. (1.5), also determines the interactions of the Higgs doublet with gauge bosons.

IV. Finally, $\mathcal{L}_{\text{Yukawa}}$ describes the interactions of the SM fermions with the Higgs doublet, which can be expressed as following:

$$\mathcal{L}_{\text{Yukawa}} \quad = \quad -\left(y^\ell_{\alpha\beta} \overline{\ell_{L\alpha}} H e_{R_\beta} + y^d_{\alpha\beta} \overline{Q}_{L_\alpha} H d_{R_\beta} + y^u_{\alpha\beta} \overline{Q}_{L_\alpha} \widetilde{H} u_{R_\beta} + H.c. \right), \tag{1.8}$$

where $\widetilde{H} = i\tau_2 H^*$ and y^x are 3×3 complex matrices that govern fermion masses and interactions, referred as Yukawa matrices, with $x = \ell$ (leptons), d(down) and u(up). The indices α, β corresponds to different generations. To ensure the gauge invariance of the Yukawa interactions in Eq. (1.8), the Higgs field H must transform as an $SU(2)_L$ doublet and can be represented as

$$H = \frac{1}{\sqrt{2}} \begin{pmatrix} \phi_1 + i\phi_2 \\ \\ \phi_3 + i\phi_4 \end{pmatrix}. \tag{1.9}$$

where $\phi_{1,2,3,4}$ correspond to four real scalar degrees of freedoms (d.o.fs).

However, in the unbroken $SU(2)_L \times U(1)_Y$ phase, gauge symmetry forbids mass terms for fermions and gauge bosons, which disagrees with what we observe. Their masses are generated through *spontaneous symmetry breaking* (*SSB*) via the Higgs mechanism, which we discuss next.

1.1.2 Spontaneous Symmetry Breaking and Higgs Mechanism

The breaking of the electroweak symmetry is determined by the parameters μ_H^2 and λ_H in Eq.(1.7). If $\lambda_H < 0$, then $V(H)$ is unbounded from below, preventing a stable vacuum. Conversely, when $\mu_H^2 > 0$ and $\lambda_H > 0$, the potential reaches a minimum at $\langle H \rangle = 0$, leaving

the electroweak symmetry unbroken. However, if $\mu_H^2 < 0$ and $\lambda_H > 0$ in Eq.(1.7), $SU(2)_L \times U(1)_Y$ symmetry undergoes spontaneous breaking [11–13]. In this case, minimizing $V(H)$ induces non-zero degenerate minima of the potential as:

$$\langle H \rangle \;=\; \sqrt{-\frac{\mu_H^2}{2\lambda_H}} = \frac{v}{\sqrt{2}}. \tag{1.10}$$

Choosing a specific vacuum state spontaneously breaks the gauge symmetry. Around the minima, the Higgs field can be written as,

$$H \;=\; \begin{pmatrix} \frac{\phi_1+\phi_2}{\sqrt{2}} \\ \frac{v+h+i\phi_4}{\sqrt{2}} \end{pmatrix} \equiv \begin{pmatrix} w^+ \\ \frac{v+h+iz}{\sqrt{2}} \end{pmatrix}. \tag{1.11}$$

Here, $v = \sqrt{-\mu_H^2/\lambda_H}$ represents the *vev* and h corresponds to the physical Higgs field, which is an excitation around this *vev*, with a mass given by $m_h^2 = 2\lambda_H v^2$. This *vev* causes the breaking of the Standard Model gauge symmetry:

$$SU(3)_c \times SU(2)_L \times U(1)_Y \longrightarrow SU(3)_c \times U(1)_Q. \tag{1.12}$$

The electric charge Q (generator of the unbroken subgroup $U(1)_Q$) is determined as a combination of isospin and hypercharge as

$$Q \;=\; T_3 + Y. \tag{1.13}$$

Following the Goldstone theorem, it is evident that after the SM symmetry is spontaneously broken: $SU(2)_L \times U(1)_Y \longrightarrow U(1)_Q$, three out of four d.o.fs in the Higgs doublet (ϕ_1, ϕ_2, ϕ_4 or, equivalently, $w^\pm$, z) become massless Goldstone bosons (*i.e.*, number of broken generators). These Goldstone bosons are *eaten* by the electroweak gauge bosons, providing them mass as

$$M_{W^\pm} = \frac{1}{2} g_2 v, \quad M_Z = \frac{1}{2}\sqrt{g_1^2 + g_2^2}\, v. \tag{1.14}$$

Meanwhile, the other combination of gauge bosons, A_μ, remains massless, which is an artefact of the unbroken $U(1)_Q$ symmetry, as given by the relation in Eq. (1.13). Hence, A_μ is identified as *photon*. These physical gauge bosons are defined by the following relations:

$$W_\mu^\pm \;=\; \frac{1}{\sqrt{2}}(W_\mu^1 \mp i W_\mu^2), \tag{1.15}$$

$$Z_\mu \;=\; \cos\theta_W\, W_\mu^3 - \sin\theta_W\, B_\mu, \tag{1.16}$$

$$A_\mu \;=\; \sin\theta_W\, W_\mu^3 + \cos\theta_W\, B_\mu, \tag{1.17}$$

where, θ_W denotes the Weinberg angle and is defined as $\theta_W = \tan^{-1}(g_1/g_2)$. The $W_\mu^\pm$ bosons carry electric charge, whereas Z_μ and A_μ remain neutral. Also, in the unitary gauge, the

Higgs field in Eq. (1.11) reduces into the form:

$$H = \begin{pmatrix} 0 \\ \frac{v+h}{\sqrt{2}} \end{pmatrix}. \tag{1.18}$$

As the Higgs field gets a *vev*, the mass matrices of the SM quarks and charged leptons can be obtained by incorporating Eq. (1.18) into Eq. (1.8) as

$$m^d_{\alpha\beta} = y^d_{\alpha\beta}\frac{v}{\sqrt{2}};\ m^u_{\alpha\beta} = y^u_{\alpha\beta}\frac{v}{\sqrt{2}} \text{ and } m^\ell_{\alpha\beta} = y^\ell_{\alpha\beta}\frac{v}{\sqrt{2}}. \tag{1.19}$$

These mass matrices are generally non-diagonal and must be diagonalized. For quarks, the diagonalization is achieved through a bi-unitary transformation, which maps the quark states from the flavor basis (labeled by the subscript α) to the mass basis (denoted by the subscript i, where $i = 1, 2, 3$) as:

$$u_{L_\alpha} = (U_u)_{\alpha i}u'_{L_i};\ d_{L_\alpha} = (U_d)_{\alpha i}d'_{L_i}\ u_{R_\alpha} = (V_u)_{\alpha i}u'_{R_i} \text{ and } d_{R_\alpha} = (V_d)_{\alpha i}d'_{R_i}, \tag{1.20}$$

Here, U_u, U_d, V_u and V_d are the 3×3 unitary matrices. Consequently, in the mass diagonal basis, the interaction of quarks with the charged gauge bosons $W^\pm$, known as charged current interactions, is derived from Eq. (1.4) as:

$$\mathcal{L}^{\rm q}_{\rm cc} = \sum_{i,j} u'_{L_i}\gamma^\mu W^+_\mu (U^\dagger_u U_d)_{ij} d'_{L_j} + H.c., \tag{1.21}$$

where the indices i, j range from 1 to 3. The mixing matrix $U^\dagger_u U_d$ is popularly known as *Cabibbo–Kobayashi–Maskawa* (CKM) unitary matrix [14, 15]. The CKM matrix is characterized by three independent mixing angles and one complex phase, and it is parametrized as,

$$V_{\rm CKM} = \begin{pmatrix} c_{12}c_{13} & c_{13}s_{12} & e^{-i\delta}s_{13} \\ -c_{23}s_{12} - e^{i\delta}c_{12}s_{13}s_{23} & c_{12}c_{23} - e^{i\delta}s_{12}s_{13}s_{23} & c_{13}s_{23} \\ s_{12}s_{23} - e^{i\delta}c_{12}c_{23}s_{13} & -e^{i\delta}c_{23}s_{12}s_{13} - c_{12}s_{23} & c_{13}c_{23} \end{pmatrix}. \tag{1.22}$$

Here $\theta_{12}, \theta_{23}, \theta_{13}$ are the mixing angles, with $c_{ij} = \cos\theta_{ij}$ and $s_{ij} = \sin\theta_{ij}$, while δ denotes the CP violating phase. Magnitude-wise, the central values of the CKM matrix elements are given by [16]

$$|V_{\rm CKM}| = \begin{pmatrix} 0.97435 & 0.22500 & 0.00369 \\ 0.22486 & 0.97349 & 0.04182 \\ 0.00857 & 0.04110 & 0.999118 \end{pmatrix} \tag{1.23}$$

Since $V_{\rm CKM}$ is non-diagonal, it induces flavor-changing interaction in the charged sector.

Therefore, in the SM, neutral interactions remain flavor-diagonal at tree level, while flavor-changing processes occur only through CKM-suppressed charged interactions in the quark sector. In contrast, for leptons,the absence of right-handed neutrinos keeps neutrinos massless. This allows the charged lepton mass matrix to be diagonalized without any additional mixing, ensuring that lepton mass and flavor eigenstates remain effectively identical. Consequently, no CKM-like mixing appears in the SM lepton sector. Finally, it is important to note that since $SU(3)_C$ remains unbroken, its eight gauge boson, called *gluons*, remain massless.

Experimentally, the SM is regarded as a well-established theory in physics, with its predictions rigorously tested and confirmed through high-precision experiments. Discovery of the W and Z bosons in $p\bar{p}$ collisions in 1983 [17–20] provided strong experimental confirmation of the SM electroweak interactions. The Z boson was studied in great detail at the Large electron-positron collider (LEP) [21, 22], where its precisely measured mass ($M_Z = 91.1875 \pm 0.0021$ GeV) and decay width provided great consistency with the electroweak theory [23, 24]. Furthermore, measurements of the W boson at LEP and the Tevatron [25, 26] yielded $M_W = 80.385 \pm 0.015$ GeV [24], while studies of the top quark at the Tevatron [27] determined its mass as $m_t = 173.5 \pm 1.0$ GeV [28, 29], both in strong agreement with theoretical expectations. A significant milestone was reached in 2012 with the discovery of the Higgs boson by the ATLAS and CMS experiments at the LHC [30–32], with subsequent measurements of its couplings to fermions and gauge bosons aligning well with the SM predictions. The *vev* of the Higgs field, which sets the scale of electroweak symmetry breaking, is determined from the muon lifetime [33] to be $v = 2M_W/g_2 \simeq (\sqrt{2}G_F)^{-1/2} \approx 246$ GeV. This, in turn, allows for the extraction of Higgs Boson couplings, measured at the LHC [34].

Despite these successes, several unresolved questions such as the true nature of dark matter, the origin of neutrino masses and the matter-antimatter asymmetry etc., suggest that the SM is not a complete theory, motivating the search for new physics beyond its framework.

1.1.3 Why the Standard Model is Incomplete?

Here, we highlight some of the intriguing issues in modern particle physics and cosmology that the Standard Model fails to explain, and are central to this thesis.

- **The presence of dark matter (DM):** Observations such as the rotation velocity curves of distant stars in the galaxies [35], gravitational lensing effects [36], etc. strongly indicate the presence of invisible matter in the Universe, commonly referred to as *dark matter* [37, 38]. Despite constituting approximately 26% of the energy budget of the Universe, the SM fails to accommodate a viable dark matter candidate. The only SM particle that comes close to such kind is the neutrino, but its tiny mass (necessity of neutrino mass is discussed below) and relativistic nature make it unsuitable for explaining the observed structure formation in the Universe. This certainly suggests us to explore beyond the SM framework. This thesis delves into different aspects of dark matter, particularly focusing on pseudo-Nambu-Goldstone bosons (pNGBs) as potential candidates, which will be explored in detail in the subsequent chapters.
- **Origin of neutrino masses:** In the SM, neutrinos are massless because right-handed neutrinos are absent. However, experimental evidences of neutrino oscillations, first

observed in atmospheric and solar neutrino experiments [39, 40] confirm that neutrinos have small yet non-zero masses. These oscillations indicate that the mass eigenstates of neutrinos differ from their flavor eigenstates, requiring a mechanism beyond the SM (BSM) to explain their masses. This thesis explores such BSM platforms in different contexts.

- **Matter-antimatter asymmetry of the Universe:** Another captivating issue that the SM cannot explain is the observed excess of matter over antimatter in the current Universe [41–47]. The existence of a matter-antimatter asymmetry is established observationally from the measured baryon-to-photon ratio [48–50]. This quantity is independently and consistently inferred from analyses of the primordial light element abundances produced during Big Bang Nucleosynthesis (BBN) [48, 51] and from the Cosmic Microwave Background (CMB), where the relative heights of acoustic peaks provide a precise determination of the same ratio [50, 52]. Both these probes require a significant excess of baryons over antibaryons to match the data, confirming the presence of a baryon asymmetry in the Universe. The dynamical generation of such baryon asymmetry requires new BSM physics. This thesis explores different mechanisms for baryon asymmetry, discussed in the following chapters, connected with the pNGBs.
- **Strong-CP problem:** This is an interesting puzzle of the SM, which is related to CP violation in the strong sector. The apparent absence of neutron electric dipole moment suggests that the CP-violating term to be either absent or extremely suppressed. This raises the natural question: why is this term so small, and why is CP violation in QCD not observed? One proposed solution is the introduction of the axion, which could dynamically cancel this CP violation and resolve the strong CP problem [53–56]. We will briefly discuss it later in this chapter and explore how axion-like particles (ALPs), a generalized version of the QCD axion, can address other compelling problems in the SM.

In addition, other interesting issues like *hierarchy problem* [57], *stability of electroweak vacuum* [58, 59], etc. are also worth noting. This thesis is focused on the phenomenology of pNGBs, particularly Majorons and ALPs, which offer elegant solutions to some of the most profound issues in particle physics, as discussed above. Since many of these issues are linked to the early Universe dynamics, the next section will briefly introduce the key concepts in early Universe cosmology. Afterward, we will delve deeper into these problems and then motivate why light degrees of freedom, such as pNGBs, are promising candidates for addressing these challenges beyond the SM.

1.2 The Expanding Universe and the Role of BSM Physics

Many of the unsolved issues of the SM are closely tied to the physics of the early Universe. Once filled with a hot and dense thermal bath of relativistic particles, the Universe has undergone several phases of evolution, transitioning from a radiation-dominated era to a matter-dominated phase, and eventually to its present state, dominated by dark energy. Understanding this thermal history is crucial for exploring how BSM physics could impact key processes like baryogenesis, dark matter production, etc. Therefore, we first briefly review

the expanding Universe and its thermal history.

1.2.1 Thermal History of the Universe

The Universe is assumed to be homogeneous and isotropic on large scales ($\approx$ 200 Mpc) [48, 49, 60, 61]. Accordingly, it is appropriate to describe the spacetime on these scales by adopting the usual Friedmann-Lemaître-Robertson-Walker (FLRW) metric as following

$$ds^2 = g_{\mu\nu}dx^\mu dx^\nu = -dt^2 + R^2(t)\left[\frac{dr^2}{1-kr^2} + r^2\left(d\theta^2 + \sin^2\theta\, d\phi^2\right)\right]. \tag{1.24}$$

Here t is the physical or cosmic time (which is the proper time measured by comoving observers), and (r, θ, ϕ) are the comoving coordinates and $g_{\mu\nu}$ is the metric tensor, defining the geometry of spacetime. The curvature parameter k determines the geometry of the Universe: flat ($k = 0$), closed ($k > 0$), or open ($k < 0$). $R(t)$ denotes the scale factor of the Universe, which evolves with time according to the dynamics determined by the Friedmann equations (as discussed below) and the energy content of the Universe. However, in the currently observed Universe, consistent with ΛCDM cosmology, the $R(t)$ is increasing with cosmic time. The expansion rate of the Universe, dubbed as the Hubble parameter ($\mathcal{H}$), is defined via the scale factor as

$$\mathcal{H} \equiv \frac{\dot{R}(t)}{R(t)}, \tag{1.25}$$

where $\dot{R}(t) = dR/dt$. It has the dimension of inverse time and remains positive in an expanding Universe, while it turns negative in a contracting Universe. The present value of the Hubble parameter is

$$\mathcal{H}_0 = 100\, h \text{ km s}^{-1} \text{ Mpc}^{-1}, \tag{1.26}$$

where h is the dimensionless parameter (referred as the reduced Hubble parameter) that can be determined through various methods. One direct way is by relating galaxy redshifts to their distances using the cosmic distance ladder, yielding $h \approx 0.73 \pm 0.01$ [62]. Another approach estimates the expansion rate based on the best-fit ΛCDM model, resulting in $h = 0.674 \pm 0.005$ [63]. This discrepancy between different measurements are known as *Hubble tension* [64], which may hint for new physics beyond ΛCDM.

Given the metric $g_{\mu\nu}$, the evolution of the Universe is dictated by Einstein's field equations, which describe how matter and energy influence the curvature of spacetime:

$$R_{\mu\nu} - \frac{1}{2}g_{\mu\nu}R = 8\pi G T_{\mu\nu}, \tag{1.27}$$

where $R_{\mu\nu}$ is known as the Ricci tensor, describing how spacetime is curved by matter, $R = g^{\mu\nu}R_{\mu\nu}$ denotes the Ricci scalar (trace of $R_{\mu\nu}$), which provides a measure of the overall curvature of spacetime at each point. The right-hand side involves the energy-momentum tensor $T_{\mu\nu}$, which acts as the source of curvature. It contains not only the local energy density but also momentum fluxes and stresses (pressures and shear) of matter and radiation. In Eq. 1.27, G denotes Newton's gravitational constant, which can be expressed as:

$G = 8\pi/M_{\rm Pl}^2$, with the Planck mass given by $M_{\rm Pl} \simeq 1.22 \times 10^{19}$ GeV. Thus, the Einstein field equations establish a direct relation between the curvature of spacetime and the local energy, momentum, and stress content. By applying these equations to the FLRW metric, one can derive the Friedmann equations, which govern the Universe's expansion based on its energy composition.

$$\mathcal{H}^2 = \frac{8\pi G}{3}\rho - \frac{k}{R^2}, \tag{1.28}$$

$$\frac{d\mathcal{H}}{dt} + \mathcal{H}^2 = \frac{\ddot{R}}{R} = \frac{4\pi G}{3}(\rho + 3\mathcal{P}). \tag{1.29}$$

While Eq. 1.28 relates the Hubble parameter $\mathcal{H}$ to the energy density of the Universe ρ, Eq. 1.29 describes how the expansion of the Universe accelerates or decelerates depending on the pressure $\mathcal{P}$. Combining these equations (Eqs. 1.28 and 1.29) gives the continuity equation

$$\frac{d\rho}{dt} + 3\mathcal{H}(\rho + \mathcal{P}) = 0, \tag{1.30}$$

which ensures the conservation of energy-momentum in an expanding Universe. The total energy density ρ and pressure $\mathcal{P}$ include contributions from various contributions, such as *radiation* (relativistic matter), non-relativistic *matter*, and the cosmological constant. These components are typically modelled as perfect fluids with an energy-momentum tensor of the form $T^{\mu}_{\nu} = \mathrm{diag}(-\rho, \mathcal{P}, \mathcal{P}, \mathcal{P})$. The equation of state for each component relates pressure to energy density as $\mathcal{P}_i = w\rho_i$, where the equation of state parameter w typically ranges between -1 and $+1$ for different forms of energy. Given the equation of state w for each element, one can easily solve the Eq. 1.30, to obtain $\rho \propto R^{-3(1+w)}$. The first and the second column of table 1.2 summarize the equation of state parameter w and how the energy density evolves with the scale factor for different components of the Universe.

Species	$w = \mathcal{P}/\rho$	$\rho(R)$	$R(t)$
Matter	0	R^{-3}	$t^{2/3}$
Radiation	$\frac{1}{3}$	R^{-4}	$t^{1/2}$
Λ	-1	R^{0}	$e^{\mathcal{H}t}$

Table 1.2: Equation of states (w), variation of energy densities with respect to the scale factor and the behavior of scale factors with time for different fluids, such as matter, radiation and cosmological constant (Λ).

While both matter and radiation get diluted because of the volume expansion $(\propto R^{-3})$, radiation experiences additional dilution because of redshift, meaning the energy of each photon decreases as $E \propto R^{-1}$. Consequently, as shown in the second column, the early Universe was radiation-dominated (RD), followed by a transition to matter domination (MD) as non-relativistic matter began to dominate the energy density. To determine the evolution of $R(t)$ in an MD, RD, or cosmological constant-dominated Universe (with a fixed w), one must solve Eq.1.30, which is listed in the last column of table 1.2.

To describe the Universe in the present epoch, it is useful to introduce the critical energy

density, ρ_c, which can be derived by rewriting the first Friedmann equation (Eq. 1.28) as

$$\frac{k}{\mathcal{H}^2 R^2} = \frac{\rho}{3\mathcal{H}^2/8\pi G} - 1 = \frac{\rho}{\rho_c} - 1, \qquad \text{with} \quad \rho_c = \frac{3\mathcal{H}^2}{8\pi G}. \tag{1.31}$$

Current cosmological models, supported by simulations and observations [63], indicate that the Universe is nearly spatially flat ($k = 0$) on large scales. In this scenario, the present energy density fractions of different components, defined as $\Omega_i^0 = \rho_i^0/\rho_c^0$, are given by the ΛCDM model [63] as

$$\Omega_m^0 \approx 0.31, \quad \Omega_\Lambda^0 \approx 0.68, \quad \Omega_r^0 \approx 10^{-5}. \tag{1.32}$$

The non-relativistic matter density, Ω_m^0, consists of both baryonic matter and dark matter, with their respective contributions (in terms of the reduced Hubble parameter h) given by [63]

$$\Omega_b^0 h^2 \approx 0.022, \quad \Omega_{\rm DM}^0 h^2 \approx 0.12. \tag{1.33}$$

1.2.2 Thermodynamics of the Early Universe

With the known energy content of the Universe, we now focus on the thermodynamics of the early Universe, where particle interactions and evolution occurred in an extremely hot and dense plasma. This allows us to treat the Universe as a thermodynamic system in (or near) equilibrium, defined by a temperature T. Therefore, we first discuss the macroscopic properties ($e.g.$, number density, energy density and pressure) of a particle species in thermal equilibrium. Subsequently, as the Universe expands and cools down, deviations from equilibrium give rise to various non-equilibrium phenomena that shape the present structure of the Universe.

1.2.2.1 Equilibrium Dynamics

From statistical mechanics, the equilibrium distribution of a particle in a plasma at temperature T follows the Fermi-Dirac (FD) or Bose-Einstein (BE) distribution:

$$f^{\rm eq}(p,T) = \frac{1}{e^{(E-\mu)/T} \pm 1}, \tag{1.34}$$

where $E = \sqrt{p^2 + m^2}$ is the energy of the species, with p is the momentum, m being the mass and μ is the chemical potential, which governs the changes in number densities of particles. The $+$ $(-)$ sign corresponds to fermions (bosons). For a particle changing process $i + j \to a + b$ to be in chemical equilibrium, the chemical potentials satisfy $\mu_i + \mu_j = \mu_a + \mu_b$. This condition ensures that the forward and reverse reaction rates balance, resulting in no net change of particle numbers over time. Generally, if number-changing interactions are rapid and no conserved quantum number constrains the particle numbers, the chemical potentials tend to zero ($\mu \to 0$) in equilibrium, as any excess is quickly erased. This justifies the common assumption of $\mu = 0$ for such species in equilibrium. However, if a charge is conserved (e.g., baryon number, lepton number, electric charge), the corresponding chem-

ical potential can remain non-zero even in equilibrium. On the other hand, kinetic equilibrium is maintained if scattering interactions are frequent enough to preserve the thermal distribution. For a relativistic ($T \gg m$) and non-relativistic ($T \ll m$) particle species, the number density (n), energy density (ρ), and pressure ($\mathcal{P}$) can be calculated using $f^{\rm eq}(p,T)$ as depicted in table 1.3, where $\langle E\rangle (\equiv \rho/n)$ is the average energy per particle, g refers to the

Nature	Species	n	ρ	$\mathcal{P}$	$\langle E\rangle$
Relativistic ($T \gg m, \mu$)	Boson	$g\frac{\zeta(3)}{\pi^2}T^3$	$g\frac{\pi^2}{30}T^4$	$\rho/3$	$\simeq 2.70T$
	Fermion	$g\frac{3}{4}\frac{\zeta(3)}{\pi^2}T^3$	$g\frac{7}{8}\frac{\pi^2}{30}T^4$	$\rho/3$	$\simeq 3.15T$
Non-Relativistic ($m \gg T$)	Boson & Fermion	$g\left(\frac{mT}{2\pi}\right)^{3/2} e^{-(m-\mu)/T}$	mn	$nT \ll \rho$	$m + 3T/2$

Table 1.3: Various macroscopic variables for relativistic and non-relativistic particle species.

number of internal degrees of freedom and $\zeta(3) \simeq 1.2$. Since the energy density (and pressure) of a non-relativistic species ($m \gg T$) is exponentially suppressed by $e^{-m/T}$ compared to a relativistic one, during the early Universe's radiation-dominated (RD) era, relativistic species dominate the total energy density:

$$\rho_{\rm tot} \simeq \rho_R = \frac{\pi^2}{30} g_\star^\rho \, T^4, \qquad g_\star^\rho = \sum_{a({\rm bosons})} g_a \left(\frac{T_a}{T}\right)^4 + \frac{7}{8} \sum_{a({\rm fermions})} g_a \left(\frac{T_a}{T}\right)^4, \tag{1.35}$$

where $g_\star^\rho$ is the number of relativistic degrees of freedom contributing to ρ_R and T_a denotes the temperature of a particle species a. The energy density $\rho_{\rm tot}$ can be linked to the RD Universe's expansion rate via the Friedmann equations, leading to the Hubble parameter for $k = 0$

$$\mathcal{H}(T) = 1.66\sqrt{g_\star^\rho}\,\frac{T^2}{M_{\rm Pl}}. \tag{1.36}$$

Another key macroscopic quantity is the total entropy density, given by $\mathcal{S} = (\mathcal{P} + \rho)/T$, which can be simplified during radiation domination ($P = \rho/3$) as follows

$$\mathcal{S} = \frac{2\pi^2}{45} g_\star^{\mathcal{S}} T^3, \tag{1.37}$$

where $g_\star^{\mathcal{S}}$ stands for the number of relativistic degrees of freedom that contribute to $\mathcal{S}$, given by

$$g_\star^{\mathcal{S}} = \sum_{a({\rm bosons})} g_a \left(\frac{T_a}{T}\right)^3 + \frac{7}{8} \sum_{a({\rm fermions})} g_a \left(\frac{T_a}{T}\right)^3. \tag{1.38}$$

The importance of the total entropy density is that it remains conserved in a comoving volume, leading to $g_\star^{\mathcal{S}} T^3 R^3 = \text{constant}$. Hence, when $g_\star^{\mathcal{S}}$ remains unchanged, $T \propto R^{-1}$. However, as particles become non-relativistic, $g_\star^{\mathcal{S}}$ changes, modifying the scaling to $T \propto (g_\star^{\mathcal{S}})^{-1/3} R^{-1}$. From the Fig. 1.1, it can be observed that although the $g_\star^{\mathcal{S}}$ and $g_\star^\rho$ generally follow each other but start to deviate when heavier particles decouple from the thermal bath. We will discuss the notion of decoupling in the following subsection.

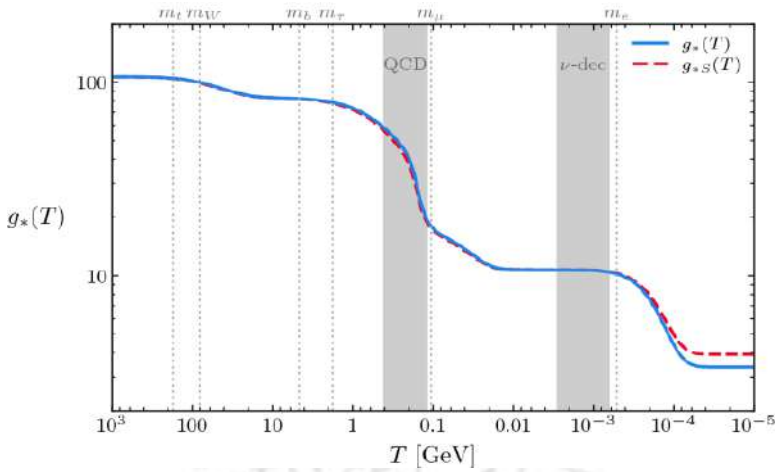

Figure 1.1: The effective number of energetic ($g_\star^\rho$) and entropic degrees of freedom ($g_\star^S$) in the SM as functions of temperature, shown in the solid blue line and dotted red line, respectively. Figure taken from [65].

It is important to emphasize that the expressions discussed above apply strictly during the RD era, when relativistic particles dominate the energy density. At later times, during matter domination, non-relativistic species significantly contribute and must be included explicitly.

1.2.2.2 Non-equilibrium Dynamics

The evolution from a hot and dense plasma to present-day stable particles and nuclei cannot be fully described under the assumption of thermal equilibrium. As the Universe expands, particles eventually become non-relativistic ($T \ll m$), causing their number density to drop exponentially. Consequently, annihilation and scattering processes with the plasma become inefficient.
To determine whether a process remains in thermal equilibrium, we compare its rate, Γ, with the cosmic expansion rate, $\mathcal{H}$. If $\Gamma/\mathcal{H} \gg 1$, the process occurs on a much shorter timescale than that of cosmic expansion, keeping the system in equilibrium. However, when $\Gamma/\mathcal{H} \ll 1$, the expansion dominates, which prevents the interactions from maintaining equilibrium and eventually results in *decoupling* of the particles. The number density of these relic particles, relative to the entropy density, remains conserved until today.

However, this criteria only provides an estimate of the temperature at which a process departures from being in equilibrium with the plasma. To accurately describe the system's evolution over time, kinetic theory is the most effective approach. This method involves studying the time evolution of the phase-space distribution function, governed by the Boltzmann equation, which we discuss below.

Considering the phase-space distribution of a particle under consideration as $f(x^\mu, p^\mu)$, the Boltzmann equation can be generically written as:

$$\hat{\mathbf{L}}[f(x^\mu, p^\mu)] = \mathbf{C}[f(x^\mu, p^\mu)] \tag{1.39}$$

where $\hat{\mathbf{L}}$ represents the Liouville operator, which, in the case of a flat, homogeneous and

isotropic Universe (where $f(x^\mu, p^\mu) \to f(t, E)$), simplifies to :

$$\hat{\mathbf{L}}[f] = \left[E\frac{\partial}{\partial t} - \mathcal{H}E^2\frac{\partial}{\partial E}\right] f(t, E). \tag{1.40}$$

In Eq. 1.39, $\mathbf{C}$ is the collision operator which accounts for the number of particles lost or gained per unit time per phase-space volume because of collisions or decays. For a species a undergoing interactions of the form $a + b \leftrightarrow c + d$, the collision operator is given by:

$$\begin{aligned}\mathbf{C}(f_a; f_b, f_c, f_d) = \int \frac{d^3\mathbf{p_b}}{(2\pi)^3 2E_b}\frac{d^3\mathbf{p_c}}{(2\pi)^3 2E_c}\frac{d^3\mathbf{p_d}}{(2\pi)^3 2E_d}(2\pi)^4\delta^{(4)}(p_a + p_b - p_c - p_d) \\ \times \Big[|\mathcal{M}_{cd\to ab}|^2 f_c f_d(1 \pm f_a)(1 \pm f_b) - |\mathcal{M}_{ab\to cd}|^2 f_a f_b(1 \pm f_c)(1 \pm f_d)\Big],\end{aligned} \tag{1.41}$$

In order to find the time evolution of number density of the particle a, we must integrate both sides of Eq: 1.39 with the factor $\int \frac{d^3\mathbf{p_a}}{(2\pi)^3}$. This yields the following expression of the Boltzmann equation (BE):

$$\frac{dn_a}{dt} + 3\mathcal{H}n_a = \int \frac{d^3p_a}{(2\pi)^3 E_a}\mathbf{C}(f_a; f_b, f_c, f_d), \tag{1.42}$$

where first term on the left represents the time evolution of the number density of species a, while second term accounts for its dilution due to expansion of the Universe.

Throughout this thesis, we will see that such out-of-equilibrium processes played a key role in many early Universe events, including (i) dark matter production and (ii) baryon asymmetry generation. Later, we will revisit these concepts in greater detail while exploring these phenomena.

1.2.3 Highlights on the Different Phases of Early Universe

The current understanding of the evolution of the Universe is primarily based on observational evidence from the Cosmic Microwave Background (CMB), Big Bang Nucleosynthesis (BBN), large-scale structure, and precision cosmology. It is widely believed that the Universe began with a phase of cosmic inflation, an extremely rapid expansion triggered by a scalar field called inflaton, which smoothed out inhomogeneities and stretched quantum fluctuations to macroscopic scales. While inflation remains hypothetical, it explains why the Universe appears nearly homogeneous and isotropic on large scales. As inflation ended, the energy stored in inflaton field was transferred to the particles of the SM in a process called reheating, initiating the radiation-dominated era.

Around $t \sim 10^{-10}$ sec. ($T \sim 100$ GeV), the Universe underwent the electroweak phase transition, where the Higgs field acquired a *vev*, giving mass to the SM particles. This time-temperature relation is derived using the Friedmann equation during the RD era, assuming an adiabatically expanding universe filled with relativistic particles in equilibrium. Using $H \simeq 1/(2t)$ and Eq. 1.36, one can find

$$t \simeq 0.3\,\frac{M_{\rm Pl}}{\sqrt{g_\star^\rho}\,T^2}. \tag{1.43}$$

As the Universe expanded and cooled, free quarks and gluons started to get confined into hadrons at around $t \sim 10^{-4}$ sec. ($T \sim 100$ MeV), marking the quark-hadron transition. Around $t \sim 1$ sec. ($T \sim 1$ MeV), the temperature dropped sufficiently enough to cause the neutrino decoupling, when the SM weak interaction goes out of equilibrium. Shortly after, when the temperature dropped below the electron/positron mass, $m_e \sim 0.5$ MeV, electrons and positrons annihilated into photons, slightly heating the photon bath relative to the neutrino background. This set the well-known ratio of $T_\nu/T_\gamma = (4/11)^{1/3}$, which, although the cosmic neutrino background has not been directly detected, is strongly supported by cosmological observations. Roughly after $t \sim 3$ min. ($T \sim 0.1$ MeV), protons and neutrons began fused to form light element nuclei like hydrogen, helium, and lithium in a process known as Big Bang Nucleosynthesis (BBN). The observed light element abundances strongly support this theoretical prediction. As expansion continued, radiation energy density declined faster than matter energy density, leading to matter-radiation equality at $t \sim 10^4$ yrs. ($T \sim 1$ eV). From that point, cold dark matter (CDM) and baryons together dominated the energy content, with CDM playing the central dynamical role. Then, around $t \sim 10^5$ yrs. ($T \sim 0.1$ eV), electrons combined with protons to form neutral hydrogen in an event known as recombination. This process led to photon decoupling, where these photons could travel freely without any scattering with charged particles (by this time, the Universe was already was already matter-dominated). These photons are observed today as the Cosmic Microwave Background (CMB) and provide a detailed snapshot of the early Universe.

After photon decoupling, the Universe entered the 'Dark Ages' until the first stars formed and partially reionized neutral hydrogen. Nevertheless, over billions of years of subsequent evolution, the cosmic matter content continued to dilute and dark energy overtook matter as the dominant component driving cosmic expansion. Despite extensive progress, both CDM and dark energy remain of unknown physical origin, their effects are inferred from cosmological observations and the dynamics of expansion and structure formation. While the Standard Models of particle physics and cosmology have been remarkably successful, many key details, especially regarding these dark components, are still unresolved. We now shift our focus to dark matter, exploring its impact in shaping the evolution of the Universe.

1.3 Dark Matter: Hidden mass in the Universe

Over last few decades, extensive amount of research on cosmological history has helped us to understand the energy content of the Universe. High-precision CMB measurements by WMAP [50] and PLANCK [66] collaboration reveal that approximately 68% of the Universe's energy density is carried by the mysterious dark energy and the invisible dark matter (DM) accounts for $\sim 26\%$ of the energy of the Universe. On the other hand, the ordinary matter (also known as "baryonic" matter), which forms the visible Universe, constitutes less than $\sim 5\%$ of the energy density of the Universe. Although dark matter is still undetected, its gravitational effects provide strong indirect evidence for its existence.

1.3.1 Evidences and Properties of Dark Matter

One of the earliest pieces of evidence for dark matter comes from the galaxy rotation curve measurements. In 1933, Fritz Zwicky [67] carried out measurements of the velocity dispersion of galaxies in the Coma cluster, and later, in 1970s, Vera Rubin [68] conducted more accurate studies of the rotation curves of galaxies, which moving near the fringes of galaxy clusters. If most of the mass were concentrated at the center, Newtonian mechanics predicts that the rotational velocity should decrease with distance as

$$v_{\rm rot}(r) = \sqrt{\frac{GM}{r}}, \tag{1.44}$$

beyond the visible extent (galactic core). However, observations revealed that the velocity profile remain nearly flat as we go further away from the center, suggesting that mass keeps increasing with radius, $M \to M(r) \propto r$. This unexpected behavior indicates the presence of an extended, non-luminous halo of massive dark matter which extends beyond the galactic disk. This phenomenon is observed in all galaxies, including NGC 6503 [35], as shown in the left panel of Fig. 1.2.

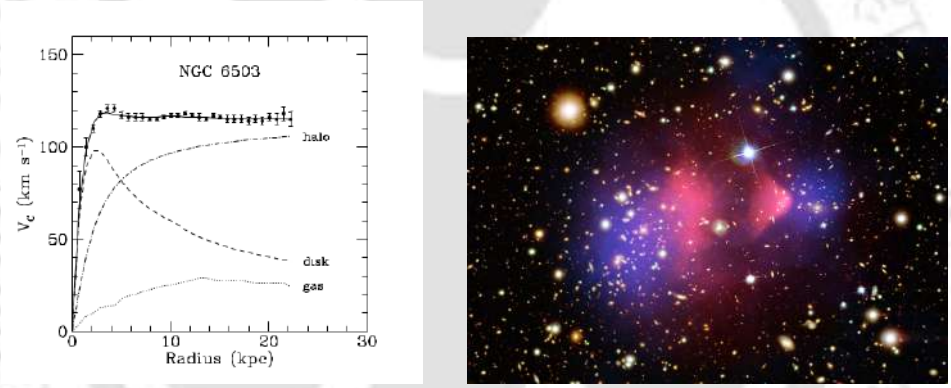

Figure 1.2: Left panel: Rotation curves of galaxy NGC 6503 [35], showing how stars, gas, and dark matter ("halo") contribute to the total velocity $v_{\rm rot}$. At large radii, dark matter dominates. **Right panel:** Bullet cluster image from NASA's Hubble Space Telescope. Image taken from chandra.harvard.edu.

There exist several other independent observations which support the existence of dark matter. A particularly compelling line of evidence is gravitational lensing, a phenomenon predicted by general relativity. According to Einstein, light bends when passing near a massive object. This effect allows astronomers to infer the mass distribution of an intervening galaxy acting as a lens for background light. By analyzing the distortion in lensed images, one can distinguish visible matter from the non-luminous matter. Bergmann and Petrosian were among the first to use this technique to study galaxy clusters. A striking confirmation of dark matter's presence comes from the Bullet Cluster [36, 69], where lensing shows a clear separation between luminous and gravitational mass. During the collision of two galaxy clusters, ordinary baryonic matter interacts and slows down, forming a hot gas cloud at the center (as shown by the pink regions in the right panel of Fig. 1.2). In contrast, dark matter, which interacts only gravitationally, passes through unaffected, forming separate mass clumps. This observation clearly suggests that dark matter is weakly interacting.

On cosmological scales, the Cosmic Microwave Background (CMB) provides strong ev-

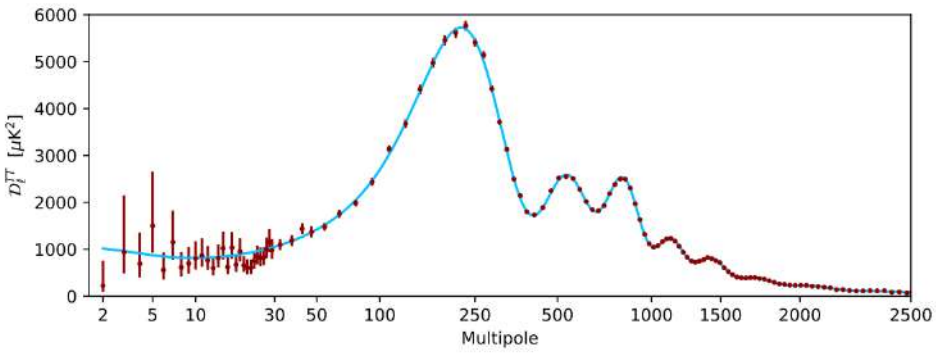

Figure 1.3: The figure shows CMB temperature fluctuations (in microkelvin) plotted against the multipole moment (l), which corresponds to the angular scale of the fluctuations. Taken from [70].

idence for dark matter. Discovered by Arno Penzias and Robert Wilson in 1964 [71], the CMB is a remnant from the Big Bang, offering a glimpse of the Universe 380,000 years after it formed. Although the temperature fluctuation of CMB is almost uniform, it has tiny temperature variations that form a pattern known as the CMB power spectrum (shown in Fig.1.3). This pattern arises from sound waves in the early Universe, where radiation pushed matter outward, while gravity pulled it back in, creating peaks and dips in the spectrum. The first peak tells us about the overall shape of the Universe. The second peak gives information about the amount of ordinary matter (baryons). The third peak reveals the presence of dark matter. Data from Wilkinson Microwave Anisotropy Probe (WMAP) [50] and PLANCK [66] suggest that the dark matter makes up about 26% of the Universe's energy density.

In a nutshell, we know that DM is electrically neutral, massive, gravitationally interacting, and either stable or long-lived compared to the age of the Universe. However, there are still plenty of questions remain unclear about the DM, such as its spin and production mechanism. Additionally, despite extensive direct and indirect searches, no experimental detection has been made so far. Nevertheless, strong astrophysical and cosmological evidences motivate us to explore about the fundamental nature of DM. Since the SM does not provide a suitable dark matter candidate, new physics is required.

1.3.2 Production of Dark Matter

There have been several studies on the particle nature and production mechanism of the dark matter. Based on the interaction strength with the thermal bath, DM is broadly categorised in two sectors: (a) **Thermal dark matter**, which was in thermal equilibrium with the primordial plasma before decoupling (e.g., weakly-interacting massive particles or WIMPs), and (b) **Non-thermal dark matter**, which interacts so feebly that it never attains thermal equilibrium and is produced via non-thermal mechanisms, like annihilation or decay of bath particles (e.g., Feebly-interacting massive particles or FIMPs). This thesis focuses on pseudo-Nambu-Goldstone bosons (pNGBs), a class of naturally light, non-thermal dark matter candidates. On the other hand, among the DM production mechanisms, two most widely studied ones are "Freeze-out" and "Freeze-in". While, the freeze-out mechanism typically describes thermal DM, Freeze-in mechanism explains a class of non-thermal DM. Let

us now discuss these mechanisms in detail.

1.3.2.1 Freeze-out Mechanism

In this scenario, the DM particle is considered to interact weakly with the SM fields and is commonly referred to as a Weakly Interacting Massive Particle (WIMP) [72–78]. Due to these interactions, WIMPs were initially in thermal equilibrium in the early Universe, continuously produced and annihilated within the thermal bath. As the Universe expanded and cooled, their interaction rate dropped, and they eventually decoupled when thermal equilibrium could no longer be maintained. Based on their kinematic state at decoupling, DM is further classified into: (i) Hot DM (HDM) – remains ultra-relativistic at decoupling, (ii) Warm DM (WDM) – decouples while still relativistic, and (iii) Cold DM (CDM) – becomes completely nonrelativistic at decoupling.
To determine the decoupling temperature of such DM, we compare its annihilation rate, Γ, with the Hubble expansion rate, $\mathcal{H}$. As discussed before, when $\Gamma/\mathcal{H} < 1$, DM interactions freeze-out, leading to its decoupling from the thermal bath. This decoupled DM abundance then remains stable and contributes to the present-day relic density. A more precise way to determine the decoupling temperature and relic abundance is by solving the Boltzmann equation (BE) for the DM particle ψ as given in Eq. 1.42. Here, n_a is replaced by n_ψ, and the collision term accounts for all number-changing processes of ψ. To illustrate, let us consider a simple case where ψ annihilates into the SM particle-antiparticle pairs $(X, \bar{X})$ via $\psi\bar{\psi} \leftrightarrow X\bar{X}$. In this case, the BE takes the form:

$$\frac{dn_\psi}{dt} + 3\mathcal{H}n_\psi = \int \frac{d^3\mathbf{p}_\psi}{(2\pi)^3 2E_\psi}\frac{d^3\mathbf{p}_{\bar{\psi}}}{(2\pi)^3 2E_{\bar{\psi}}}\frac{d^3\mathbf{p}_X}{(2\pi)^3 2E_X}\frac{d^3\mathbf{p}_{\bar{X}}}{(2\pi)^3 2E_{\bar{X}}}(2\pi)^4\delta^{(4)}(p_\psi + p_{\bar{\psi}} - p_X - p_{\bar{X}}) \times \Big[|\mathcal{M}_{X\bar{X}\to\psi\bar{\psi}}|^2 f_X f_{\bar{X}}(1 \pm f_\psi)(1 \pm f_{\bar{\psi}}) - |\mathcal{M}_{\psi\bar{\psi}\to X\bar{X}}|^2 f_\psi f_{\bar{\psi}}(1 \pm f_X)(1 \pm f_{\bar{X}})\Big]. \tag{1.45}$$

The above expression can be simplified using the following approximations:
(i) No CP Violation: Assuming CP symmetry in the interaction processes, the CPT theorem ensures that the matrix elements for forward and reverse reactions are equal:

$$|\mathcal{M}_{\psi\bar{\psi}\to X\bar{X}}|^2 = |\mathcal{M}_{X\bar{X}\to\psi\bar{\psi}}|^2. \tag{1.46}$$

(ii) Negligible Quantum Statistics Effects: In the early Universe, Pauli blocking and Bose enhancement effects are insignificant, allowing the approximation $1 \pm f_a \approx 1$
(iii) Thermal Equilibrium of the SM Particles: Since the SM particles remain in equilibrium, their distribution functions simplify to:

$$f_X = f_X^{\rm eq} = e^{-E_X/T}, \qquad f_{\bar{X}} = f_{\bar{X}}^{\rm eq} = e^{-E_{\bar{X}}/T}. \tag{1.47}$$

Finally, the presence of delta function enforces energy conservation, $E_\psi + E_{\bar{\psi}} = E_X + E_{\bar{X}}$,

which allows the collision term to be written in the following form:

$$\frac{dn_\psi}{dt}+3\mathcal{H}n_\psi=\int\frac{d^3\mathbf{p}_\psi}{(2\pi)^3 2E_\psi}\frac{d^3\mathbf{p}_{\bar\psi}}{(2\pi)^3 2E_{\bar\psi}}\frac{d^3\mathbf{p}_X}{(2\pi)^3 2E_X}\frac{d^3\mathbf{p}_{\bar X}}{(2\pi)^3 2E_{\bar X}}(2\pi)^4\delta^{(4)}(p_\psi+p_{\bar\psi}-p_X-p_{\bar X})$$
$$\times|\mathcal{M}_{\psi\bar\psi\to X\bar X}|^2\left(f_\psi^{\rm eq}f_{\bar\psi}^{\rm eq}-f_\psi f_{\bar\psi}\right). \tag{1.48}$$

Rewriting this in terms of the actual DM number density (n_ψ) and the equilibrium number density $n_\psi^{\rm eq}$ we obtain

$$\frac{dn_\psi}{dt}+3\mathcal{H}n_\psi=-\langle\sigma v\rangle_{\psi\bar\psi\to X\bar X}\left[n_\psi^2-(n_\psi^{\rm eq})^2\right], \tag{1.49}$$

where $n_\psi^{\rm eq}$ represents the equilibrium DM number density:

$$n_\psi^{\rm eq}=\frac{g_{\rm eff}T^3}{2\pi^2}\left(\frac{m_\psi}{T}\right)^2K_2(m_\psi/T), \tag{1.50}$$

with $g_{\rm eff}=g\ (3g/4)$ for bosonic (fermionic) DM and $\langle\sigma v\rangle_{\psi\bar\psi\to X\bar X}$ refers to the thermally averaged cross section for the process $\psi\bar\psi\to X\bar X$, given by [79–81]

$$\begin{aligned}\langle\sigma v\rangle_{\psi\bar\psi\to X\bar X}=&\frac{1}{(n_\psi^{\rm eq})^2}\int\frac{d^3\mathbf{p}_\psi}{(2\pi)^3 2E_\psi}\frac{d^3\mathbf{p}_{\bar\psi}}{(2\pi)^3 2E_{\bar\psi}}\frac{d^3\mathbf{p}_X}{(2\pi)^3 2E_X}\frac{d^3\mathbf{p}_{\bar X}}{(2\pi)^3 2E_{\bar X}}(2\pi)^4\\&\times\delta^{(4)}(p_\psi+p_{\bar\psi}-p_X-p_{\bar X})|\mathcal{M}_{\psi\bar\psi\to X\bar X}|^2e^{-(E_\psi+E_{\bar\psi})/T}\\=&\frac{1}{8Tm_\psi^4K_2^2(\frac{m_\psi}{T})}\int_{4m_\psi^2}^\infty\sqrt{s}(s-4m_\psi^2)K_1\left(\frac{\sqrt{s}}{T}\right)\sigma_{\psi\psi\to XX}ds,\end{aligned} \tag{1.51}$$

where $K_{1,2}$ denote the modified Bessel functions, s is the center of mass energy and T is the temperature of the thermal bath. It is always convenient to transform the BE in terms of the dimensionless variable $Y_\psi=n_\psi/\mathcal{S}$ to scale out the effect of cosmic expansion (with $\mathcal{S}$ being the entropy as in Eq. 1.37) as

$$\frac{dY_\psi}{dt}=-\langle\sigma v\rangle_{\psi\bar\psi\to X\bar X}\left[Y_\psi^2-(Y_\psi^{\rm eq})^2\right]. \tag{1.52}$$

Since the thermally averaged cross section depends on the bath temperature T, it is more convenient to introduce another dimensionless variable $x=m_\psi/T$. Assuming a radiation-dominated Universe, the relation between time and x is given by [48]:

$$t=\frac{0.301}{\sqrt{g_*}}\frac{M_{\rm Pl}}{T^2}=\frac{0.301}{\sqrt{g_*}}\frac{M_{\rm Pl}}{m_\psi^2}x^2, \tag{1.53}$$

which results in the final form of BE as

$$\frac{dY_\psi}{dx}=-\frac{x\,\mathcal{S}}{\mathcal{H}(T=m_\psi)}\langle\sigma v\rangle_{\psi\bar\psi\to X\bar X}\left[Y_\psi^2-(Y_\psi^{\rm eq})^2\right], \tag{1.54}$$

where $\mathcal{H}(T=m_\psi)=1.66g_*^{1/2}m_\psi^2/M_{\rm Pl}=\mathcal{H}(T)x^2$. By solving the Boltzmann equation numerically, one can track how a particle evolves with the expansion of the Universe by analyzing the comoving number density Y_ψ. For freeze-out DM, we assume $Y_\psi(x=0)=$

$Y_\psi^{\rm eq}$. Eventually, the yield at the decoupling, $Y_{\rm fo}$, can be derived by solving the BE when

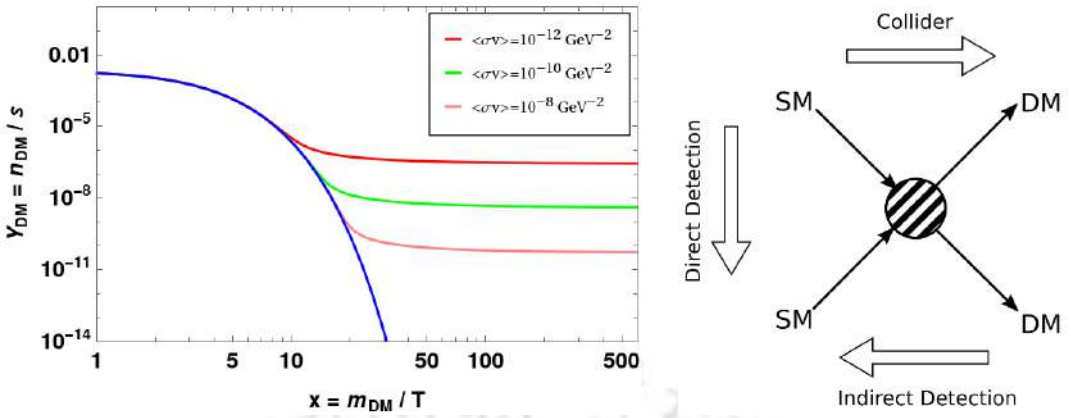

Figure 1.4: Left panel: Freeze-out of WIMP type DM in terms of the abundance Y_ψ. Different colors (Red, Green, Pink) corresponds to different values of annihilation cross-sections, as indicated in the figure. The solid blue line shows the equilibrium abundance $Y_\psi^{\rm eq}$. **Right panel:** Cartoon of DM searches, taken from [82].

$\Gamma(\equiv n_\psi \langle\sigma v\rangle) \ll \mathcal{H}$ and remains constant thereafter. This behavior is shown in the left panel of Fig.1.4 for a DM mass of 1 GeV with different values of the thermally averaged cross-section. As expected, a larger cross-section leads to a later thermal freeze-out.
The current DM relic density can then be expressed in terms of this thermal yield

$$\begin{aligned} \Omega h^2 &= \frac{m_\psi Y_\psi(x\to\infty)}{\mathcal{S}_0\rho_c} h^2 \\ &= 2.75\times10^8 \left(\frac{m_\psi}{\rm GeV}\right) Y_\psi(x\to\infty), \end{aligned} \tag{1.55}$$

where $\rho_c = 1.05\times10^{-5}h^2$ GeV cm^{-3} is the critical energy density and $\mathcal{S}_0 = 2970$ cm^{-3} corresponds to the present entropy density of the Universe. WMAP [50] and Planck [66] data indicates that $\Omega_{\rm DM}h^2 = 0.120\pm0.001$ [10] at 68% confidence level, with $h = (\mathcal{H}_0/100)\,{\rm kms}^{-1}{\rm Mpc}^{-1}$. Interestingly, if a DM particle has a mass around the weak scale and interacts via weak interaction-mediated annihilation, its predicted relic abundance matches the CMB observations. This remarkable coincidence is known as the *WIMP miracle*.

It is pertinent here to briefly discuss about the detection prospects of DM. The detection of WIMP dark matter relies on three main approaches: direct detection, indirect detection, and collider searches, as shown in cartoon Fig. 1.4 (right panel). The interactions that explain the correct relic density for DM are also capable of producing DM particles at colliders, like LHC, leading to missing energy signals. Direct detection experiments like LUX [83], XENON-1T [84] and PandaX-II [85,86] etc. to observe nuclear recoils caused by WIMPs scattering off atomic nuclei. The most recent direct search comes from LUX-ZEPLIN (LZ) [87]. On the other hand, indirect detection looks for signals from WIMP annihilation or decay into stable particles, such as gamma rays, neutrinos, electrons etc.via experiments like PAMELA [88], Fermi-LAT [89], MAGIC [90] etc. Despite these extensive efforts, no conclusive evidence for WIMPs has been found, pushing searches toward lower interaction cross-sections and alternative DM candidates.

1.3.2.2 Freeze-in Mechanism

Contrary to the idea of DM freeze-out, where DM was assumed to remain in thermal equilibrium with the visible sector in the early universe, the freeze-in mechanism occurs when the interaction between DM and the thermal bath is extremely feeble, $\sim \mathcal{O}(10^{-10})$. In this case, DM is never able to attain thermal equilibrium and therefore, is assumed to be absent or present with negligible abundance in the early Universe, and then gradually produced from the decays or annihilations of bath particles. This process, first proposed by Hall et al. [91] in 2009, is known as freeze-in, and the corresponding DM candidate is called a feebly interacting massive particle (FIMP).

To understand how FIMP evolves over time, we again refer to the Boltzmann equation, as given in Eq.1.42. Let us consider a simple case, where DM (ψ) is primarily produced through the decay of a heavier thermal bath particle (X) via $X \to \psi\psi$. Since the interaction strength is very small, annihilation processes contributing to DM production can be ignored. Additionally, one can safely assume that the initial abundance of DM is zero or negligible, due to such feeble coupling. Under these conditions, the collision term in Eq. 1.41 simplifies to:

$$\mathbf{C}(f_\psi; f_\psi, f_X) = \int \frac{d^3\mathbf{p}_\psi}{(2\pi)^3 2E_\psi} \frac{d^3\mathbf{p}_X}{(2\pi)^3 2E_X} (2\pi)^4 \delta^{(4)}(p_X - 2p_\psi) \Big[|\mathcal{M}_{X\to\psi\psi}|^2 f_X (1 \pm f_\psi)^2 \Big]. \tag{1.56}$$

By assuming $1 \pm f_\psi \sim 1$ and $f_X = f_X^{\rm eq}$, and expressing Eq. 1.42 in terms of the comoving number density $Y_\psi = n_\psi/\mathcal{S}$, the Boltzmann equation simplifies to:

$$\frac{dY_\psi}{dx} = \frac{1}{\mathcal{H}x} Y_X^{\rm eq} \langle \Gamma_{X\to\psi\psi} \rangle, \tag{1.57}$$

which describes the evolution of the FIMP DM yield Y_ψ with respect to the dimensionless parameter $x = M_X/T$, where M_X denotes the mass of the decaying particle, X. Here the thermal average of the decay width of the X particle, $\langle \Gamma_{X\to\psi\psi} \rangle$, is given by $\Gamma_{X\to\psi\psi} K_1(x)/K_2(x)$. As shown in Fig. 1.5, starting from negligible abundance, the DM yield increases due to the decay of X and eventually saturates when the number density of X particle becomes Boltzmann-suppressed, $\sim e^{-M_X/T}$. Unlike the WIMP scenario, in this case, the DM yield increases as the coupling between DM and bath particle, $\lambda_{X\psi}$ (or, the decay width) increases. Once the asymptotic yield $Y_\psi(\infty)$ is obtained, one can use Eq. 1.55 to calculate the DM relic density.

So far, we have discussed the DM freeze-in production from the decay or annihilation of the bath particles in the context of renormalizable interactions. To be specific, this kind of freeze-in production is referred as *IR freeze-in*. However, there exist another class of popular freeze-in mechanism, called *Ultra Violet (UV) freeze-in* [92], where DM production is driven by non-renormalizable higher-dimensional interactions, which, in turn, suggests that the thermal bath temperature remains lower than the mass of the mediator connecting DM to the SM. Being connected to such effective interactions, unlike IR freeze-in, UV freeze-in does not require extremely feeble renormalizable coupling. Here, DM is primarily generated through

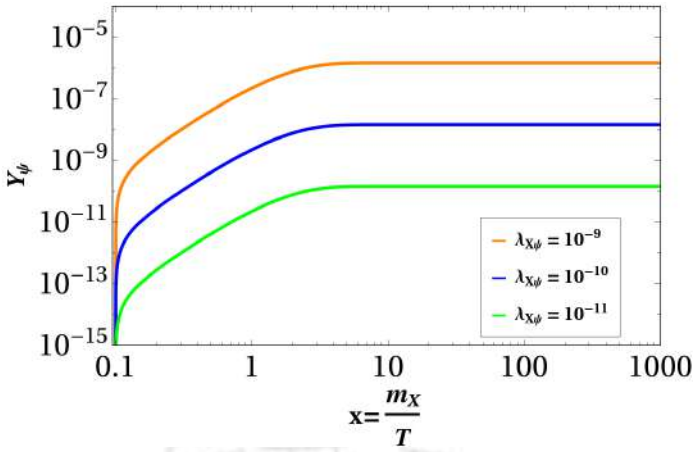

Figure 1.5: Abundance of freeze-in DM (Y_ψ) with respect to $x = M_X/T$ for different choices of $\lambda_{X\psi}$.

scattering processes in the thermal bath, which depend on the bath temperature. As a result, the DM yield in this case is dominated by the highest temperature of the Universe, which is typically taken as the reheating temperature, $T_{\rm RH}$, following a primordial inflation.

Let us consider a toy model, where a scalar DM (χ) is coupled to the thermal bath through the following non-renormalizable higher-dimensional interaction:

$$\mathcal{L}_{d=5} = \frac{1}{\Lambda}\chi\phi\psi_1\psi_2, \tag{1.58}$$

where ϕ is a boson, which is assumed to be in thermal equilibrium, ψ_1 and ψ_2 are two bath fermions, and Λ indicates the characteristic high scale at which the effective operator is generated, which is assumed to be larger than $T_{\rm RH}$. A key contribution to the dark matter yield arises arise from the non-renormalizable operator through a four-particle interaction like $\phi\psi_1 \to \chi\psi_2$. Using the conventional Boltzmann equation in Eq. 1.42, one can investigate the change in DM number density (n_χ) via $\phi\psi_1 \to \chi\psi_2$ process as

$$\frac{dn_\chi}{dt} + 3\mathcal{H}n_\chi = \int \frac{d^3\mathbf{p}_{\psi_1}}{(2\pi)^3 2E_{\psi_1}} \frac{d^3\mathbf{p}_{\phi}}{(2\pi)^3 2E_{\phi}} \frac{d^3\mathbf{p}_{\psi_2}}{(2\pi)^3 2E_{\psi_2}} \frac{d^3\mathbf{p}_{\chi}}{(2\pi)^3 2E_{\chi}} (2\pi)^4\delta^{(4)}(p_{\psi_1} + p_\phi - p_{\psi_2} - p_\chi)$$
$$\times \left[|\mathcal{M}_{\phi\psi_1\to\chi\psi_2}|^2 f_\phi f_{\psi_1} - |\mathcal{M}_{\chi\psi_2\to\phi\psi_1}|^2 f_\chi f_{\psi_2}\right]. \tag{1.59}$$

Assuming the states in thermal bath (ψ_1, ψ_2, ϕ) are Maxwell-Boltzmann distributed ($f_i \sim e^{-E_i/T}$) and negligible abundance of DM ($f_\chi \simeq 0$), we neglect the latter term in Eq. 1.59 (proportional to f_χ) and rewrite the Boltzmann equation as [80, 91]

$$\frac{dn_\chi}{dt} + 3\mathcal{H}n_\chi \approx \frac{T}{2048\pi^6}\int ds\, d\Omega\, \sqrt{s}|\mathcal{M}_{\phi\psi_1\to\chi\psi_2}|^2 K_1(\sqrt{s}/T), \tag{1.60}$$

where s represents the center of mass energy of the interaction at temperature T. Assuming the masses of the relevant particles are negligible compared to the temperature,the squared matrix element can be expressed in a simplified form as:

$$|\mathcal{M}_{\phi\psi_1\to\chi\psi_2}|^2 \sim \frac{s}{\Lambda^2}, \tag{1.61}$$

such that [80,91]

$$\frac{dn_\chi}{dt} + 3\mathcal{H}n_\chi \approx \frac{T}{512\pi^5}\int_0^\infty ds\, s^{3/2}K_1(\sqrt{s}/T) \simeq \frac{T^6}{16\pi^5\Lambda^2}. \tag{1.62}$$

By expressing $Y_\chi = n_\chi/\mathcal{S}$, changing the variable from t to T and integrating over s, one arrives at

$$\frac{dY_{\rm UV}}{dT} \simeq -\frac{1}{\mathcal{S}\mathcal{H}T}\frac{T^6}{16\pi^5\Lambda^2}. \tag{1.63}$$

Integrating this from the maximum temperature of the Universe (typically $T_{\rm RH}$) down to the present time ($T_0 \approx 0$) and using the expressions for $\mathcal{S}$ and $\mathcal{H}$, the present-day DM yield can be determined [91,92]

$$Y_{\rm UV} \simeq \frac{180}{1.66\ (2\pi)^7 g_\star^{\mathcal{S}}\sqrt{g_\star^\rho}}\left(\frac{T_{\rm RH}M_{\rm Pl}}{\Lambda^2}\right), \tag{1.64}$$

which can be directly translated to DM relic density through Eq. 1.55, as mentioned earlier.

Since this thesis focuses on the phenomenology of pNGBs, which inherently involves explicit global symmetry breaking terms in higher order, we will come across UV freeze-in-like DM scenarios in the later chapters. Therefore, in this thesis, UV freeze in plays a crucial role in the DM phenomenology. There exist another well-known DM production mechanism, known as the *misalignment mechanism* [93–97], which is particularly relevant in the context of very light pNGBs such as QCD axion and ALPs. Unlike WIMP or FIMP production, which involves particle interactions like annihilation or decay, in misalignment mechanism, DM axions are produced in the early Universe as a result of coherent oscillations of the axion field. we will expound it later while discussing axion and ALPs. For now, in the next section, we delve into another key deficit of the SM, the generation of neutrino mass, with a focus on the type-I seesaw mechanism, which plays a crucial role in leptogenesis and will be important in Chapter 2.

1.4 The Origin of Neutrino Mass

Neutrinos are unique among the SM fermions which are electrically neutral and do not have right handed counterparts. This prevents the construction of a renormalizable Dirac type mass term for the neutrinos (like other fermions in the SM) and therefore, neutrinos remain massless in SM. However, several experiments like kamLand [98], Super-Kamiokande [99], K2K [100], etc. observed deficits in different type of neutrino fluxes (emerging from various sources) compared to the predicted amounts of flux, which suggests that one flavor state of neutrino must have oscillated into some other neutrino flavor states while propagating large distances. This phenomenon is known as *neutrino oscillation*, which contradicts the SM prediction that neutrinos are massless. Neutrino oscillation occurs when neutrinos have different masses and their flavor states are mixtures of the mass eigenstates. If, for example, the masses of two states are same, they will evolve identically and no oscillation will happen. Similarly, if the flavor and mass states match exactly (no mixing), then each flavor will evolve independently without changing into another. Therefore, with non-zero neutrino masses and mixing, one can include additional rotation for leptons in analogy with the quark sector

(in 1.20) as

$$e_{L_\alpha} = (U_e)_{\alpha i} e'_{e_i};\ \ \nu_{L_\alpha} = (U_\nu)_{\alpha i} \nu'_{L_i} \ \text{ and } \ e_{R_\alpha} = (V_e)_{\alpha i} e'_{R_i}, \tag{1.65}$$

substituting these rotations from between flavor and mass eigenstates back in Eq.(1.4), one obtain the leptonic charged current interactions as the following

$$\mathcal{L}_{\text{CC}}^{\text{leptons}} = \frac{g_2}{\sqrt{2}} \left(\overline{e_L}\ \overline{\mu_L}\ \overline{\tau_L}\right) \gamma^\mu W_\mu^+ \begin{pmatrix} \nu_{e_L} \\ \nu_{\mu_L} \\ \nu_{\tau_L} \end{pmatrix} = \frac{g_2}{\sqrt{2}} \left(\overline{e'_L}\ \overline{\mu'_L}\ \overline{\tau'_L}\right) U_e^\dagger \gamma^\mu W_\mu^+ U_\nu \begin{pmatrix} \nu'_{e_L} \\ \nu'_{\mu_L} \\ \nu'_{\tau_L} \end{pmatrix}. \tag{1.66}$$

Therefore, analogous to the CKM matrix in the quark sector, here, $U = U_e^\dagger U_\nu$ represents the mixing matrix in the lepton sector and is widely known as the Pontecorvo-Maki-Nakagawa-Sakata (PMNS) matrix [101].

Although the lightest neutrino mass and is unknown, the total neutrino mass is bounded from above by cosmological observations as: $\sum m_\nu < 0.12\ (0.15)$ eV, considering a normal (inverted) neutrino mass hierarchy [63, 102]. Therefore, to incorporate non-zero neutrino mass, one must go beyond the SM by adding new particles or by allowing higher-dimensional, non-renormalizable operators, or a combination of both. Additionally, the nature of neutrino, whether it is Dirac or Majorana type, is not clear. For Dirac neutrinos, one needs to introduce three gauge singlet right handed neutrinos (RHNs) N_R to allow the neutrino Yukawa interaction:

$$-\mathcal{L}_{\text{Dirac}} = y^\nu \overline{\ell_L} \widetilde{H} N_R + H.c.. \tag{1.67}$$

While this interaction preserves lepton number, the neutrino Yukawa coupling, y^ν, needs to be very small ($\sim \mathcal{O}(10^{-12})$) in this case to remain consistent with the observed order of neutrino mass. On the other hand, being electrically neutral, neutrinos could be their own antiparticle, indicating their possible Majorana nature. In that case, even though a direct mass term like $m\overline{\nu_L}\nu_L^C$ is forbidden by the SM gauge symmetry, one can write a gauge invariant dimension-5 Weinberg operator $y^\nu(\ell_L H)(H\ell_L)/\Lambda$ [103] (with Λ being some high cut-off scale in the theory) to generate small neutrino masses while violating lepton number by two units. Unlike Dirac neutrinos, Majorana neutrinos do not require an 'unnatural' Yukawa coupling y^ν as long as Λ is very high ($\mathcal{O}(10^{14})$ GeV). This effective framework can be embedded into UV-complete models, which are widely known as seesaw mechanisms. There exist several novel variations of seesaw mechanism in the existing literature, which include Type-I seesaw [104–110], Type-II seesaw [110–114], Type-III seesaw [115], inverse seesaw [116,117] etc. Neutrino masses can also rise at the loop level, as proposed by some of the models like Zee-Wolfenstein Model [118], Zee-Babu Model [119,120], Ma-Model [121]. In the next subsection, we will particularly focus on the type-I seesaw mechanism which will be relevant in Chapter 2 of this thesis.

1.4.1 Type-I Seesaw Mechanism

Type-I seesaw mechanism [104, 107–110, 122] remains the most simple and attractive one to explain the generation of tiny neutrino mass by connecting it with the presence of very heavy mass scale. In this framework, the particle spectrum of the SM is extended by three[2] SM gauge singlet and electrically neutral RHNs, N_{R_i} with $i = 1, 2, 3$. Therefore, the relevant Lagrangian for neutrino mass can be written as

$$-\mathcal{L}_{\text{seesaw}} = y^{\nu}_{\alpha i}\overline{\ell_{L\alpha}}\widetilde{H}N_{R_i} + \frac{1}{2}M_{ij}\overline{N^c_{R_i}}\,N_{R_j} + H.c. \tag{1.68}$$

Here, the first term corresponds to the neutrino Yukawa interaction, while the second term implies the bare Majorana mass for RHNs, which is gauge-invariant (yet lepton-number violating) term due to the zero isospin and hypercharges of RHNs. As the Higgs field acquires a *vev*, the neutrino mass terms can be arranged as

$$\mathcal{L}_{mass} = \frac{1}{2}(\overline{\nu_L}\;\;\overline{N^c_R}) \begin{pmatrix} 0 & m_D \\ (m_D)^T & M_R \end{pmatrix} \begin{pmatrix} \nu^c_L \\ N_R \end{pmatrix} + H.c., \tag{1.69}$$

where $(m_D)_{\alpha i} = y^{\nu}_{\alpha i}v/\sqrt{2}$ denotes the Dirac mass, which is a 3×3 matrix. Similarly, for 3 added RHNs, M_R is also a 3×3 matrix, which makes the neutrino mass matrix in Eq. 1.69 a 6×6 matrix. Considering $m_D \ll M_R$, the block-diagonalization of the 6×6 neutrino mass matrix leads to two non-zero eigenvalue matrices of order 3×3 each, given by

$$m_{\nu} \simeq -m_D M_R^{-1}(m_D)^T, \tag{1.70a}$$

$$M_{\text{heavy}} \simeq M_R. \tag{1.70b}$$

The light neutrino mass matrix m_ν can be further diagonalized to obtain its mass eigenvalues and mixing:

$$U^*_{\nu} m_{\nu} U^{\dagger}_{\nu} = diag(m_1, m_2, m_3) = m^d_{\nu}, \tag{1.71}$$

where $m^d_\nu = diag(m_1, m_2, m_3)$ represents the mass eigenvalues. If the charged lepton mass matrix is assumed to be diagonal, U_ν coincides with the PMNS matrix U. Similarly, the heavy RHN matrix M_{heavy} can be diagonalized via orthogonal transformation with a Unitary matrix V_N, given by

$$V^*_N M_{\text{heavy}} V^{\dagger}_N = diag(M_1, M_2, M_3) = M^d_R. \tag{1.72}$$

1.4.1.1 Casas-Ibarra Parametrization

As seesaw models involve large number of unknown parameters, it is necessary to parametrize them. One of the most convenient method is to use the Casas-Ibarra Parametrization [124],

[2] In a minimal type-I seesaw model, two RHNs are sufficient to account for the origin of the neutrino mass [123].

which combines both high and low-energy parameters. It uses the diagonal matrices m_ν^d, M_R^d, the PMNS matrix, U and an unknown complex orthogonal matrix, $\mathcal{R}$.

To illustrate the parametrization, one can employ Eqs. 1.70a and 1.71 and consider $M_R \simeq M_R^d$ to find

$$\begin{aligned} m_\nu^d &= U^*[-m_D M_R^{-1}(m_D)^T]U^\dagger \\ \implies 1 &= -\frac{v^2}{2}\left[(m_\nu^d)^{-1/2}U^* y^\nu (M_R^d)^{-1/2}\right]\left[(M_R^d)^{-1/2}(y^\nu)^T U^\dagger (m_\nu^d)^{-1/2}\right] \\ \implies 1 &= \left[-i\frac{v}{\sqrt{2}}(m_\nu^d)^{-1/2}U^* y^\nu (M_R^d)^{-1/2}\right]\left[-i\frac{v}{\sqrt{2}}(m_\nu^d)^{-1/2}U^* y^\nu (M_R^d)^{-1/2}\right]^T \end{aligned} \tag{1.73}$$

Therefore, denoting the combination $\left[-i\frac{v}{\sqrt{2}}(m_\nu^d)^{-1/2}U^* y^\nu (M_R^d)^{-1/2}\right]$ as a complex orthogonal matrix $\mathcal{R}$, the Yukawa coupling matrix (y^ν) can be expressed as following

$$y^\nu = i\frac{\sqrt{2}}{v}U^\dagger (m_\nu^d)^{-1/2}\mathcal{R}(M_R^d)^{-1/2}, \tag{1.74}$$

which is widely known as the Casas-Ibarra parametrization. We will utilize it in chapter 2.

Apart from generating light neutrino masses, the type-I seesaw mechanism is closely connected to *Baryogenesis via Leptogenesis*, the most prominent way to address another captivating issue unsolved within the SM, the matter-antimatter asymmetry of the Universe, which we explore in the thesis works. To provide a better understanding of this issue, we discuss it below.

1.5 Matter-Antimatter Asymmetry of the Universe

The near-identical nature of the fundamental interactions for particles and antiparticles indicates that the Universe should contain matter and antimatter in equal amounts. In that case, large-scale matter-antimatter annihilations would have taken place throughout the Universe, producing strong and detectable γ-ray emission. However, we do not observe any significant γ-ray emission due to matter-antimatter annihilation in our solar system [125], which suggests a lack of antimatter. While antimatter can be observed in cosmic rays and in particle accelerators only, a significant amount of asymmetry exists between the matter and the antimatter, which can be quantified by the baryon to photon ratio: $\eta_B = (n_B - n_{\bar{B}})/n_\gamma$ or the baryon to entropy ratio: $Y_B = (n_B - n_{\bar{B}})/\mathcal{S}$.

Cosmological observations provide two precise and independent determinations of this asymmetry:

1. **BBN:** The primordial abundances of light nuclei (^{4}He, D, ^{3}He, ^{7}Li) formed during BBN are highly sensitive to η_B as the rate at which protons and neutrons combine into nuclei depends on the baryon number density. Therefore, by comparing the observed abundances of these light nuclei with theoretical predictions, one can extract η_B, which gives [126]

$$\eta_B^0 = (5.7 - 6.5)\times 10^{-10}, \quad Y_B^0 = (8.2 - 8.8)\times 10^{-11} \quad (95\%\ \text{CL}). \tag{1.75}$$

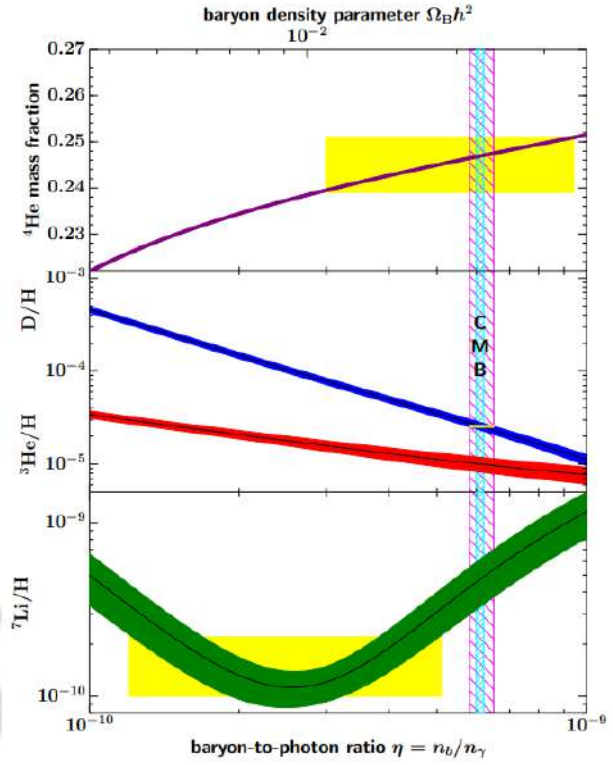

Figure 1.6: Predictions of the primordial abundances of ^{4}He, D, ^{3}He, and^{7}Li as a function of cosmic baryon density in the standard model of Big-Bang nucleosynthesis. The bands show the 95% CL range [126], with yellow boxes representing the observed light element abundances. The narrow blue vertical band corresponds to the CMB measurement of the cosmic baryon density, and the wider magenta band represents the D+4He BBN concordance range (at 95% CL). Adapted from [127].

2. **CMB**: Formed shortly after recombination, the CMB is the relic radiation from when the Universe cooled enough for neutral atoms to form. The acoustic oscillations of the photon-baryon fluid prior to recombination imprint patterns in the CMB temperature anisotropies. The relative heights of these acoustic peaks depend sensitively on the baryon density. Therefore, by comparing highly precise CMB measurements from satellites such as WMAP and Planck with detailed theoretical models, cosmologists extract η_B with remarkable accuracy as [63]

$$\eta_B^0 = (6.12 \pm 0.04) \times 10^{-10} \quad \text{or} \quad Y_B^0 = (8.7 \pm 0.06) \times 10^{-11}. \tag{1.76}$$

Fig 1.6 illustrates the predicted primordial abundances of ^{4}He, D, ^{3}He, and^{7}Li as functions of baryon density in the standard BBN model. Here, the narrow blue vertical band represents the cosmic baryon density measured by CMB (as presented in Eq. 1.76), while the wider magenta band corresponds to the observation from BBN at 95% CL [126]. The overlap of these bands highlights the consistency between CMB and BBN measurements, despite the significant time gap between these two epochs. This agreement provides a striking confirmation of the observed baryon asymmetry.

As any pre-existing asymmetry between matter and antimatter would have been erased by inflation, a possible way to explain the observed baryon asymmetry is to assume that the Universe began with an equal amounts of matter and antimatter, but eventually, an excess

of baryon over antibaryon was dynamically generated. This process is known as *baryogenesis*. There are three necessary ingredients required for dynamical generation of baryon asymmetry, widely known as the Sakharov condition [128], as the following:

1. **Baryon Number (B) Violation:** If the Universe began with no initial asymmetry and all the fundamental interactions preserved baryon number, then a baryon asymmetry cannot be developed unless some fundamental interaction violated baryon number.

2. **C and CP violation:** To dynamically generate a baryon asymmetry, the processes that produce baryons and those that produce antibaryons must proceed at different rates. If charge conjugation symmetry (C) is conserved, then particles and antiparticles would always behave identically. This means every baryon-generating process would have an exactly corresponding antibaryon-generating process with the same probability, even if CP is violated. In that case, no net baryon asymmetry can be generated, because any excess generated through CP violation would be exactly balanced by its C-conjugated process. On the other hand, if only C is violated but CP is conserved, then although particles and antiparticles may behave differently, the rates for a particle (with baryon number B) and its CP-conjugate process generating an antiparticle (with baryon number $-B$) would be equal. As a result, no net baryon asymmetry would have been generated. Thus, to generate a baryon asymmetry, both C and CP need to be violated.
3. **Departure from equilibrium:** Even with the above two conditions, the baryon asymmetry generated by these processes would evolve with the temperature of the Universe. If the system remains in thermal equilibrium throughout, every interaction creating an asymmetry would be canceled by its reverse process, erasing the baryon asymmetry entirely. Therefore, to preserve the generated asymmetry, the system must undergo a departure from equilibrium, which can be achieved by the criteria, $\Gamma < \mathcal{H}$, as discussed in subsection 1.2.2.

In the SM, lepton number (L) and baryon number (B) are violated non-perturbatively (via sphaleron process), while both C and CP are violated by weak interactions. However, the amount of CP violation in the CKM matrix is too small to account for the observed baryon asymmetry. Additionally, the electroweak phase transition (EWPT), which could provide the necessary departure from equilibrium, needed to strongly fist-order [129,130], which is however not possible for the Higgs boson mass of 125 GeV [8,9,30]. Hence, the SM fails to generate enough baryon asymmetry and one needs to go beyond the SM. There exist several possibilities in the literature which have been proposed to explain the matter-antimatter asymmetry [42,43,131–136]. Among them, a widely studied approach is *baryogenesis via leptogenesis* [43] due to its strong connection with the type-I seesaw mechanism.

The Type-I seesaw mechanism naturally satisfies the three Sakharov conditions: (i) lepton number is violated through the Majorana mass terms of RHNs, (ii) the complex nature of neutrino Yukawa coupling sources the CP violation and (iii) the decay process of the RHNs into the SM Higgs and the SM leptons at $T \lesssim M_N$ can occur out-of-equilibrium as a result of the expansion of the Universe. This leads to the generation of a finite amount of lepton asymmetry, which is then partially converted into a baryon asymmetry via the

non-perturbative electroweak sphaleron process.

1.5.1 Baryogenesis via leptogenesis

The relevant Lagrangian in this case is same as given in Eq. 1.68. Due to the Yukawa interaction RHNs could be abundantly produced in the early Universe ($T \gg M_N$) via inverse decays ($\ell_{L_\alpha} + H \to N_i$ and $\bar{\ell}_{L_\alpha} + \bar{H} \to N_i$) and $2-2$ scatterings mediated via Higgs boson. Then, as the temperature goes below the masses of RHNs, the out of equilibrium decays of the respective heavy RHNs ($N_i \to \ell_{L_\alpha} + H$ and $N_i \to \bar{\ell}_{L_\alpha} + \bar{H}$), due to the same Yukawa interaction, generate a finite amount of CP asymmetry in each lepton flavor direction. The CP asymmetry can be parametrized as

$$\varepsilon_i^\alpha = \frac{\Gamma(N_i \to \ell_{L_\alpha} + H) - \Gamma(N_i \to \bar{\ell}_{L_\alpha} + \bar{H})}{\sum_\alpha \left\{\Gamma(N_i \to \ell_{L_\alpha} + H) + \Gamma(N_i \to \bar{\ell}_{L_\alpha} + \bar{H})\right\}}, \tag{1.77}$$

where $\Gamma(N_i \to \ell_{L_\alpha} + H)$ and $\Gamma(N_i \to \bar{\ell}_{L_\alpha} + \bar{H})$ correspond to the decay width of the process $N_i \to \ell_{L_\alpha} + H$ and $N_i \to \bar{\ell}_{L_\alpha} + \bar{H}$, respectively. The denominator here represents the total decay width of N_i and at the tree level, can be estimated as

$$\sum_\alpha \left\{\Gamma(N_i \to \ell_{L_\alpha} + H) + \Gamma(N_i \to \bar{\ell}_{L_\alpha} + \bar{H})\right\} = \frac{(y^{\nu\dagger} y^\nu)_{ii}}{8\pi} M_i. \tag{1.78}$$

To generate a finite amount of CP asymmetry, both tree-level and one-loop level decays of

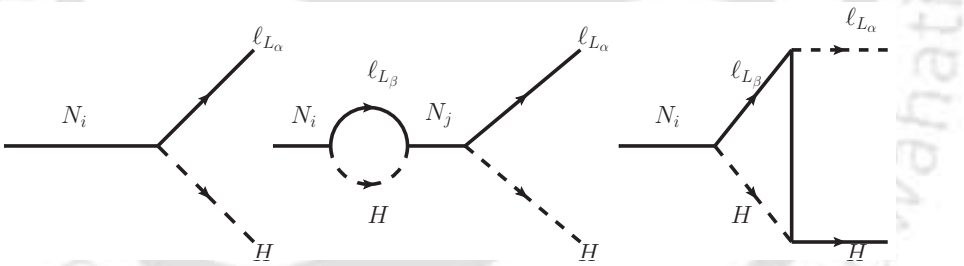

Figure 1.7: Tree level and one-loop level Feynman diagrams for the decay of the RHNs.

RHNs must be considered, taking into account self-energy and vertex corrections (shown in 1.7), as the asymmetry vanishes at tree level. The CP asymmetry then arises from the interference of the tree-level and one-loop level decay amplitudes. Importantly, at least two RHNs are needed for a non-zero CP asymmetry. In presence of a hierarchical RHN mass scenario ($M_1 < M_2 < M_3$), the net asymmetry arises only from the decays of lightest RHN (N_1) as it stays in thermal equilibrium for a longer period of time, thereby erasing the asymmetries generated by N_2 and N_3 through washout effects. Though the net asymmetry can still be affected by lepton-number-violating $2 \to 2$ scatterings. Once a net lepton asymmetry is established, sphaleron interactions convert it into a baryon asymmetry. In Chapter 2, we provide a detailed discussion of such thermal leptogenesis, including the generation and evolution of asymmetry through Boltzmann equations in the context of our work.

Apart from the conventional leptogenesis introduced by Fukugita and Yanagida [43], it is pertinent here to mention two other variants of leptogenesis, which we have explored

in this thesis: (a) *resonant leptogenesis*, where CP asymmetry is resonantly enhanced due to two nearly degenerate heavy Majorana neutrinos, and (b) *spontaneous leptogenesis*, where a dynamical CPT violation in the early Universe generates a lepton asymmetry while lepton number violation remains in thermal equilibrium. We will discuss these mechanisms in detail in Chapter 2 and Chapter 3, respectively.

1.6 New Physics via Light Scalars: Pseudo-Nambu-Goldstone Bosons

So far, we have explored some of the key unresolved issues of the SM, each providing strong motivation to look for the BSM physics. Starting with the quest of dark matter, it has long been guided by the WIMP paradigm and similar dark matter candidates. However, as discussed earlier, the non-observation of WIMPs in direct detection experiments (as can be seen from Fig. 1.8, taken from the latest studies [87, 137]) has led the particle physics community to explore alternative dark matter candidates. On the other hand, the most well-known explanation for the origin of neutrino mass, the type-I seesaw mechanism, relies on the presence of extremely heavy right handed neutrinos. Similarly, the leading solution of the existing matter-antimatter asymmetry of the Universe, baryogenesis via leptogenesis, involves the decay of new heavy leptonic states, such as the RHNs in the type-I seesaw mechanism. In the simplest seesaw leptogenesis scenario, successful baryogenesis requires Majorana masses to be $M_N \gtrsim 10^9$ GeV [138], making direct experimental tests of these models extremely challenging. With no clear idea on the scale of new physics, the modern ap-

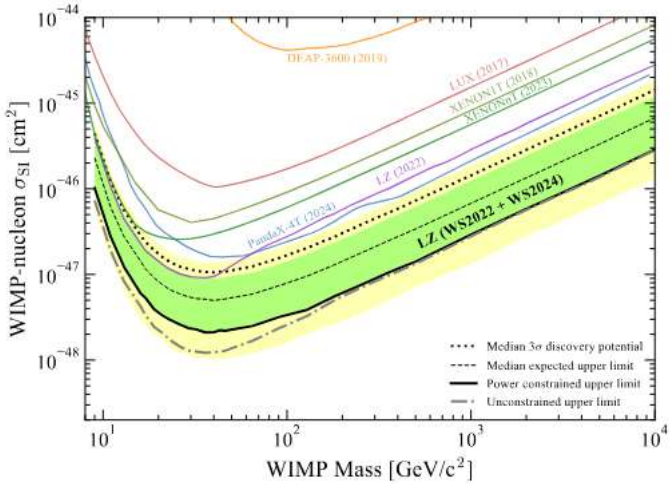

Figure 1.8: Most significant upper bounds on the spin-independent cross section between WIMPs and nucleons. Figure taken from the article reporting the best current bound, obtained by the LUX-ZEPLIN (LZ) collaboration [87, 137].

proach to BSM searches has become more agnostic, heavily driven by effective field theories (EFTs), an useful tool to study the indirect effects of new physics, which might actually exist at some energy scales far beyond the electroweak scale. The standard model EFT (SMEFT) is one such framework, where the SM is treated as a low-energy approximation of a more complete high energy theory, and constraints on new physics can be derived by studying deviations in precision measurements.

Beyond this EFT framework, another promising direction is to consider that new physics appears at lower energy scales in terms of light, feebly interacting particles. Their small masses and feeble couplings can arise naturally from fundamental symmetries or dynamical mechanisms. Such particles can influence astrophysical processes like stellar cooling and may also appear in collider experiments as missing energy or through new signatures if they are short lived. Among these candidates, pseudo-Nambu Goldstone bosons (pNGBs) are particularly well-motivated. These particles naturally emerge from spontaneous breaking of global symmetries and remain light as their masses are tied to explicit symmetry breaking or anomaly. Due to their feeble coupling, naturally suppressed by symmetry breaking scale, pNGBs are ideal candidates for dark matter. Additionally, pNGBs may also appear in various BSM frameworks, including solutions to the strong CP problem (axions), neutrino mass generation (Majorons) and play pivotal role in baryogenesis, and as mediator between the visible and dark sectors. We provide here the background formalism for such pNGBs while their phenomenologies are explored in Chapters 2, 3 and 4.

In the rest of this section, we will discuss the emergence of pNGBs from breaking of global symmetries, followed by a class of models which can naturally accommodate the pNGBs, mainly focusing on Axion and Majoron, and their broader generalization to axion-like particles (ALPs).

1.6.1 Goldstone's Theorem

The Goldstone's theorem asserts that for a continuous global symmetry G, such as $\phi(x) \to e^{i\alpha}\phi(x)$ with a constant $\alpha \in \mathbb{R}$, its spontaneous breaking to its subgroup H automatically leads to the emergence of $\dim(G-H)$ massless particles, one for each broken generators of the theory. This theorem predicts the existence of massless Goldstone bosons.

We now present a classical proof of Goldstone's theorem [139]. Consider a Lagrangian involving fields $\phi_i(x)$, given by

$$\mathcal{L} = \text{derivative terms} - V(\phi_i), \tag{1.79}$$

Assuming ϕ^0 to be the constant field value that minimizes the potential

$$\left(\frac{\partial V}{\partial \phi_i}\right)_{\phi_i(x)=\phi^0} = 0, \tag{1.80}$$

one can expand the potential around this minimum, which yields

$$V(\phi_i) = V(\phi^0) + \frac{1}{2}\sum_{i,j}(\phi_i - \phi^0)(\phi_j - \phi^0)\left(\frac{\partial^2 V}{\partial\phi_i\partial\phi_j}\right)_{\phi^0} + ..., \tag{1.81}$$

where the second derivative matrix, $\left(\frac{\partial^2 V}{\partial\phi_i\partial\phi_j}\right)_{\phi^0}$, is identified as a symmetric mass matrix (m_{ij}^2) for the fields ϕ_i. Since ϕ^0 is a minimum, its eigenvalues are non-negative. Goldstone's theorem can be proved if one can show that each continuous symmetry, which is not a symmetry of the minimum (ϕ^0), leads to a massless mode. In order to do so, we consider an infinitesimal symmetry transformation of the ϕ_i field: $\phi_i \to \phi_i + \delta\phi_i$, which must keep the

original potential $V(\phi_i)$ (as well as the whole Lagrangian in Eq. 1.79) invariant. This yields

$$V(\phi_i) = V(\phi_i + \delta\phi_i) \quad \rightarrow \quad \delta\phi_i \frac{\partial V(\phi)}{\partial \phi_i} = 0. \tag{1.82}$$

Now, taking a derivative with respect to ϕ_j and evaluating at the minimum ($\phi = \phi^0$), we get

$$\left(\frac{\partial\, \delta\phi_i}{\partial \phi_j}\right)_{\phi^0} \left(\frac{\partial V(\phi)}{\partial \phi_i}\right)_{\phi^0} + \delta\phi_i|_{\phi^0} \left(\frac{\partial^2 V}{\partial \phi_j \partial \phi_i}\right)_{\phi^0} = 0. \tag{1.83}$$

The first term goes to zero since ϕ^0 is the minimum of potential. For the other term, one can readily see that if the symmetry leavs the vacuum invariant, then $\delta\phi_i|_{\phi^0} = 0$ and no massless state appears, otherwise, if spontaneous symmetry breaking happens and the vacuum is not symmetric under the original symmetry, then $\delta\phi_i|_{\phi^0} \neq 0$, and hence, we get a zero eigenvalue of the mass matrix m_{ij}, with $\delta\phi_i|_{\phi^0}$ being the corresponding eigenvector. These are the massless Goldstone bosons.

An example: global $U(1)$ symmetry

Let us take a simple example to understand how Goldstone bosons arise from spontaneous symmetry breaking. To do so, we take a complex field, $\phi(x)$, with the Lagrangian

$$\mathcal{L} = \frac{1}{2}(\partial_\mu \phi^\star)(\partial^\mu \phi) + m^2(\phi\phi^\star) - \frac{\lambda}{4}(\phi\phi^\star)^2, \tag{1.84}$$

which remains invariant under the $U(1)$ transformation: $\phi(x) \rightarrow e^{i\alpha}\phi(x)$, with α being a constant. As already argued in Section 1.1.2, the potential in this case, $V(\phi) = -m^2(\phi^\star\phi) + \lambda(\phi^\star\phi)^2$, has a minimum at $|\phi|^2 = m^2/2\lambda = v_\phi/\sqrt{2}$. So, the field ϕ thus acquires a *vev* $\langle\phi\rangle = v_\phi/\sqrt{2}$. Since the vacuum is not symmetric under the original $U(1)$, the symmetry is spontaneously broken and a massless state (a Goldstone boson) is expected.

To illustrate this, we parametrize the original complex field ϕ in polar representation as

$$\phi(x) = \frac{v_\phi + \rho(x)}{\sqrt{2}} e^{ia(x)/v_\phi}, \tag{1.85}$$

where ρ is the radial mode and a is the angular counterpart. Under $U(1)$ transformations, the radial mode stays unchanged but the angular mode obtains a shift symmetry, $a \rightarrow a + v_\phi\alpha$. Hence, the angular mode denotes the excitations along the flat, radial direction of the potential. Plugging the parametrization of ϕ into Eq. 1.84, the kinetic term results

$$\mathcal{L} = \frac{1}{2}(\partial^\mu \rho)(\partial_\mu \rho) + \frac{1}{2}\left(1 + \frac{\rho}{v_\phi}\right)^2 (\partial^\mu a)(\partial_\mu a) - \lambda v_\phi^2 \rho^2 - \lambda v_\phi \rho^3 - \frac{\lambda}{4}\rho^4, \tag{1.86}$$

while $a(x)$ disappears from the potential. Evidently, the radial mode ρ gets a mass $m_\rho^2 = 2\lambda v_\phi^2$, but the angular mode a, which corresponds to moving along the flat direction, remains massless. This excitation is identified as the Goldstone boson. Interestingly, Since $a(x)$ is a function of spacetime, it appears via derivative interactions. Therefore, any process involving a Goldstone boson has amplitudes proportional to its momentum, which vanish

in the limit of zero four-momentum. Also, v_ϕ is the symmetry breaking scale which can be very large. In such a large v_ϕ limit, one finds that the heavy field ρ (with $m_\rho^2 = 2\lambda v_\phi^2$) completely decouples from the light mode a. This suggests that high scale physics can be probed via the low-energy interactions of massless Goldstone mode, without involving the heavy field. We will utilize this feature in the upcoming chapters.
It is important to note that the complex scalar field ϕ can also be written in a linear representation, where it is decomposed as

$$\phi(x) = \frac{1}{\sqrt{2}}[v_\phi + \rho(x) + ia(x)]. \tag{1.87}$$

Substituting this into the Lagrangian in Eq. 1.84 results

$$\mathcal{L} = \frac{1}{2}(\partial^\mu \rho)(\partial_\mu \rho) + \frac{1}{2}(\partial^\mu a)(\partial_\mu a) - \lambda v_\phi^2 \rho^2 - \lambda v_\phi \rho(\rho^2 + a^2) - \frac{\lambda}{4}(\rho^2 + a^2)^2, \tag{1.88}$$

where constant terms are neglected. It is clear that this form of Lagrangian lacks $U(1)$ symmetry as it describes fluctuations around a vacuum aligned along the real axis. As expected, the a remains massless, representing the Goldstone boson.

Although the interaction terms for a seems to be different between the polar (Eq. 1.86) and linear (1.88) representations, physical observables remain the same due to the reparametrization theorem, which states that if there exist two sets of fields $\Phi^A(x)$ and $\widetilde{\Phi}^A(x)$ such that

$$\widetilde{\Phi}^A(x) = \Phi^A(x) + \text{ higher orders in fields}, \tag{1.89}$$

then all the on-shell matrix elements computed in either parametrisation will be identical [140]. To illustrate, we consider the decay of $\rho(p) \to a(p_1) + a(p_2)$, where p and p_1 (and p_2) denote four-momentums of the incoming ρ and two outgoing a particles, respectively. In polar form, the interaction $\rho(\partial^\mu a)(\partial_\mu a)/v_\phi$ (from Eq. 1.86)gives

$$i\mathcal{M}_{\text{polar}} = -\frac{2ip_1.p_2}{v_\phi}, \tag{1.90}$$

where the 2-factor appears due to the presence of two a fields in the interaction term. On the other hand, in linear form, the interaction term $-\lambda v_\phi \rho a$ (for Eq. 1.88) is responsible for the same decay channel, which yields

$$i\mathcal{M}_{\text{linear}} = -2i\lambda v_\phi. \tag{1.91}$$

Using the mass of the radial component ρ as $m_\rho^2 = 2\lambda v_\phi^2$ and on-shell conditions $p^2 = m_\rho^2$ and $p_1^2 = p_2^2 = 0$, we find

$$2\lambda v_\phi = \frac{m_\rho^2}{v_\phi} = \frac{(p_1 + p_2)^2}{v_\phi} = \frac{2p_1.p_2}{v_\phi}, \tag{1.92}$$

which confirms that the amplitudes emerging from both the polar and linear representations are exactly equal. This clarification is important because, for our convenience, we use the linear parametrization in Chapter 2 (related to Majoron phenomenology) and the polar one

in Chapters 3 and 4 (where phenomenology of ALP is discussed). In the following, we will discuss how this massless Goldstone bosons can acquire mass in presence of explicit symmetry breaking.

1.6.2 Explicit Symmetry Breaking and Pseudo-Nambu-Goldstone bosons

The properties of Goldstone bosons discussed so far arise from having an exact global symmetry in the Lagrangian. However, in reality, exact global symmetries are rarely seen in nature. Instead, most physical systems are governed by approximate symmetries, which are explicitly broken at some high energy scale Λ. Such breaking can be captured using effective field theory as an extension of the Standard Model. In some cases, renormalizable soft-breaking terms may also be present. In either case, these explicit symmetry-breaking effects must vanish as $\Lambda \to \infty$, implying that the coefficients of these terms scale as inverse powers of Λ [141].

Moreover, it is broadly believed that global symmetries are violated by quantum gravity. One way to understand this is that global charges can disappear by being absorbed by evaporating black holes or wormholes. On the other hand, local (gauge) charges like electric or magnetic charge are protected by Gauss's law and cannot just disappear, even if the charge falls into a black hole, because a black hole carrying electric charge cannot fully evaporate without violating charge conservation [142]. This leads to the idea that quantum gravity does not break gauge symmetries but break the global ones [142]. As a result, explicit symmetry breaking terms are generated by quantum gravity through higher-dimensional operators suppressed by the Planck scale [143].

A key consequence of such explicit global symmetry breaking is that the Goldstone bosons may acquire a mass as well as non-derivative interactions. Since the breaking is weak (either suppressed by very high scale or soft-breaking terms), the mass is expected to be small. These slightly massive Goldstone bosons are known as pseudo-Nambu Goldstone bosons or pNGBs. For example, let us consider an explicit global symmetry breaking term

$$V_{\text{soft}-\text{breaking}} = -\frac{m^2}{4}(\phi^2 + \phi^{\star 2}), \tag{1.93}$$

which is a soft-breaking term because the term $(\phi^2+\phi^{\star 2})$ has mass dimension less than four. Using the polar form of ϕ from Eq. 1.85, this term yields

$$\begin{aligned} V_{\text{soft}-\text{breaking}} &= -\frac{m^2}{4}(v_\phi + \rho)^2 \cos\left(\frac{2a}{v_\phi}\right) \\ &= -\frac{m^2}{4} v_\phi^2 \left(1 + 2\frac{\rho}{v_\phi} + \frac{\rho^2}{v_\phi^2}\right)\left(1 - 2\frac{a^2}{v_\phi^2} + \ldots\right), \end{aligned} \tag{1.94}$$

which leads to a non-zero pNGB mass m_a

$$m_a^2 = m^2. \tag{1.95}$$

The same result can also be obtained using the linear representation of ϕ from Eq. 1.87. Clearly, in the limit $m \to 0$, the symmetry of the theory is enhanced.

1.6.3 PNGBs in SM: Pions and Mesons

The most well-known examples of pNGBs in the SM are the pions. To understand this, let us only focus on the first generation of quarks. Ignoring the quark masses, the quark sector has a chiral symmetry: $SU(2)_L \times SU(2)_R$. The relevant part of Lagrangian for the quarks is

$$\mathcal{L} \supset \overline{Q_L} i\not{\partial} Q_L + \overline{Q_R} i\not{\partial} Q_R, \tag{1.96}$$

which remains invariant under separate transformations of LH and RH quark doublets, $Q_L = (u_L \;\; d_L)^T$ and $Q_R = (u_R \;\; d_R)^T$, as given by,[3]

$$\begin{pmatrix} u_L \\ d_L \end{pmatrix} \to g_L \begin{pmatrix} u_L \\ d_L \end{pmatrix}, \quad \begin{pmatrix} u_R \\ d_R \end{pmatrix} \to g_R \begin{pmatrix} u_R \\ d_R \end{pmatrix}, \tag{1.97}$$

with $g_L \in SU(2)_L$ and $g_R \in SU(2)_R$. As the Universe cooled below the QCD confinement scale, $T \sim \Lambda_{\rm QCD} \sim 150$ MeV, quarks form bound states, and the quark bilinear condensate $\overline{Q_L} Q_R \sim \Lambda^3_{\rm QCD}$ became non-zero. This breaks the chiral symmetry $SU(2)_L \times SU(2)_R$ down to the vector subgroup subgroup $SU(2)_V$, that transforms LH and RH fields in the same way. Since three generators are broken in this process, Goldstone's theorem predicts the existence of three massless Goldstone bosons, which are known as pions. However, in reality, up and down quarks possess small yet non-zero masses, which explicitly breaks $SU(2)_L \times SU(2)_R$ symmetry as evident from the mass term

$$\mathcal{L} \supset -\overline{Q_L} \begin{pmatrix} m_u & 0 \\ 0 & m_d \end{pmatrix} Q_R + \text{H.c.}. \tag{1.98}$$

As a result, the pions acquire a small mass

$$m_\pi^2 \sim \frac{\Lambda^3_{\rm QCD}}{f_\pi^2}(m_u + m_d), \tag{1.99}$$

where f_π denotes the pion decay constant and become pNGBs. Eq. 1.99 can be formally derived using chiral perturbation theory, which we will not discuss here. It is clear that in the limit $m_{u,d} \to 0$, pion masses vanish, confirming that pions are the lightest pNGBs in the SM.

The idea can also be extended by considering three lightest quarks, (u, d, s), with the third lightest quark being the strange quark, with mass $m_s \sim 100$ MeV. The kinetic terms of Eq. 1.97 now exhibit a larger symmetry:

$$U(3)_L \times U(3)_R = U(1)_L \times U(1)_R \times SU(3)_L \times SU(3)_R. \tag{1.100}$$

As in the two-flavor case, the SSB of $SU(3)_L \times SU(3)_R \to SU(3)_V$ gives rise eight pNGBs, which correspond to the known mesons: three pions $(\pi^{0,\pm})$, four Kaons $(K^0, \overline{K^0}, K^\pm)$ and

[3] Actually, the Lagrangian possesses a larger symmetry: $U(2)_L \times U(2)_R = SU(2)_L \times SU(2)_R \times U(1)_L \times U(1)_R$.

the eta meson (η), all with masses around the QCD scale $\Lambda_{\rm QCD}$.
Additionally, there is also ninth generator associated with the breaking of $U(1)_L \times U(1)_R \to U(1)_V$, which should generate a ninth pNGB with similar mass, the η' meson. However, η' is observed to be much heavier, $m_{\eta'} \sim 1$ GeV. This discrepancy is historically known as the *missing meson problem*. The main reason behind this mismatch is that the axial part of $U(1)_L \times U(1)_R$, $U(1)_A$ is already explicitly broken due to the axial anomaly. This means the divergence of the associated axial current J^μ_A receives quantum corrections (via the triangle diagram), and leads to a non-zero divergence: $\partial_\mu J^\mu_A \neq 0$ [144].

1.7 PNGBs Beyond the SM: The Cases of Majorons and Axions

Below, we will explore two prominent BSM examples of pNGBs, that result from the SSB of a global $U(1)$ symmetry: the Majoron and the axion, which are central topics of this thesis.

1.7.1 Majoron: A Signature of Lepton Number Breaking

Lepton number, L, and baryon number, B, are accidental global symmetries of the SM. Also, individual lepton flavor numbers L_e, L_μ, and L_τ are conserved separately in SM interactions, forbidding processes such as $\mu \to e\gamma$ or $\tau \to \mu\gamma$ etc. (although these processes conserve the total lepton number $L = L_e + L_\mu + L_\tau$). However, these symmetries are not exact: individual lepton flavor numbers are violated in nature due to neutrino oscillations, and quantum anomalies break the conservation of each separate lepton flavor and baryon number current in the SM. At the quantum level, each lepton flavor current are anomalous with

$$\partial_\mu J^\mu_L = \frac{g^2 N_f}{32\pi^2} W^a_{\mu\nu} \widetilde{W}^{a,\mu\nu}, \tag{1.101}$$

where $\widetilde{W}^{a,\mu\nu} = \frac{1}{2}\epsilon^{\mu\nu\alpha\beta} W^a_{\alpha\beta}$ is the dual of the gauge field strength tensor and N_f is the number of generations. A very similar result exists for the baryon number. These anomalies imply that nonperturbative electroweak processes, such as sphalerons, can violate $B+L$ while the combinations $B-L$ and $L_i - L_j$ (differences between lepton flavors) are anomaly-free and thus strictly conserved at the quantum level with the SM.
Total lepton number violation can arise in extensions of the Standard Model, particularly if neutrinos are Majorana in nature. For example, in the type-I seesaw mechanism, adding heavy right-handed neutrinos (RHNs) with Majorana masses directly break lepton number at high scales.
Therefore, to systematically account for the lepton number violation, one can promote lepton number to a global $U(1)_L$ symmetry and consider it to be broken spontaneously via a complex scalar field Φ with $L = -2$:

$$-\mathcal{L}_{\rm seesaw} \;=\; y^\nu_{\alpha i} \overline{\ell_{L\alpha}} \widetilde{H} N_{R_i} + \frac{1}{2} f_{ij} \Phi \overline{N^c_{R_i}}\, N_{R_j} + H.c.. \tag{1.102}$$

Once the Φ field acquires a *vev*

$$\Phi = \frac{v_\phi + \phi + i\chi}{\sqrt{2}}, \tag{1.103}$$

the RHNs obtain a Majorana mass term as $M_N = f v_\phi/\sqrt{2}$ and the angular mode χ emerges as the Goldstone boson, namely Majoron [145]. Hence, the phenomenology of Majoron is automatically connected to the origin of neutrino mass.
However, the Majoron is exactly massless if $U(1)_L$ is an exact global symmetry. One requires an explicit breaking of lepton number, such as soft-breaking term or higher dimensional operators, to generate a small Majoron mass, making it a pNGB. Such a light Majoron is an attractive candidate for dark matter, which is motivated by the fact that it generically has feeble couplings to the SM being suppressed by the scale of symmetry breaking. This ensures that it may be stable enough to form DM [146,147]. Due to the small couplings, the preferred mechanism to produce Majoron DM is freeze-in, for instance through the coupling to the Higgs or RHNs.
At tree-level, Majoron interacts solely with the RHNs as

$$-\mathcal{L} \supset \frac{i f_{ij}}{2\sqrt{2}} \chi N_i \gamma^5 N_j, \tag{1.104}$$

As Majoron is generally assumed to be much lighter than RHNs, the only possible decay mode of Majoron at tree level is into light neutrinos, which follows from the interaction in Eq. 1.104 via active-sterile neutrino mixing after the electroweak symmetry breaking takes place. The decay width of this channel is given by [148]

$$\Gamma_{\chi\to\nu\nu} = \frac{m_\chi}{16\pi v_\phi^2} \sum_j m_{\nu_j}^2. \tag{1.105}$$

Therefore, in order to be a viable DM candidate, Majoron must possess a lifetime greater than the age of the Universe, $\tau_U \sim 10^{19}$ sec. Furthermore, the same decay channel ($\chi \to \nu\nu$) also offers indirect detection prospects of Majoron via monochromatic neutrinos in experiments, which provide stringent constraints on the Majoron lifetime. Loop-induced decay of Majoron into two photons are also possible but highly suppressed.

We will explore the detailed phenomenology of the Majoron in Chapter 2, where Majoron is assumed to be a viable freeze-in dark matter via additional $U(1)_L$ breaking higher dimensional interaction. We will continue to use χ and v_ϕ to denote the Majoron field and the $U(1)_L$ breaking scale, respectively.

1.7.2 The Axion and Its Extensions: Axion-like Particles

Another classic example of pNGBs is axion, which was proposed to solve one of the striking puzzles of the SM, the strong CP problem. Below, we briefly introduce the strong CP problem and explain how the axion addresses it. We also discuss the more generalized case of axion-like particles (ALPs), followed by an overview on the related constraints.

1.7.2.1 The Strong CP Problem and its axionic solution

The theory of strong interactions is formulated using the QCD Lagrangian:

$$\mathcal{L}_{\rm QCD} = -\frac{1}{4} G^a_{\mu\nu} G_a^{\mu\nu} + \sum_q \bar{q}(i\not{D} - m_q)q + \bar{\theta}\frac{g_s^2}{32\pi^2} G^a_{\mu\nu}\widetilde{G}_a^{\mu\nu}, \tag{1.106}$$

where m_q denotes the quark mass matrix and $G^a_{\mu\nu}$ is the gluon field strength tensor. Importantly, there are two sources of CP violation present in Eq. 1.106: first, the phase in the quark mass matrix m_q, which is complex in principle, and second, the topological term $\sim \bar{\theta} G^a_{\mu\nu}\widetilde{G}^{\mu\nu}_a$, which violates P and T, and hence CP. Since CP is already violated in the weak sector of the SM, there is no symmetry protecting these terms from being non-zero. Hence, CP violation is expected in QCD as well. Furthermore, a chiral rotation of the quark field: $q \to e^{i\gamma_5\theta_q/2}q$ (to remove the complex phase in m_q) introduces a shift in $\bar{\theta}$ due to axial anomaly as

$$\partial_\mu J^\mu_A = 2im_q\bar{q}\gamma_5 q + \frac{g_s^2 N}{32\pi^2} G^a_{\mu\nu}\widetilde{G}^{\mu\nu}_a, \tag{1.107}$$

as we discussed in the subsection 1.6.3. This makes the physically observable CP violating parameter to be $\theta_{\rm QCD} = \bar{\theta} + {\rm Arg}\ ({\rm det} M_q)$ [149], where M_q is the mass matrix for multiple quark flavors. Consequently, such $\theta_{\rm QCD}$ term induces neutron electric dipole moment [150, 151], which is heavily constrained by the experiments [152, 153], placing in turn an upper bound on $\theta_{\rm QCD}$ as

$$|\theta_{\rm QCD}| \lesssim 10^{-10}. \tag{1.108}$$

However, there is no reason why the sum of these two contributions, having independent origins, cancel in such a fine-tuned value. Such smallness of $\theta_{\rm QCD}$ is therefore a puzzle in SM, which is popularly termed as the *strong CP problem*. The most appreciated solution of this puzzle was given by Roberto Peccei and Helen Quinn [53] in 1977 by promoting $\theta_{\rm QCD}$ to a dynamical field, that eventually relaxes in a CP conserving vacuum state. To achieve this, a new global axial $U(1)$ symmetry, popularly known as $U(1)_{\rm PQ}$, was introduced, which is spontaneously broken by a complex scalar field Φ, parametrized as

$$\Phi(x) = \eta(x) e^{ia(x)/f_a}, \tag{1.109}$$

with the potential

$$V(\Phi) = \frac{\lambda}{4}(|\Phi|^2 - f_a^2/2)^2, \tag{1.110}$$

where f_a is the $U(1)_{\rm PQ}$ breaking scale and $a(x)$ is the resulting Goldstone Boson of the broken $U(1)_{\rm PQ}$ symmetry, called *axion*. Under a $U(1)_{\rm PQ}$ transformation with parameter ϵ, the axion exhibits a shift-symmetry, given by

$$a(x) \to a(x) + \epsilon f_a, \tag{1.111}$$

However, due to the axial anomaly, the shift symmetry is explicitly broken, and $a(x)$ becomes a pNGB, which couples anomalously to gluons:

$$\mathcal{L} \supset \frac{a(x)}{f_a}\frac{g_s^2}{32\pi^2} G^a_{\mu\nu}\widetilde{G}^{\mu\nu}_a. \tag{1.112}$$

Hence, the effective θ-term becomes $\theta_{\rm eff}(x) \equiv \theta_{\rm QCD} + a(x)/f_a$, which can be driven to zero by minimizing the axion potential (generated by the non-perturbative QCD), thereby dynamically solving the strong CP problem. The Vafa-Witten theorem [154] ensures that QCD

dynamics favour a CP-conserving minimum.
A form of the axion potential, based on instanton calculations [155], is given by

$$V(a) = m_\pi^2 f_\pi^2 \frac{m_u m_d}{(m_u + m_d)^2} \left[1 - \cos\left(\frac{a}{f_a}\right)\right], \tag{1.113}$$

which yields the axion mass as

$$m_a^2 = \left(\frac{\partial^2 V(a)}{\partial a^2}\right)_{\min} = \frac{m_\pi^2 f_\pi^2}{f_a^2} \frac{m_u m_d}{(m_u + m_d)^2} \simeq \left[5.7\ \mu\text{eV}\ \left(\frac{10^{12}\ \text{GeV}}{f_a}\right)\right]^2. \tag{1.114}$$

This is the zero-temperature mass, which applies only after the QCD phase transition ($T < T_{\text{QCD}} \sim 160$ MeV) [156]. For temperature above T_{QCD}, the temperature-dependent axion mass can be parametrized as [157]

$$m_a(T) \simeq \beta m_a \left(\frac{T_{\text{QCD}}}{T}\right)^\gamma, \tag{1.115}$$

where m_a denotes the zero-temperature axion mass (follows from Eq. 1.114), $\gamma \approx 4$ [156], and $\beta \approx 0.026$ [158]. At much lower energies, the interactions of axion can be characterized with EFT, with the following Lagrangian

$$\mathcal{L}_{int} = \frac{g_s^2}{32\pi^2} \frac{a}{f_a} G\widetilde{G} + \frac{1}{4} g_{a\gamma\gamma} a F_{\mu\nu} \widetilde{F}^{\mu\nu} + i \frac{g_{aN}}{2m_N} \partial_\mu (\bar{N}\gamma^\mu\gamma^5 N) + i \frac{g_{af}}{2m_f} \partial_\mu a (\bar{\psi}\gamma^\mu\gamma^5\psi) \tag{1.116}$$

where N and ψ_f are the nucleon and fermion fields, respectively, and $F_{\mu\nu}$ is the electromagnetic field strength tensor. The couplings $g_{a\gamma\gamma}$, g_{aN}, g_{af} all scale as f_a^{-1}.
The axion-photon coupling is a very important quantity, which arises from two sources: first, a model-independent part from the axion-meson mixing at low energies, described by chiral perturbation theory at energy below Λ_{QCD}, and, second, a model-dependent contribution from fermions charged under both electromagnetism and $U(1)_{\text{PQ}}$, and can be combined as [159]

$$g_{a\gamma\gamma} = \frac{\alpha_{\text{em}}}{2\pi f_a} \left(\frac{E}{A} - 1.92\right), \tag{1.117}$$

where E and A represents the electromagnetic and color anomaly contributions of the axial current associated with axion.

There are several ways to realize $U(1)_{\text{PQ}}$ symmetry which act as UV completions for the axion effective potential in Eq. 1.116. The originally proposed axion model, referred to as the Peccei-Quinn-Weinberg-Wilczek (PQWW) axion model [53,55,56], was based on a two-Higgs doublet setup with f_a near electroweak scale, which eventually got ruled out by beam dump and other experimental constraints [160, 161]. Two other widely popular models are the Dine-Fischler-Srednicki-Zhitnitsky (DFSZ) [162,163] and Kim-Shifman-Vainshtein-Zakharov (KSVZ) [164,165] models, which allow much larger values of f_a, thereby yielding very light and weakly interacting "invisible" axion ($m_a \sim \mu$eV).

1.7.2.2 Generalization of QCD Axion to Axion-Like Particles (ALPs)

The axion-like particles or ALPs form as a broader class of particles that generalizes the idea of QCD axion to address other open problems of the SM. However, unlike the QCD axion, they are not necessarily tied to solving the strong CP problem. These are light, pseudoscalar bosons that arise when a global, anomalous symmetry is spontaneously broken at high energy. Their masses can come from non-perturbative effect in a hidden strongly coupled hidden sector (similar to QCD axions) or from explicit symmetry breaking [166]. ALPs naturally appear in many BSM scenarios, including models with flavor symmetries [167–171], supersymmetry [172], and especially in string theory [173–177] etc.

The key difference between the QCD axion and ALPs is that ALPs do not follow a fixed relation between their mass m_a and decay constant f_a, unlike QCD axion. However, as their potential is assumed to be generated by some QCD-like strong sector, it can be parametrized in a similar way as QCD:

$$V_{\rm ALP}(a) = m_a^2 f_a^2 \left[1 - \cos\left(\frac{a}{f_a}\right)\right]. \tag{1.118}$$

One can definitely write $m_a^2 f_a^2 \sim \Lambda^4$, but as Λ is unknown, this is just a reshuffling of the parameters. Because of this freedom, ALPs can span a much wider range in the (m_a, f_a) parameter space compared to QCD axions.

Being pNGBs in nature, ALPs are expected to be light and couple very weakly to the SM sector. Additionally, due to the pseudoscalar nature, they can couple to the electromagnetic field strength through terms like $F\widetilde{F}$, similar to the QCD axion. As a result, the low-energy effective theory of ALPs is closely resemble those of QCD axions, which means that many experiments designed to detect QCD axions are also sensitive to ALPs.

1.7.2.3 Axions as Dark Matter: The Misalignment Mechanism

So far, we have discussed how the QCD axion solves the strong CP problem and how ALPs generalize this idea in many BSM frameworks. Besides this motivation, axions also have other useful features that make them strong candidates for new physics. In the rest of this chapter, we will use *axions* to refer collectively to both the QCD axion and ALPs.

One of the strong reasons to study axions is that they are excellent dark matter candidates in the sense that they are stable over the cosmological time scale and their couplings with the ordinary matters are highly suppressed. The axion can be produced via thermal or non-thermal processes in the early universe. Among these, an interesting mechanism is the vacuum misalignment mechanism [93–95], a model-independent, non-thermal process that relies on the cosmological evolution of the axion field. It naturally leads to a population of axions that behaves like cold dark matter. The term "misalignment" will become clear as we go along.

To understand this mechanism, we start by considering the evolution of the axion field in an expanding Universe. After the spontaneous breaking of the $U(1)$ global symmetry ($U(1)_{\rm PQ}$ symmetry for QCD axion), the axion's dynamics are governed by a simple La-

grangian

$$\mathcal{L}_a = \frac{1}{2}(\partial_\mu a)(\partial^\mu a) - V(a), \tag{1.119}$$

where, following Eq. 1.118, the axion potential is written as

$$V(a) = m_a^2 f_a^2 \left[1 - \cos\left(\frac{a}{f_a}\right)\right]. \tag{1.120}$$

The dynamics of the axion field a, considering an expanding Universe, follows from the action

$$S_a = \int d^4x\sqrt{-g}\,\mathcal{L}_a, \quad \text{with } \sqrt{-g} = R^3, \tag{1.121}$$

where $\sqrt{-g}$ stems from the determinant of the metric $g^{\mu\nu}$ in a flat FRW Universe (as expressed in Eq. 1.24). Considering a spatially homogeneous axion field ($a(t, r, \theta, \phi) \to a(t)$), the equation of motion of axion can be obtained as

$$\ddot{a} + 3\mathcal{H}(T)\dot{a} + m_a^2(T) f_a \sin\left(\frac{a}{f_a}\right) = 0, \tag{1.122}$$

where $\mathcal{H}$ denotes the Hubble parameter and 'dot' refers the derivative with respect to time. Conveniently, one can define a dimensionless variable $\theta \equiv a/f_a$ to rewrite the equation

$$\ddot{\theta} + 3\mathcal{H}(T)\dot{\theta} + m_a^2(T)\sin(\theta) = 0, \tag{1.123}$$

In early Universe, when $m_a(T) \ll \mathcal{H}$, the axion field is overdamped such that θ is approximately constant. Therefore, during this period, the field is frozen at some initial angle $\theta = \theta_I$, known as the *misalignment angle*. As the temperature of the Universe decreases, the axion mass term becomes relevant and eventually, the axion undergoes oscillation at a temperature $T_{\rm osc}$ which satisfies

$$m_a(T_{\rm osc}) = 3\mathcal{H}(T_{\rm osc}). \tag{1.124}$$

This marks the onset of oscillations, with frequency $\sim m_a$, in the regime $m_a(T) \geq 3\mathcal{H}$. For the QCD axion, this typically occurs near $T \sim \Lambda_{\rm QCD}$, where the QCD axion mass turns on. These oscillations turn out to behave like cold dark matter. To see this, we solve the axion field equation in the oscillatory regime using a WKB ansatz:

$$\theta(t) = A(t)e^{i\Theta(t)}, \tag{1.125}$$

where, $A(t)$ and $\Theta(t)$ are real valued functions, and importantly, θ is also real. Inserting this into Eq. 1.123, we get

$$\frac{\ddot{A}}{A} - \dot{\Theta}^2 + 3\mathcal{H}\frac{\dot{A}}{A} + m_a^2 = 0 \tag{1.126}$$

$$\dot{A} + A\left(\frac{3\mathcal{H}}{2} + \frac{\ddot{\Theta}}{\dot{\Theta}}\right) = 0 \tag{1.127}$$

In the WKB limit (where $A(t)$ is a slowly varying function), where $\ddot{A}/A,\ \mathcal{H}\dot{A}/A \ll \dot{\Theta}^2,\ m_a^2$,

Eq. 1.126 gives

$$\dot{\Theta}^2 = m_a^2 \quad \Longrightarrow \quad \Theta(t) = \int dt' m_a(t') \; + \; \text{constant}. \tag{1.128}$$

So, Eq. 1.127 becomes

$$\dot{A} + A\left(\frac{3\mathcal{H}}{2} + \frac{\dot{m}_a}{2m_a}\right) = 0, \tag{1.129}$$

which is solved by

$$A(t) = \frac{C}{R^{3/2}\sqrt{m_a(t)}} \tag{1.130}$$

for some constant C. The full solution becomes (considering the real part only, as θ is real)

$$\theta(t) = \frac{C}{R^{3/2}\sqrt{m_a(t)}} \cos \int dt' m_a(t'). \tag{1.131}$$

C can be determined from by considering the axion energy density before and after oscillations. Before oscillation ($\mathcal{H} > m_a$), axion was frozen at θ_I and therefore,

$$\rho_a(t) = \frac{1}{2} m_a^2(t) f_a^2 \theta_I^2 \tag{1.132}$$

After the oscillation starts ($\mathcal{H} < m_a$), using Eq. 1.131 and taking the mean over the fast oscillations, we find

$$\langle \rho_a(t) \rangle = \frac{C^2}{2m_a} \frac{f_a^2 m_a(t)^2}{R^3}. \tag{1.133}$$

Matching these two energy densities at $T_{\rm osc}$ yields

$$C^2 = m_a(T_{\rm osc}) R^3(T_{\rm osc}) \theta_I^2. \tag{1.134}$$

So the energy density of axion for $T < T_{\rm osc}$ becomes

$$\rho_a(T) \simeq \frac{1}{2} m_a(T_{\rm osc}) m_a(T) f_a^2 \theta_I^2 \left(\frac{R(T_{\rm osc})}{R(T)}\right)^3. \tag{1.135}$$

This shows that upon oscillation, the energy density of axion behaves as: $\rho_a \propto m_a(T)/R(T)^3$, which resembles non-relativistic matter. Using conservation of entropy of the Universe, $R(T_{\rm osc})^3/R(T_0)^3 = \mathcal{S}(T_0)/\mathcal{S}(T_{\rm osc})$ ('0' denotes today), the energy density of axion at the present day can be expressed as

$$\rho_a(T_0) \simeq \frac{1}{2} m_a(T_{\rm osc}) m_a(T_0) f_a^2 \theta_I^2 \left(\frac{\mathcal{S}(T_0)}{\mathcal{S}(T_{\rm osc})}\right). \tag{1.136}$$

Finally, the axion relic density can be computed utilizing $T_{\rm osc}$ and temperature dependent axion mass $m_a(T)$ (given in Eq. 1.115) as [157]

$$\begin{aligned} \Omega_a h^2 = \frac{\rho_a(T_0)\mathcal{S}_0 h^2}{\rho_{c,0}} &\simeq 0.12 \left(\frac{28\ \mu\text{eV}}{m_a}\right)^{7/6} \left(\frac{\theta_I}{2.15}\right)^2 \\ &\simeq 0.12 \left(\frac{f_a}{12\times 10^{12}\ \text{GeV}}\right)^{7/6} \left(\frac{\theta_I}{2.15}\right)^2. \end{aligned} \tag{1.137}$$

For a generic ALP, $m_a(T_{\rm osc}) = m_a(T_0) = m_a$ holds, which yields

$$\Omega_a h^2 \simeq 0.12 \left[\frac{100}{g_\star^S(T_{\rm osc})}\right]^{\frac{1}{4}} \left[\frac{m_a}{10^{-9}\ {\rm GeV}}\right]^{\frac{1}{2}} \left[\frac{f_a}{4\times 10^{11}\ {\rm GeV}}\right]^2 \theta_I^2. \tag{1.138}$$

Therefore, in a nutshell, the term "misalignment" refers to the fact that, in early Universe the axion field is misaligned from the minimum of its potential and later it oscillates around it, behaving like a cold DM. Such evolution of axion field is depicted in Fig. 1.9.

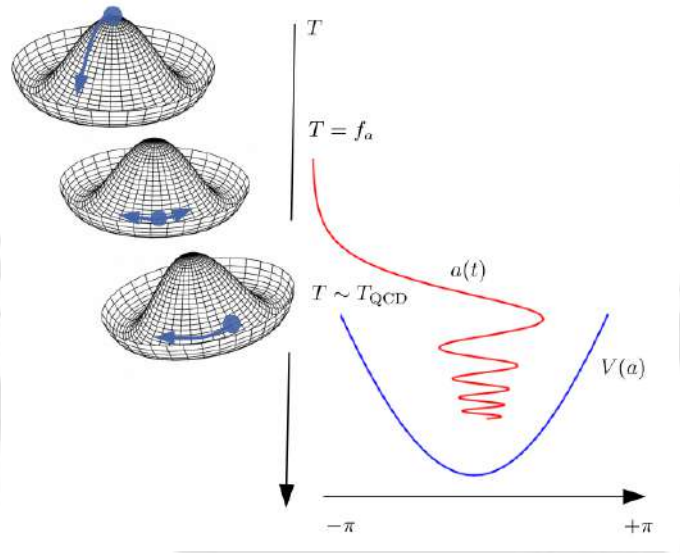

Figure 1.9: A schematic diagram illustrating the vacuum misalignment mechanism for QCD axion. The PQ scalar gets a *vev* at $T \sim f_a$, creating a massless axion field. As the Universe cools to $T \sim T_{\rm QCD}$, QCD effects tilt the potential, giving the axion a mass, which triggers axion oscillations around the minimum. Figure courtesy: Andreas Pargner [178].

So far, the axion field is assumed to be homogeneous. This is valid if the global symmetry (e.g., $U(1)_{\rm PQ}$ for the QCD axion) is broken before or during inflation, so a single patch with a fixed initial angle θ_I gets stretched to fill the entire visible Universe. In such cases, θ_I is a free parameter, and considering the naturalness, it is commonly assumed as

$$\theta_I \sim \mathcal{O}(1), \qquad \text{for pre inflationary scenarios.} \tag{1.139}$$

Although this is not a strict prediction as smaller values of θ_I ($\sim 0.1, \sim 0.01$) are equally allowed, but would correspond to finely tuned initial conditions.

On contrary, if the symmetry breaks after inflation, different regions in the Universe have uncorrelated initial angles. Averaging them gives

$$\langle \theta_I^2 \rangle \approx \frac{1}{\pi}\int_0^\pi d\theta\ \theta^2 = \frac{\pi^2}{3}, \qquad \text{for post inflationary scenarios.} \tag{1.140}$$

So, in both cases, $\theta_I \sim \mathcal{O}(1)$ unless a specific mechanism sets it. Also, topological defects can form when the symmetry breaks. These are inflated away in the pre-inflationary scenario but can survive and decay in the post-inflationary case, which may produce additional DM axions [179–182].

Kinetic Misalignment Mechanism

A modified version of the misalignment mechanism, called the kinetic misalignment mechanism, was proposed in [183, 184]. Unlike the standard case, where the axion field starts from rest ($\dot{\theta}_I = 0$), here it starts with a large non-zero velocity, $\dot{\theta}_I \neq 0$, implying that θ_I is not simply a constant. This can happen if there is explicit breaking of the $U(1)$ symmetry in the early Universe, similar to the Affleck-Dine mechanism [134, 185].

As a result, the axion field carries a significant initial kinetic energy $\rho_\theta = f_a^2\dot{\theta}_I^2/2$. If this is larger than the potential barrier height ($2m_a^2 f_a^2$), the field rolls over many minima. But since kinetic energy drops much faster ($\propto R^{-6}$) than potential energy ($\propto R^{-3}$), the field eventually slows down and gets trapped, leading to oscillation around a particular minima. Hence, the actual onset of oscillation gets delayed in this case and occurs at a temperature $T^\star_{\rm osc}$ where

$$\dot{\theta}(T^\star_{\rm osc}) = 2m_a. \tag{1.141}$$

This delay in oscillation results in an enhanced axion abundance compared to the conventional misalignment scenario.

1.7.2.4 Searches for Axion

Given their strong theoretical motivations, axions are being actively investigated through various ongoing and planned experimental methods. These search strategies include laboratory experiments, astrophysical observations, and cosmological studies. For detailed reviews on the constraints, see [127, 186–188]. Below, we briefly summarize these different search approaches.

Laboratory searches

The interaction of an axion with two photons offers a promising way to search for it experimentally. As mentioned earlier in subsection 1.7.2, the relevant interaction is given by

$$\mathcal{L}_{a\gamma\gamma} = -\frac{1}{4} g_{a\gamma\gamma} a F_{\mu\nu}\widetilde{F}^{\mu\nu} = g_{a\gamma\gamma} a \mathbf{E}.\mathbf{B}. \tag{1.142}$$

This allows a photon with polarisation parallel to an external magnetic field to convert into an axion and vice versa, a phenomena known as the Primakoff effect. This principle is utilized many experimental searches for axions.

- **Helioscopes:** Axion helioscopes aim to detect solar axions. These experiments use a long dipole magnet aimed at the Sun, allowing the incoming solar axions to convert into detectable photons via Primakoff effect, which are then detected in an X-ray detector. A lack of any signal sets a limit on the axion-photon coupling $g_{a\gamma\gamma}$. Currently, the leading helioscope experiment is CERN Axion Solar Telescope (CAST) [189], which has placed a bound of $g_{a\gamma\gamma} < 0.66 \times 10^{-10}$ GeV^{-1} for $m_a \lesssim 0.02$ eV [190], which is comparable to constraints from astrophysical observations. The next-generation helioscope, BabyIAXO [191] is expected to improve this sensitivity significantly.

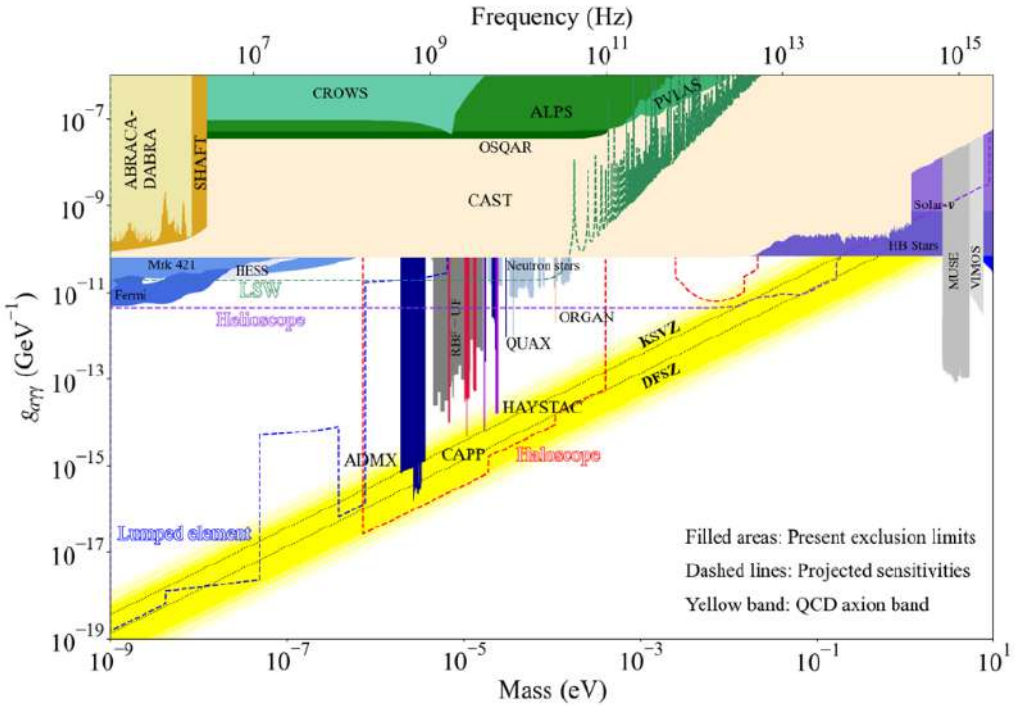

Figure 1.10: Existing and projected limits on the axion-photon coupling with respect to the axion mass. Figure is taken from the reference [188].

- **Haloscopes:** Originally proposed by Sikivie [192], haloscopes aim to detect dark matter axions from the galactic halo by converting them into photons inside a microwave cavity placed in a magnetic field. When the cavity's resonance frequency matches the axion mass, an enhancement in the signal is observed. Axion Dark Matter Experiment (ADMX) [193] is a leading haloscope, which currently excludes axions in $2.81 - 3.31$ μeV mass range [194]. Heavier axions are targeted by dielectric haloscopes such as MADMAX [195] and dish antenna such as BRASS [196], while lighter axions are probed using LC circuits in DMRadio [197] and WISPLC [198].

- **Other Laboratory experiments:** Another way to search for axions is through fully-controlled setups like Light-Shining-through-a-wall or LSW experiments [199, 200]. Here, a laser passes through a magnetic field where photons can convert into axions, which then traverse a light-tight barrier, and convert back into photons on the opposite side. Experiments like ALPS [201], OSQAR [202] etc. use such technique, though they are currently less sensitive than helioscopes. The upgraded ALPSII [203] aims to improve this. Other setups include polarization-based searches like PVLAS [204].

Astrophysics and Cosmology

In addition to lab-based searches, axion signatures are also widely investigated though several astrophysical and cosmological observations. These include the impacts of structure formation seen in the Lyman-α forest [205] data, X-ray signals from axion-photon conversion in cosmic magnetic fields [206–209], changes in stellar evolution inferred from horizontal branch stars [210]. Thermal relic axions can leave imprints on the CMB and BBN [211, 212]. A key constraint comes from supernova SN1987A, where emission of axion via nucleon

bremsstrahlung ($N+N \to N+N+a$) leads to energy loss. This sets a bound for QCD axion as $f_a \gtrsim 4 \times 10^8$ GeV (or, equivalently, $m_a \lesssim 16$ meV) [213]. However, ALPs with lower f_a remain theoretically appealing and testable in current experiments [186], including colliders [214, 215] and beam-dump experiments [216]. This difference stems from the fact that ALPs do not have a fixed relation between mass and decay constant, unlike the QCD axion. This freedom allows ALPs to evade the supernova bound in two ways. First, heavy ALPs with masses $\gtrsim \mathcal{O}(100\ \text{GeV})$ cannot be produced efficiently inside the supernovae core as the core temperature in typical supernovae is ~ 30 MeV, rendering the SN bound effectively inapplicable. Second, for small f_a, ALPs interact too strongly and become trapped within the core, preventing their escape and significantly reducing their contribution to cooling. This "trapping regime" relaxes conventional supernovae constraints. Notably, QCD axions with smaller f_a can also be trapped. However, lowering f_a for QCD axion may raise their mass into the MeV regime, maintaining efficient production in the supernova and sustaining strong constraints despite trapping. This makes the SN1987A bound particularly robust for the QCD axion, whereas generic ALPs can more easily escape it [217–219].

We will investigate more on ALP phenomenology in Chapters 3 and 4, using notations a and f_a to represent the ALP field and its decay constant, respectively.

1.8 Objective and layout of the thesis

The primary object of this thesis is to explore the phenomenology of two prominent pseudo-Nambu-Goldstone bosons, the Majorons and ALPs, which offer elegant solutions to some of the key open questions in particle physics and cosmology, such as the mystery of dark matter and the baryon asymmetry of the Universe. As pNGBs emerge from the spontaneous breaking of approximate global symmetries, they are naturally light and feebly interacting with the SM, making them ideal candidates for probing in several current and future experiments through decays into photons or neutrinos, or via missing energy signals at colliders. Furthermore, due to their Goldstone nature, their interactions are suppressed by the symmetry breaking scale, which makes them an attractive candidate for non-thermal dark matter, such as in the freeze-in or misalignment scenarios, as outlined earlier. These frameworks can also link DM physics with other BSM sectors. For instance, a Majoron DM model naturally connects neutrino physics with DM, while the QCD axion DM ties together the strong CP problem and DM. In some models, ALPs can play a role of a mediator between DM and the SM, especially with low f_a, ALP may bridge DM and collider physics. Additionally, homogeneous ALP fields can also drive baryogenesis via spontaneous leptogenesis thanks to their derivative interaction to the SM fermions.

This thesis focuses on these aspects of pNGB phenomenology, particularly for Majorons and ALPs. In this chapter (Chapter 1), we have so far outlined an overview of the SM and its shortcomings, and introduced pNGBs as well-motivated extensions that can address these issues. Chapter 2 delves into the phenomenology of the Majoron as freeze-in DM originating from explicit $U(1)_L$ breaking at the non-renormalizable level, and further explores their connection to thermal leptogenesis. Chapter 3 focuses on ALPs, examining on their production via misalignment mechanism in presence of additional explicit symmetry breaking. This

chapter also explores their role in a relatively low-scale spontaneous leptogenesis in presence of an inert Higgs doublet. Chapter 4 examines the role of ALP as a mediator between the SM sector and the dark sector, and further investigates the prospects of probing the such ALP-portal fermion DM at electron-positron colliders. Finally, Chapter 5 concludes with a summary of the results.

Chapter 2

Phenomenological Aspects of Majorons as Dark Matter

2.1 Introduction

In this chapter we will analyze the phenomenology of the Majoron as a freeze-in dark matter. As we discussed previously, Majoron, the pNGB associated to a global lepton number symmetry (LNS), $U(1)_L$, can render itself as a promising dark matter (DM) candidate [146, 147, 220–225] due to its feeble coupling with the SM.

Previous studies with such Majoron field (χ) as a freeze-out kind of DM have mostly been engineered through the SM Higgs (H) portal interaction of the form $\lambda_{\chi H}\chi^2 H^\dagger H$, an explicit LNS breaking term, which helps in realizing the observed DM relic abundance [222, 225]. Such an interaction is suggestive of the scalar singlet DM scenario [226] and obviously, there exists a one-to-one correspondence between the mass of the DM (m_χ) and the LNS breaking parameter $\lambda_{\chi H}$. However, contrary to the natural expectation that an explicit symmetry breaking parameter should be sufficiently small in t'Hooft's sense [57], it is observed that $\lambda_{\chi H}$ needs to be large enough ($\mathcal{O}(0.1)$ or so) in order to satisfy the correct relic density. Secondly, with the XENON-1T results, the entire parameter space of m_χ ranging below TeV (except the Higgs resonance region) is basically ruled out in this minimal Majoron scenario [225, 226]. The Majoron also possesses a derivative coupling with its CP-even partner, similar to other pNGBs, through which it can annihilate into the SM particles via s-channel mediated process by the CP-even scalar leading to a possible DM relic satisfaction. In case of pNGB as DM (not a Majoron), such a scenario can evade the direct detection experiment bounds [227–231] as a result of the small momentum transfer of DM through the derivative coupling causing suppression in elastic scattering amplitude with nuclei. However, in case of Majoron as DM, it fails to explain the stability criteria as Majorons would decay to light neutrinos (ν) via active sterile mixing connected to the neutrino mass generation in type-I seesaw [104, 108, 109].

On the other hand, Majorons may also emerge as Feebly interacting massive particle (FIMP) DM [91] where it is produced in the early Universe from the decay of some particle, a natural choice of which is the RHN (N). As the Majoron interaction strength with the SM

particles is expected to be suppressed by the $U(1)_L$ breaking scale (the seesaw scale) [232], treating Majoron as FIMP type DM remains as a viable option [148, 222, 233]. However, from the previous studies, it becomes apparent that with the tree-level coupling between the RHNs and the scalar singlet (the one responsible for breaking the LNS), sufficient production of Majorons cannot take place from the decay of RHNs [234]. This is primarily because the decay rate ($N \to \chi\nu$) is proportional to the tiny light neutrino mass on top of the usual suppression by LNS breaking scale. However, the situation changes if a tiny LNS breaking Higgs-portal coupling $\lambda_{\chi H}$ is introduced. The correct DM relic abundance[1] for Majorons, produced from the decay of the SM Higgs boson $h \to \chi\chi$, requires the portal coupling $\lambda_{\chi H} \sim O(10^{-10})$ which in turn fixes the Majoron mass m_χ having a unique value ~ 3 MeV [148,222,233]. Though such small portal coupling obeys the naturalness criteria, it suffers from a fine-tuned situation in terms of Majoron mass. Another possibility is to realize non-thermal Majoron production from the annihilation of the SM Higgs via UV freeze-in framework [234] where the Majoron mass is found to be relatively heavy (contrary to the light pNGB boson in UV freeze-in scenario [235]).

Since LNS is closely tied to the type-I seesaw mechanism, and therefore, the origin of neutrino mass, the possibility Majoron serving as a DM candidate naturally connects DM and neutrino physics. Moreover, as discussed in subsection 1.5.1, the dynamical origin of the baryon asymmetry of the Universe via thermal leptogenesis is also closely linked to the type-I seesaw mechanism, which paves a way to further connect leptogenesis with neutrino masses, and dark matter within the setup of Majoron model. In the minimal version of type-I seesaw mechanism, only two massive right-handed neutrinos (RHN) are sufficient to account for the neutrino oscillation data [123]. If these sterile RHNs have an (approximately) off-diagonal mass matrix, they can form two nearly degenerate Majorana states [236]. Such a setup paves the way for resonant leptogenesis [237,238] framework, offering a natural and viable explanation for the observed baryon asymmetry, even with comparatively low RHN masses.

With this motivation, in section 2.2, we explored the phenomenology of Majoron freeze-in DM in presence of additional $U(1)_L$ breaking interaction, which turns out to be beneficial as it opens up a large region of viable DM parameter space. Furthermore, in section 2.3, we establish a novel connection between Majoron dark matter and resonant leptogenesis, where the same term that drives DM production induces the mass splitting required for leptogenesis.

2.2 Majorons Revisited: light dark matter as FIMP

In this work (based on [239]), with the aim of broadening the Majoron mass range (toward the lighter side) while the minimality and naturalness are retained, we propose a new production mechanism for Majoron as a FIMP-type DM. Instead of introducing any Higgs-portal coupling with Majorons, we introduce here a dimension-5 LNS breaking operator. Being suppressed by the cut-off scale, it can be regarded as a soft breaking of LNS

[1] Direct detection bound is automatically evaded due to the presence of such a small portal coupling, contrary to the freeze out case, involved.

which takes care of the production of Majorons via RHN annihilations. Also, we keep the framework minimal in the sense that no additional fields other than the two SM singlet right-handed neutrinos (related to neutrino mass generation) and a LNS breaking (SM singlet) red complex scalar field, are required. We primarily focus on the lighter side of Majoron mass $[\mathcal{O}(\text{keV}) - \mathcal{O}(\text{GeV})]$, which remains attractive as this mass regime can be experimentally probed by several direct and indirect searches. For example, Majorons of MeV scale and beyond can be potentially detectable via mono-energetic neutrino flux in experiments like Borexino [240], KamLAND [241], and Super-Kamiokande (SK) [242]. Also, sensitive bounds from various γ-ray observations such as INTEGRAL [243], COMPTEL/EGRET [244], Fermi-LAT [245] etc. are applicable in this mass regime.

2.2.1 Majoron as Dark matter

As we build our framework extending the original Majoron model where a Majoron can be considered as a dark matter [146, 147], a brief discussion on the basic structure of it and related limitations are relevant to discuss first. The SM is extended by including two singlet right-handed neutrinos ($\mathcal{N}_{R_{i=1,2}}$) and a singlet complex scalar field (Φ) such that a global lepton number symmetry $U(1)_L$ prevails. As a result, a lepton number of $L = -2$ units is assigned to Φ while the SM lepton doublets (ℓ_{L_α}) as well as the RHNs carry a lepton number $L = 1$. As discussed previously in subsection 1.7.1, the renormalizable part of the Lagrangian (in the charged lepton diagonal basis) involving neutrinos is given by

$$-\mathcal{L} \supset \frac{f_i}{2}\Phi\overline{\mathcal{N}^c_{R_i}}\mathcal{N}_{R_i} + y^\nu_{\alpha i}\,\overline{\ell_{L\alpha}}\widetilde{H}\mathcal{N}_{R_i} + H.c., \tag{2.1}$$

where, H is the SM Higgs doublet and $y^\nu_{\alpha i}$ is the neutrino Yukawa coupling with $\alpha = e, \mu, \tau$ and $i = 1, 2$. The Majorana masses of RHNs are generated after the $U(1)_L$ symmetry breaking via Φ *vev* v_ϕ. Without loss of generality, we consider the generated RHN mass matrix $M_R = f v_\phi/\sqrt{2}$ to be diagonal with $f = \text{diag}(f_1, f_2)$. Once the electroweak (EW) symmetry is broken by the Higgs *vev* v as $\langle H\rangle = (0, v/\sqrt{2})^T$, active neutrino masses are generated through this minimal type-I seesaw mechanism [238] $m_\nu = m_D M_R^{-1} m_D^T$, where $(m_D)_{\alpha i} = y^\nu_{\alpha i} v/\sqrt{2}$ ($v = 246$ GeV).

The $U(1)_L$ symmetric scalar potential involving H and Φ is given by,

$$V(H, \Phi) = V_H - \frac{\mu^2_\Phi}{2}|\Phi|^2 + \frac{\lambda_\Phi}{2}|\Phi|^4 + \lambda_{H\Phi}|H|^2|\Phi|^2, \tag{2.2}$$

where $V_H = -\mu^2_H H^\dagger H + \lambda_H (H^\dagger H)^2$ is the usual the SM Higgs potential and $\lambda_{H\Phi}$ is the Higgs portal coupling of Φ. The stability of the potential is guaranteed by: λ_Φ, λ_H and $\lambda_{H\Phi} + \sqrt{2\lambda_H\lambda_\Phi} \geq 0$.

Once the $U(1)_L$ global symmetry is broken spontaneously, $\Phi = (v_\phi + \phi + i\chi)/\sqrt{2}$ (we use the linear representation throughout this chapter), a NGB (the CP-odd component) or the massless Majoron χ results. The Majoron mass can be generated once an explicit LNS breaking term,

$$-\mathcal{L}_{\text{LNB}} = -\frac{m^2}{4}(\Phi^2 + \Phi^{*2}), \tag{2.3}$$

is introduced. Such a term breaks the $U(1)_L$ to Z_2 (under which $\Phi \to -\Phi$) and induces a mass for the Majoron as $m_\chi^2 = m^2$. This mass term is however expected to be small (soft breaking) in t'Hooft's sense as $m \to 0$ limit enhances the overall symmetry of the framework. As stated earlier, it has been argued [142, 143, 146, 246, 247] that smallness of the pNGB mass can be related to explicit global symmetry (here LNS) breaking at large scale, such as at Planck scale ($M_{\rm Pl}$) by gravity effects [248–253]. To realize it, Planck suppressed non-renormalizable operators of the form $\Phi^n/M_{\rm Pl}^{n-4} + H.c.$ with $n > 4$ can be incorporated which are only soft (being non-renormalizable, such terms vanish in the limit $M_{\rm Pl} \to \infty$) explicit symmetry breaking term(s). The mass of the Goldstone then follows after the spontaneous breaking of the global symmetry.

Furthermore, the portal coupling can also be considered to be small ($\lambda_{H\Phi} \ll 1$) which is technically natural from the point of view of enhanced Poincare symmetry in the limit $\lambda_{H\Phi} \to 0$ [254, 255]. Considering a large hierarchy between the scales of lepton number and EW symmetry breaking along with tiny Higgs portal coupling, the mixing generated between the CP-even parts of Φ and H turns out to be negligible which results into the following masses of the scalar fields as

$$m_h^2 \simeq 2\lambda_H v^2, \quad m_\phi^2 \simeq \lambda_\Phi v_\Phi^2, \quad m_\chi^2 \simeq m^2, \tag{2.4}$$

where m_h is the mass of the SM Higgs boson as 125 GeV [31].

2.2.1.1 Seesaw Mechanism and Interactions of Majorons

Using the linear representation of the $U(1)_L$ breaking field $\Phi = (v_\phi + \phi + i\chi)/\sqrt{2}$, the following interaction of Majoron results via Eq. 2.1,

$$-\mathcal{L} \supset \frac{if_i}{2\sqrt{2}} \chi \overline{\mathcal{N}_{R_i}^c} \mathcal{N}_{R_i} + H.c.. \tag{2.5}$$

Furthermore, after the EWSB, a mixing between left and right-handed neutrinos takes place via the Dirac mass $m_D = y^\nu v/\sqrt{2}$ and consequently the mass terms involving ν_L and N_R can be written as,

$$-\mathcal{L}_m = \begin{pmatrix} \overline{\nu_L} & \overline{\mathcal{N}_R^c} \end{pmatrix} \begin{pmatrix} 0 & m_D \\ m_D^T & M_R \end{pmatrix} \begin{pmatrix} \nu_L^c \\ \mathcal{N}_R \end{pmatrix}, \tag{2.6}$$

where the generation indices are suppressed. This yields the light and heavy neutrino mass matrices m_ν and M ($\simeq M_R$, already diagonal) respectively in the rotated basis $(\widetilde{\nu}_L^c \;\; \mathcal{N})^T$, where[2] $\widetilde{\nu}_L^c = -i(\nu_L^c - \theta \mathcal{N}_R)$ with the active-sterile mixing matrix $\theta = m_D^* M_R^{-1}$ and $\mathcal{N} \equiv \mathcal{N}_R$. A further diagonalization of m_ν by the $U_{\rm PMNS}$ [24] leads to the diagonal mass matrix diag(m_{ν_j}, M_i) in the mass eigenstate basis $(n_j \;\; \mathcal{N}_i)^T$. Defining the Majorana mass eigenstates of light ($\nu_j = n_j + n_j^c$) and heavy neutrinos ($N_i = \mathcal{N}_i + \mathcal{N}_i^c$) by ν_j and N_i respectively, the interaction terms of Majoron (followed from Eq. 2.5) with light and heavy neutrino mass

[2] M_R being diagonal, N coincides with $\mathcal{N}_R$.

eigenstates can be written as

$$-\mathcal{L}_{\chi\nu\nu} = -\sum_{j,k}\mathcal{L}_{\chi\nu_j\nu_k} = -\frac{\chi}{2\sqrt{2}}\sum_{j,k}\left(\sum_i if_i\overline{\nu_j}P_R\nu_k V^T_{ji}V_{ik} + H.c.\right) \tag{2.7}$$

and

$$-\mathcal{L}_{\chi N\nu} = -\sum_{i,j}\mathcal{L}_{\chi N_i\nu_j} = \frac{\chi}{2\sqrt{2}}\sum_{i,j} f_i\left(\overline{\nu_j}P_R N_i V^T_{ji} + \overline{N_i}P_R\nu_j V_{ij}\right) + H.c., \tag{2.8}$$

where $V = \theta^\dagger U$.

2.2.1.2 Production and Decay of Majorons

As we are looking for Majoron as FIMP, the interactions of Majorons mentioned above are suggestive of its primary production via $N_i \to \chi\nu$, the associated decay width of which is given by,

$$\Gamma_{N_i\to\chi\nu} = \frac{M_i^3}{32\pi v_\phi^2}\sum_{j=1,2,3}|V_{ij}|^2. \tag{2.9}$$

Such a decay width can be shown to be approximately proportional to light neutrino mass ($\Gamma_{N_i\to\chi\nu} \simeq \frac{1}{32\pi}\left(\frac{M_i}{v_\phi}\right)^2\sum_j m_{\nu_j}$) [256] and hence suppressed. Also, this particular decay channel of N_i opens up only after the electroweak symmetry breaking (EWSB) as the interaction in Eq. 2.8 contributing to this decay is proportional to the active-sterile neutrino mixing. Considering the RHNs are in thermal equilibrium at a temperature $T > M_i$ and the branching of this decay remains sizeable enough compared to other decays of N_i ($e.g.$ N_i to the SM ones via neutrino Yukawa interactions), the relic contribution of Majoron can be expressed as [91],

$$\Omega_\chi h^2 \approx \frac{1.09\times10^{27}}{g_\star^{\mathcal{S}}\sqrt{g_\star^\rho}}m_\chi\sum_i\frac{g_i\Gamma_{N_i\to\chi\nu}}{M_i^2}, \tag{2.10}$$

where $g_\star^{\mathcal{S},\rho}$ is the effective number of degrees of freedom in the bath and $g_i = 2$ denotes the internal spin degrees of freedom of RHN.

On the other hand, following Eq. 2.7, Majoron can decay into light neutrinos having the decay width

$$\Gamma_{\chi\to\nu\nu} = \frac{m_\chi}{16\pi v_\phi^2}\sum_j m_{\nu_j}^2 \simeq \frac{1}{10^{19}s}\left(\frac{m_\chi}{1\text{ MeV}}\right)\left(\frac{8\times10^8\text{ GeV}}{v_\phi}\right)^2\left(\frac{\sum_j m_{\nu_j}^2}{2.6\times10^{-3}\text{ eV}^2}\right). \tag{2.11}$$

In getting the sum of the light neutrino mass-squared in Eq. 2.11, the best fit values of atmospheric and solar mass-splittings are used from neutrino oscillation data [102] where we consider a normal hierarchy of light neutrinos along with $m_{\nu_1} = 0$. For the Majoron to be a viable dark matter candidate, its lifetime must exceed the cosmological stability bound

$$\Gamma^{-1}_{\chi\to\nu\nu} > \tau_U. \tag{2.12}$$

Here we denote $\tau_U \sim \mathcal{O}(10^{19})$ sec as the lower limit on the lifetime of dark matter decaying

into invisible channels [257], as constrained by CMB and LSS observations [258]. Notably, the bound τ_U ($\sim$ 100 Gyr) is stronger than the age of the Universe, $t_U \simeq 4 \times 10^{17}$ sec ($\sim$ 14 Gyr), ensuring that dark matter remains stable well beyond the cosmic age. Using Eqs. 2.10 and 2.11, the above relation can therefore be employed to provide a limit on the relic contribution of Majoron as given by

$$\Omega_\chi h^2 < 1.28 \times 10^{-9} \left(\frac{10^{19}\ \text{sec}}{\tau_U}\right). \tag{2.13}$$

The contribution turns out to be insignificant in making up the dark matter relic $\Omega_\chi h^2 \simeq 0.120 \pm 0.001$ [63].

Apart from the interactions with neutrinos mentioned in Eqs. 2.7 and 2.8, Majorons also have interaction with the CP-even scalar ϕ. However, in view of negligible portal coupling $\lambda_{H\Phi}$, this ϕ field can not be present in the thermal bath of the early Universe consisting of the SM fields. Since ϕ has no such important role to play, it is generally assumed that the ϕ field is heavy enough ($m_\phi \sim v_\Phi$, *i.e.* with $\lambda_\Phi \sim \mathcal{O}(1)$) compared to the rest of the masses involved in the set-up and hence decoupled. Other possibility of χ production is from the process $H^\dagger H \to \chi\chi$ which is again proportional to tiny Higgs portal coupling and suppressed by m_ϕ. This turns out to be a possibility of having heavy Majorons $\sim$ TeV [234]. Here, however, we plan to explore lighter Majorons as DM.

2.2.2 The Proposal

As we have discussed above, the minimal Majoron set-up cannot accommodate the required relic density of FIMP like DM as Majoron. In order to make it a viable option, we extend this set-up by introducing an explicit dimension-5 $U(1)_L$ breaking term

$$-\mathcal{L}_{\text{d}_5} = \frac{\alpha_i}{2\Lambda}\left[\Phi^2 + (\Phi^*)^2\right]\overline{\mathcal{N}_{R_i}^c}\mathcal{N}_{R_i} + H.c., \tag{2.14}$$

where Λ is a cut-off scale. Here we follow a guideline considering that the explicit breaking of the global symmetry (LNS) takes place at some high scale ($\Lambda \leq M_{\text{Pl}}$) [259, 260] the manifestation of which is through the appearance of *non-renormalizable* operators (of dimension 5 or more, suppressed by powers of Λ) only. Hence, the operator in Eq. 2.14 is the only leading order LNV operator[3] involving RHNs and Φ field. For simplicity, we consider the coefficients α_i appearing in Eq. 2.14 to be $\mathcal{O}(1)$ and omit them for further discussion.

Note that the term of Eq. 2.14 being a higher order one, the $U(1)_L$ symmetry is only softly broken. This is similar to the origin of the Majoron mass of Eq. 2.3 where the smallness of m is connected to higher order explicit LNV operator. As per our guideline above, such a mass term $m^2(\Phi^2 + \Phi^{*2})$ may originate from a non-renormalizable explicit symmetry breaking term, *e.g.* $k\frac{|\Phi|^4}{\Lambda^2}(\Phi^2 + \Phi^{*2})$, which results $m^2 = k\langle\Phi\rangle^2\left[\frac{\langle\Phi\rangle}{\Lambda}\right]^2$ after spontaneous symmetry breaking and explains naturally the smallness of it as $\langle\Phi\rangle \ll \Lambda$.

Such a term[4] also contributes to the mass of the RHNs, after the spontaneous breaking

[3] The usual dimension-5 operator contributing to light neutrino mass, $\frac{c_{ij}}{\Lambda} L_i H L_j H$, may also be present. However, assuming c_{ij} to be small enough, we ignore this term for the analysis without loss of any generality.

[4] Disappearance of any cross generation term is ensured in the mass-diagonal basis of RHNs.

of $U(1)_L$ symmetry, as given by

$$M_i = v_\phi \left(\frac{f_i}{\sqrt{2}} + \frac{v_\phi}{\Lambda} \right). \tag{2.15}$$

Note that the inclusion of such a term carries the potential of generating a sizeable population of Majorons via the four-point interaction between Majorons and RHNs

$$-\mathcal{L}_{\rm int} = \frac{1}{2\Lambda} \chi^2 \overline{N_i^c} N_i, \tag{2.16}$$

induced by Eq. 2.14 after the $U(1)_L$ symmetry is spontaneously broken. This term contributes to the production of Majorons via $NN \to \chi\chi$ annihilation, somewhat similar to the UV freeze-in scenario (discussed in the section 1.3.2) as we elaborate below. Although suppressed by the cut-off scale Λ, this process turns out to be crucial in producing Majorons as it could remain in operation at a very early Universe (after the $U(1)_L$ symmetry breaking), contrary to the usual Majoron production from RHN decay $N \to \chi\nu$ being effective after the EWSB at temperature $T_{\rm EW}$.

2.2.2.1 Majoron Production via annihilation

As proposed above, the introduction of the effective interaction between RHNs and Majorons as in Eq. 2.16 opens up the new production channel for Majorons via annihilation of RHNs (see Fig. 2.1) once the $U(1)_L$ symmetry is broken at a temperature[5] $T_L \sim v_\phi$. It is interesting to note that the RHNs receive their masses from the spontaneous breaking of the $U(1)_L$ symmetry around this temperature only. Now, these RHNs may or may not be in thermal equilibrium. First, we consider the RHNs to be in equilibrium (as case[A]) and thereafter we investigate the situation when the abundance of RHNs at T_L to be negligible (as case [B]) to begin with which is expected to be increased thereafter gradually by the neutrino Yukawa interaction. Following the discussion before, we assume the Higgs portal coupling $\lambda_{H\Phi}$ negligible and consider ϕ being heavy to be decoupled field.

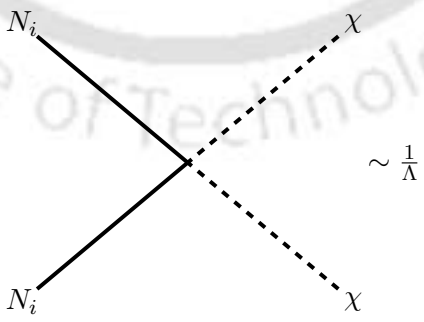

Figure 2.1: Annihilations of RHNs to Majorons

To study the evolution of the yield of Majoron as DM, we use the Boltzmann equation written in terms of the temperature (T) and the comoving number density of χ as $Y_\chi = n_\chi/\mathcal{S}$

[5]We consider the reheating temperature after inflation (T_R) to be bigger than T_L, though smaller than Λ.

(here $\mathcal{S}$ is the entropy density). A general form of this equation (irrespective of whether N_i and/or χ are in equilibrium) can be written as follows [48, 261]

$$\begin{aligned}\mathcal{H}T\frac{dY_\chi}{dT} = &-2\mathcal{S}\sum_i \langle\sigma v\rangle_{N_iN_i\to\chi\chi} Y_{N_i}^{\mathrm{eq}^2}\left(\frac{Y_{N_i}^2}{Y_{N_i}^{\mathrm{eq}^2}} - \frac{Y_\chi^2}{Y_\chi^{\mathrm{eq}^2}}\right)\\ &-\sum_{i,j}\langle\Gamma_{N_i\to\chi\nu_j}\rangle Y_{N_i}^{\mathrm{eq}}\left(\frac{Y_{N_i}}{Y_{N_i}^{\mathrm{eq}}} - \frac{Y_\chi Y_{\nu_j}}{Y_\chi^{\mathrm{eq}}Y_{\nu_j}^{\mathrm{eq}}}\right)\theta(T_{\mathrm{EW}}-T).\end{aligned} \tag{2.17}$$

Here, $\mathcal{H}$ is the Hubble rate and $\mathcal{S}$ dnotes the entropy density of the Universe as expressed in Eqs. 1.36 and 1.37, respectively. The yield of a particle species a in thermal equilibrium (Y_a^{eq}) is given by,

$$Y_a^{\mathrm{eq}}(T) = \frac{45g_a}{4\pi^4 g_\star^{\mathcal{S}}(T)}\left(\frac{m_a}{T}\right)^2 K_2\left(\frac{m_a}{T}\right), \tag{2.18}$$

where $g_a = 1(2)$ (for scalar (fermion)) and m_a are the internal degrees of freedom and mass of the particle species respectively. K_2 is the modified Bessel's function of the second kind. $\langle\sigma v\rangle$ and $\langle\Gamma\rangle$ are thermally averaged cross section and decay width respectively, the estimate of which are described below in the following section. The relic density of χ is obtained after substituting the freeze-in abundance $Y_\chi(T_0)$ in Eq. 1.55, where T_0 is the present temperature.

2.2.3 Dark Matter phenomenology

We now study the role of the higher dimensional interaction of Eq. 2.14 in obtaining the relic density of the Majoron field χ which is expected to play the role of freeze-in DM. From the discussion of the previous section, we understand that this operator contributes to the production of Majorons from the annihilations of RHNs. The matrix element squared for the annihilation process $N_iN_i \to \chi\chi$ is given by,

$$|\overline{M}|^2_{N_iN_i\to\chi\chi} = \frac{1}{\Lambda^2}\left(s - 4M_i^2\right), \tag{2.19}$$

leading to the cross section

$$\sigma_{N_iN_i\to\chi\chi} = \frac{1}{16\pi s}\sqrt{\frac{s-4m_\chi^2}{s-4M_i^2}}\,|\overline{M}|^2_{N_iN_i\to\chi\chi}, \tag{2.20}$$

where $\sqrt{s}$ is the centre of mass energy of the process at a temperature T.

We consider $U(1)_L$ symmetry to be broken below the reheating temperature, T_{RH} indicating $T_L < T_{\mathrm{RH}}$. Since the origin of the Majoron field is intertwined with the breaking of this global symmetry, the initial temperature for studying the χ abundance through the Boltzmann equation(s) (via Eq. 2.17) can be considered as $T_L \sim v_\phi$ [147] instead of the reheating temperature as in UV freeze-in scenario [92]. In this way, we do not need to invoke a parameter outside the framework (such as T_{RH}) in the parameter space scan. However, without any prior knowledge on T_{RH} and keeping in mind that RHNs get their masses at T_L, RHNs may or may not be in equilibrium at this temperature.

With the above points in mind, below we proceed for the evaluation of the freeze-in relic density of Majoron as DM corresponding to two cases: [A] RHNs are in thermal equilibrium

and [B] RHNs are not in thermal equilibrium at T_L and find out the relevant parameter space. The initial abundance of the χ particle is considered to be zero at this temperature T_L in both cases. As we have already seen in section 2.2.1 that the contribution $N_i \to \chi\nu$ channel to the χ abundance is almost negligible, we proceed further without it.

2.2.3.1 RHNs: in thermal bath at T_L

With the consideration that the RHNs are already in thermal equilibrium and abundance of χ remains vanishing at T_L, the Majorons can be produced from the annihilation via dimension-5 operator whose yield can be estimated by the following Boltzmann equation for χ

$$\frac{dY_\chi}{dT} \simeq -\frac{2\mathcal{S}}{\mathcal{H}T}\sum_i \langle\sigma v\rangle_{N_iN_i\to\chi\chi} Y_{N_i}^{\rm eq^2}\left[1-\frac{Y_\chi^2}{Y_\chi^{\rm eq^2}}\right], \tag{2.21}$$

which is a simplified form of Eq. 2.17. First term in $r.h.s$ of Eq. 2.21 refers to the production of χ due to the annihilation of RHNs where the factor 2 in front arises due to production of two Majorons in the final state. The second term in the $r.h.s$ related to the back reaction $\chi\chi \to N_iN_i$ (and $\chi\nu \to N_i$) is not important as χ starts with a negligible abundance in general. However, for light Majoron (of $\sim$ keV mass), the χ abundance near freeze-in temperature can be comparable (though remains smaller) to its equilibrium abundance where this term would be significant. On the other hand, the equilibrium abundance of RHNs is given by

$$Y_{N_i}^{\rm eq}(T) = \frac{45 g_i}{4\pi^4 g_\star^{\mathcal{S}}(T)}\left(\frac{M_i}{T}\right)^2 K_2\left(\frac{M_i}{T}\right), \tag{2.22}$$

with $g_i = 2$. The thermally averaged cross-section appearing in Eq. 2.21, can be expressed as [79]

$$\langle\sigma v\rangle_{N_iN_i\to\chi\chi} = \frac{1}{8M_i^4 T K_2^2(M_i/T)}\int_{4M_i^2}^{\infty}\sigma_{N_iN_i\to\chi\chi}(s-4M_i^2)\sqrt{s}K_1\left(\sqrt{s}/T\right)ds. \tag{2.23}$$

By integrating Eq. 2.21 from $T_L \sim v_\phi$ (from where χ production takes place) to T_0 (today), we can obtain the yield of χ.

Note that the parameters involved in analyzing the Majoron or χ production are: f_1, f_2 (related to RHN masses M_1, M_2), v_ϕ, m_χ and the cut-off scale Λ. For simplicity, we consider the couplings (real) f_1, f_2 to be same ($f_1 = f_2 = f$) and fix f at some natural value, $f = 0.01$ so that the degenerate RHN masses $M_i = M$ always remain below v_ϕ. Thereafter, we employ the Boltzmann equation (Eq. 2.21) to perform a scan over the parameter space so as to satisfy the DM relic density by the χ field. In doing so, we implicitly consider Λ being the cut-off scale is bigger than v_ϕ, however, bounded by the largest scale $M_{\rm Pl}$. Furthermore, the stability criteria via Eq. 2.12 must be satisfied. We also incorporate an upper limit on v_ϕ as the maximum value for the reheating temperature is generally considered to be $T_{\rm RH}^{\rm max} \sim 10^{15}$ GeV [262] ($v_\phi < T_{\rm RH}$ as stated earlier).

Our findings are displayed in Fig. 2.2 (left panel) by the coloured region corresponding

to the correct DM relic abundance in the $m_\chi - v_\phi$ plane. The colours in this relic satisfied $m_\chi - v_\phi$ space are indicative of the corresponding Λ value in the right-side colour bar. The gradient of the colour (from blue to dark red side) is increased with the increase in Λ which saturates at $M_{\rm Pl}$. The lower boundary of the allowed parameter space follows from the stability constraint while the top-left disallowed region (white patch) is limited by a specific choice $v_\phi/\Lambda < f/\sqrt{2}$, so that the dimension-5 operator's contribution to the RHN mass (see Eq. 2.15) remains sub-dominant. On the other hand, the top-right disallowed region corresponds to $\Lambda > M_{\rm Pl}$. The leftmost region of the allowed parameter space is bounded

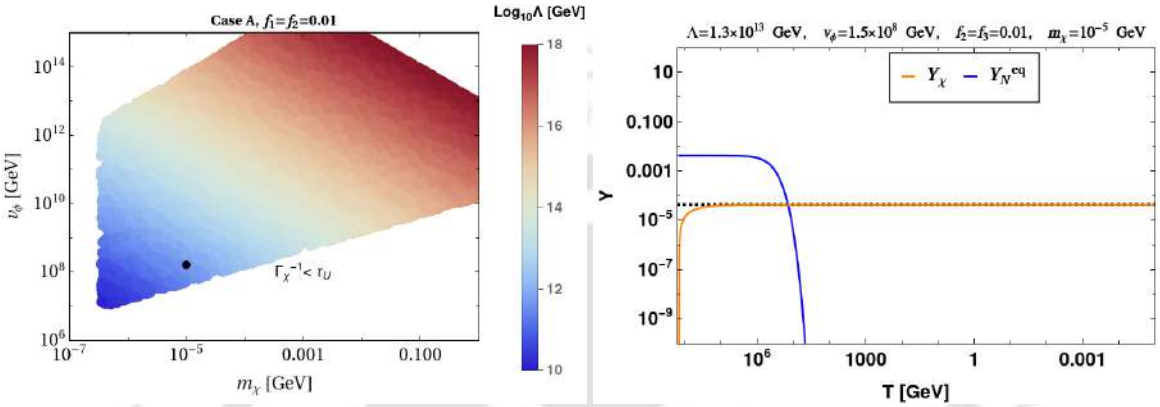

Figure 2.2: Left panel: Case A (degenerate RHNs are in thermal equilibrium at T_L): DM parameter space satisfying correct relic density represented by coloured region in v_ϕ vs m_χ plane, while Λ are in colour side-bar. The black dot indicates the BP considered in Table 2.1. **Right panel:** Evolution of Y_χ (solid orange), $Y_{N_i} = Y_{N_i}^{\rm eq}$ (solid blue) against T (GeV) are shown corresponding to the BP for case A from Table 2.1 with degenerate RHNs ($f_1 = f_2 = 0.01$). The grid line indicates the correct yield for the observed DM relic abundance.

by the model-independent limit [92] on the Majoron mass $m_\chi < \mathcal{O}(0.1)$ keV, signifying that the Majorons can never be able to reach thermal equilibrium. We find for Majoron as light dark matter in the range 0.1 keV - 1 GeV, the Lepton number breaking scale v_ϕ and Λ fall in the following range,

$$m_\chi : 0.4\,\text{keV} - 1\,\text{GeV};$$
$$v_\phi : 10^6\,\text{GeV} - 10^{15}\,\text{GeV};$$
$$\Lambda : 10^{10}\,\text{GeV} - 10^{18}\,\text{GeV}.$$

In order to demonstrate the freeze-in of the Majoron, we include the right panel in Fig. 2.2 where the abundance of the χ field is presented as a function of temperature T. This corresponds to a specific benchmark set of points (BP) from the parameter space as included in Table 2.1 (indicated by a dark dot on the allowed parameter space in the left panel of Fig. 2.2). Note that as the RHNs are in thermal equilibrium from the beginning (indicated by the blue line), the maximum production of χ (in the orange line) from the RHN annihilation takes place near the temperature T_L itself, where the $U(1)_L$ is broken. Such a behaviour is similar to the usual UV freeze-in scenario. The horizontal grid line corresponds to the yield of χ producing the correct relic abundance for $m_\chi = 10$ keV. Note that this result remains unchanged even if we consider non-degenerate RHNs. Since both the RHNs (even if $M_1 \neq M_2$) are considered to be in thermal equilibrium at T_L, it does not affect the production

of χ from N_i annihilation which happens to be around T_L. Next, we proceed to investigate the situation when RHNs are not in the thermal bath.

BP	Λ (GeV)	v_ϕ (GeV)	m_χ (GeV)
case A	1.3×10^{13}	1.5×10^{8}	10^{-5}
case B.1	10^{12}	1.6×10^{8}	10^{-5}

Table 2.1: Benchmark Point (B.P.) for case A and case B.1. For both cases $f_1 = f_2 = 0.01$ is considered.

2.2.3.2 RHNs: not part of the thermal bath at T_L

Here, we consider the case where RHNs are not in thermal equilibrium[6] at T_L. Hence, we do not expect an identical behaviour for the Majoron production in terms of its dominant production near T_L. Rather, first the RHNs are being produced from the thermal bath by the inverse decay process: $\ell_L H \to N_i$ and consequently the Majoron abundance should be increased from the annihilations of the RHNs gradually.

Initially, we presume negligible abundance of both the χ and the N_i at T_L. Then we solve the coupled Boltzmann equations for Majoron as well as RHNs (N_i) as given by,

$$\frac{dY_{N_i}}{dT} = \frac{2\mathcal{S}}{\mathcal{H}T}\langle\sigma v\rangle_{N_iN_i\to\chi\chi}\left(Y_{N_i}^2 - \frac{(Y_{N_i}^{\rm eq})^2}{(Y_\chi^{\rm eq})^2}Y_\chi^2\right) + \frac{1}{\mathcal{H}T}\langle\Gamma_{N_i\to\ell_L H}\rangle\left(Y_{N_i} - Y_{N_i}^{\rm eq}\right), \quad (2.24)$$

$$\frac{dY_\chi}{dT} = -\frac{2\mathcal{S}}{\mathcal{H}T}\sum_i\langle\sigma v\rangle_{N_iN_i\to\chi\chi}\left(Y_{N_i}^2 - \frac{(Y_{N_i}^{\rm eq})^2}{(Y_\chi^{\rm eq})^2}Y_\chi^2\right), \quad (2.25)$$

where, $\langle\sigma v\rangle_{N_iN_i\to\chi\chi}$ follows from Eq. 2.23 and $\langle\Gamma_{N_i\to\ell_L H}\rangle$ is the thermal averaged decay width of $N_i \to \ell_L H$ expressed as,

$$\langle\Gamma_{N_i\to\ell_L H}\rangle = \Gamma_{N_i\to\ell_L H}\frac{K_1(M_i/T)}{K_2(M_i/T)}, \quad (2.26)$$

with

$$\Gamma_{N_i\to\ell_L H} = \sum_\alpha \frac{|y^\nu_{\alpha i}|^2 M_i}{8\pi}. \quad (2.27)$$

Note that in this case, the neutrino Yukawa coupling $y^\nu_{\alpha i}$ plays important role in the production of RHNs from the thermal bath which in turn affects the production of Majorons. The structure of $y^\nu_{\alpha i}$ can be extracted using the Casas-Ibarra (CI) parametrization [124] as:

$$y^\nu = i\frac{\sqrt{2}}{v}U^\dagger D_{\sqrt{m_\nu}}\mathcal{R}D_{\sqrt{M_R}}, \quad (2.28)$$

where $D_{\sqrt{m_\nu}}$ ($D_{\sqrt{M_R}}$) is the squared-root of the diagonal active neutrino (RHN) mass matrix, and U is the PMNS mixing matrix consisting of the three mixing angles and a CP-

[6] Recall that RHNs become massive at T_L only.

violating phase. Here, $\mathcal{R}$ is a complex orthogonal matrix. We take the lightest active neutrino mass to be zero so as to define the D_{m_ν} from the best fit values [263, 264] of the two mass squared differences from neutrino oscillation data [263]. The fitted values [263, 264] of mixing angles and CP phase can be used to define U. As we are working with two RHNs, the structure of the $\mathcal{R}$ matrix is chosen here as [238],

$$\mathcal{R} = \begin{pmatrix} 0 & 0 \\ \cos\theta_R & \sin\theta_R \\ -\sin\theta_R & \cos\theta_R \end{pmatrix}, \tag{2.29}$$

where θ_R is in general a complex angle. With these inputs along with $v = 246$ GeV and a specific choice of θ_R, one can define the neutrino Yukawa coupling y^ν which is used in evaluating the decay width of RHNs appearing in the set of Boltzmann equations.

With Degenerate RHNs

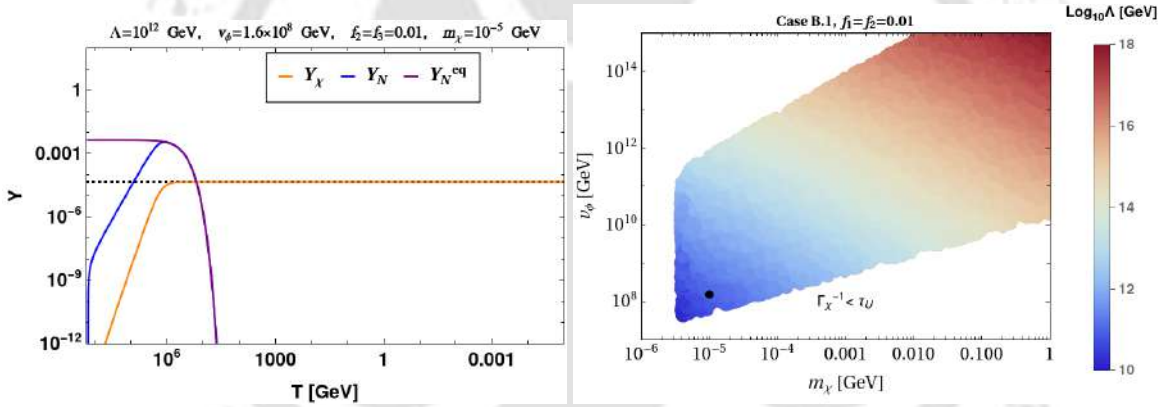

Figure 2.3: Left panel: Evolution of Y_χ (solid orange), Y_{N_i} (solid blue) and $Y_{N_i}^{\rm eq}$ (solid purple) against T (GeV) are shown corresponding to the BP for case B.1 from Table 2.1 with degenerate RHNs and $\theta_R = \pi/4$. The black dotted line indicates the correct yield for the observed DM relic abundance. **Right panel:** Case B.1 (degenerate RHNs are not in thermal equilibrium at T_L): DM parameter space satisfying correct relic density represented by coloured region in v_ϕ vs m_χ plane, while Λ are in colour side-bar. The black dot indicates the BP considered in Table 2.1.

In order to check the expectations for the χ abundance and its freeze-in scenario compared to case A, we provide Fig. 2.3 where, in left panel, benchmark set of parameters are assigned as per Table 2.1, second row (namely, case B.1). Furthermore, in line with the discussion for case A, here also we consider the degenerate RHNs (by choosing same values for f_1 and f_2 as f). We find that starting with negligible initial abundance, the yield of N_i (indicated by the blue line) has gradually increased via the inverse decay and finally around $T \sim M$, it catches the equilibrium abundance (purple line), thanks to the Yukawa coupling $(y^\nu_{\alpha i})$. Note that there exists an additional parameter θ_R in this case as y^ν depends upon it. We fix it[7] to be as $\pi/4$. Similar to case A, production of χ occurs from the four-point inter-

[7]This particular choice of θ_R with degenerate RHN mass corresponds to the same decay widths for both the RHNs, hence N_1 and N_2 reach equilibrium simultaneously. A general picture is demonstrated in the next

actions between the RHNs and χ (after $U(1)_L$ symmetry breaking). However, contrary to case A, the production of χ here extends over a period from T_L to $T \sim M$. The freeze-in of χ occurs near the point when N_i enters into thermal equilibrium.

We then perform a parameter space scan with fixed $f = 0.01$ and $\theta_R = \pi/4$ which produced the correct relic density by Majoron field which is provided in the right panel of Fig. 2.3. We find the following range of parameters

$$\begin{aligned} m_\chi &: 3 \text{ keV} - 1 \text{ GeV}; \\ v_\phi &: 10^7 \text{ GeV} - 10^{15} \text{ GeV}; \\ \Lambda &: 10^{10} \text{ GeV} - 10^{18} \text{ GeV}. \end{aligned}$$

allowed from the DM relic satisfaction point of view. Similar to case A, the top-left boundary appears due to the consideration $v_\phi/\Lambda < f/\sqrt{2}$ where we have restricted ourselves for m_χ below 1 GeV. The other imposed condition $v_\phi < T_{\rm RH}^{\rm max} \sim 10^{15}$ GeV represents the upper limit of v_ϕ in the parameter space as reflected in Fig. 2.3 (right panel). Contrary to case A, here the leftmost boundary of the parameter space has shifted to $m_\chi \sim 3$ keV. This shift arises in case B.1 as a result of delayed thermal equilibration of RHNs which marks the efficient production of χ (from RHN annihilations) near $T \sim M_i$ compared to case A. Moreover, for the same reason we notice that corresponding to a similar set of parameters (m_χ, v_ϕ) in case A, we require here a relatively smaller Λ to satisfy the correct relic (refer to Table 2.1). This is reflected in Fig. 2.3 (right panel) where Λ remains well within its upper limit $M_{\rm Pl}$ so as not to exhibit any disallowed region (which exists for Fig. 2.2 (left panel) beyond $m_\chi > 2$ MeV). We also find that there exists a lower limit on the spontaneous symmetry breaking scale, $v_\phi > 4 \times 10^7$ GeV (bottom leftmost corner in the right panel of Fig. 2.3) [258].

With Non-Degenerate RHNs

So far, we consider the case with degenerate RHNs (taking $f_1 = f_2$). However, in a more general case where the two RHNs are not of the same mass ($i.e.$ $f_1 \neq f_2$), it will be interesting to investigate the behaviour of DM yield especially in the context of case B, where RHNs are not in thermal equilibrium at $T \sim T_L$. To elaborate it further, we start with same choices for $v_\phi, m_\chi, \theta_R, f_2$ related to case B.1 as in Table 2.1, whereas differ in choosing $f_1 = 0.001$ ($i.e.$ $M_1 < M_2$). It turns out that this non-degeneracy leads to a relatively lower $\Lambda = 7.7 \times 10^{11}$ GeV (in comparison to $\Lambda = 10^{12}$ GeV with $f_1 = f_2 = 0.01$, see Fig. 2.3, left panel) in order to satisfy the correct relic for χ. The associated evolution of the Majoron abundance is shown in Fig. 2.4. This new set of parameters is indicated in first row of Table 2.2. As observed in Fig. 2.4, the production of χ initially takes place from N_2 annihilation during the epoch when N_2 (with heavier mass) gradually approaches its equilibrium density (at $T \sim M_2$) due to inverse decay process. However, the production of Majoron continues beyond this temperature as the production from N_1 annihilation sets in. This introduces a kink in the yield of Majoron which is demonstrated in the inset of the figure. Finally the yield of χ freezes in when the lighter RHN (N_1) enters equilibrium at $T \sim M_1$.

subsection.

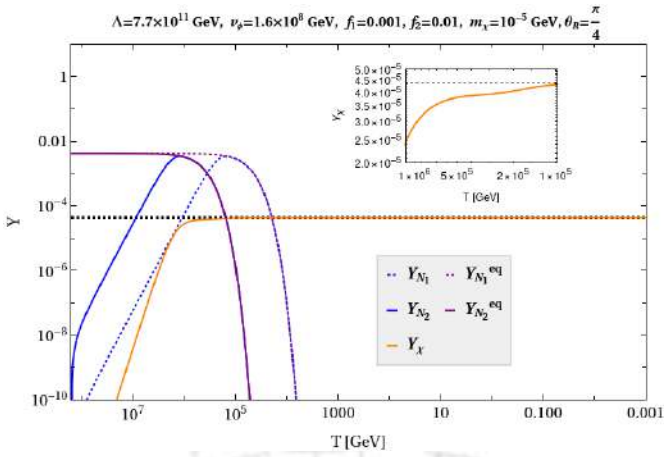

Figure 2.4: Evolution of Y_χ (solid orange), Y_{N_1} (dashed blue) and Y_{N_2} (solid blue) along with $Y_{N_1}^{\rm eq}$ (dashed purple) and $Y_{N_2}^{\rm eq}$ (solid purple) against T (GeV) are shown corresponding to the BP from 1st row, Table 2.2 (with $f_1 = 0.001,\ f_2 = 0.01$). The black dotted line indicates the correct yield for the observed DM relic abundance. In the inset, Y_χ is shown between $T \sim M_1$ and $T \sim M_2$.

v_ϕ (GeV)	m_χ (GeV)	f_1	f_2	θ_R	Λ (GeV)
1.6×10^8	10^{-5}	0.001	0.01	$\frac{\pi}{4}$	7.7×10^{11}
1.5×10^{13}	2.5×10^{-3}	0.009	0.1	$2.5 + 1.463i$	2×10^{16}

Table 2.2: Benchmark Points (BP) for case B.2 with non-degenerate RHNs.

We incorporate a set of benchmark parameters in the second row of Table 2.2 to mark the dependence on the other parameter θ_R (which in general can be complex) through y^ν matrix. As in this case, initially, the abundance of RHNs is negligible and it enters equilibrium via the neutrino Yukawa interaction, θ_R plays important role in determining the strength of this interaction and in a way affects the production of Majoron as well from RHN annihilation. Here, we consider a complex[8] $\theta_R = 2.5 + 1.463i$. The corresponding evolution of $N_{1(2)}$ and Majoron abundances are shown in the left panel of Fig. 2.5 by blue dotted (solid) and orange lines respectively. To exhibit the effect of θ_R on the abundance of χ, we now choose a real $\theta_R = 2.5$ while keeping all other parameters unchanged and exhibit the evolutions of RHNs and χ (by red dotted (solid) and green lines respectively) in the same figure. As we can see, this makes the Majoron under-abundant.

With this particular choice of θ_R $(= 2.5 + 1.463i)$ and $f_1 = 0.009, f_2 = 0.1$, we represent the result of another parameter space scan in the right panel of Fig. 2.5 in $v_\phi - m_\chi$ plane. We note that the allowed parameter space becomes broadened in comparison with Fig. 2.2 (left panel) and 2.3 (right panel). This is due to the inclusion of additional parameter in the set-up in the form of different f_1 and f_2 along with complex θ_R. The role of a complex angle θ_R can be significant in the context of the model-dependent constraints on Majoron (such as constraint on $\chi \to \gamma\gamma$ channel etc.) as we discuss it in the following section.

[8]Note that a complex θ_R can be the source of CP violation in leptogenesis. This particular choice of θ_R is related to correct baryon asymmetry generation via leptogenesis with $M_{1(2)}$ considered here [265,266].

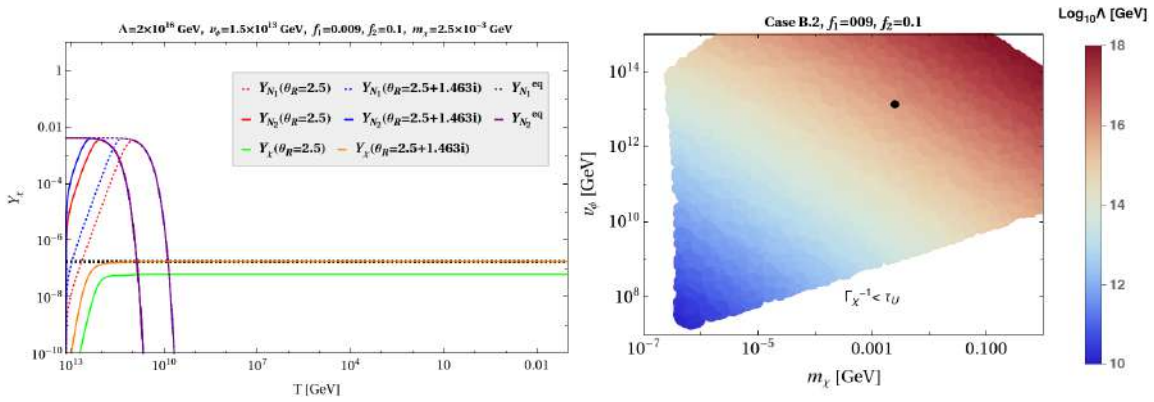

Figure 2.5: Left panel: Evolution of Y_χ, Y_{N_1} and Y_{N_2} for two different choices of θ_R (2.5 and $2.5+1.463i$) along with $Y_{N_1}^{\rm eq}$ and $Y_{N_2}^{\rm eq}$ are plotted against T (GeV). All other parameters correspond to the BP from Table 2.2, second row. The black dotted line indicates the correct yield for the observed DM relic abundance. **Right panel:** Case B.2 (non-degenerate RHNs are not in thermal equilibrium at T_L): parameter space satisfying correct DM relic density represented by coloured region in v_ϕ vs m_χ plane, while Λ are in colour side-bar. Here, θ_R is kept fixed as $2.5 + 1.463i$. The black dot indicates the BP considered in Table 2.2, second row.

2.2.4 Constraints

As already discussed, the presence of the decay channel $\chi \to \nu\nu$ can make the Majoron unstable. Hence, in order to make the Majoron a viable dark matter, the condition $\tau_\chi > \tau_U$ needs to be employed which translates into the following expression from the recent analysis [258] using *Planck* [267] with CMB lensing [268] and BAO data as [258],

$$\Gamma(\chi \to \nu\nu) < 1.29 \times 10^{-19}\ \text{s}^{-1}.$$

We have already incorporated this limit on the parameter space. We now turn our attention to other constraints applicable to the parameter space obtained in our set-up originating from supernova, cosmology as well as some indirect search experiments.

The same tree-level coupling of Majoron with light neutrino mass eigenstates (see Eq. 2.7) may also experience a constraint from supernova (SN). The basic idea stems from the fact that inside the supernova core, Majorons can be produced through the process $\nu\nu \to \chi$ (mainly ν_e takes part inside the SN core). Provided the neutrino-Majoron coupling parametrized by $g_{\chi\nu\nu} \equiv \sum_i m_{\nu_i}/2v_\phi$ is large, such Majorons would affect [233, 269–273] the neutrino signal emitted from a core collapsing SN which is otherwise consistent with the binding energy released during SN explosion as measured for SN1987A [274, 275]. Such a consideration leads to a disallowed range of the coupling $g_{\chi\nu\nu}$: $(10^{-7} - 10^{-5})$ for $m_\chi < 10$ MeV and $(10^{-9} - 10^{-6})$ for $m_\chi < 200$ MeV, as evaluated in [269]. However, our parameter space scan indicates that $v_\phi \gtrsim \mathcal{O}(10^7)$ GeV and accordingly $g_{\chi\nu\nu} \lesssim 2.5 \times 10^{-18}$ (where $\sum_i m_{\nu_i} \simeq 0.05$ eV is inserted). Hence, it remains way below the limit from supernova constraint.

Also, this Majoron decay into light neutrinos may produce observable monochromatic neutrino fluxes which can be analyzed in dedicated experiments such as Borexino (testable at 4 MeV $< m_\chi <$ 60 MeV) [240], KamLAND (testable at 16 MeV $< m_\chi <$ 60 MeV) [241], SK (within 30 MeV $< m_\chi <$ 200 MeV [242, 276] and IceCube (up to 10 TeV) [277]. The study in [148] translates these constraints as the lower bound on the lepton number breaking

scale v_ϕ against m_χ above MeV. We have taken their limits from [148] and imposed upon the parameter space obtained in both cases A and B.1 as shown in the left and right panels in Fig. 2.6, respectively. As a result, it restricts the obtained parameter space further.

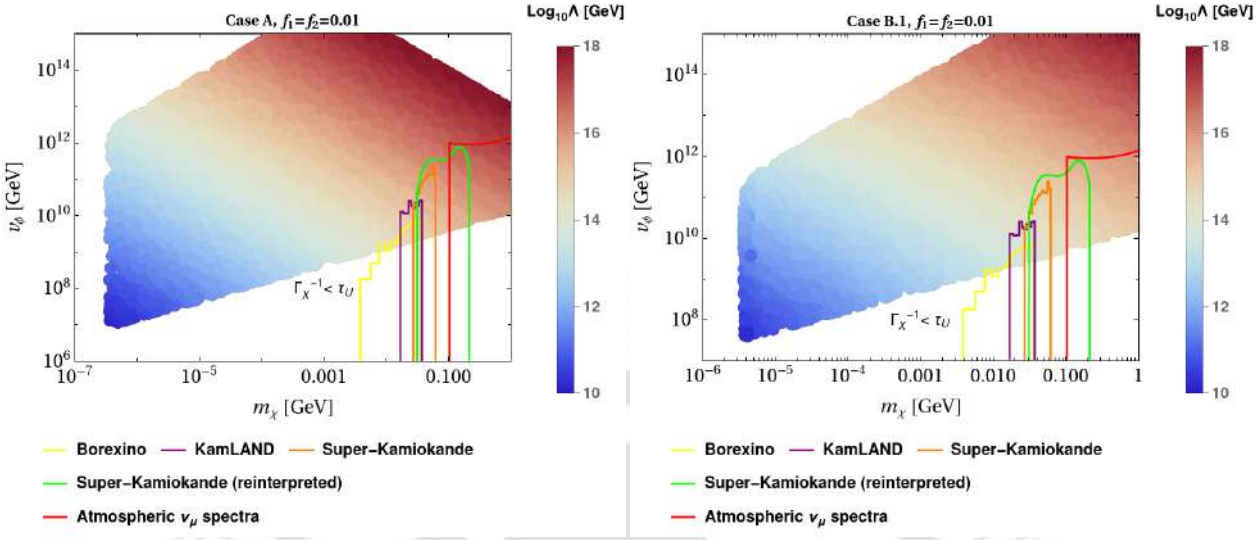

Figure 2.6: Left panel: v_ϕ (GeV) vs m_χ (GeV) parameter space for case A (when degenerate RHNs are in thermal equilibrium at T_L) combined with neutrino lines search experiment results. The solid lines for different experiments imply the lower bounds on v_ϕ. **Right panel:** v_ϕ (GeV) vs m_χ (GeV) parameter space for case B.1 (when degenerate N_i are not in thermal equilibrium at T_L) combined with neutrino lines search experiment results. The solid lines for different experiments imply the lower bounds on v_ϕ.

Apart from the model independent decay channel ($\chi \to \nu\nu$), there exists another interesting decay channel of Majoron: $\chi \to \gamma\gamma$ which can be induced in two-loops [148]. Following [148], a simplified expression for the associated decay width turns out to be [148, 278],

$$\Gamma\left(\chi \to \gamma\gamma\right) \simeq \frac{\alpha^2 (\mathrm{tr}\mathcal{K})^2}{4096\pi^7} \frac{m_\chi^3}{v^2} \left| \sum_f N_c^f T_3^f Q_f^2 g\left(\frac{m_\chi^2}{4m_f^2}\right) \right|^2 , \tag{2.30}$$

where f denotes all the SM fermions having color multiplicity as $N_c^f = 3(1)$ for quarks (leptons), T_3^f is the isospin, Q is the corresponding electric charge in units of $e = \sqrt{4\pi\alpha}$. The loop function is given by

$$g(x) = -\frac{1}{4x}\left(\log|1 - 2x + 2\sqrt{x(x-1)}|\right)^2 ,$$

having $x = m_\chi^2/4m_f^2$. Here $\mathcal{K}$ is a model-dependent parameter given by $\mathcal{K} = m_D m_D^\dagger/(v v_\phi)$, a dimensionless hermitian coupling matrix. Such γ emission lines can be probed by many experiments such as INTEGRAL γ observatory [243], COMPTEL/EGRET [244], Fermi-LAT [245]. In addition, the diffuse X-ray background observed by HEAO [279] was looking for the emission line over $3 - 48$ keV range, while other X-ray telescopes like *chandra* [220, 224] and XMM [280] cover the energy range $0.3 - 12$ keV. Similarly, the γ-ray line emission of 20 keV- 7 MeV can be covered by INTEGRAL SPI observations [243]. Energies above 7 MeV is covered by a combination of COMPTEL and EGRET γ-ray telescopes. Fermi γ-ray telescope [245] recently searches the emission line within $7 - 200$ GeV energy range.

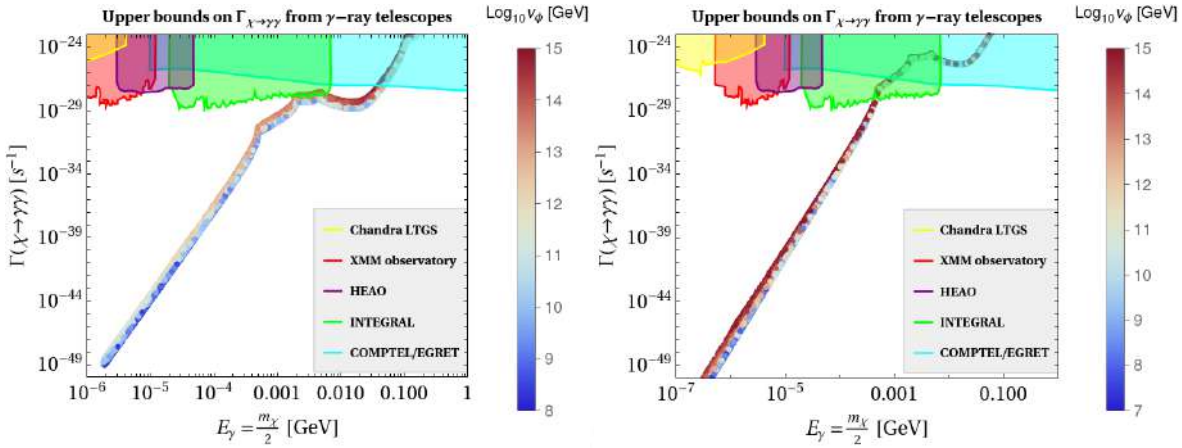

Figure 2.7: $\Gamma_{\chi\to\gamma\gamma}$ vs $E_\gamma = \frac{m_\chi}{2}$ with v_ϕ in side colourbar. **Left panel**: case B.1 ($f_1 = f_2 = 0.01,\ \theta_R = \frac{\pi}{4}$) and **right panel**: case B.2 ($f_1 = 009,\ f_2 = 0.1,\ \theta_R = 2.5 + 1.463i$). The line emission constraints (from different γ-ray observations) are shown along with the model prediction.

We first evaluate the $\mathcal{K}$-matrix for each m_χ from the allowed parameter space (using v_ϕ and neutrino Yukawa coupling y^ν via Eq. 2.28) of Figs. 2.3 (right panel) and 2.5 (right panel). After plugging this $\mathcal{K}$ into Eq. 2.30, respective $\Gamma(\chi \to \gamma\gamma)$ is plotted against $E_\gamma = m_\chi/2$ in left (for case B.1) and right (case B.2) panels of Fig. 2.7 for the entire allowed parameter space obtained in our proposal where the limits from different X-ray and γ-ray observations are also shown. The differently coloured shaded patches on the upper side of each plot indicate the excluded regions for different experiments, the description of which is given in the inset of each figure. It can be seen that the Majoron mass below MeV can easily evade these bounds making the cosmological bound most effective in the sub-MeV mass regime. Whereas, relatively larger values of v_ϕ appear to be somewhat constrained for $m_\chi \sim 3.5 - 13$ MeV mass for case B.1. Alongside, Majoron masses beyond 100 MeV, in this case, fall within the sensitivities of the observations by COMPTEL and EGRET. For case B.2, it can be seen from Fig. 2.7 that the entire $m_\chi \gtrsim 0.8$ MeV region turns out to be within the exclusion limits of X-ray and γ-ray emission line bounds for this particular choice of θ_R. However, this conclusion is not very robust as it can be altered for a different choice of θ_R, and hence model dependent. This stems from the fact that the decay width $\Gamma(\chi \to \gamma\gamma)$ depends on the $\mathcal{K}$ matrix which is governed by the choice of complex θ_R. In case of real θ_R, however, the $\mathcal{K}$ remains independent of θ_R. For this reason, we do not incorporate a separate figure for case A (with real θ_R) which would result in a similar plot as the left panel of Fig. 2.7.

It is interesting to note that the lighter side of the Majoron dark matter in our analysis, in particular 1-10 keV mass region, apparently coincides with the conventional warm dark matter (WDM) mass regime. Such keV scale WDM experiences a stringent constraint from observations of Lyman-α forest [281–287], thereby imposing a limit: $m_{\rm WDM} \gtrsim (1.9-5.3)$ keV at 95% CL with the inherent assumption that the WDM maintains a thermal distribution. However, the Majoron here is a FIMP type DM which never attains thermal equilibrium. Hence, the above mentioned bound requires modification [288–290] before applying to our case.

To have a mapping between the above constraint on conventional thermal $m_{\rm WDM}$ onto

a modified one for FIMP type DM mass $m_{\rm FDM}$, following [289, 290], we define a quantity called *warmness* associated to the DM (stands for either WDM or FDM) as $\omega_{\rm DM} = \widetilde{\omega}_{\rm DM}\frac{T_{\rm DM}}{m_{\rm DM}}$, where

$$\widetilde{\omega}^2_{\rm DM} = \frac{\int d^3q q^2 f_{\rm DM}(q)}{\int d^3q f_{\rm DM}(q)}, \tag{2.31}$$

and $T_{\rm DM}$ represents the temperature of the DM which is related to the temperature of the thermal bath (T) via

$$T_{\rm DM} = \left(\frac{g^{\mathcal{S}}_\star(T)}{g^{\mathcal{S}}_\star(T_{\rm dec})}\right)^{1/3} T = \mathcal{A}T. \tag{2.32}$$

Here $T_{\rm dec}$ corresponds to a temperature when the DM production becomes most efficient. In Eq. 2.31, the physical momentum p is scaled as $q = p/T_{\rm DM}$, and $f_{\rm DM}$ corresponds to the phase space distribution of the respective DM.

For a feebly interacting DM like Majoron as χ in our case, the phase space distribution can be obtained [290] considering the main production process: $NN \to \chi\chi$ as

$$f_\chi(q) \simeq \frac{1}{\mathcal{H}(T_{\rm dec})}\int_{x_i}^{x_f} dx \frac{x}{E_\chi} C[f_\chi], \tag{2.33}$$

where, $x = M_1/T$, $\mathcal{H}(T_{\rm dec})$ is the Hubble expansion rate at $T_{\rm dec} \sim M_1$ (beyond which it freezes in) and $C[f_\chi]$ denotes the collision term corresponding to χ production channel: $NN \to \chi\chi$. Using Eq. 2.16, the simplified expression of $C[f_\chi]$ for such process can be written as [291],

$$C[f_\chi] \simeq \frac{4g_N^2 g_\chi \Gamma(2) T^5}{(2\pi)^2\Lambda^2 p^2}\left(\frac{p}{T}\right)^2 e^{-p/T}, \tag{2.34}$$

where $g_N = 2$ and $g_\chi = 1$ are the spin degrees of freedom of RHN and χ respectively. Employing Eq. 2.34 into Eq. 2.33 and integrating it within the limits between $x_i = M_1/v_\phi$ (we consider the production of χ initiates at $T = T_L \sim v_\phi$) and $x_f = 1$ (production of χ gets ceased at $T \sim M_1$), the phase-space distribution of Majoron can be expressed, upto a proportionality factor, as,

$$f_\chi(q) \propto \int_{x_i}^{x_f} dx \frac{1}{qx\mathcal{A}(x)} e^{-q\mathcal{A}(x)}. \tag{2.35}$$

With this phase-space distribution for χ, we find $\widetilde{\omega}_\chi \simeq 2.45$ whereas for a thermal scalar WDM, $\widetilde{\omega}_{\rm WDM}$ is found to be 3.22.

As mentioned earlier, finally one aims to convert the existing lower bound on $m_{\rm WDM}$ onto $m_{\rm FDM}$ $(i.e.\ m_\chi$ here) and that is done by equating the warmness (ω) of thermal WDM to that of χ (non-thermal Majoron) [289, 290]. Using the relation between ω and $\widetilde{\omega}$, such a consideration leads to

$$m_\chi = m_{\rm WDM}\left(\frac{\widetilde{\omega}_\chi}{\widetilde{\omega}_{\rm WDM}}\right)\frac{T_\chi}{T_{\rm WDM}}. \tag{2.36}$$

While the temperature of Majoron (T_χ) can be obtained from Eq. 2.32 with $T_{\rm dec} \sim M_1$, the temperature of the thermal WDM $(T_{\rm WDM})$ is to be extracted from the correct relic satisfaction of WDM via,

$$\Omega_{\rm WDM}h^2 = \frac{g_{\rm WDM}}{2}\left(\frac{m_{\rm WDM}}{94\ {\rm eV}}\right)\left(\frac{T_{\rm WDM}}{T_\nu}\right)^3, \tag{2.37}$$

where $g_{\rm WDM} = 1$ (for scalar) and $\Omega_{\rm WDM}h^2 = 0.12$. Using Eq. 2.36, the thermal WDM mass ($m_{\rm WDM}$) involved in the Lyman-α bound can be translated into m_χ (FIMP type DM produced via $NN \to \chi\chi$ process) as

$$m_\chi \simeq 5.3 \text{ keV} \left(\frac{m_{\rm WDM}}{3 \text{ keV}}\right)^{4/3} \left(\frac{106.75}{g_\star^{\mathcal{S}}(T_{\rm dec})}\right)^{1/3}. \tag{2.38}$$

Here $g_\star^{\mathcal{S}}(T_{\rm dec}) = g_\star^{\mathcal{S}}(M_1) \sim 106.75$ as $M_1 \gg T_{\rm EW}$. Using $m_{\rm WDM} = 3$ keV as the a reference value, we therefore obtain an approximate lower bound on Majoron mass from Lyman-α observation as, $m_\chi \geq 5.32$ keV, specific to our case. This estimate is somewhat conservative, as more recent dedicated analyses of structure formation find stringent limits on the freeze-in dark matter as $m_\chi \gtrsim 15$ keV [292, 293].

2.2.5 Conclusion

In this work, we relooked into the original Majoron model, the existence of which is due to the spontaneous breaking of global lepton number symmetry. Its feeble coupling with the SM fields renders itself as a natural candidate for FIMP-like dark matter. Earlier studies showed that though it is plausible to have Majorons as FIMP-like dark matter, satisfying the observed DM relic abundance remains a challenge and Majoron mass can either be 2.7 MeV or heavy $\sim$ TeV. In an effort to explore the possibility of having Majorons as a viable FIMP type DM candidate in a broader range (and below GeV) so as to make it interesting from the observational point of view, we include a higher order explicit lepton number breaking term in the Lagrangian involving RHNs and the spontaneous symmetry breaking scalar field. While such an interaction presents itself as a natural soft symmetry-breaking term (due to the suppression by the cut-off scale), it introduces new feeble interaction for Majorons, thereby introducing new production channel for Majorons via annihilation of the RHNs. As a result, a viable parameter space of freeze-in type of Majoron dark matter follows in the range $\mathcal{O}$(keV - GeV).

It is perhaps pertinent here to compare our results with other works which include such higher order Majorons-RHNs interactions. In [222], such interaction arised effectively from $f\Phi NN$ term (also responsible for RHN mass $M_N = f\langle\Phi\rangle$) via the t-channel RHN mediated diagram and simultaneously a contact-interaction results while using non-linear representation of pNGB field. The associated cross-section for the Majoron production via $NN \to \chi\chi$ turned out to be proportional to f^4/M_N^2 whereas in our case, we have an explicit LNV interaction $NN\chi^2$ which is independent of f or M_N, thereby extending the freedom in satisfying the relic density constraint. Hence the 'two Majorons and two sterile neutrinos' contribution exercised in [222], though present here too, becomes subdominant (we fix $f = 0.01$) compared to the contribution of our explicit LNV dimension 5 operator. Additionally, [222] has two types of Majoron production channels: (i) $h \to \chi\chi$ followed from an explicit tree level LNV term $\lambda\chi^2 H^\dagger H$ which is absent in our analysis (as from the very beginning we consider the breaking of LN only at higher order). There the parameter λ is also linked with $f\Phi NN$ coupling via logarithmic divergent neutrino loop. This channel turned out to be important in limiting the Majoron mass from above: $m_\chi \lesssim 0.0015$ GeV in [222]. (ii) On the other hand,

in [222], the Majoron mass had a lower limit $m_\chi \gtrsim 10^{-7}$ GeV where the Majoron production is dominated by $NN \to \chi\chi$ process. Along a similar line, the work of [223] also considered the $NN \to \chi\chi$ process which proceeds via t-channel exchange of heavy RHNs. The paper however focussed on two possible candidates of dark matter: lightest RHN N_1 and Majoron χ. With $m_\chi < M_N$, the case is similar to that of [222].

In a nutshell, the presence of a separate dimension-5 operator in our work relaxes the tension among the parameters which results an extended parameter space for m_χ. Our analysis shows that an adequate region of parameter space consistent with Majoron as dark matter satisfying correct relic abundance in the keV-GeV mass range can be obtained. While this entire mass regime is important in the context of supernova cooling, the above-MeV region is also fascinating to be probed by monochromatic neutrino lines. Even though the bounds from such experiments turn out to be more stringent than the naively considered lifetime of the Universe, the parameter space undergoes a rich dark matter phenomenology and finally provides compelling evidences in the form of gamma-ray lines that can be probed by ongoing and future experiments indicating some tantalizing connection between dark matter and neutrino physics.

2.3 Connecting Resonant Leptogenesis with Majoron Dark Matter

In this follow-up work [294], we consider the above scenario of Majoron as FIMP-type DM with resonant leptogenesis. To be explicit, we discuss a concrete $U(1)_L$ symmetric model of neutrino mass based on the type I seesaw mechanism, involving two right-handed neutrinos and a $U(1)_L$ breaking scalar field having Z_2 odd parity, coupled to the RHNs at tree level. However, slightly different from the previous setup, here, the construction leads to off-diagonal nonzero entries in the RHN mass matrix that result into two exactly degenerate RHNs. Then, the inclusion of dimension-5 $U(1)_L$ breaking terms not only breaks such a degeneracy but also opens up new annihilation channels of RHNs to Majorons, thereby making Majoron production possible via freeze-in scenario [9] in line with the previous work([239]). Note that the same splitting that removes the degeneracy of RHNs turns out to be also instrumental in producing the matter-antimatter asymmetry via resonant leptogenesis.

We perform a combined analysis of Majorons as FIMP type dark matter and resonant leptogenesis and establish the parameter space which implies a relation involving neutrino mass, dark matter and the baryon asymmetry of the Universe. In doing so, we realize that contrary to the usual expectation of resonant leptogenesis happening near the TeV scale or so, here we end up a relatively high scale resonant leptogenesis scenario in order to be consistent with the Majoron DM parameter space, which can also be of interest for further investigation.

The layout of the remainder of the section is as follows. In subsection 2.3.1, we define the new setup, featuring both global $U(1)_L$ conserving and breaking terms. In subsection 2.3.2, we discuss Majoron FIMP DM following a similar way as discussed previously in subsection 2.2.1. In subsection 2.3.3, we discuss resonant leptogenesis in the considered model and calculate the lepton asymmetry for a benchmark point consistent with those required

[9] A similar concept was explored in [265], where the soft breaking of lepton number symmetry played a key role in the freeze-in production of dark matter.

for Majoron FIMP DM. In subsection 2.3.4, we discuss in detail the parameter space compatible with Majoron FIMP DM and resonant leptogenesis, highlighting the role of non-renormalizable $U(1)_L$-breaking operator common to both effects and the CP asymmetry contributions from self energy and vertex correction terms. Finally, subsection 2.3.5 concludes this section.

2.3.1 The type I seesaw Set-up

Similar to the subsection 2.2.1, here, we extend the SM by including two singlet right handed neutrinos ($\mathcal{N}_{1,2}$) and a SM singlet complex scalar field (Φ), charged under a global $U(1)_L$. The only key difference here is that, we introduce an additional Z_2 symmetry, under which all the SM fields and one of the RHNs $\mathcal{N}_1$ are even, while $\mathcal{N}_2$ and Φ carry odd, as summarized in table 2.3. As a result, though the field contents are the same, our setup is relatively

Symmetries	Φ	$\mathcal{N}_1$	$\mathcal{N}_2$
$U(1)_L$	-2	1	1
Z_2	$-$	$+$	$-$

Table 2.3: Beyond the SM particles and their charges under global $U(1)_L$ and Z_2 symmetries.

different than the previously considered Majoron model in terms of the renormalizable part of the Lagrangian. Here, we consider the following part of the type I seesaw Lagrangian, which respects both $U(1)_L$ and Z_2 symmetry,

$$-\mathcal{L}_{\rm SC} \supset \frac{f}{2}\Phi\overline{\mathcal{N}_1^C}\mathcal{N}_2 + y_{\alpha 1}\overline{\ell_L}_\alpha \widetilde{H}\mathcal{N}_1 + H.c.. \tag{2.39}$$

Here $y_{\alpha 1}$ defines the coupling corresponding to the neutrino Yukawa interaction involving $\alpha = e, \mu, \tau$ lepton doublets with RHN $\mathcal{N}_1$. The other RHN does not contribute to the neutrino Yukawa interaction at this renormalizable level due to Z_2 charge assignment of the fields involved. Once the $U(1)_L$ symmetry is spontaneously broken ($\Phi = (\phi + v_\phi + i\chi)/\sqrt{2}$), Φ field acquires a *vev* which leads to the RHN mass matrix (in flavor basis of RHNs) as

$$M_R = \begin{pmatrix} 0 & M \\ M & 0 \end{pmatrix}, \tag{2.40}$$

with $M = fv_\phi/\sqrt{2}$. It then follows that such a construction leads to an exactly degenerate pair of RHNs (barring a relative phase) having mass $M_1 = M_2 = fv_\phi/\sqrt{2}$ at the renormalizable level.

Upon the spontaneous symmetry breaking (SSB) of global $U(1)_L$, the massless Nambu-Goldstone Boson (namely Majoron χ) also results in presence of the scalar potential involving Φ and H as given in Eq. 2.2. Similar to earlier, we ignore the mixing between the CP even part of H and Φ here as well.

2.3.1.1 Explicit $U(1)_L$ breaking terms of higher order

The massless Majorons would get mass once the explicit lepton number symmetry breaking terms are introduced making them massive pseudo-Goldstone boson (pNGB) [141]. We incorporate the same soft-symmetry breaking term as in Eq. 2.3 to induce a non-zero Majoron mass $m_\chi^2 = m^2$. Coincidentally, the soft breaking term (in Eq. 2.3) breaks $U(1)_L$ to a residual Z_2 symmetry, which is respected by Φ.

The $U(1)_L$ symmetry, being a global one, is expected to be explicitly broken also by gravity effect at the Planck scale [248–253] or even at a lower cut-off scale Λ in the context of weak gravity conjecture as in [259, 260], as mentioned earlier. To be specific, here, we consider a similar explicit $U(1)_L$ breaking terms at dimension-5 level involving Φ and two RHNs (while keeping the Z_2 symmetry intact) as

$$\begin{aligned} -\mathcal{L}_L = &\frac{c_1}{2\Lambda}\left[\Phi^2 + (\Phi^*)^2\right]\overline{\mathcal{N}_1^C}\mathcal{N}_1 + \\ &\frac{c_2}{2\Lambda}\left[\Phi^2 + (\Phi^*)^2\right]\overline{\mathcal{N}_2^C}\mathcal{N}_2 + \frac{y_{\alpha 2}}{\Lambda}\overline{\ell_{L\alpha}}\widetilde{H}\mathcal{N}_2(\Phi + \Phi^*) + H.c.. \end{aligned} \tag{2.41}$$

While the first two terms contribute to the diagonal elements of the RHN mass matrix as well as production of Majorons after $U(1)_L$ is spontaneously broken, the third term in the RHS of Eq. 2.41 signifies the Yukawa interaction of the second RHN ($\mathcal{N}_2$). The uniform coupling of this interaction with Φ and Φ^* is ensured in presence of a CP symmetry [227] under which $\Phi \to \Phi^*$. The case of non-uniform coupling in considered in appendix A.1.1. Note that other terms in Eqs. 2.3, 2.41 are also consistent with such a symmetry consideration. As a result, the Majoron is not involved in this Yukawa interaction. The involvement of this Yukawa coupling is crucial in making the light neutrino mass matrix to be consistent with neutrino oscillation data. The other standard dimension-5 operator contributing to the light neutrino mass, $\frac{\delta_{ij}}{\Lambda}\overline{\ell_{Li}}H\overline{\ell_{Lj}}H$, might also be present [103]. However, assuming δ_{ij} is sufficiently small, we exclude this contribution from the analysis without any loss of generality. Also, the presence of such Z_2-odd charge of Φ, even for the $U(1)_L$ breaking contribution, ensures that terms such as $\Phi^3|H|^2$ do not appear at the dimension 5 level.

2.3.1.2 Effect of explicit $U(1)_L$ breaking on RHN mass

After the SSB of $U(1)_L$, the relevant Lagrangian inclusive of the explicit lepton number breaking contribution for RHN mass, in the flavor basis of RHN $(\mathcal{N}_1\ \mathcal{N}_2)^T$, is given by

$$\mathcal{L} \supset \frac{1}{2}\begin{pmatrix}\overline{\mathcal{N}_1^C} & \overline{\mathcal{N}_2^C}\end{pmatrix}\begin{pmatrix}\kappa_1 & M \\ M & \kappa_2\end{pmatrix}\begin{pmatrix}\mathcal{N}_1 \\ \mathcal{N}_2\end{pmatrix}, \tag{2.42}$$

where $\kappa_i = c_i v_\phi^2/\Lambda$ corresponds to the diagonal contribution to the mass matrix of RHNs arising from the first two dimension-5 explicit breaking operators of Eq. 2.41. Considering $c_1 = c_2 = 1$ for simplification purpose (hence, $\kappa_{1,2} = \kappa$ say), we diagonalize this RHN mass matrix (M_R) through a unitary operator V following the relation $V^* M_R V^\dagger = M_R^d$, where

$$M_R^d = \mathrm{diag}[M + \kappa, M - \kappa], \tag{2.43}$$

is the diagonal RHN mass matrix (barring a phase) in the basis of the RHNs: $(N_{R_1}\ N_{R_2})^T$, connected to the flavor basis as: $\mathcal{N}_1 = \frac{1}{\sqrt{2}}(N_{R_1}+iN_{R_2})$ and $\mathcal{N}_2 = \frac{1}{\sqrt{2}}(N_{R_1}-iN_{R_2})$. Hence, the dominant contribution to RHN mass comes from the renormalizable part of the Lagrangian while the small splitting (κ) emerges from the dimension-5 operators. These nearly degenerate RHNs would take part in resonant leptogenesis as we will discuss in a later section.

2.3.1.3 Neutrino mass

The Lagrangian for the neutrino sector is given by

$$-\mathcal{L}_\nu = y^\nu_{\alpha i}\overline{\ell_L}_\alpha \widetilde{H} N_{R_i} + \frac{f v_\phi}{2\sqrt{2}}(\overline{N^C_{R_1}} N_{R_1} + \overline{N^C_{R_2}} N_{R_2}) + \frac{\kappa}{2}(\overline{N^C_{R_1}} N_{R_1} - \overline{N^C_{R_2}} N_{R_2}) + H.c., \quad (2.44)$$

defined in the RHNs as well as charged lepton mass diagonal bases. Note that y^ν contributing to the Dirac mass of the neutrinos via $m_D = y^\nu v/\sqrt{2}$ after the EWSB, appears here as an effective Yukawa, originating from both the tree level and higher order Yukawas (due to the rotation of the RHN flavor to mass basis) as

$$y^\nu_{\alpha 1} = \frac{1}{\sqrt{2}} y_{\alpha 1} + \frac{v_\phi}{\Lambda} y_{\alpha 2}, \quad y^\nu_{\alpha 2} = \frac{i}{\sqrt{2}} y_{\alpha 1} - i\frac{v_\phi}{\Lambda} y_{\alpha 2}, \quad (2.45)$$

once the $U(1)_L$ symmetry is spontaneously broken.

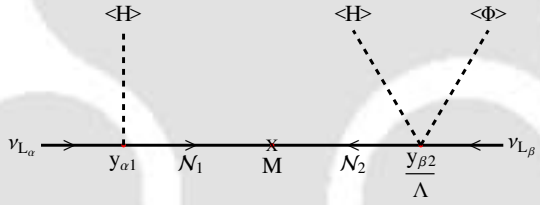

Figure 2.8: Schematic diagram for generation of the light neutrino mass, m_ν.

As a result, after the EWSB (by then, $U(1)_L$ is already broken), the mass terms involving ν_L and N_{R_i} $(i = 1, 2)$ can be cast (suppressing the generation indices) into

$$-\mathcal{L}_\nu \supset \frac{1}{2}\begin{pmatrix}\overline{\nu_L} & \overline{N^C_R}\end{pmatrix}\begin{pmatrix}0 & m_D \\ m_D^T & M_R^d\end{pmatrix}\begin{pmatrix}\nu_L^C \\ N_R\end{pmatrix}. \quad (2.46)$$

The light and heavy neutrino mass matrices can now be obtained (with $m_D < M_R^d$) in the rotated basis $(\widetilde{\nu}^c_L\ N_R)^T$ via the type-I seesaw relations [238]: $m_\nu \simeq m_D(M_R)^{-1}m_D^T$ and $M_R \equiv M_R^d$ (already diagonal), where $\widetilde{\nu}^c_L = -i(\nu^c_L - \theta_{\rm as}N_R)$ and $\theta_{\rm as} = m_D^* M_R^{-1}$ being the active-sterile neutrino mixing matrix. Finally, after m_ν is futher diagonalised by the PMNS matrix (U) [24], final neutrino mass eigenstates $(n_j\ N_{R_i})^T$ can be obtained. Hereafter, we will use the notation of Majorana mass basis $\nu_j = n_j + n_j^c$ and $N_i = N_{R_i} + N^c_{R_i}$ for all the interactions. The RHN masses, written in this Majorana mass basis, and their mass-splitting (ΔM) turn

out to be[10]:

$$M_{1,2} = \frac{f v_\phi}{\sqrt{2}} \pm \frac{v_\phi^2}{\Lambda}; \qquad \Delta M = 2\frac{v_\phi^2}{\Lambda}. \tag{2.47}$$

Note that the neutrino Yukawa coupling matrix y^ν plays an important role in fixing the neutrino mass, mixing as well as the amount of asymmetry in leptogenesis, which will be evident as we proceed. Here, it is then pertinent to discuss its expected order of magnitude from the neutrino oscillation data [102], considering a normal hierarchy of the light neutrinos. In addition, the presence of two RHNs in the present setup compels us to consider the lightest active neutrino mass to be zero. The structure of y^ν can be estimated using the Casas Ibarra (CI) parametrization [124]

$$y^\nu = i\frac{\sqrt{2}}{v} U^\dagger D_{\sqrt{m_\nu}} \mathcal{R} D_{\sqrt{M_R^d}}, \tag{2.48}$$

where $D_{\sqrt{m_\nu}}$ ($D_{\sqrt{M_R^d}}$) is the squared root of the 3×3 (2×2) diagonal active neutrino [263, 264] (RHN) mass matrix. $\mathcal{R}$ is a complex orthogonal matrix, of the form [238] as in Eq. 2.29:

$$\mathcal{R} = \begin{pmatrix} 0 & 0 \\ \cos\theta_R & \sin\theta_R \\ -\sin\theta_R & \cos\theta_R \end{pmatrix}, \tag{2.49}$$

where θ_R is a complex angle in general ($\theta_R = z_R + i z_I$). For concreteness, we provide a typical y^ν below

$$y^\nu = \begin{pmatrix} -0.0023 - 0.00043i & 0.0013 - 0.0011i \\ 0.0029 + 0.00053i & -0.0012 + 0.001i \\ -0.0013 - 0.0014i & 0.0035 - 0.00050i \end{pmatrix}, \tag{2.50}$$

which is obtained using a set of reference values of the parameters (involved in parameter space scan of the upcoming sections), as shown in the following table 2.4 along with the choice of $\theta_R = \frac{\pi}{4} + 0.42i$. Such a choice of parameters implies $M_1 = 1.4\times 10^{10}$ GeV and $M_2 = 1.36\times 10^{10}$ GeV. It is also interesting to point out that such a y^ν is consistent with Eq.

Λ (GeV)	v_ϕ (GeV)	f
1.5×10^{14}	1.95×10^{11}	0.1

Table 2.4: Reference values of the parameters used for y^ν estimation (see Eq. 2.50).

2.45 with the choice of $y_{\alpha 1} \sim \mathcal{O}(10^{-3})$ where $y_{\alpha 2} \sim \mathcal{O}(1)$ as $\frac{v_\phi}{\Lambda} = 10^{-3}$ is already of similar order as y^ν.

[10]With $\kappa_1 \neq \kappa_2$, mass splitting would have an additional parameter $(c_1 + c_2)/2 \neq 1$, the effect of which is just to redefining/shifting the values of the parameters involved so as to remain consistent with the phenomenology of the scenario, without loss of generality.

2.3.2 DM phenomenology

We now turn our discussion on the Majoron being a dark matter candidate and for that purpose, we plan to estimate the number density of Majorons. As discussed elaborately in subsection 2.2.1, within the setup of the minimal type-I seesaw mechanism (via Eq. 2.39), tree-level coupling of Majorons to RHNs is not sufficient to produce enough Majorons to account for the correct DM relic density. Consequently, by following a similar approach as in subsection 2.2.2, we find that the production of Majorons can take place via a freeze-in scenario and we elaborate on such production channels and stability criteria of Majoron to be a successful dark matter candidate.

2.3.2.1 Majoron production from RHNs and stability

Here, we introduce dimension-5 lepton number violating operators and show how these lead to a viable phenomenology of the Majoron as a freeze-in dark matter candidate, with the assumption that Majoron was initially absent in the early Universe. As mentioned earlier, the inclusion of the additional higher dimensional operators in Eq. 2.41 induce the following interactions after the $U(1)_L$ symmetry gets spontaneously broken as

$$\frac{(\Phi^2+(\Phi^*)^2)\overline{\mathcal{N}_1^C}\mathcal{N}_1}{2\Lambda}+\frac{(\Phi^2+(\Phi^*)^2)\overline{\mathcal{N}_2^C}\mathcal{N}_2}{2\Lambda}\supset\frac{\chi^2}{2\Lambda}(\overline{N_1^C}N_1-\overline{N_2^C}N_2). \tag{2.51}$$

With such effective interactions, Majorons could be dominantly produced from the annihilations of RHNs, which leads to a signature of UV freeze-in [92, 295–297] as we discuss below. Note that any deviation from the universal coupling (ensured by assuming the CP symmetry, $\Phi\to\Phi^*$) with Φ and Φ^* of the Yukawa interaction may result Majoron instability (contributing toward $\chi\to\nu\nu$, in addition to the existing contribution given in Eq. 2.11) due to the presence of higher dimensional terms in the construction (see appendix A.1.1). However, such decay widths being suppressed (or at most of similar order) compared to the one in Eq. 2.11, the inclusion of Majoron's lifetime greater than the age of the Universe would automatically take care of this constraint, making it a viable dark matter candidate in our construction.

2.3.2.2 Majorons as Freeze-in dark matter

With the effective interactions of Majorons with RHNs as indicated in Eq. 2.51, the Majorons can be produced from the annihilations of RHNs in the early Universe. In this case, contrary to the usual freeze-in scenario of Majoron production from RHN decay, the production of Majoron dark matter crucially depends on the maximum temperature of the thermal bath. It is important to note that in contrast to the assumption $v_\phi < T_{\rm RH}$ made in the DM production scenario of the earlier section 2.2, here, we will consider the breaking of $U(1)_L$ symmetry to take place prior to the reheating temperature ($T_{\rm RH}$) of the Universe, *i.e* during inflation or in the reheating phase, with $v_\phi > T_{\rm RH}$. Such a choice of hierarchy between v_ϕ and $T_{\rm RH}$ is also consistent with our assumption of ϕ being decoupled from the study below $T_{\rm RH}$. Hence, in our case, dark matter production is sensitive to $T_{\rm RH}$ (unlike in Section 2.2, where it was sensitive to v_ϕ), which is considered as a free parameter in our study. We further

consider the RHNs to be present in the thermal bath requiring $T_{\rm RH} > M_i$ and a sizeable neutrino Yukawa interactions so as they can be responsible for thermal leptogenesis. As a result, a specific hierarchy between the energy scales $v_\phi > T_{\rm RH} > M_i$ is essential for this setup. Furthermore, since both the $U(1)_L$ and Z_2 symmetries are spontaneously broken when Φ obtains a non-zero *vev* prior to $T_{\rm RH}$ here ($i.e.$ during inflation or extended reheating period), any topological defects formed during this symmetry breaking would be diluted during inflation.

To analyse the evolution of DM yield originated from the annihilations of RHNs as discussed above, we solve the Boltzmann equation, similar as in Eq. 2.21, expressed in terms of the co-moving number density Y_χ $(= n_\chi/\mathcal{S})$ and the temperature (T) as follows [48, 261]

$$\frac{dY_\chi}{dT} \simeq -\frac{2\mathcal{S}}{\mathcal{H}T}\sum_i \langle\sigma v\rangle_{N_iN_i\to\chi\chi} Y_{N_i}^{\rm eq^2}\left[1-\frac{Y_\chi^2}{Y_\chi^{\rm eq^2}}\right], \tag{2.52}$$

where $\mathcal{H}$, $\mathcal{S}$ and $Y^{\rm eq}$ follow from Eqs. 1.36, 1.37 and 2.18, respectively. In Eq. 2.52, another production channel of Majoron $e.g.$ $N_i \to \chi\nu$ is not included as it contributes negligibly to the DM abundance being suppressed by the active-sterile neutrino mixing. Another contribution to the process $N_iN_i \to \chi\chi$ proceeds via t-channel RHN mediation, which however drives IR freeze-in [91] and remains subdominant compared to our scenario as discussed in [222, 234]. Here, $\langle\sigma v\rangle_{N_iN_i\to\chi\chi}$ is the thermally averaged cross-section of the process $N_iN_i \to \chi\chi$ as expressed in Eq. 2.23, where σ denotes the cross-section of the process $N_iN_i \to \chi\chi$ as

$$\sigma_{N_iN_i\to\chi\chi} = \frac{1}{16\pi s}\sqrt{\frac{s-4m_\chi^2}{s-4M_i^2}}\,|\overline{M}|^2_{N_iN_i\to\chi\chi}, \tag{2.53}$$

with

$$|\overline{M}|^2_{N_iN_i\to\chi\chi} = \frac{1}{\Lambda^2}\left(s-4M_i^2\right). \tag{2.54}$$

The final yield of the Majoron DM can be obtained by integrating Eq. 2.52 from $T_{\rm RH}$ (reheating temperature) to T_0 (present temperature). One then obtain the final relic density of χ by replacing the present DM abundance $Y_\chi(T_0)$ in

$$\Omega_\chi h^2 = 2.755\times10^8\left(\frac{m_\chi}{\rm GeV}\right)Y_\chi(T_0), \tag{2.55}$$

which should reproduce the observed dark matter relic density, $\Omega_{\rm DM}h^2 = 0.12\pm0.0012$ [63].

The main parameters involved in our analysis of dark matter production are f, Λ, $T_{\rm RH}$ and m_χ. Another important parameter is v_ϕ which enters in the RHN masses as $M_i = \left(\frac{fv_\phi}{\sqrt{2}} \pm \frac{v_\phi^2}{\Lambda}\right)$. However, for the DM phenomenology, the role of v_ϕ is not very significant as the DM yield, being dominated by UV freeze-in scenario, primarily depends on Λ and $T_{\rm RH}$ rather than the masses of the parent particles. Specifically, the Majoron yield (Y_χ) approximately follows the relation $Y_\chi \propto T_{\rm RH}/\Lambda^2$ as evident from Eqs. (2.52) - (2.54).

Since v_ϕ is not directly entering in the DM phenomenology except its involvement in the RHN mass and splitting (which are anyway insensitive to Majoron yield), we have chosen certain (mild) hierarchies between v_ϕ and $T_{\rm RH}$ as benchmark values for our analysis. For

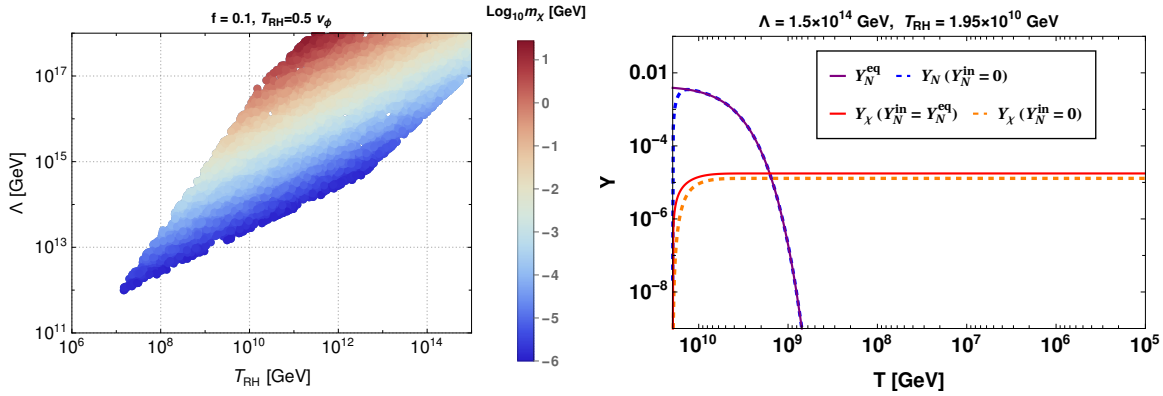

Figure 2.9: DM parameter space satisfying correct relic density represented by colored region in $T_{\rm RH}$ vs Λ plane, while m_χ are in color side-bar (left) and a benchmark point (right) are shown. Here $f = 0.1$ and the ratio $T_{\rm RH}/v_\phi = 0.5$ is considered.

example, in Fig. 2.9, a ratio of $T_{\rm RH}/v_\phi = 0.5$ and $f = 0.1$ is chosen. The left panel of Fig. 2.9 illustrates the DM parameter space in the $T_{\rm RH} - \Lambda$ plane with m_χ, obtained in order to satisfy the correct relic for each point in the parameter space, is shown in the color bar (with blue to dark red color gradient). As can be seen from Fig. 2.9 (left panel), we scan over a large region of the parameters; (i) $T_{\rm RH}$: 10^6 GeV $-$ 10^{15} GeV; (ii) Λ : 10^{11} GeV $-$ 10^{18} GeV & (iii) $m_\chi \gtrsim 1$ keV. While doing the scan, the conditions imposed on the parameters are the following: (a) $v_\phi > T_{\rm RH} > M_i$ as stated earlier and (b) $f/\sqrt{2} > v_\phi/\Lambda$ which follows from the fact that the contribution to the RHNs mass from the dimension-5 operator must remain subdominant compared to the renormalizable one. While boundary at the right side stems from the condition $f/\sqrt{2} > v_\phi/\Lambda$ (considering the ratio of $T_{\rm RH}/v_\phi = 0.5$), the left-side boundary signifies the Majoron DM must be stable following the essential criteria, $\Gamma^{-1}_{\chi\to\nu\nu} > \tau_U$. On the other hand, the top and the bottom boundary of the parameter space signifies the viable Majoron DM mass range, *i.e.* $\mathcal{O}(100)$ GeV $\geq m_\chi \geq 1$ keV, as evident from the color bar. In the right panel of Fig. 2.9, we have shown the DM yield (solid red line) for the benchmark point mentioned in table 2.4, which falls within the allowed parameter space of the left panel. As expected, the maximum production of the DM occurs at the very initial temperature, which is $T_{\rm RH}$. In Fig. 2.10, we have shown the parameter space satisfy-

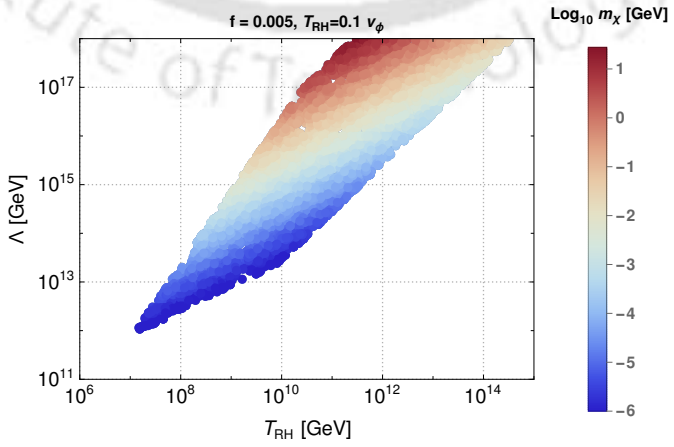

Figure 2.10: DM parameter space satisfying correct relic density represented by colored region in $T_{\rm RH}$ vs Λ plane, while m_χ are in color side-bar with $f = 0.005$ and the ratio $T_{\rm RH}/v_\phi = 0.1$.

ing correct DM relic density with a difference choice of ratio $T_{\rm RH}/v_\phi = 0.1$. It turns out that the parameter space in this case (in Fig. 2.10) gets shrunk compared to Fig. 2.9 (left panel) due to less number of points, satisfying the criteria $v_\phi > T_{\rm RH} > M_i$ and $f/\sqrt{2} > v_\phi/\Lambda$.

It is perhaps pertinent to discuss the situation, contrary to our earlier assumption, where the RHNs are not part of the thermal bath initially at $T_{\rm RH}$. In this case, the RHNs would attain thermal equilibrium through the inverse decay $\ell_{L\alpha} H \to N_i$ process, proportional to the neutrino Yukawa coupling $y^\nu_{\alpha i}$. However, how quickly they attain equilibrium depends solely on the strength of $y^\nu_{\alpha i}$. Since the Majorons are mainly produced from the annihilation of these RHNs in our framework, such Majoron production could be delayed depending on the time the RHNs would take to thermalise themselves. In order to explore that, we plot the yield of the RHNs for the same set of parameters $(\Lambda, f, T_{\rm RH})$ as used to plot $Y_N^{\rm eq}$ in Fig. 2.9 (right panel), but with zero initial abundance now, and depict it by blue dashed line. As seen, Y_N reaches the equilibrium abundance at a temperature slightly below $T_{\rm RH}$ due to the presence of the sizeable neutrino Yukawa coupling $y^\nu_{\alpha i} \sim \mathcal{O}(10^{-3})$, corresponding to the benchmark values of Tab. 2.4. This tiny delay in reaching thermal equilibrium for the RHNs results a relatively less freeze-in abundance of Majorons (orange dashed line). Hence, the correct relic abundance for the Majoron as DM would follow with a mild shift in m_χ value (from earlier value 2.5×10^{-5} GeV to a new one, 3.5×10^{-5} GeV). Since the neutrino Yukawa remains sizeable enough for the entire parameter space, our conclusion with thermalised RHNs at $T_{\rm RH}$ would mostly remain unchanged in case of zero abundance of RHNs, apart from a slight modification in Majoron mass to a relatively higher side.

In addition to the Majoron DM stability condition, another stringent constraint follows from monochromatic neutrino searches by experiments like Borexino [240], KamLAND [241], SuperKamiokande [242, 276], and IceCube [277], due to the model-independent decay of Majorons into light neutrinos. These experiments restricts the Majoron parameter space for $m_\chi \gtrsim 4$ MeV [288, 298]. Additionally, Majoron decay into two photons (induced in two-loops) provides another channel for probing the parameter space through several γ-ray observations [278, 288]. We have already discussed these constraints in detail in subsection 2.2.4 and also mentioned later in appendix A.1.2.

2.3.3 Resonant Leptogenesis

After getting the DM allowed parameter space, we are now in a position to discuss the leptogenesis scenario keeping in mind that the same set of operators of Eq. 2.51 contributing toward Majoron production will also be responsible for breaking the degeneracy of RHN mass, hence playing a key role in leptogenesis too. Before entering the details of the leptogenesis, specific to our set-up, we provide a brief overview of leptogenesis in general, more specifically the resonant case. The dynamical generation of lepton asymmetry takes place in an the era of radiation dominated Universe, below[11] $T_{\rm RH}$ ($M_i < T_{\rm RH}$), when the RHNs starts decaying.

Below the reheating temperature, the RHNs can be produced from the thermal bath due to inverse decay via the neutrino Yukawa interaction. The same interaction also keeps them

[11] For a generation of lepton asymmetry during the reheating phase *i.e.* when $M_i > T_{\rm RH}$, we refer the readers to [299–310].

in the equilibrium with the SM bath till the temperature of the Universe remain larger than their masses. Thereafter, their out of equilibrium decay to the SM Higgs and lepton doublet begins having a decay width, given by

$$\Gamma_{N_i\to\ell_L H} = \frac{|y^\nu_{ii}|^2}{8\pi} M_i. \tag{2.56}$$

One can track the abundance of the RHNs in the expanding Universe by solving the following Boltzmann equations:

$$\frac{dY_{N_i}}{dx} = -\frac{1}{\mathcal{H}x\mathcal{S}}\left[\frac{Y_{N_i}}{Y^{\rm eq}_{N_i}} - 1\right](\gamma_{N_i} + 2\gamma_{h_s} + 4\gamma_{h_t}), \tag{2.57}$$

where

$$\gamma_{N_i} = n^{\rm eq}_{N_i}\frac{K_1(x)}{K_2(x)}\Gamma_{N_i}, \tag{2.58}$$

$x = M_1/T$ with T being the temperature of the Universe. Additionally, γ_{h_s} and γ_{h_t} signify the reaction rates of Higgs mediated $\Delta L = 1$ processes involving the SM top quarks, *e.g.*, $N_i L \to qt$ (s-channel) and $N_i t \to Lq$ (t-channel), which are defined by

$$\gamma_{h_{s,t}} = \frac{M_i}{64\pi^2 x}\int ds\hat{\sigma_h}(s)\sqrt{s}K_1\left(\frac{x\sqrt{s}}{M_i}\right), \tag{2.59}$$

where

$$\hat{\sigma_h}(s) = \frac{y_t^2(y^{\nu^\dagger}y^\nu)_{ii}}{4\pi}\left(1 - \frac{M_i^2}{s}\right)^2. \tag{2.60}$$

Finally, $Y_{N_i} = n_{N_i}/\mathcal{S}$ denotes the comoving number density of the RHNs with n_{N_i} being the number density of the RHNs. Looking at Eq. 2.57, one notices that the first term in the squared bracket on the right hand side (r.h.s) comes with a negative sign and hence is responsible for the depletion of RHNs' abundance resulting primarily from its decay to the SM particle, while the second term is responsible for their production from bath due to the inverse decay.

The out of equilibrium decays of RHNs together with the lepton number violation (present due to Majorana masses of RHNs) and the CP violation originating from the neutrino Yukawa sector (as evident from the structure of y^ν via CI parametrisation) are the three necessary and sufficient conditions, namely the Sakharov's conditions [128], required for the dynamical generation of lepton asymmetry. It can be inferred from the DM phenomenology of the previous section that the RHN masses in our case ($\sim f v_\phi$), satisfying the correct relic, fall in a broad range from a very heavy to as light as 10^4 GeV. In this connection, one can recall that the standard thermal leptogenesis works for the RHN mass above 10^9 GeV, the so-called Davidson-Ibarra bound [138]. However, this conclusion is based on the hierarchical nature of RHNs. In case degenerate RHNs are present, like the present case, the asymmetry production can be significantly enhanced. In order to quantify such enhanced production of asymmetry, we proceed below for the evaluation of the CP asymmetry.

The CP asymmetry parameter ϵ_{N_i} associated to the decay of the i-th RHN can be ex-

pressed as

$$\epsilon_{N_i} = \frac{\sum_\alpha [\Gamma_{N_i \to \ell_{L\alpha} H} - \Gamma_{N_i \to \overline{\ell_{L\alpha}} \bar{H}}]}{\sum_\alpha [\Gamma_{N_i \to \ell_{L\alpha} H} + \Gamma_{N_i \to \overline{\ell_{L\alpha}} \bar{H}}]}, \tag{2.61}$$

which results from the interference of the tree-level decay of N_i and the one loop, vertex and self energy, diagrams. The general expression for such CP asymmetry (after flavor sum) can be estimated as [136, 237, 311–314]

$$\epsilon_{N_i} = -\sum_{j \neq i} \frac{M_i \Gamma_{N_j}}{M_j^2} \left(\frac{V_{ij}}{2} + S_{ij} \right) \frac{\mathrm{Im}(y^{\nu^\dagger} y^\nu)^2_{ij}}{(y^{\nu^\dagger} y^\nu)_{ii} (y^{\nu^\dagger} y^\nu)_{jj}}, \tag{2.62}$$

where

$$V_{ij} = 2 \frac{M_j^2}{M_i^2} \left[\left(1 + \frac{M_j^2}{M_i^2} \right) \ln \left(1 + \frac{M_i^2}{M_j^2} \right) - 1 \right], \tag{2.63}$$

$$\text{and} \quad S_{ij} = \frac{M_j^2 (M_j^2 - M_i^2)}{(M_j^2 - M_i^2)^2 + M_i^2 \Gamma_{N_j}^2}, \tag{2.64}$$

denote the vertex correction and self energy corrections respectively. At this stage, it is important to point out that though the contributions of the vertex and self energy corrections are of similar order for hierarchical RHNs, the self energy contributions dominate over the other in case of (closely) degenerate RHNs. This is mainly because, in the limit of quasi-degenerate RHNs masses *i.e.* $M_i \approx M_j$, the CP asymmetry can be maximised with $M_i^2 - M_j^2 \sim M_i \Gamma_{N_j}$ such that $S_{ij} \gg V_{ij} \sim \mathcal{O}(1)$ [237]. Alongside, the remaining part of Eq. 2.62 can be put in the form (with $\theta_R = z_R + i z_I$) [314]

$$F_y = \frac{\mathrm{Im}(y^{\nu^\dagger} y^\nu)^2_{ij}}{(y^{\nu^\dagger} y^\nu)_{ii} (y^{\nu^\dagger} y^\nu)_{jj}} \approx \left| \frac{2(m_2^2 - m_3^2) \sin(2z_R) \sinh(2z_I)}{(m_2 - m_3)^2 \cos(2z_R)^2 - (m_2 + m_3)^2 \cosh(2z_I)^2} \right|, \tag{2.65}$$

for normal hierarchical neutrinos which turns out to be $\mathcal{O}(0.7)$ for the choice of $\theta_R = 0.78 + 0.42i$ which we considered throughout the analysis and using the best fit values of neutrino mass splittings (with lightest neutrino eigenvalue m_1 set to zero) [263]. Note that this particular choice of θ_R maximises the CP asymmetry, hence implying that $F_y \lesssim \mathcal{O}(0.7)$ for other choices of θ_R. Such an enhancement of the CP asymmetry is the key ingredient of the resonant leptogenesis mechanism for which, even with light RHNs as low as TeV or so, it can satisfy the baryon asymmetry of the Universe via leptogenesis at the cost of imposing a precise degree of degeneracy between the two RHNs. In the present scenario of the minimal Majoron model, the splitting $\Delta M = 2v_\phi^2/\Lambda$ is fixed for any specific point on the DM parameter space satisfying correct relic density, as in Fig. 2.9 (upper panel) and 2.10. Therefore, for each such point, one can check the validity of the resonant leptogenesis mechanism in order to satisfy the BAU where the complex angle in the orthogonal R matrix play crucial role.

Once the CP asymmetry is obtained, the evolution of the L asymmetry can be studied by

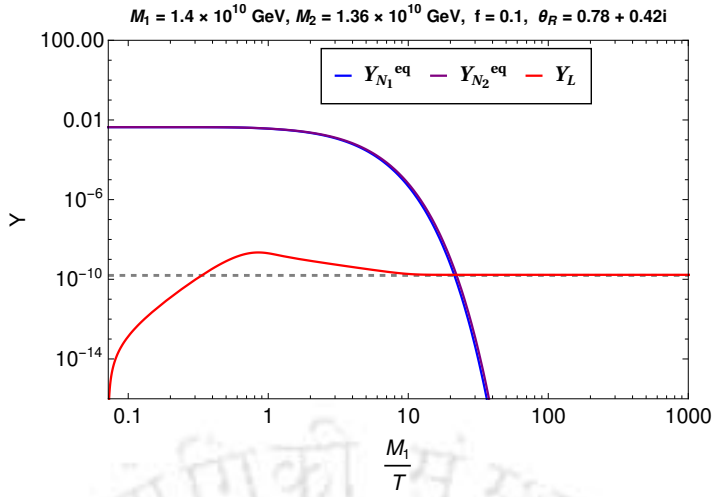

Figure 2.11: Evolution of the yields of RHNs and lepton asymmetry (using table 2.4).

simultaneously solving the Boltzmann equation shown in Eq. 2.57, together with [136,315],

$$\frac{dY_L}{dx} = \sum_i \frac{1}{\mathcal{H}x\mathcal{S}} \left[\epsilon_{N_i} \left(\frac{Y_{N_i}}{Y_{N_i}^{eq}} - 1 \right) - \frac{Y_L}{2Y_l^{eq}} \right] \gamma_{N_i} - \frac{Y_L}{Y_l^{eq}} \gamma_\sigma \tag{2.66}$$

where Y_L denotes the amount of asymmetry generated in the lepton sector and γ_σ signifies the rates of $\Delta L = 1$ scatterings processes, as mentioned in Eq. 2.59. Here, the term proportional to ϵ_{N_i} in the r.h.s is responsible for the growth in the asymmetry $Y_L = Y_l - Y_{\bar{l}}$, which then gets washed out primarily due to the inverse-decays $\ell_L H \to N_i$ and $\overline{\ell_L}\bar{H} \to N_i$. Finally, as the temperature drops below M_i, the inverse decay processes get suppressed by $e^{-M_i/T}$, resulting in a saturation in the lepton asymmetry. Additionally, $\Delta L = 2$ scattering processes such as $H \to \overline{\ell_L}\bar{H}$ and $\ell_L \ell_L \to HH$ (mediated by N_i) also contribute in wash-out of the lepton asymmetry, which is however less efficient compared to the inverse decay processes, due to the involvement of $(y^{\nu\dagger}y^\nu)^2$. The asymptotic yield in lepton asymmetry Y_L^∞ (at $x \to \infty$) is eventually converted into the baryon asymmetry Y_B through electroweak sphalerons at temperatures above $T \sim 130$ GeV, as described by the relation $Y_B = (28/51)Y_L^\infty \simeq 8.75 \times 10^{-11}$ [46]. Here we do not incorporate the flavor effects on leptogenesis[12] for simplicity. We use Fig. 2.11 to demonstrate the evolution of the abundance of RHN together with the lepton asymmetry, Y_L for the benchmark point shown in table 2.4 for which the observed baryon asymmetry is satisfied with $\theta_R = 0.78 + 0.42i$.

Notice that unlike the usual motivation of lowering the scale of RHNs (typically of order TeV or so) from its collider search point of view while employing the resonant leptogenesis scenario, the present construction requires a relatively heavier RHNs (10^6 GeV and above) to have a successful leptogenesis. This is because the DM phenomenology in this scenario demands a heavier RHN ($v_\phi > T_{\rm RH}$) together with larger Λ as seen from Figs. 2.9 (left panel) and 2.10. It is however ensured that the mass difference between the two almost degenerate RHNs are large enough compared to their respective decay width(s) so as to maintain the validity of the perturbative calculation. As stated earlier, the mass splitting between the two

[12]For flavor effects on thermal leptogenesis, we direct the readers to [266, 316–320] and for flavor effects on leptogenesis during a non-instantaneous reheating epoch, we refer the readers to [321, 322].

RHNs depends on v_ϕ and Λ and hence, is fixed for a specific set of values of (v_ϕ, Λ). It turns out that $\epsilon_{N_i} \sim 6 \times 10^{-6}$ is required to produce the lepton asymmetry that can explain the observed baryon asymmetry.

2.3.4 Correlating DM parameter space with Leptogenesis

As discussed separately in the previous two subsections, in this work, the explicit breaking of the lepton number at dimension 5 contributes to both the DM phenomenology and the generation of baryon asymmetry which in turn provides an interesting correlation between the DM parameter space to the generation of lepton asymmetry. To demonstrate it, we consider the entire DM parameter space satisfying correct relic density (as in left panel of Fig. 2.9 and Fig. 2.10) and evaluate the corresponding baryon asymmetry of the Universe where the only additional parameter (apart from the common parameters: Λ, $T_{\rm RH}$ and f), entering solely in leptogenesis, is the complex angle θ_R. Although the $U(1)_L$ breaking scale, v_ϕ, is not directly involved in the DM analysis, it remains a crucial parameter for resonant leptogenesis as it directly contributes to the generation of tree level RHN (degenerate) masses and their mass-splittings. As mentioned in the DM phenomenological discussion, we assume $v_\phi > T_{\rm RH}$ and consider a fixed hierarchy between $T_{\rm RH}$ and v_ϕ for convenience. Specifically, we consider two benchmark hierarchies as (a) $T_{\rm RH} = 0.5\, v_\phi$ and $f = 0.1$ and (b) $T_{\rm RH} = 0.1\, v_\phi$ for $f = 0.005$. In addition, the ratio $T_{\rm RH}/v_\phi$ should satisfy $T_{\rm RH}/v_\phi \gtrsim f/\sqrt{2}$ which arises from the consideration, $T_{\rm RH} > M_i$ $(\sim f v_\phi/\sqrt{2})$ ensuring that the RHNs can be considered to be in thermal equilibrium. With these considerations, we scan the entire parameter space by varying $\Lambda, T_{\rm RH}$ and m_χ and look for the common parameter space satisfying the correct baryon asymmetry via leptogenesis and Majoron dark matter, as explained below. The impact of choosing different θ_R on such common parameter space is also highlighted.

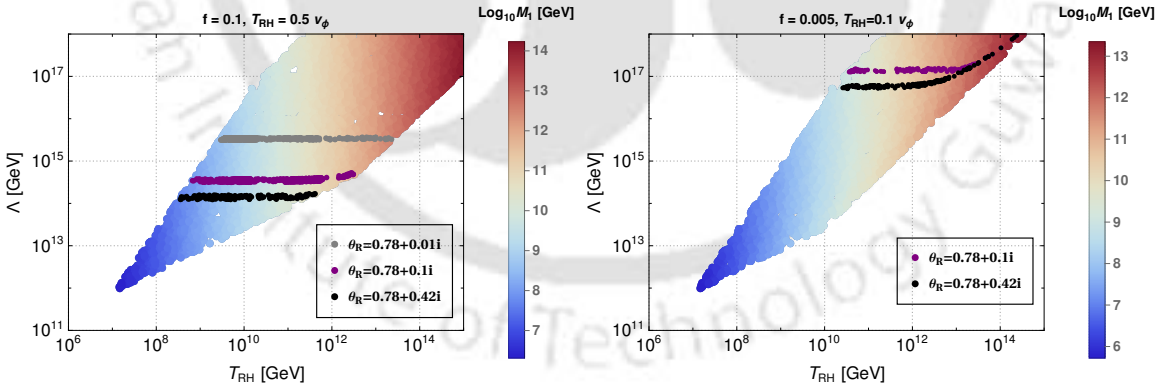

Figure 2.12: The correct BAU satisfied parameter spaces are indicated on DM-parameter space (from left panel of Figs. 2.9 and 2.10) by black, purple and gray patches, for different choices of θ_R (indicated in plot legends).

In Fig. 2.12, we illustrate a common parameter space for Majoron as DM and resonant leptogenesis signifying the correct baryon asymmetry of the Universe in a single comprehensive plot in $\Lambda - T_{\rm RH}$ plane. Additionally, the variation of the RHN mass is shown in color bar. In the left (right) panel of Fig. 2.12, the baryon asymmetry and DM parameter space (satisfying correct DM relic density) is indicated by the black patch with $T_{\rm RH}/v_\phi = 0.5\ (0.1)$ and $f = 0.1\ (0.005)$ for an optimum choice of $\theta_R = 0.78 + 0.42i$. It is observed that this particular θ_R maximizes the CP asymmetry parameter. It then turns out that for such choices

of f and $T_{\rm RH}/v_\phi$ in the left panel of Fig. 2.12, successful resonant leptogenesis is obtained for RHN masses in the range $10^8 - 10^{11}$ GeV, while the Majoron as DM (satisfying correct relic density) falls in the mass range, $m_\chi \sim \mathcal{O}(\text{keV} - \text{MeV})$, this is also visible from Fig. 2.14. Similarly, for a lower choice of f $(= 0.005)$ (associated to smaller RHN masses), the mass splitting must be more fine-tuned, demanding higher values of Λ to keep ϵ_{N_i} fixed. As shown in the right panel of Fig. 2.12 for $T_{\rm RH} = 0.1\ v_\phi$ and $f = 0.005$, $\Lambda \gtrsim 6 \times 10^{16}$ GeV is required along the black patches to satisfy the correct resonance condition. Consequently, for these points, higher values of m_χ $(\mathcal{O}(0.01\ \text{GeV}) - \mathcal{O}(\text{GeV}))$ as well as $T_{\rm RH}$ (that translates to a larger values of RHN masses[13], in the range $\mathcal{O}(10^9\ \text{GeV}) - \mathcal{O}(10^{12}\ \text{GeV})$) are needed to satisfy correct relic density.

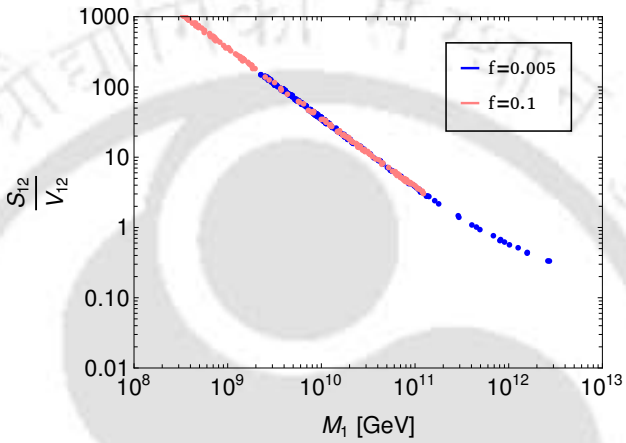

Figure 2.13: Plot showing the relative importance between the self energy and vertex contributions against M_1 for two choices of f. For $f = 0.1$, it stops around $M_1 \sim 10^{11}$ GeV.

The requirement of satisfying the correct BAU boils down to generating a CP asymmetry of order $\epsilon_N \gtrsim 7 \times 10^{-6}$ as the washout (η) of the produced lepton asymmetry via inverse decay is limited roughly by $\eta \lesssim 10^{-3}$, in terms of the DM parameter space[14]. This excludes the DM parameter space satisfying correct relic density below the black patch with $\theta_R = 0.78 + 0.42i$. We observe that for $\theta_R = 0.78 + 0.42i$, the BAU satisfied black patch corresponds to a specific Λ value for the left panel with $f = 0.1$ and $T_{\rm RH}/v_\phi = 0.5$ while for the right panel, such a patch exhibits similar pattern till a point (close to $T_{\rm RH} \sim 10^{12}$ GeV or $M_1 \sim 10^{11}$ GeV) beyond which it shows a Λ dependence. The same pattern is observed for different choices of θ_R as indicated in the Fig. 2.12. However, choosing a θ_R other than the benchmark value $0.78 + 0.42i$ (which maximises the CP asymmetry) would restrict the parameter space from leptogenesis point of view as the amount of enhancement due to resonant leptogenesis is limited with those values of θ_R. This is actually reminiscent of the two distinct regimes of ϵ_N where the self energy domination over the vertex contribution characterises the fixed-Λ regime (the range remains insensitive to v_ϕ) while the Λ-dependent range stands for vertex correction dominated era. To make it more explicit, we include the Fig. 2.13, where the relative strength of the self energy to vertex contributions in ϵ_{N_1} is depicted against the variation of RHN mass M_1. For $f = 0.1$, it stops around $M_{1,2} \sim \mathcal{O}(10^{11})$ GeV signifying that M_1 is limited by such a value from the DM satisfied parameter space

[13]Decay of such heavy RHNs may emit gravitational waves via *bremsstrahlung* during leptogenesis [323].
[14]The actual contribution toward washout is however evaluated using the Boltzmann equations.

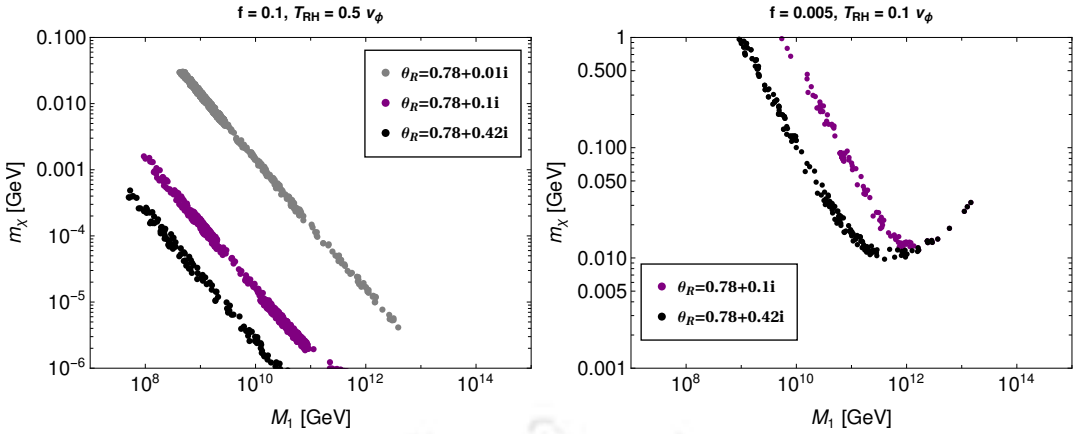

Figure 2.14: Correlation between masses of Majoron and RHNs, obtained from DM-relic and BAU satisfaction.

for $\Lambda \sim 1.5 \times 10^{14}$ GeV. However, for the smaller choice of f, the DM parameter space allows for a higher M_1, thereby resulting into the probe of Λ-dependent regime in this case. So, overall, it is seen that the 1-loop vertex correction starts contributing significantly for $M_1 \sim M_2 \gtrsim \mathcal{O}(10^{11})$ GeV. Therefore, we find that the study establishes a one-to-one correspondence between masses of the Majoron as DM and the RHN mass responsible for neutrino mass generation and BAU, as indicated in Fig. 2.14, thereby providing an intricate link between the two apparently disconnected problems of particle physics and cosmology. Note that the typical behaviour of the right plot, above and below $M_1 \sim 10^{11}$ GeV, is suggestive of the characteristic switchover from the self energy domination to the vertex correction dominated phase. Interestingly, such correlations shown in Fig. 2.14 can be probed in various monochromatic neutrino search experiments, gamma-ray and X-ray observations along the same line as discussed in subsection 2.2.4 (see appendix A.1.2).

2.3.5 Summary and Conclusion

In this work, we have studied a Majoron model, extending the SM gauge symmetry with a global lepton number symmetry $U(1)_L$, augmented by a discrete Z_2 symmetry, including two RHNs and a scalar responsible for SSB of $U(1)_L$. While the spontaneous breaking of the $U(1)_L$ naturally generates two exactly degenerate right handed neutrinos via the tree level terms respecting the lepton number symmetry, a tiny explicit lepton number breaking (but Z_2 symmetric) terms of dimension-5 breaks the degeneracy. The RHNs are not only responsible for generating the light neutrino masses via type I seesaw, but also contribute dominantly to the Majoron production in the early Universe. The quasi-degenerate RHNs allow an explanation of the baryon asymmetry of the Universe via resonant leptogenesis. It also opens up an interesting correlation between the Majoron as DM and BAU, not hitherto explored in the literature.

The construction of the present Majoron model however includes a few assumptions such as imposing discrete symmetries and typical hierarchies among mass scales, which pave the way in obtaining such correlation. To begin with, we consider the explicit $U(1)_L$ breaking to take place only by higher dimensional operators. The presence of an underlying Z_2 symmetry not only restricts number of such operators to appear, but also helps

in obtaining exactly degenerate pair of RHNs in absence of $U(1)_L$ explicit breaking terms. In continuation, a uniform coupling (or same cut-off scale) of the $U(1)_L$ breaking terms quadratic in RHNs, contributing toward the mass splitting ΔM, is considered without loss of generality. On the other hand, a CP symmetry under which $\Phi \to \Phi^*$ is present which ensures the dimension-5 Yukawa interaction of the second RHN to couple with Φ and Φ^* uniformly. We further consider the ordering of mass scales, $v_\phi > T_{\rm RH} > M_i$, in order to achieve correct DM phenomenology as well as in realizing leptogenesis.

We analysed the parameter space satisfying both the DM relic density and the BAU. The reheating temperature and the (effective) cut-off scale, signifying the explicit breaking of the global $U(1)_L$ symmetry, are bounded by 10^{15} GeV and Planck scale respectively. The analysis suggests a sub-GeV Majoron relevant to monochromatic neutrino search experiments, together RHNs in the mass range from intermediate (10^6 GeV) to high (10^{13} GeV) scales. Unlike typical resonant leptogenesis occurring at the TeV scale, the high-scale resonant leptogenesis here has a characteristic dependence of self energy and vertex contributions to the CP asymmetry for RHN masses around $\mathcal{O}(10^{11})$ GeV.

Overall, this chapter not only provides a mechanism for the production of light Majoron DM as a FIMP but also relates the baryon asymmetry of the Universe via a high-scale resonant leptogenesis as well as the generation of tiny neutrino masses, offering a unified approach to resolve some of the most fundamental questions in particle physics and cosmology.

Chapter 3

Aspects of Axion-like Particles and Their Phenomenology

3.1 Introduction

The previous chapter discussed the phenomenology of Majoron, a pNGB arises from the breaking of global lepton number symmetry. In this chapter we will focus the phenomenology of ALPs, a generalization of the originally introduced QCD axion [53]. As introduced earlier in subsection 1.7.2, ALPs are generically classified as the pNGBs associated to the spontaneous breaking of a QCD-like anomalous global symmetry, prevalent in many extensions of the SM and therefore, do not in general carry any specific relation between its mass (m_a) and the decay constant (f_a). This allows them to span over a wide range in the ($m_a - f_a$) plane, making them attractive from detection point of view.
As discussed elaborately in subsection 1.7.2.3, ALPs can be produced via the *misalignment mechanism* once they begin oscillating at $T_{\rm osc}$, satisfying $3\mathcal{H} \sim m_a$, and eventually behaving like matter ($\rho_a \propto R^{-3}$). As evident from Eq. 1.138, the relic density satisfaction of such ALP provides a standard correlation involving m_a and f_a which turns out to be well restricted by several cosmological constraints as well from ALP search experiments as summarized in subsection 1.7.2.4. Considering all such aspects, it turns out that the ALPs being DM should be very light (below keV).

In this chapter, we will utilize the misalignment mechanism to explore the ALP phenomenology. In section 3.2, we scrutinize the cosmic evolution of dark matter ALPs in presence of an additional explicit global symmetry-breaking term involving the SM Higgs doublet, which results in modifying the standard misalignment-induced oscillation behavior and therefore, the relic density. Then, in section 3.3, we present an ALP-driven spontaneous leptogenesis scenario in presence of a lepton number violating interaction assisted by Inert Higgs Doublet (IHD) and a non-zero ALP velocity, induced by the misalignment mechanism, acts as an effective chemical potential, leading to a shift in the energy density between the SM ($B - L$) charged fermions and anti-fermions.

3.2 Effects of Electroweak Symmetry Breaking on Axion-like Particles as Dark Matter

In this work [324], we propose to include a higher order shift symmetry breaking Higgs portal interaction of ALPs which contributes to its mass (m_{aE}) after the electroweak symmetry breaking (EWSB) on top of its existing mass, m_{a0}, presumably followed from non-perturbative instanton effect. Inclusion of such additional mass m_{aE} is expected to modify the frequency of ALP oscillation after the EWSB. This would have profound effect on the relic density and hence on the ALP parameter space in m_a, f_a plane, where $m_a^2 = {m_{a0}}^2 + {m_{aE}}^2$. We find that depending upon the onset of conventional ALP oscillation (connected with its mass m_{a0} only) before or after the EWSB and associated modification of it after EWSB, the standard correlation between ALP mass and decay constant can be altered significantly leading to opening up of otherwise excluded (restricted) parameter space ($e.g.$ keV-GeV range) for ALPs.

There are some studies focusing on modification of the PQ axion or ALP potential. For example, in ref. [325], the authors examine the effect of tiny (limited by neutron electric dipole moment) explicit Peccei-Quinn (PQ) symmetry breaking on the PQ axion dynamics and its role as DM. In this case, the PQ axion initially starts oscillating about a wrong minimum guided by the explicit PQ breaking term and afterward it oscillates about the true minimum leading to a modification of the conventional PQ parameter space. Ref. [326] recently analyses the effect of introducing a PQ breaking term on axiverse that encompasses the PQ axion, an ALP and a hypothetical mixing between them. In another work, ref. [327] discusses the effect of adding a non-periodic potential to ALP and thereby find the possibility of accommodating a large misalignment angles which may change the conventional (m_a, f_a) parameter space of ALPs. Another modification of axion or ALP potential is referred as *kinetic misalignment* ([183,184,328]). In this scenario, a higher dimensional explicit PQ breaking potential and a large initial field value for the PQ symmetry breaking field lead to a nonzero initial ALP velocity which in turn, triggers a delayed ALP oscillation bringing modifications in the relic abundance as well as in parameter space of ALPs. A more general treatment of the effect of initial conditions of ALP and its effects on the (m_a, f_a) parameter space can be found in ref. [329]. Ref. [330] discusses about the impact of ALP mass modification on its relic abundance, within the context of the type-II seesaw mechanism.

Our proposal differs from the existing works in a sense that it relies on the electroweak symmetry breaking phase (most natural and unavoidable phase) for modifying the ALP potential, without changing its minimum though. The new mass term for ALP that originates at EWSB may provide a dominant or sub-dominant contribution to the effective final mass of the ALP (m_a). Depending on the onset of ALP oscillation before or at EWSB, the standard misalignment mechanism gets modified so as to obtain a new parameter space, in (m_a, f_a) plane, carrying significant differences with the standard one which might be interesting from ALP search experiments. It turns out that such a Higgs portal interaction of ALPs allows us to probe for light ALPs. Interactions involving ALP and Standard Model (SM) Higgs have also been exercised in few references [331–333], however in different contexts. Specifically, a higher dimensional operator consisting of axion and Higgs are discussed

in [333] which is responsible for a new minimum of ALP inducing an epoch of kination and generation of gravitational waves. Contrary to our proposal, the ALP there neither plays the role of DM nor obtains a shift in its mass during EWSB.

The outline of the work is as follows. In the next subsection, we discuss the standard ALP scenario and following this, we move for studying the evolution of ALPs in our modified scenario. The observation and constraints are elaborated in sections 3.2.2 and 3.2.3 respectively. Finally we conclude in section 3.2.5.

3.2.1 Standard Misalignment Mechanism and ALP as DM

In this subsection, we briefly revisit the cosmological evolution of ALPs produced via the misalignment mechanism (for a detailed discussion, refer to the subsection 1.7.2.3), assuming their existence prior to the end of primordial inflation as a result of spontaneous breaking of a global $U(1)$ symmetry during inflation. After inflation (followed by a reheating era), the ALP field $a(\mathbf{x}, t)$, which is the angular d.o.f. of the $U(1)$-breaking complex scalar field, is expected to be spatially homogeneous, hence described by $a(t)$ only, and gets frozen at an initial value a_I parametrised by the misalignment angle $\theta_I = a_I/f_a$ (with $\dot{\theta}_I = 0$), as long as the Hubble remains larger compared to its mass m_{a0}. The ALP field a, parametrized by $\theta = a/f_a$, follows the classical equation of motion in the background of expanding Universe as given by

$$\ddot{\theta} + 3\mathcal{H}(T)\dot{\theta} + \frac{1}{f_a^2}\frac{\partial}{\partial\theta}V_0 = 0, \tag{3.1}$$

where V_0 denotes the standard ALP potential, parametrized by

$$V_0 = m_{a0}^2 f_a^2 \left(1 - \cos\frac{a}{f_a}\right). \tag{3.2}$$

Eventually, ALP starts to oscillate when the Hubble parameter drops below the its mass $3\mathcal{H}(T^0_{\rm osc}) = m_{a0}$, where $T^0_{\rm osc}$ defines the onset temperature of oscillations:

$$T^0_{\rm osc} \simeq 1.5 \times 10^7 \text{ GeV} \left(\frac{100}{g_\star(T^0_{\rm osc})}\right)^{1/4} \left(\frac{m_{a0}}{10^{-3}\text{ GeV}}\right)^{1/2}. \tag{3.3}$$

With no initial velocity, at $T^0_{\rm osc}$, the ALP energy density can be expressed as

$$\rho_a(T^0_{\rm osc}) = \frac{1}{2} m_{a0}^2 f_a^2 \theta_I^2. \tag{3.4}$$

For $T \lesssim T^0_{\rm osc}$, Eq. 3.1 implies that field would perform fast oscillations with slowly decreasing amplitude where the average energy density $\langle\rho_a\rangle$ scales as R^{-3}. Therefore, after $T^0_{\rm osc}$, ALP behaves like pressure-less dust, with its energy density redshifting as matter:

$$\rho_a(T_0) = \rho_a(T^0_{\rm osc}) \frac{m_a(T_0)}{m_{a0}(T^0_{\rm osc})} \left(\frac{R_{\rm osc}}{R_0}\right)^3 \tag{3.5}$$

$$= \frac{1}{2} m_{a0}(T^0_{\rm osc}) m_a(T_0) f_a^2 \theta_I^2 \left(\frac{R_{\rm osc}}{R_0}\right)^3, \tag{3.6}$$

Assuming a temperature independent ALP mass and adiabatic expansion, the present-

day relic density becomes

$$\Omega_a h^2 = \frac{h^2}{2\rho_{c,0}} m_{a0}^2 f_a^2 \theta_I^2 \left(\frac{g_{\star s}(T_0)}{g_{\star s}(T_{\rm osc}^0)}\right)\left(\frac{T_0}{T_{\rm osc}^0}\right)^3, \tag{3.7}$$

Substituting $T_{\rm osc}^0$ into Eq. 3.7 gives the estimate of the ALP relic density:

$$\Omega_a h^2 \simeq 0.12 \left[\frac{\theta_I}{\mathcal{O}(1)}\right]^2 \left[\frac{100}{g_\star(T_{\rm osc}^0)}\right]^{\frac{1}{4}} \left[\frac{m_{a0}}{10^{-9}\,\text{GeV}}\right]^{\frac{1}{2}} \left[\frac{f_a}{4\times 10^{11}\,\text{GeV}}\right]^2, \tag{3.8}$$

from which a correlation between the two parameters m_{a0} and f_a can easily be obtained.

3.2.2 Higgs portal interaction and ALP

Here, we introduce an explicit higher order shift symmetry breaking term in the ALP potential involving the SM Higgs. As a result, a new contribution toward the mass of ALP originates once the electroweak symmetry breaking takes place. The appearance of such a mass term for ALP at an intermediate phase (during its evolution) in addition to m_{a0} (connected to non-perturbative dynamics) not only enables the effective mass of the ALP (m_a) and its decay constant (f_a) to treat as independent parameters, but also modifies the frequency of ALP oscillation at EWSB as we observe below.

We first consider the Lagrangian involving a global $U(1)$ symmetry breaking complex scalar field $\Phi = \eta e^{i\theta}/\sqrt{2}$, as

$$\mathcal{L} = \frac{1}{2}(\partial\eta)^2 + \frac{1}{2} f_a^2 (\partial\theta)^2 - \lambda\left(\eta^2 - f_a^2/2\right)^2, \tag{3.9}$$

where $\theta = a/f_a$ as parametrised in the earlier section. Once the $U(1)$ global symmetry is spontaneously broken, the potential for the ALP field a is given V_0 of Eq. 3.2. We now introduce additional dimension-6 shift symmetry breaking term involving the SM Higgs doublet H, as given by

$$V_1 = \frac{|H|^4}{\Lambda^2}\Phi^2 e^{i\alpha} + H.c., \tag{3.10}$$

where the phase α in Eq. 3.10 can take values in the range $0 \le \alpha \le \pi$ [334] and Λ acts as a cut-off scale with $\Lambda > f_a$, indicating that the explicit breaking of the global symmetry may take place at some high scale ($\Lambda \lesssim M_{\rm Pl}$) [259, 260]. Based on this known possibility that gravity effects explicitly break a global symmetry [248–251, 253] at Planck scale $M_{\rm Pl}$ (or even at a scale much smaller than the Planck one, as recently shown by [260] in the context of weak-gravity conjecture [335]), we discuss the origin of such an operator in Appendix-B.1.1. The specific construction mentioned there is also capable of disallowing another dimension-6 explicit $U(1)$ symmetry breaking term $\frac{|H|^2}{\Lambda^2}\Phi^4\exp(i\alpha) + H.c.$ which can be present otherwise. Note that this additional operator can be excluded from a naive consideration too by keeping the order of explicit $U(1)$ breaking (by amount of $U(1)$ charges) minimal. While we mostly focus on the explicit breaking operator as in Eq. 3.10 only for the rest of the analysis, we show in Appendix-B.1.2 that inclusion of the additional dimension-6 operator may lead to an altogether different phenomenology.

The phenomenologically relevant part of the potential for the ALP or the θ field, after

the spontaneous breaking of the PQ-like global symmetry, then turns out to be

$$V_a = m_{a0}^2 f_a^2 \left(1 - \cos\frac{a}{f_a}\right) + \frac{|H|^4}{\Lambda^2} f_a^2 \cos\left(\frac{2a}{f_a} + \alpha\right). \tag{3.11}$$

At a temperature sufficiently higher than the electroweak scale, $T > T_{\rm EW} \sim 150$ GeV, the temperature correction to the SM Higgs potential helps the SM Higgs to have a single minimum at origin [48]. Hence the Higgs field is expected to settle at origin as a result of which this term does not contribute till the temperature becomes comparable to $T_{\rm EW}$ when H gets a *vev*, $H = (v+h)/\sqrt{2}$ with $v = 246$ GeV. After the EWSB, the ALP receives a new contribution to its mass such that its effective mass m_a satisfies the relation

$$m_a^2 \equiv \left(\frac{d^2 V_a}{da^2}\right)_{\rm min} = m_{a0}^2 \cos\theta_{\rm min} - \frac{v^4}{\Lambda^2}\cos(2\theta_{\rm min} + \alpha), \tag{3.12}$$

where $\theta_{\rm min} = a_{\rm min}/f_a$ denotes the newly developed minimum of the ALP potential after EWSB. The value of $\theta_{\rm min}$ can be estimated as a solution to the equation,

$$\sin\theta = \frac{q}{2}\sin(2\theta + \alpha), \quad \text{with } q = \frac{v^4/\Lambda^2}{m_{a0}^2}, \tag{3.13}$$

obtained by minimising the ALP potential. Clearly, the new potential minimum depends on the choice of α and other parameters (Λ and m_{a0}). We pursue with $\alpha = \pi$ for the rest of the analysis that results into the effective mass of the ALP given by,

$$m_a^2 = m_{a0}^2 + \frac{v^4}{\Lambda^2}. \tag{3.14}$$

Such a choice of $\alpha = \pi$ is motivated primarily from the fact that the minimum of the ALP potential ($\theta_{\rm min} = 0$) remains unaffected due to the presence of this additional contribution to ALP potential via Eq. 3.10. However, for conventional QCD axion, such explicitly breaking term should be incorporated very carefully as any alteration of the minimum can spoil the resolution of the strong CP problem, the strong-CP violating angle being heavily constrained by neutron electric dipole moment [153] (widely referred as Axion quality problem [143, 246, 336]). With a general axion like particles, such a solution of $\theta_{\rm min}$ is not necessarily be connected to the solution of the strong CP problem. To investigate the impact of different α values on $\theta_{\rm min}$ and hence on relic, we incorporate an analysis in the later part of the following sub-section.

Appearance of such a mass term would affect the evolution of the ALP field, in terms of its change in oscillation frequency, immediately after the EWSB. To analyse it further, we divide the study into two cases depending on whether the ALP starts its oscillation at a temperature $T^0_{\rm osc}$ (due to m_{a0}) prior to EWSB temperature $T_{\rm EW}$ or not, as

$$\begin{aligned} &\text{Case [A]}: \quad T^0_{\rm osc} > T_{\rm EW}, \\ &\text{Case [B]}: \quad T^0_{\rm osc} \leq T_{\rm EW}. \end{aligned} \tag{3.15}$$

Note that the demarcation between these two cases is set by the condition

$$m_{a0} = 3\mathcal{H}(T_{\rm EW}), \tag{3.16}$$

which translates (assuming a radiation dominated universe) into $m_{a0} > 10^{-13}$ GeV (for case [A]) and $m_{a0} \leq 10^{-13}$ GeV (for case [B]) where we use $T_{\rm EW} = 150$ GeV.

3.2.2.1 ALP oscillation starts before EWSB

Here the ALP is expected to start its oscillation at a temperature $T^0_{\rm osc}$ higher than $T_{\rm EW}$, connected to its mass m_{a0}. So, the evolution of this ALP for the period $T^0_{\rm osc}$ to $T_{\rm EW}$ is guided by Eq. 3.1. Near the onset of its oscillation at $T = T^0_{\rm osc}$, it carries an energy density same as of Eq. 3.4. At $T = T_{\rm EW}$, due to the electroweak symmetry breaking, the higher order Higgs portal interaction provides an additional contribution to its mass as specified in Eq. 3.14. As a result, the evolution of the ALP is now governed by the same form of Eq. 3.1, however replacing m_{a0} by m_a via Eq. 3.14, $i.e.$

$$\ddot{\theta} + 3\mathcal{H}(T)\dot{\theta} + m_a^2\theta = 0. \tag{3.17}$$

The shift of ALP mass across the EWSB can be incorporated in estimating the ALP energy density ρ_a, crucial in determining the ALP relic density, before and after the electroweak phase transition in line with the discussion in the context of Eqs. 3.5-3.6 as pursued below. The discontinuity of m_a around EWSB can be guided by an appropriate logistic function (as shown in appendix-B.1.3) in case one tries to explore evolution of the θ field as function of scale factor R (normalised by $R_{\rm in}$, which is the scale factor at the onset of oscillation, $T^0_{\rm osc}$.), depicted in Fig. 3.1.

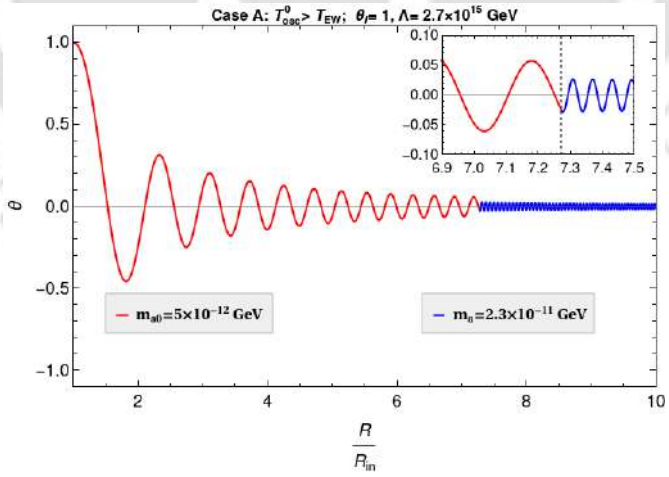

Figure 3.1: Evolution of θ before EWSB (solid red) and after EWSB (solid blue) against $R/R_{\rm in}$ in case A ($T^0_{\rm osc} > T_{\rm EW}$). In the inset, the evolution of θ is shown in the vicinity of $T_{\rm EW}$ (the dashed grey vertical gridline of the inset diagram corresponds to $T_{\rm EW}$).

Considering the conservation of ALP number density in a co-moving volume across

EWSB, the ρ_a immediately after the EWSB (at $T_{<\rm EW}$) can be written, via Eq. 3.5, as

$$\rho_a(T_{<\rm EW}) = \rho_a(T_{>\rm EW}) \left(\frac{R_>}{R_<}\right)^3 \left[\frac{m_a(T_{<\rm EW})}{m_a(T_{>\rm EW})}\right]. \tag{3.18}$$

Here $\rho_a(T_{>\rm EW})$ is the energy density of the ALP just before the EWSB (at $T_{>\rm EW}$) given by

$$\rho_a(T_{>\rm EW}) = \rho_a(T^0_{\rm osc}) \left(\frac{R_{\rm in}}{R_>}\right)^3, \tag{3.19}$$

While the mass of the ALP before EWSB is $m_a(T_{>\rm EW}) = m_{a0}$, $m_a(T_{<\rm EW}) = m_a$ results after EWSB as given by Eq. 3.14. Here, $R_>$ and $R_<$ are the scale factors of the universe at temperatures $T_{>\rm EW}$ and $T_{<\rm EW}$ respectively.

The energy density of the ALP today (associated with temperature T_0) can be written as

$$\begin{aligned}\rho_a(T_0) &= \rho(T_{<\rm EW}) \left(\frac{R_<}{R_{\rm To}}\right)^3 \\ &= \rho_a(T^0_{\rm osc}) \frac{m_a}{m_{a0}} \left[\frac{g_{\star s}(T_0)}{g_{\star s}(T^0_{\rm osc})}\right] \left(\frac{T_0}{T^0_{\rm osc}}\right)^3,\end{aligned} \tag{3.20}$$

where Eqs. 3.18, 3.19 are employed and $R_{\rm To}$ corresponds to today's scale factor.

Using the expressions of $\rho_a(T^0_{\rm osc})$ of Eq. 3.4, $T^0_{\rm osc}$ as given by Eq. 3.3 and plugging them in $\rho_a(T_0)$ of Eq. 3.20, we find the ALP relic density today as

$$\Omega_a h^2 \simeq 0.12 \left(\frac{\theta_I}{1}\right)^2 \left(\frac{100}{g_\star(T^0_{\rm osc})}\right)^{1/4} \left(\frac{m_a}{6\times 10^{-8}\ {\rm GeV}}\right) \sqrt{\frac{10^{-9}\ {\rm GeV}}{m_{a0}}} \left(\frac{f_a}{5\times 10^{10}\ {\rm GeV}}\right)^2. \tag{3.21}$$

Apart from m_{a0}, the m_a dependence relies on the cut-off scale Λ. Unlike the standard dependence of relic on m_{a0} and f_a via Eq. 3.8, here in case-[A], the final relic density also involves the third parameter Λ, the cut-off scale of the theory which is apparent though the involvement of m_a in Eq. 3.21 apart from m_{a0}.

The effective mass m_a being the final mass of the ALP which is phenomenologically more relevant than m_{a0}, we choose to consider the three parameters as m_a, f_a and Λ for our phenomenological analysis. To make the parameters dependence of the relic density explicit, we provide the result of the parameter space scan in $m_a - f_a$ plane shown in the left and right panels of Fig. 3.2, where the dependence of Λ and m_a/m_{a0} are indicated in the respective color maps maintaining $f_a \leq \Lambda \leq M_{\rm Pl}$. All the points in m_a and f_a plane satisfy the correct relic density $\Omega_a h^2 \simeq 0.12$ [63]. The gradients of the colors inside the color maps ranging from dark red to blue (for the left panel of Fig. 3.2) and yellow to brown (for the right panel of Fig. 3.2) indicate the one to one correspondence between the $\{m_a, f_a\}$ set of values with Λ and m_a/m_{a0} respectively for case-[A]. The narrow green line (merged with the borderline of the parameter space of both panels in Fig. 3.2) represents the relic-satisfied parameter space for standard scenario with ALP mass, equivalent to m_a, from the very beginning. To clarify further, for the green line only, the ALP oscillation begins at some other temperature (say T_*) than $T^0_{\rm osc}$ satisfying $3\mathcal{H}(T_*) = m_a(T_*)$. In terms of the extended

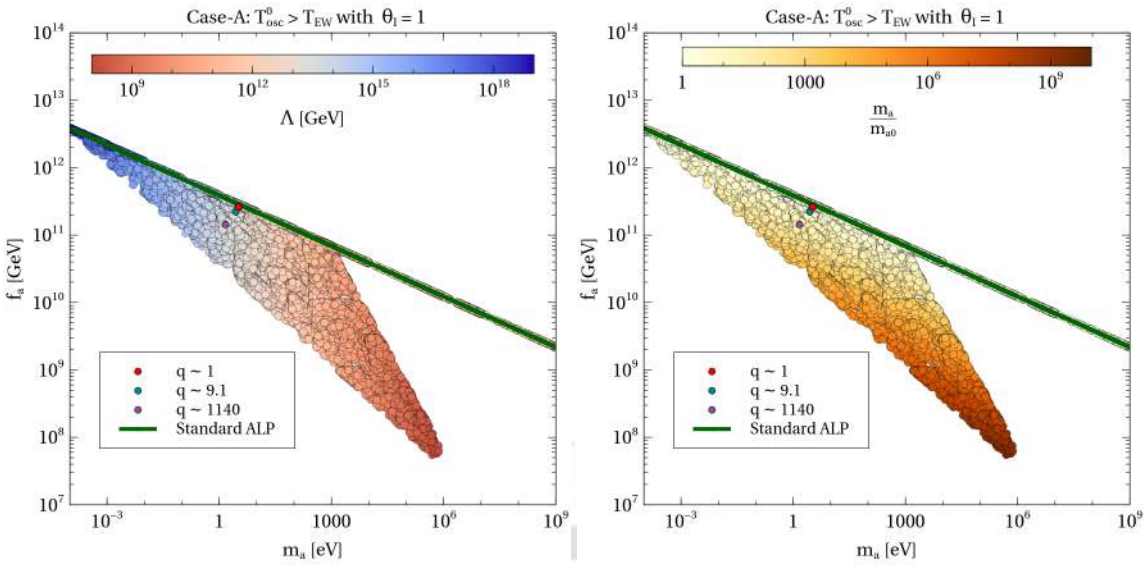

Figure 3.2: Comparison between parameter spaces satisfying correct DM relic density for case A ($T^0_{\rm osc} > T_{\rm EW}$) and standard case in ($m_a - f_a$) plane, while variations of Λ (left panel) and m_a/m_{a0} (right panel) are shown in the color bar. The bold dots in red, dark cyan and purple are points taken for studying further dependence of $\theta_{\rm min}$ on α.

parameter space as obtained in our scenario, this green line acts as the borderline of the parameter space implying that on this line, the change in the ALP mass during EWSB (in presence of the Higgs portal interaction) in very negligible $i.e.\ m_a/m_{a0} \simeq 1$, which is clear from the right panel of Fig. 3.2. Interestingly, the rest of the extended region allows for a significant gain in ALP mass during EWSB, $e.g.\ m_a/m_{a0} \sim \mathcal{O}(10^9)$ for $\{m_a, f_a\} = \{10^{-3}, 5\times 10^7\}$ GeV, as evident from the top-color-bar of Fig. 3.2 (right panel).

Note that, the presence of the higher dimensional Higgs portal coupling of the ALP allows such broadening of parameter space (particularly for f_a) which would be very significant from experimental perspective clubbed with other constraints which we will discuss in the next section 3.2.3. The broadening of the parameter space is an artefact of intermediate change in ALP oscillation frequency as shown in Fig. 3.1. Considering the ALP to constitute 100% of dark matter energy density in the universe, the upper part of the parameter space in this case (which is merged with the standard case) is excluded by the overabundance of dark matter while the excluded region below this (the left and right border lines of the allowed parameter space) is due to the consideration: $\Lambda > f_a$. In terms of ALP mass, the lower limit on m_a is kept as 10^{-13} GeV here so as to keep $T^0_{\rm osc}$ above $T_{\rm EW}$, the higher side of m_a can even be extended beyond the specified value (1 GeV) of the figure. The other constraint, $\Lambda < M_{\rm Pl}$ is only important at the leftmost region of the parameter space in this case as the minimum contribution from dim-6 operator to ALP mass is $\simeq v^2/M_{\rm Pl} = 5\times 10^{-15}$ GeV. However, such a correlation involving m_a and the decay constant f_a deserves a further scrutiny from several astrophysical and cosmological bounds which we will discuss in a subsequent section.

It is perhaps pertinent here to comment on the choice of the phase, α. We noted that for the specific choice of $\alpha = \pi$, the $\theta_{\rm min}$ remains at the origin even after the EWSB. However, for an arbitrary α, this may not be the case always, indicating a possible impact on the final relic density of ALP. To investigate this, we first use Eq. 3.13 to demonstrate the variation of

$\theta_{\rm min}$ against α for some choices of q values. For this purpose we pick up three different sets of parameters $[m_{a0}, f_a, \Lambda]$ (corresponding to three different q values) from the parameter space of Fig. 3.2: (a) $[2.31 \times 10^{-9},\ 2.61 \times 10^{11}, 2.62 \times 10^{13}]$ GeV, marked in red dark dot having $q \sim 1$, (b) $[8.74 \times 10^{-10},\ 2.22 \times 10^{11}, 2.29 \times 10^{13}]$ GeV, marked in dark cyan dark dot having $q \sim 9.1$, and (c) $[4.35 \times 10^{-11}, 1.44 \times 10^{11}, 4.12 \times 10^{13}]$ GeV, marked in purple dark dot having $q \sim 1140$. We then employ these three q values to obtain $\theta_{\rm min}$ as function of α for each q as depicted in Fig. 3.3 (left panel). Firstly we note that with $\alpha = 0$, the potential minimum in terms of $\theta_{\rm min}$ depends on the choice of q. To be specific, $\theta_{\rm min}$ remains at origin for $q \leq 1$ while it becomes $|\theta_{\rm min}| = \cos^{-1}(1/q)$ for $q > 1$. For non-zero α, $\theta_{\rm min}$ picks a distinct value. Hence, a correlation between $\theta_{\rm min}$ and α is noticed in this case as observed in Fig. 3.3 (left panel). However, for $\alpha = \pi$, $\theta_{\rm min}$ turns out to be zero irrespective of q, signifying $\alpha = \pi$ to be an unique choice.

Corresponding to left panel of Fig. 3.3, a variation in relic density with α is shown in the right panel of Fig. 3.3. It is evident that a maximum relic density results for $\alpha = \pi$. This is simply because the relic density being proportional to the effective ALP mass attains its maximum value for $\alpha = \pi$ as can be seen from Eq. 3.13 (or 3.14). Any other choice of α obviously produces a reduced relic density as the resulting mass remains smaller than its maximum value. As indicated in Fig. 3.3 (right panel), the change in relic density is only significant for $q \lesssim \mathcal{O}(10)$. For a sizeable q ($v^4/\Lambda^2 \gg m_{a0}^2$), the variation in relic density is almost negligible with $0 \leq \alpha \leq \pi$. However, such a decrease in relic density can also be compensated by appropriate scaling of f_a value which is not directly entering in determining the $\theta_{\rm min}$.

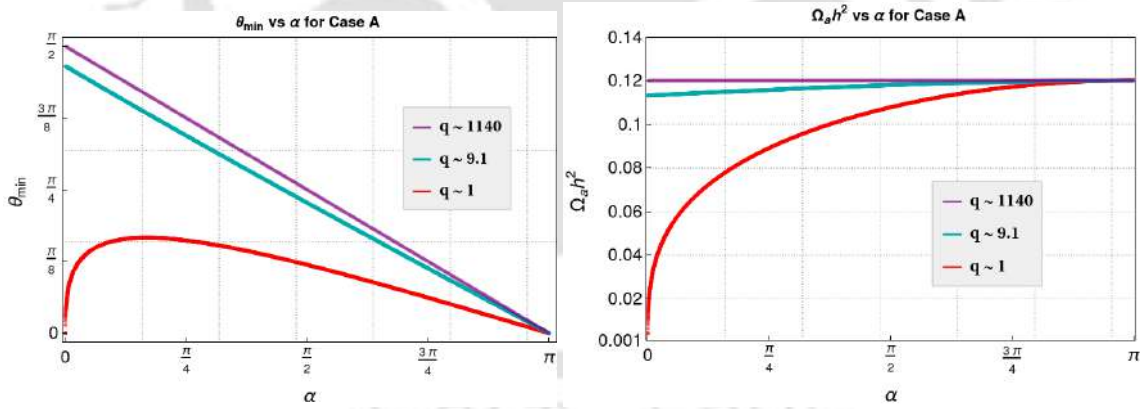

Figure 3.3: Left panel: variation of ALP potential minimum in terms of $\theta_{\rm min}$ against α. The three lines corresponds to three reference points, taken from the parameter spaces in Fig. 3.2 having different values of q. **Right panel**: Variation of the ALP relic density ($\Omega_a h^2$) vs α. The three lines corresponds to three reference points, taken from the parameter spaces in Figs. 3.2 having different values of q.

3.2.2.2 ALP oscillation starts after EWSB

Now we elaborate on the possibility where the ALP is scheduled to start its conventional oscillation (connected to its mass m_{a0} only) after EWSB. As discussed earlier, this can materialize only if $m_{a0} < \mathcal{O}(10^{-13})$ GeV. In this case, even if the global symmetry is spontaneously broken during or before inflation, the ALP field got stuck at the misalignment angle θ_I. The situation may alter with the presence of dim-6 Higgs portal interaction we include in this

work leading to two possibilities: (a) the effective mass after EWSB m_a immediately satisfies the condition $m_a(T_{\rm EW}) \geq 3\mathcal{H}(T_{\rm EW})$, thanks to the Higgs portal contribution toward m_a; (b) even with the additional contribution to its mass, m_a satisfies the condition $m_a(T) = 3\mathcal{H}(T)$ with a temperature smaller than $T_{\rm EW}$ and hence ALP oscillation starts later.

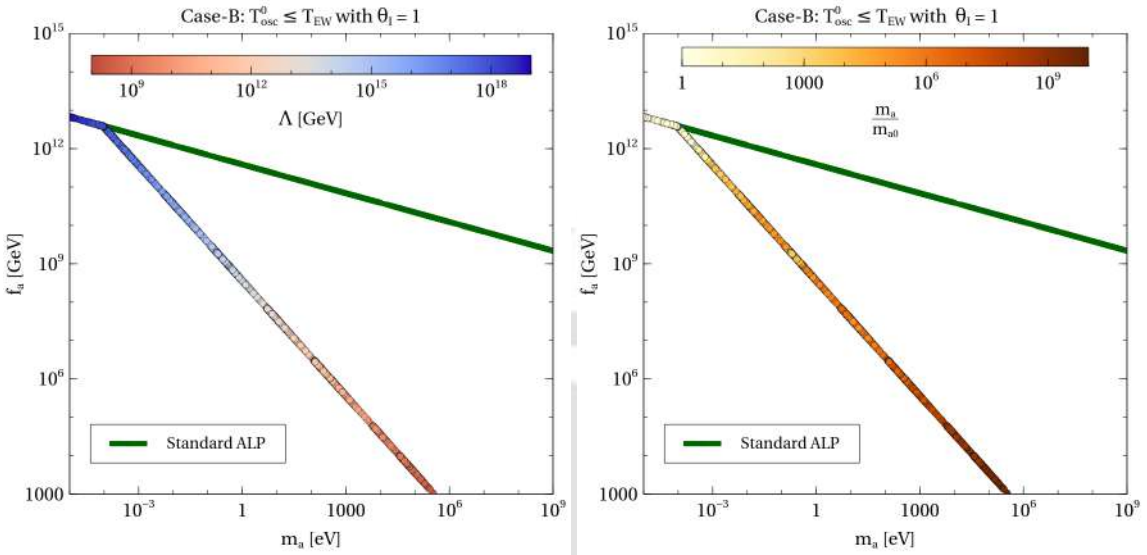

Figure 3.4: Comparison between parameter spaces satisfying correct DM relic density for case B ($T^0_{\rm osc} \leq T_{\rm EW}$) and standard case in ($m_a - f_a$) plane, while variations of Λ (left panel) and m_a/m_{a0} (right panel) are shown in the color bar.

We notice that contrary to case [A], there would not be any abrupt change in ALP oscillation here as the oscillation begins already with the effective mass at or below EWSB. The evolution of ALP then proceeds according to the Eq. 3.17. The rest of the prescription for evaluating the final relic is similar to the standard case discussed in the subsection 3.2.1. The $m_a - f_a$ parameter space satisfying the final relic for this case is represented in the left and right panels Figs. 3.4 while the corresponding values of Λ parameter and the ratio m_a/m_{a0} are shown in top bar, respectively. In the same plot, the standard ALP ($i.e$ without Higgs portal coupling) DM parameter space satisfying correct relic density having ALP mass equivalent of m_a from the beginning is indicated by the green patch for comparison purpose. The relic satisfied parameter space in this case [B] is not broadened (absence of elongated relic satisfied patch as in case [A]) compared to the conventional or standard parameter space as there is no such intermediate change in oscillation frequency. However the standard ALP parameter space for this range of final ALP mass changes its gradient due to a different onset of ALP oscillation era (it starts at $T_* > T_{\rm EW}$ related to its mass equivalent of m_a). It is found that except for large Λ satisfying $\Lambda \sim \mathcal{O}(M_{\rm Pl})$, the Higgs portal operator provides dominant contribution to ALP final mass, $i.e.$ $m_a = \sqrt{m^2_{a0} + \frac{v^4}{\Lambda^2}} \simeq \frac{v^2}{\Lambda}$. The minimum contribution to ALP mass obtainable from the dim-6 Higgs portal is of order $v^2/M_{\rm Pl} \simeq 5 \times 10^{-15}$ GeV which sets the boundary of m_a to its lower side. Around this large Λ, both m_{a0} and Higgs portal contributions are comparable (refer to right panel of Fig. 3.4) explaining the overlap of the two parameter space lines near $m_{a0} \sim 10^{-13}$ GeV.

3.2.3 Constraints on ALP parameter space

In the previous subsection, we analyse the DM parameter space satisfying correct relic density of ALP characterized by its final mass m_a and the decay constant f_a. However, such a parameter space can be further constrained from astrophysical and cosmological limits as well as few laboratory and telescope searches provided one considers an ALP-photon coupling [337, 338] of the form

$$\frac{g_{a\gamma\gamma}}{4} F_{\mu\nu}\widetilde{F}^{\mu\nu} a, \tag{3.22}$$

where $F_{\mu\nu}$ and $\widetilde{F}^{\mu\nu}$ are the electromagnetic field strength tensor and its dual respectively. The effective coupling $g_{a\gamma\gamma}$ can be written in terms of the ALP decay constant f_a as

$$g_{a\gamma\gamma} = \frac{\alpha}{2\pi f_a} C_{a\gamma\gamma}. \tag{3.23}$$

Generally, $C_{a\gamma\gamma}$ is expected to be $\mathcal{O}(1)$ and α is the fine-structure constant.

Such an ALP-photon coupling opens up several windows of observation on which a considerable effort is being devoted now-a-days. These ALPs might get produced within the searing plasma of stars via interactions with photons. Such process may subsequently impact the stellar evolution leading to an overall energy loss of a star while escaping. Therefore, the non-observance of any unwanted energy loss in stars sets bounds on the parameter $g_{a\gamma\gamma}$ [213, 339]. A stringent bound on $g_{a\gamma\gamma} < 6.6 \times 10^{-11}$ GeV^{-1} emerges from the study of evolution of the horizontal branch (HB) stars [210]. Also, the Sun is a likely source of ALPs (solar ALP), which are detectable on Earth in a telescope with a macroscopic magnetic field via reverse Primakoff process, commonly known as the *Helioscope* [192]. We have used the latest findings with best sensitivity from the CERN Axion Solar Telescope (CAST) which also puts constraints on $g_{a\gamma\gamma}$ similar to those derived from the study of HB stars as, $g_{a\gamma\gamma} < 6.6 \times 10^{-11}$ GeV^{-1} for $m_a < 0.02$ eV [190]. The ALP-photon interaction is also constrained by the measurements of solar neutrino flux as $g_{a\gamma\gamma} < 7 \times 10^{-10}$ GeV^{-1} for $m_a \lesssim \mathcal{O}(\text{keV})$ [340]. Other important constraints emerge from the cavity experiments such as Rochester-Brookhaven-Florida and University of Florida (RBF and UF) and Axion Dark Matter Experiment (ADMX) which are sensitive for the ALP mass ranges of $4.5 - 16.3$ μeV [341–343] and $1.9 - 3.3$ μeV [344] respectively. Telescope searches including Visible Multi-Object Spectrograph (VIMOS) and Multi Unit Spectroscopic Explorer (MUSE) further constrain the ALP mass ranges of $4.5 - 5.5$ eV and $2.7 - 5.3$ eV respectively [127, 345].

Searches for ALP are also actively done by various laboratory experiments. One such experimental approach is the light shining through a wall (LSW) experiment [346] where a laser beam is expected to be converted into axion or ALPs after being exposed to a high magnetic field. Subsequently, these converted particles pass through an opaque wall and upon re-converting into photons via a second magnetic field behind the wall, they provide indirect evidence for the presence of ALPs. The current best limit by such LSW experiments are given by OSQAR (Optical Search for QED Vacuum Birefringence, Axions, and Photon Regeneration) as $g_{a\gamma\gamma} < 3.5 \times 10^{-8}$ GeV^{-1} for $m_a < 0.3$ meV [347].

The cosmological constraint of $\Gamma^{-1}_{a\to\gamma\gamma} \geq \tau_U$ (with τ_U being the age of the Universe and $\Gamma_{a\to\gamma\gamma} = g^2_{a\gamma\gamma} m_a^3/64\pi$ representing the decay width of ALP) serves as a key condition in

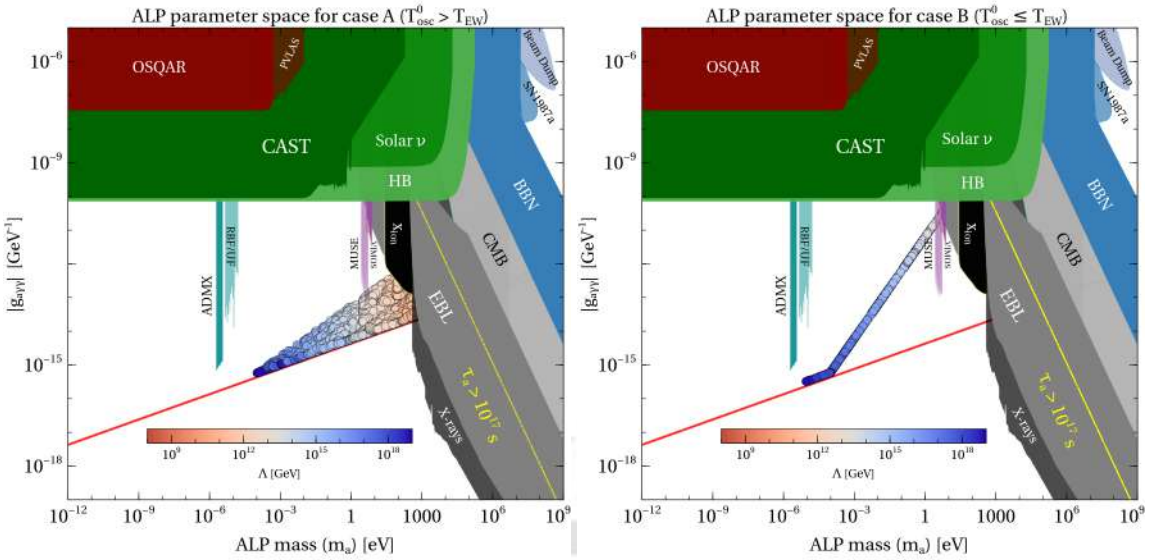

Figure 3.5: Excluded regions in ALP parameter space by various constraints along with the relic-satisfied ALP parameter space denoted by dark-red to blue patch for case A (*upper panel*) and blue patch for case B (*lower panel*) in m_a-$g_{a\gamma\gamma}$ plane. The solid red line represents the ALP as DM from conventional misalignment mechanism (with $C_{a\gamma\gamma} = 1$).

guaranteeing the stability of the non-thermally produced cosmic ALPs as a viable dark matter over the universe lifetime [348]. If $\Gamma^{-1}_{a\to\gamma\gamma} < \tau_U$, the extra radiations impart additional limits on $g_{a\gamma\gamma}$ extending to very large ALP masses [349]. Additionally, photons from ALP decays can be seen as peaks on top of the known backgrounds in the galactic x-ray spectra and must not surpass the extragalactic background light (EBL) [350]. Also, ALP decaying into photons can lead to the ionization of primordial hydrogen, and the constraint comes from the requirement to prevent this ionization from making a crucial contribution to the optical depth after recombination and hence ensuring the consistency of BBN with observations [211,212,349]. Other cosmological constraints comes from the excess photons (when decay occurs during opaque universe) include spectral distortions in the CMB spectrum and increase in T_γ (photon temperature) relative to T_ν (neutrino temperature), thus modifying the value of $N_{\rm eff}$ inferring from WMAP [212].

The bounds regarding all these constraints are shown in the Fig. 3.5 which are taken from the updated online repository `AxionLimits` [351]. In Fig. 3.5, the yellow line acts as the demarkation line below which the ALP may serve as a viable dark matter ($\Gamma^{-1}_{a\to\gamma\gamma} > \tau_U \simeq 10^{17}$ sec). On the other hand, the red line corresponds to the ALP dark matter contour (satisfying observed DM relic abundance) originating from the standard misalignment mechanism (as discussed in section 3.2.1) representative of the green line displayed in Figs. 3.2,and 3.4 with the consideration of $C_{a\gamma\gamma} = 1$ (which is followed throughout the analysis). The obtained parameter spaces in our scenario (Figs. 3.2 and 3.4) of cases [A] and [B] are further constrained by these bounds and the residual allowed parameter regions in $m_a - g_{a\gamma\gamma}$ plane (converted from $m_a - f_a$) are demonstrated in top and bottom panels of Fig. 3.5 respectively. Note that as seen from Fig. 3.5 corresponding to case A, ALP masses ranging from $\mathcal{O}$(keV) to 10^{-13} GeV (serves as the lower limit for this case as per our previous discussion) are allowed with larger couplings (by several orders of magnitude) compared to the conventional

picture (red line). Similarly, higher ALP-photon couplings are permitted for case B as well, where the upper limit of allowed ALP mass turns out to be $\mathcal{O}(10)$ eV while the lower limit is set at $m_a \approx 5 \times 10^{-15}$ GeV, which is the minimum mass contribution arising from the dimension-6 operator. It is important to note that for standard misalignment of ALP (without any higher dimensional soft symmetry breaking term), the lower limit of ALP mass can be extrapolated upto very small values ($\sim 10^{-24}$ eV) [337].

3.2.4 Isocurvature perturbations

In the present scenario, where the PQ-like symmetry is assumed to be broken during inflation, the ALP field should experience quantum fluctuations having an amplitude denoted by $\delta a \simeq \mathcal{H}_{\rm inf}/2\pi$ $(or,\ \delta\theta_I \simeq \mathcal{H}_{\rm inf}/2\pi f_a)$, where $\mathcal{H}_{\rm inf}$ is the Hubble parameter during inflation. These quantum fluctuations give rise to isocurvature perturbation of the cold dark matter [352–354]. In cosmology, isocurvature perturbations refer to fluctuations in the relative number densities of different components (such as photons, baryons, dark matter), while leaving the total energy density or the curvature of spacetime unaffected. This occurs here because the ALP makes a negligible contribution to the total energy density during inflation. Such isocurvature perturbations are tightly constrained from the measurements of the CMB anisotropies[1]. The contribution of ALP to CDM isocurvature perturbation $\mathcal{S}_{\rm CDM}$ can be expressed as

$$\mathcal{S}_{\rm CDM} = \frac{\delta\rho_{\rm CDM}}{\rho_{\rm CDM}} = \frac{\Omega_a}{\Omega_{\rm CDM}}\frac{\delta\rho_a}{\rho_a}. \tag{3.24}$$

In our scenario, ALP contributes entirely to relic density of CDM $i.e.\ \Omega_{\rm CDM} = \Omega_a$. The spectrum of CDM isocurvature perturbation in the Fourier space is given by

$$\mathcal{P}_{\rm iso}(k) = \left(|(\mathcal{S}_{\rm CDM})_k|\right)^2, \tag{3.25}$$

k is the comoving wavenumber, to be evaluated at the pivot scale k_* defined by $k_*/a_0 = 0.05$ Mpc^{-1}. The limit imposed by $Planck$ [63] on CDM isocurvature perturbation with respect to the adiabatic power, $\mathcal{P}_{\rm adi}(k_*) \approx 2.2 \times 10^{-9}$, is expressed as [63]

$$\beta_{\rm iso} = \frac{\mathcal{P}_{\rm iso}(k_*)}{\mathcal{P}_{\rm iso}(k_*) + \mathcal{P}_{\rm adi}(k_*)} < 0.038. \tag{3.26}$$

The ALP density perturbation $\mathcal{S}_{\rm CDM}$ of Eq. 3.24 can also be recast as

$$\mathcal{S}_{\rm CDM} = 2\frac{\delta\theta_I}{\theta_I}, \tag{3.27}$$

using $\delta\rho_a/\rho_a \simeq 2\delta\theta_I/\theta_I$ which follows from Eq. 3.4. Considering the misalignment angle θ_I to be $\mathcal{O}(1)$ and employing the fluctuation of the misalignment angle during inflation, $\delta\theta_I \simeq \mathcal{H}_{inf}/2\pi f_a$, into Eqs. 3.27 and 3.25, we obtain

$$\mathcal{P}_{iso} = \left(\frac{\mathcal{H}_{\rm inf}}{\pi f_a}\right)^2 \left(\frac{\mathcal{O}(1)}{\theta_I}\right)^2. \tag{3.28}$$

[1]These ALP fluctuations however do not play any role in the overall density fluctuations of the universe.

Following the constraint in Eq. 3.26 and considering $\theta_I = 1$ as in the previous sections, we obtain an upper bound on the inflationary Hubble scale $\mathcal{H}_{\rm inf}$ as

$$\mathcal{H}_{\rm inf} < 2.9 \times 10^{-5} f_a. \tag{3.29}$$

Depending on the specific cases in our scenario, we can derive a few more constraints as a consequence of Eq. 3.29 [97] as we discuss in the following.

For case A ($T^0_{\rm osc} > T_{\rm EW}$), the ALP mass at the onset of oscillation can be constrained by the required condition $3\mathcal{H}_{\rm inf} > 3\mathcal{H}(T^0_{\rm osc}) = m_{a0}$. Using Eq. 3.29 and setting $\Omega_a h^2 \simeq 0.12$ in Eq. 3.21, we obtain the following relation

$$\left(\frac{m_a}{6\times 10^{-8}\ {\rm GeV}}\right)\left(\frac{f_a}{5\times 10^{10}\ {\rm GeV}}\right)^{3/2} < 6.6\times 10^{7}, \tag{3.30}$$

where $g_\star(T^0_{\rm osc}) \simeq 100$ is considered.

On the other hand, for case B ($T^0_{\rm osc} \leq T_{\rm EW}$), the constraints can appear in two different ways: (i) when the ALP with effective mass m_a starts to oscillate at $T = T_{\rm EW}$ only, the criteria $3\mathcal{H}_{\rm inf} > 3\mathcal{H}(T_{\rm EW})$ along with Eq. 3.29 leads to

$$f_a > 1.08 \times 10^{-9}\ {\rm GeV}. \tag{3.31}$$

(ii) Secondly, if the oscillation temperature of the ALP with effective mass m_a is itself smaller than $T_{\rm EW}$ (no intermediate change in the ALP mass takes place), we need to utilize the criteria $3\mathcal{H}_{\rm inf} > m_a$. Here, similar to case A, using Eq. 3.29 and setting $\Omega_a h^2 \simeq 0.12$ in Eq. 3.8 (with m_{a0} replaced by m_a), we obtain

$$f_a > 1.86 \times 10^{8}\ {\rm GeV}. \tag{3.32}$$

The correlations obtained in Eq. 3.30 and constraints on f_a as in Eqs. 3.31-3.32 are evidently weaker than the other restrictions shown in the previous subsection and obeyed by the allowed parameter space in the respective cases. The constraint in Eq. 3.29 is however significant in the context of gravitational wave detection. As inflation can give rise to the generation of gravitational waves through tensor perturbations, the generation of tensor perturbations during inflation is directly correlated with the Hubble parameter [354] as

$$r = 1.6\times 10^{-5}\left(\frac{\mathcal{H}_{\rm inf}}{10^{12}\ {\rm GeV}}\right)^2, \tag{3.33}$$

which can be translated in our scenario as

$$r < 1.34\times 10^{-12}\left(\frac{f_a}{10^{13}\ {\rm GeV}}\right)^2 \tag{3.34}$$

which is very small number to be predicted in near future as the current observational constraint on the tensor mode, $r \lesssim 0.1$, is derived from the Planck measurements of the CMB [355].

3.2.5 Conclusion

Axion-like particles are well motivated dark matter candidates which are thought to be produced primarily through the misalignment mechanism in the early universe. In this study, we have explored the impact of electroweak symmetry breaking on the evolution of such ALP DM in presence of an explicit shift symmetry breaking dimension-6 Higgs portal interaction of it. We observe that such an operator may significantly contribute to the ALP mass during the EWSB which further initiates a change in the oscillation frequency, thereby deviating from the standard misalignment mechanism in terms of final outcome. We have shown that depending on the standard ALP oscillation temperature (which is determined by the ALP mass originating from non-perturbative dynamics only), the change in the ALP mass across EWSB gives rise to a significant modifications in relic-density allowed parameter space compared to the standard misalignment mechanism.

Our findings can be broadly categorised into two: (a) one in which we obtain an extended parameter space (in $m_a - f_a$ plane) compared to the standard misalignment mechanism, applicable when the non-perturbative mass of ALP m_{a0} exceeds 10^{-13} GeV and (b) secondly, where we obtain a parameter space with a different slope (in $m_a - f_a$ plane) compared to the standard one which applies when m_{a0} falls below 10^{-13} GeV.

Finally, taking into account all the existing constraints from several terrestrial experiments, astrophysical and cosmological bounds on the $m_a - g_{a\gamma\gamma}$ plane (translated from $m_a - f_a$ plane) characterising ALP's interaction with photons, we have identified a significant residue of newly opened up parameter space (from the point of view of correct DM relic abundance) in the sub-keV ALP mass regime to be compatible as non-thermal dark matter. These constraints also play a crucial role in restricting the lower limit on the cut-off scale Λ (as evident from Fig. 3.5), thereby forbidding the other possibility of ALP production via freeze-in from the decay or annihilations of the Higgs, which requires relatively smaller values of Λ ($\lesssim \mathcal{O}(10^9)$ GeV). Interestingly, the predicted ALP-photon couplings turn out to be notably larger compared to the case of conventional misalignment, opening up opportunities for exploration through upcoming experiments.

3.3 Spontaneous Leptogenesis with sub-GeV ALPs

While the previous section (section 3.2) explores ALP as a viable dark matter candidate of the Universe, in this section we will examine the role of ALPs in generating the observed matter-antimatter asymmetry of the Universe. In the context of the QCD axion, a very important aspect is its coupling with the CP *violating* topological gluon density $aG\widetilde{G}/f_a$, suppressed by the scale of spontaneous symmetry breaking f_a [53–56, 162–165], which is the key to solve the strong CP problem, as discussed in section 1.7.2. Axion can also couple to other SM gauge bosons via chiral anomaly. Similar to the QCD axion, ALPs can also interact with the SM gauge fields through dimension-5 operator: $aF\widetilde{F}/f_a$ with F being the SM gauge field strength, while a shift symmetric derivative coupling of ALPs with the SM fermion current such as Baryon (j_B^μ) or Lepton (j_L^μ) current of the form $\partial_\mu a j_X^\mu/f_a$ may also be introduced at the effective level.

Being feebly coupled to the SM fields and the presence of arbitrariness involved in its

decay constant and mass in a wide possible range, the ALP phenomenology turns out to be quite rich and intriguing [93–95, 97, 157, 324, 337, 356] in explaining some of the unresolved problems of particle physics and cosmology. For example, the above mentioned derivative coupling of ALPs with j_B^μ is capable of explaining the baryon asymmetry of the Universe (BAU) via spontaneous baryogenesis [357, 358]. In such a process, a dynamical CPT violation arises from the presence of a time-dependent, homogeneous ALP field in the early Universe. When the global symmetry associated with the ALP is spontaneously broken before inflation, any spatial fluctuations in the ALP field are inflated away, resulting in a nearly homogeneous field value across the causal Universe. After inflation, as the Hubble expansion rate drops below the ALP mass ($\mathcal{H} \lesssim m_a$), the ALP field, initially displaced from the minimum of its potential, begins to oscillate coherently about the potential minimum. This process generates a nonzero classical velocity (a time-dependent background value) $\dot{a}(t)$, reducing the derivative interaction of ALP as $\dot{a}(t) j_B^0/f_a$, which results in a spontaneous breaking of CPT symmetry during the period when $\dot{a}(t)$ is non-zero, as the particular solution (the background field configuration) selects a preferred direction in time. Evidently, such dynamical CPT violation causes a shift in energy levels of particles relative to antiparticles. Such a situation accompanied by a baryon number violating interaction in thermal equilibrium can be responsible for generation of BAU while disregarding the Sakharov's third condition [128].

A similar approach can also be exercised by replacing j_B^μ with the SM lepton current j_L^μ in the CPT violating source term, thereby realising spontaneous leptogenesis [359–368]. As long as any L or effectively $B-L$ violating interaction ($e.g.$, resulting from Weinberg operator $\ell_L \ell_L H H/\Lambda$ with Λ as cut-off scale) stays in thermal equilibrium, the production of $B-L$ asymmetry continues until such interaction decouples from the thermal bath at temperature $T_d^{\rm H}$. Beyond this point, the $B-L$ asymmetry gets frozen which is later converted into the baryon asymmetry through sphaleron processes. However, in an endeavour to realise this, there are certain aspects which restrict the mechanism to take place only at very high temperature. In particular, the requirement of keeping the Weinberg operator in thermal equilibrium while the same being responsible for generating correct order of magnitude of light neutrino mass m_ν sets a bound $T_d^{\rm H} \gtrsim 10^{13}$ GeV. On the other hand, in order to attain a non-zero velocity $\dot{\theta}$ in the context of standard misalignment mechanism [93–97], the ALP must start oscillating at $T_{\rm osc}$ by then, $i.e.$ $T_{\rm osc} > T_d^{\rm H}$. Note that ALP oscillation starts when its mass (m_a) becomes comparable to the Hubble expansion rate ($\mathcal{H}$) in radiation dominated Universe, indicative of the fact that reheating temperature of the Universe after inflation $T_{\rm RH}$ also has to be larger than $T_{\rm osc}$. Such a stipulated hierarchy among the three crucial temperatures ($T_{\rm RH} > T_{\rm osc} > T_d^{\rm H} \sim 10^{13}$ GeV) associated to the mechanism not only demands a large value of the reheating temperature but also suggests the ALP to be heavy enough[2], $m_a \gtrsim 10^9$ GeV [362, 370].

In this work (based on [371]), we aim to bring down the scale of spontaneous leptogenesis attributed to much lighter ALPs (sub-GeV range) that can be probed in several ongoing and future experiments. For example, collider experiments (BaBar, CLEO, LEP, and the

[2] In case modified ALP potential [364] is in place such as slow roll is incorporated, the limit becomes $m_a \gtrsim 10^5$ GeV [361, 369].

LHC) explore ALPs up to GeV scale via missing-energy signals [372, 373], whereas beam-dump searches and the FASER experiment in LHC are sensitive to ALPs with masses below $\mathcal{O}(1)$ GeV [216, 374, 375] and exceeding a few MeV [376], respectively. Simultaneously, a realisation of such scenario with a relatively low reheating temperature would be a welcome development in view of the lower bound on $T_{\rm RH} \gtrsim \mathcal{O}(\text{few MeV})$.

As stated above, the high $T_d^{\rm H}$ is a result of a tension between the satisfaction of light neutrino mass and to keep (B-L)-violating interaction in thermal equilibrium by the same operator. We therefore propose the inclusion of another lepton number violating operator analogous to the Weinberg operator but replacing the SM Higgs by an IHD Φ, $\ell_L \ell_L \Phi\Phi/\Lambda$. Being unrestricted by the neutrino mass, such IHD aided lepton number violating operator plays pivotal role in reducing the associated decoupling temperature T_d^{Φ} while the satisfaction of neutrino mass is through the Weinberg operator. Though $T_d^{\rm H}$ remains unaltered (as its coefficient has to be consistent with correct neutrino mass), it is the $\ell_L \ell_L \Phi\Phi/\Lambda$ operator which can remain in thermal equilibrium till a much lower temperature, thanks to the difference in coupling coefficients in front, and allows for a lighter ALPs. Such a low temperature realisation of spontaneous leptogenesis has not been explored in the literature to the best of our knowledge. We further extend this novel platform to a next level by allowing a non-zero initial value for ALP velocity (after inflation) which helps bringing down the ALP mass further down to $\mathcal{O}(10)$ keV-MeV range unlike the existing literature [361, 369]. Although such non-zero initial ALP velocity has already been utilized within the framework of axiogenesis [328, 377–379] and its extensions [380–383] to explain the baryon asymmetry with lighter ALPs, in this work we will focus specifically on the mechanism of spontaneous leptogenesis.

3.3.1 Spontaneous Leptogenesis with Weinberg operator

The presence of derivative interaction $\partial_\mu a j_X^\mu / f_a$ involving $j_X^\mu = \bar{\psi}_{X_i} \gamma^\mu \psi_{X_i}$ with $\psi_{X_i} \in$ SM lepton (ℓ_i) and quark (q_i) doublets and right handed singlets of different flavors i) in the background of the ALP field plays a pivotal role in realising spontaneous leptogenesis. While the homogeneous nature of a field reduces the interaction to be dependent on time derivative of a only, the associated j_X^0 relates it to the number density of particles n_X (and anti-particles $n_{\bar{X}}$) as

$$\frac{c_X}{f_a}(\partial_\mu a) j_X^\mu \to \frac{c_X}{f_a} \dot{a}(n_X - n_{\bar{X}}), \tag{3.35}$$

where $c_X (\in c_\ell \text{ and } c_q)$ is considered as a flavor-universal coupling constant (for ℓ_i and q_i, respectively). A non-zero $\dot{a}$ therefore causes the above interaction to be CPT violating in nature which exhibits a shift in energy for individual particles (by $\frac{c_X}{f_a}\dot{a}$) and anti-particles (by $-\frac{c_X}{f_a}\dot{a}$) reminiscent of an effective chemical potential, $\mu_X = -\mu_{\bar{X}} = c_X \dot{a}/f_a$ where the particles and anti-particles are assumed to be in thermal equilibrium.

The effective chemical potential μ_X thus generated acts as a seed for an *equilibrium* number-density asymmetry $(n_X^{\rm eq} - n_{\bar{X}}^{\rm eq})$ between leptons (quarks) and anti-leptons (anti-quarks) provided there exists a $L(B)$ violating interaction in thermal equilibrium. Hence it is possible to generate an equilibrium $B - L$ asymmetry $n_{B-L}^{\rm eq}$, expressed in terms of the

chemical potential $\mu_{B-L} = (59/78)\dot{\theta}$ (estimated in [364,384]) as

$$n^{\rm eq}_{B-L} = (n^{\rm eq}_q - \bar{n}^{\rm eq}_q) - (n^{\rm eq}_\ell - \bar{n}^{\rm eq}_\ell) \simeq \frac{1}{6}\mu_{B-L}T^2, \tag{3.36}$$

where thermal distribution of $\ell, \bar{\ell}$ $(q, \bar{q})$ at temperature $T < T_{\rm RH}$ is employed.

A natural choice of such $B - L$ violating interaction is the Weinberg operator [103], responsible for neutrino mass generation,

$$\mathcal{L}^{\rm H}_L = \frac{1}{2}\kappa_{ij}\frac{(\bar{\ell}_{L_i}\widetilde{H})(\widetilde{H}^T\ell^C_{L_j})}{\Lambda}, \tag{3.37}$$

where H is the SM Higgs doublet with the definition $\widetilde{H} \equiv i\sigma_2 H^\star$, κ is the coupling matrix, and ℓ_L is the SM left handed lepton doublet and Λ is the cut-off scale. This induces neutrino mass matrix $m_\nu = \kappa\frac{v^2}{2\Lambda}$ after H gets a *vev* $v = 246$ GeV.

Note that this $B - L$ violating interaction remains in thermal equilibrium till a point, characterized by decoupling temperature $T^{\rm H}_d$, beyond which the corresponding interaction rate $\Gamma^{\rm H}_{\not L}$ becomes comparable (or smaller) to Hubble $\mathcal{H}(= 1.66\sqrt{g_\star}T^2/M_{\rm Pl}$ in radiation-dominated Universe, below $T_{\rm RH})$ where $\Gamma^{\rm H}_{\not L} = 4n^{\rm eq}_\ell\langle\sigma v\rangle \approx 3n^{\rm eq}_\ell\sum_i m^2_{\nu_i}/(2\pi v^4)$. Here $\langle\sigma v\rangle$ denotes the thermally averaged cross section for lepton number violating processes ($\ell_L\ell_L \leftrightarrow HH, \ell_L H \leftrightarrow \bar{\ell}_L, \overline{H}$) arising *solely* from Eq. 3.37 and $n^{\rm eq}_\ell \approx 2T^3/\pi^2$. Using the latest fit for neutrino data [102], $\sum_i m^2_{\nu_i} \sim \Delta m^2_{atm} = 2.5\times10^{-3}$ eV^2 (considering normal hierarchy and lightest neutrino to be massless), the decoupling temperature is uniquely fixed at $T^{\rm H}_d \simeq 2\times10^{13}$ GeV which serves as a characteristic scale that determines the final $B - L$ asymmetry (n_{B-L}). This is because, below $T^{\rm H}_d$, $n^{\rm eq}_{B-L}$ eventually gets frozen which would further be converted into final baryon asymmetry (n_B) by weak sphalerons [385–387] via $n_B = (28/79)n_{B-L}$. A more precise estimate of the final asymmetry is to be obtained employing Boltzmann equation [361,364].

It is interesting to note that the other important ingredient to realise n_{B-L} is related to the fact that the ALP field must have non-zero velocity $(\dot{\theta})$ before Universe reaches $T^{\rm H}_d \sim 10^{13}$ GeV. In the context of standard misalignment mechanism, the ALP field is assumed to be stuck at some initial value $\theta_I = \mathcal{O}(1)$ after inflation, say at reheating $T_{\rm RH}$, until the condition $3\mathcal{H}(T_{\rm osc}) = m_a$ is achieved after which it moves toward the minimum of its potential, hence acquiring a non-zero velocity. The oscillation temperature $T_{\rm osc}$ followed from this relation is given by

$$T_{\rm osc} \simeq 1.5\times10^{13}\ {\rm GeV}\left(\frac{100}{g_\star(T_{\rm osc})}\right)^{1/4}\left(\frac{m_a}{10^9\ {\rm GeV}}\right)^{1/2}. \tag{3.38}$$

In order to fulfil all the requirements, a very restrictive range of high temperature emerges, $T_{\rm RH} > T_{\rm osc} > T^{\rm H}_d \sim 10^{13}$ GeV, to realise spontaneous leptogenesis. Furthermore, as shown in [384], unless $T^{\rm H}_d$ can be lowered below the temperature where the weak sphaleron enters equilibrium ($T_{\rm ws} \sim 10^{12}$ GeV) [388], the residual asymmetry would vanish.

3.3.2 Spontaneous Leptogenesis with Inert Higgs Doublet

The relation of Eq. 3.38 is certainly indicative of heavy ALPs ($m_a \gtrsim 10^9$ GeV) while, as stated in the introduction, a light ALP would be interesting from experimental viewpoint. Also, the reheating temperature can in principle be substantially lower than 10^{13} GeV [321, 389–392] (depending on the coupling of inflaton with the SM fields) and in that case, the above scenario would no longer in use. We note that the main obstacle to realise the spontaneous leptogenesis at a lower temperature follows from the necessity of $B-L$ breaking interaction originated from Weinberg operator to remain in thermal equilibrium via $\Gamma^{\rm H}_{\not L} \gtrsim \mathcal{H}$ condition, which is also intricately tied up with neutrino mass generation. As a resolution to this problem, we propose to include another $B-L$ violating operator,

$$\mathcal{L}^{\Phi}_{\not L} = \frac{1}{2}\frac{(\bar{\ell}_{L_i}\widetilde{\Phi})(\widetilde{\Phi}^T \ell^C_{L_j})}{\Lambda}, \text{ with } \Phi = \begin{bmatrix} \Phi^+ \\ \\ \Phi^0 \end{bmatrix} \;\&\; \widetilde{\Phi} \equiv i\sigma_2\Phi^\star \tag{3.39}$$

analogous to Weinberg operator, replacing the SM Higgs by an IHD Φ which does not carry any *vev*. The IHD being secluded from neutrino mass generation[3] has the potential to allow a greater flexibility between the decoupling temperature of the relevant $B-L$ violating interaction (T^{Φ}_d associated to $\mathcal{L}^{\Phi}_{\not L}$) and reheating temperature ($T_{\rm RH}$). Inclusion of IHD brings an additive benefit in terms of its contribution to dark matter candidate (protected by the Z_2 symmetry). While the involvement of gauge coupling in case of IHD ensures its presence in the thermal bath at an early Universe, it is well known that the lightest neutral component of the IHD can play the role of a freeze-out type of dark matter. Several studies show that in principle there would be two mass regimes of the IHD as DM, one is below 80 GeV and the other is above 550 GeV, for which the relic density and direct detection limits are satisfied [121, 393–408]. Such mass regimes are not affected by the additional dimension-5 interaction of Eq. (3.39) we considered, primarily because of the suppressed nature of the interaction.

In presence of both the $B-L$ violating operators, we first observe that $T^{\rm H}_d$ remains essentially unchanged as the associated interaction rate $\Gamma^{\rm H}_{\not L}$ solely depends on neutrino mass (*i.e.* independent to Λ). On the other hand, interaction rate associated to $\mathcal{L}^{\Phi}_{\not L}$ being $\Gamma^{\Phi}_{\not L} = 3g n^{\rm eq}_{\ell}/(8\pi\Lambda^2)$ with $g = 324/23$ (see Appendix 2.2.1), T^{Φ}_d can be made much smaller than $T^{\rm H}_d$ as

$$T^{\Phi}_d \simeq 4\times 10^6 \text{ GeV} \left(\frac{g_\star}{100}\right)^{1/2} \left(\frac{\Lambda}{10^{12}\text{ GeV}}\right)^2, \tag{3.40}$$

signifying that the IHD assisted interaction may persist in thermal equilibrium for a prolonged period than the case with Weinberg operator ($\mathcal{L}^{\rm H}_{\not L}$) alone. As shown in Fig. 3.6, the decoupling temperature associated to the new interaction, T^{Φ}_d, can be reduced by following the relation of Eq. (3.40). Note that with any such Λ corresponding to a particular T^{Φ}_d, the neutrino mass can be made of right order by adjusting the coupling parameter κ involved in $m_\nu = \kappa\frac{v^2}{2\Lambda}$. However, in order the elements of this coupling matrix should satisfy $\kappa_{ij} \lesssim 1$,

[3] It can be noted that a contribution to light neutrino mass may also originate at two-loop using both the dimension-5 operators (Eqs. (3.37) and (3.39)). However, due to the involvement of an effective coefficient $\sim 1/\Lambda^3$, its contribution will be highly suppressed.

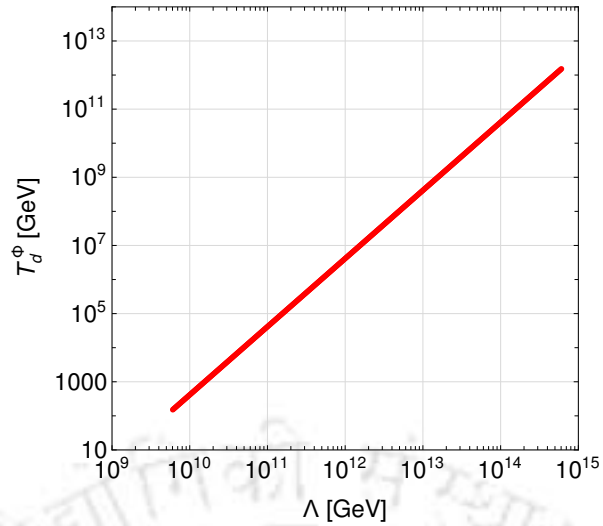

Figure 3.6: Variation of decoupling temperature T_d^{Φ} (GeV) against the cut-off scale Λ (GeV).

a restriction on the higher value of Λ follows as seen in Fig. 3.6.

Before estimating the $B-L$ asymmetry in this case, let us analyse the ALP dynamics starting from $T_{\rm RH}$ in order to estimate its velocity $\dot{\theta}$ which is crucial in determining n_{B-L}. The global $U(1)$ symmetry is considered to be broken before inflation rendering the ALP as a homogeneous field having effective potential $V(a) = m_a^2 f_a^2 \left(1 - \cos\frac{a}{f_a}\right)$ which obeys the following equation of motion,

$$\ddot{a} + 3\mathcal{H}\dot{a} + \frac{\partial V(a)}{\partial a} = \frac{c_X}{f_a R^3}\partial_t(R^3 j_X^0). \tag{3.41}$$

The r.h.s of Eq. 3.41 representing a back-reaction term, originated from $c_X(\partial_\mu a)j_X^\mu/f_a$, can be safely excluded while studying the ALP evolution for $T < T_{\rm RH}$ with the consideration $f_a \gtrsim T_{\rm RH}$. However, solving Eq. 3.41 requires to specify initial conditions associated to a. We set the initial field value of ALP, a_I, to be $a_I = a(T_{\rm RH}) = f_a$ (equivalently, $\theta_I = 1$). In addition, initial condition on $\dot{\theta}_I$ can be set to zero (referred as case A) under conventional misalignment mechanism [93–97] or non-zero (case B) within the so-called kinetic misalignment mechanism [183, 184, 377, 379–383, 409, 410] as discussed below.

[**A: Freeze-in scenario**] Primarily, with $\theta_I = \mathcal{O}(1)$ and $\dot{\theta}_I = 0$, ALP would start oscillating at $T_{\rm osc}$ defined by Eq. 3.38 and gain non-zero $\dot{\theta}$ obtainable using the solution of Eq. 3.41. With the approximated ALP potential near minimum $V(\theta) \simeq m_a^2 f_a^2 \theta^2/2$, solution of Eq. (3.41) can approximately (neglecting r.h.s.) be given by

$$\theta(t) \simeq \theta_I\, \Gamma\left(\frac{5}{4}\right)\left(\frac{2}{m_a t}\right)^{1/4} J_{1/4}(m_a t), \tag{3.42}$$

in radiation-dominated Universe, where $J_{1/4}$ refers to the Bessel's function of first kind. From $\theta(t)$, the ALP velocity $\dot{\theta}$ can easily be estimated at any point of time. Provided $T_{\rm osc} > T_d^{\rm a}$ can be realised with suitable choices of m_a and Λ (as in Table 3.1), $n_{B-L}^{\rm eq}$ is obtained using Eq. (3.36) with $\mu_{B-L} = -(8/3)\dot{\theta}$ in our case (see Appendix B.2.1). Then a precise estimate

of final n_{B-L} results by solving the Boltzmann equation

$$\dot{n}_{B-L} + 3\mathcal{H} n_{B-L} = -\Gamma^{\Phi}_{\not L}\left(n_{B-L} - n^{\rm eq}_{B-L}\right). \tag{3.43}$$

through decoupling epoch.

Fig. 3.7 (upper panel) demonstrates the evolution of the equilibrium $B-L$ asymmetry $Y^{\rm eq}_{B-L} = n^{\rm eq}_{B-L}/\mathcal{S}$ (indicated by the red curve) and the resultant $B-L$ asymmetry $Y_{B-L} = n_{B-L}/\mathcal{S}$ (marked in blue line) obtained as a solution to Eq. (3.43), against normalised scale factor $R/R_{\rm end}$ ($R_{\rm end}$ being the scale factor at the end of inflation, set at $R/R_{\rm end} = 1$) for benchmark point BP1, mentioned in Table 3.1. As can be seen from Fig. 3.7, the $Y^{\rm eq}_{B-L}$, being proportional to the ALP velocity $\dot{\theta}$, tracks the evolution of θ. Hence, $Y^{\rm eq}_{B-L}$, initially starting from zero in this case, oscillates following the ALP oscillation at a temperature $T \leq T_{\rm osc}$. On the other hand, while the $B-L$ violating interaction prevails in thermal equilibrium, Y_{B-L} traces closely the $Y^{\rm eq}_{B-L}$ and starts to grow gradually from zero once the ALP field starts moving toward its minimum marking the onset of oscillation and reaches a peak value when the ALP field initially crosses $\theta = 0$, attaining maximum velocity. Subsequently, the ALP oscillation amplitude gets red-shifted by $(T/T_{\rm osc})^{3/2}$ and the asymmetry *freezes in* (as $B-L$ violating operator decouples) at correct $Y_B \approx 8.7\times10^{-11}$ value [66]. We find that ALPs with $m_a \gtrsim 5\times10^4$ GeV can accurately reproduce the baryon asymmetry in this case. For further lighter m_a, sufficient amount of $B-L$ asymmetry would not result as the ALP velocity $\dot{\theta}$, related to its mass, can't be made arbitrarily large. Below we provide an alternate scenario where a low-mass ALP (in sub-GeV regime) can successfully accompanied by correct baryon asymmetry.

BP	Λ (GeV)	$T_{\rm RH}$ (GeV)	m_a (GeV)	$\dot{\theta}_I$
[A] BP1	1.02×10^{14}	7.4×10^{11}	7×10^4	0
[B] BP2	5.25×10^{12}	4.5×10^9	1	$-10^5 m_a$

Table 3.1: Benchmark Points (BPs) for case A (standard misalignment) and case B (kinetic misalignment).

[**B: Freeze-out scenario**] Contrary to case-A, here we propose to attribute a significantly large initial velocity to ALPs $\dot{\theta}_I \neq 0$, the origin of which can be connected to an explicit breaking of the $U(1)$ symmetry, *e.g.* considered in kinetic misalignment mechanism [183, 184]. Such a velocity is however bounded by

$$|\dot{\theta}_I| \lesssim \mathcal{O}(1)\frac{T^2_{\rm RH}}{f_a}, \tag{3.44}$$

condition, which follows from the argument that at $T = T_{\rm RH}$, ALP's kinetic energy $(\dot{\theta}^2 f_a^2/2)$ remains sub-dominant compared to the energy density of the Universe $(\pi^2 g_\star T^4_{\rm RH}/30)$. Also, if the initial kinetic energy of ALP is larger than the height of the ALP potential $(2m_a^2 f_a^2)$, the ALP field will leap across the potential minima till a point where they become equal and

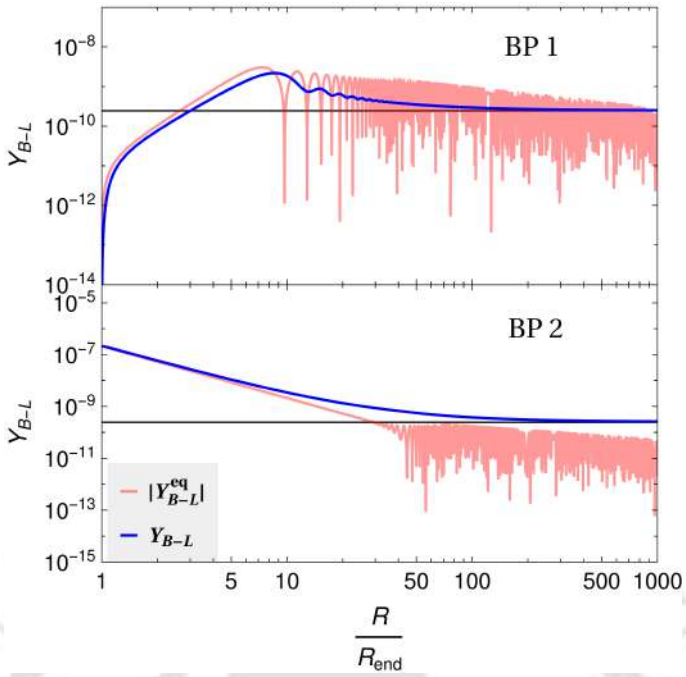

Figure 3.7: *Freeze in* (**upper panel**) and *Freeze out* (**lower panel**) of $B-L$ asymmetry $Y_{B-L}(|Y^{\rm eq}_{B-L}|)$ displayed against $R/R_{\rm end}$ for BP1 and BP2, respectively, with solid blue line (oscillating light red shade). The black gridline represents correct value of Y_{B-L} which generates $Y_B \approx 8.7 \times 10^{-11}$.

ALP field being trapped in a specific minimum starts performing the oscillation. Thus actual ALP oscillation commences at $T^{\star}_{\rm osc}$, governed by $\dot{\theta}(T^{\star}_{\rm osc}) = 2m_a$. However, for kinetic misalignment, $T^{\star}_{\rm osc} > T^{\Phi}_{d}$ is no more a necessary condition as ALP starts evolving with an existing chemical potential at $T = T_{\rm RH}$ itself, given by non-zero $\dot{\theta}_I$. Hence, to generate the desired baryon asymmetry using $\mathcal{L}^{\Phi}_{L}$, the necessary conditions $T_{\rm RH} > T^{\Phi}_{d}$ and $T_{\rm RH} > T^{\star}_{\rm osc}$ should be met.

Here we observe from Fig. 3.7 (bottom panel) that highest value of asymmetry emerges right at the beginning due to large initial $\dot{\theta}_I$ (see Table 2.1, BP2) as Y_{B-L} follows $Y^{\rm eq}_{B-L}$. Note that $T_{\rm RH}$ being smaller than $T^{\rm H}_{d}$, the $\ell_L\ell_L HH$ interaction does not contribute to it. The $B-L$ asymmetry finally *freezes out* as the $\ell_L\ell_L\Phi\Phi$ interaction decouples from equilibrium. We perform a parameter space scan involving $m_a, T_{\rm RH}$ and Λ having initial conditions: $\theta_I = 1$ and $\dot{\theta}_I = -10^5 m_a$ satisfying correct baryon asymmetry. The result is depicted in Fig. 3.8 in $m_a - T_{\rm RH}$ plane (with Λ in the colour-bar[4]) focusing on an extended range of ALP mass in the sub-GeV realm associated to $T_{\rm RH} < \mathcal{O}(10^9)$ GeV. While the lower limit of the scan remains robust with this initial condition, achieving correct BAU with a much lighter ALP remains plausible by using a further larger $\dot{\theta}_I$.

Finally, we address the fate of these ALPs at a later stage, following the freeze-in or freeze-out of the $B-L$ asymmetry, as it continues to oscillate thereafter. It is pertinent to note that even if ALP possesses a large initial velocity (as in case B), the kinetic energy of ALPs being scaled as $\rho^{\rm K.E.}_{a} \propto R^{-6}$ will quickly die out and become negligibly small in comparison to its potential energy density ($\propto R^{-3}$) as well as ρ_R ($\propto R^{-4}$). This results into trapping of the ALP within one potential well within which it starts to oscillate. Therefore its energy

[4]With each Λ, there exists κ followed from $m_\nu = \kappa v^2/(2\Lambda)$.

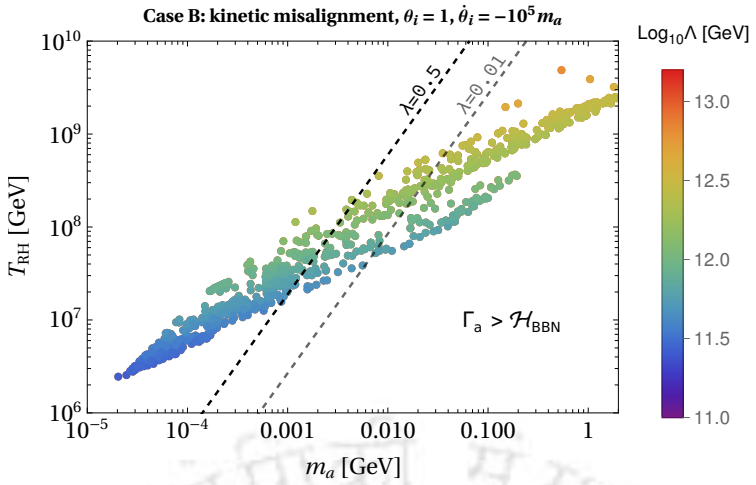

Figure 3.8: Parameter scan for case B: $\dot{\theta}_I \neq 0$ in $m_a - T_{\rm RH}$ plane. Here $\dot{\theta}_I = -10^5 m_a$ is considered. In the color map, the parameter Λ is specified in log-scale.

density is thereafter dominated by its potential energy which scales as $\rho_a(T) \propto R(T)^{-3}$. As a result of which, although the energy density of ALP are set to be sub-dominant compared to the thermal bath at the time of reheating, a possibility may open up where the ALP can dominate the energy density of the Universe at the time of BBN. Hence, it is preferable that they should decay (with decay rate Γ_a) prior to BBN so as not to disturb BBN prediction, *i.e.* $\Gamma_a \gtrsim \mathcal{H}_{\rm BBN}$ [369, 390, 411]. ALPs are primarily expected to decay into the SM leptons as well as WW/ZZ (provided kinematically allowed) via their effective interactions [412] which can be parametrised by $\Gamma_a = \beta m_a^3/f_a^2$, with $\beta < \mathcal{O}(1)$. Using this along with the criteria considered $T_{\rm RH} = \alpha f_a$ where $\alpha \leq 1$, the residual allowed parameter space falls in right side of black dashed $T_{\rm RH} - m_a$ contour lines (acting as boundary of $\Gamma_a \geq \mathcal{H}_{\rm BBN}$) for specific choices of $\lambda\ (= \beta\alpha^2) < 1$ in Fig. 3.8 that could be sensitive to upcoming ALPs searches. The constraints on such decaying ALP in the mass regime of Fig. 3.8 also stem from astrophysics (e.g. stellar evolution [413] as well as emission and decays of ALP out of supernova SN1987A [414–417]), electron and proton beam dump experiments (e.g. SLAC E137 [375, 418], CHARM and NuCal [216] etc.) and collider experiments like CLEO and BaBar [372, 373], LEP-I and II [419–421], Belle-II [422], PrimEx [423] etc., which are shown in Fig. 3.9 considering the ALP-photon interaction given by $g_{a\gamma\gamma} a F\widetilde{F}/4$. The ALP-photon coupling $g_{a\gamma\gamma}$ is related to the ALP decay constant (f_a) as

$$g_{a\gamma\gamma} = \frac{\alpha}{2\pi f_a} C_{a\gamma\gamma}, \tag{3.45}$$

where $C_{a\gamma\gamma}$ is considered to be $\mathcal{O}(1)$ and α refers to the fine structure constant. Note that f_a is not directly involved in the evolution of baryon asymmetry except the requirement $f_a \gtrsim T_{\rm RH}$ (see discussion related to Eq. 3.41). Keeping this in mind, we choose two specific relations among f_a and $T_{\rm RH}$ to demonstrate the parameter space obtained in Fig. 3.8 onto $m_a - g_{a\gamma\gamma}$ plane (in Fig. 3.9) as (a) $f_a = T_{\rm RH}$ (marked with triangular points) and (b) $f_a = 100\ T_{\rm RH}$ (marked with cross points). As seen from Fig. 3.9, for both choices of f_a, the allowed parameter space in our case lies below the current exclusion limits from both astrophysics and experiments (collider and beam dump), which can be probed in future.

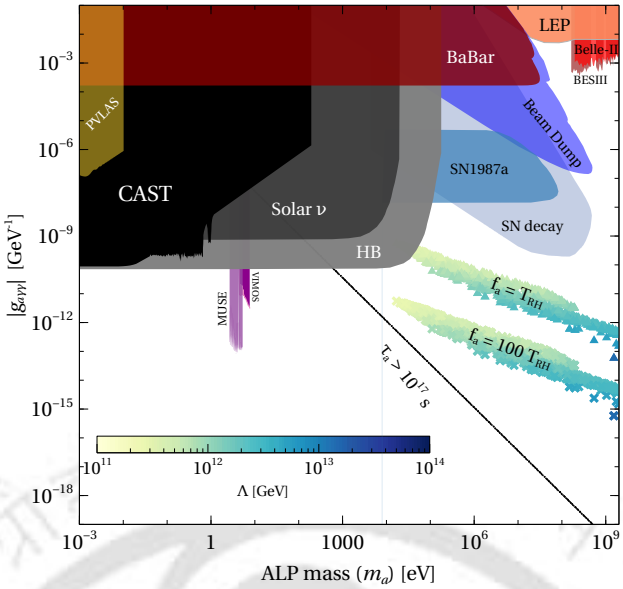

Figure 3.9: ALP parameter space in $m_a - g_{a\gamma\gamma}$ plane for case B ($\dot{\theta}_I = -10^5 m_a$) with exclusion regions from various constraints. In the color map, the parameter Λ is specified in log-scale.

3.4 Summary

To summarize, in this section, we propose a unique scenario of leptogenesis for generating the BAU by incorporating a dynamic CPT violating effect involving light ALPs in presence of a thermally equilibrated lepton number violating interactions in the early Universe. Traditionally, such possibility comprises lepton number violating dimension-5 Weinberg operator that simultaneously can account for neutrino mass. However, this being in thermal equilibrium only at very high temperature ($T \gtrsim 10^{13}$ GeV) in the early Universe, such mechanism turns out to be redundant both for the low reheating scenarios and those with light ALPs, which are otherwise interesting from experimental point of view. This work resolves both these downsides at one go, hitherto unexplored in the literature, by introducing a $B - L$ breaking operator (analogous to the Weinberg operator) involving IHD instead of the SM Higgs. Using the freedom associated with this new operator, *i.e.* not being connected to neutrino mass, the decoupling temperature of lepton number violating interactions can be significantly lowered. This enables the generation of correct BAU via *freeze-in* with low $T_{\rm RH}$ while simultaneously accounts for lighter ALPs $m_a \sim 5 \times 10^4$ GeV even without any initial ALP velocity. The study further extends to lower the mass ALPs down to $\sim \mathcal{O}(10)$ keV-MeV leading to *freeze-out* production of BAU, where a large initial velocity of ALP is considered making it intriguing for search of ALPs. Moreover, the IHD here can serve as a potential potential dark matter candidate, bridging the connection with another unresolved problem securing minimality of the construction.

Chapter 4

Collider Prospects of ALP-portal Fermionic Dark Matter

In the previous chapter, we mainly focused on the non-thermal production of ALPs via the misalignment mechanism and explored their role as DM as well as in generating the baryon asymmetry of the Universe through spontaneous leptogenesis. As discussed in the previous chapters, over several decades, extensive experimental searches, astrophysical and cosmological observations have been carried out across diverse mass and coupling (phenomenologically, most important one is ALP-photon coupling) ranges of such axion and ALPs, leading to stringent constraints on the parameter space.

In this chapter, we shift our attention to thermally produced heavy ALPs with significantly large ALP-photon couplings, which have attracted experimental interest. In this regime ($m_a \gtrsim \mathcal{O}(\mathrm{MeV})$), ALPs are sensitive to be probed in various flavor and collider experiments like BaBar [373], LEP [424] and LHC [214] as well as in current and future beam-dump experiments [216, 374, 375]. Notably, such massive ALPs cannot serve as viable DM candidates as their decay into two photons leads to instability over cosmological timescale. Therefore, we explore their role as mediators between DM and SM sector, where a Dirac fermion (Ψ) serves as the DM candidate. Considering a scenario where the GeV scale ALPs only interact with electroweak gauge bosons, DM can achieve the correct relic abundance through annihilation into two photons during freeze-out. Such role of ALPs as mediators have been extensively explored in the literature [418, 425–433]. However, stringent constraints from indirect detection experiments can significantly restrict the parameter space. These constraints can be evaded if DM annihilation is resonantly enhanced during freeze-out, allowing the correct relic abundance to be achieved for $f_a \sim \mathcal{O}(200)$ GeV. Interestingly, such GeV-scale ALPs with $f_a \sim \mathcal{O}(200)$ GeV can also be probed at high-energy colliders. Once produced, ALPs can decay into photons, charged leptons, light hadrons, or jets, leading to multi-photon, multi-lepton, and multi-jet signals that motivate collider searches. An intriguing possibility in our setup is ALP can dominantly decay into two DM particles (considering $m_a \gtrsim 2m_\Psi$), which would show up as missing energy at colliders. This establishes a direct connection between DM phenomenology and collider searches, further highlighting the role of ALPs as mediators.

Thanks to the absence of the QCD background and PDF uncertainty, lepton colliders allow us to investigate different new physics (NP) scenarios in a pristine environment. Moreover, the availability of partially polarized beams proves advantageous for reducing the SM background and facilitating the dominance of any NP signal over the SM background. Therefore, in this chapter, our focus is to estimate the sensitivity of the different ALP-SM couplings through associate production of ALPs at future electron-positron colliders such as International Linear Collider (ILC) [434, 435]. Study of ALP-fermion coupling has been studied through di-lepton + missing energy final state signal through W-boson fusion at the ILC [436, 437]. Considering ALPs as the long lived particle (LLP), determination of future sensitivity of ALP-fermion coupling has been explored at the e^+e^- collider [438]. Study of multi-photons, multi-leptons and multi-jets signal to estimate future bounds on different ALP-SM couplings have been performed at the e^+e^- colliders [439–442]. Our focus will be two folded, first to show the detectability of the ALP via mono-photon plus missing energy signal, and second, to estimate the ALP-photon coupling from the proposed experimental sensitivity of upcoming e^+e^- machine.

This work is structured as follows: In Section 4.1, we outline the phenomenological framework of the study. The DM phenomenology is discussed in Section 4.2. A detailed collider analysis is presented in Section 4.3. In Section 4.4, we briefly explore standard χ^2 analysis and evaluate the collider accuracy with which the ALP-photon coupling can be estimated. We conclude our findings in Section 4.5, and in Section C.1, we discuss a possible UV completion of the model framework.

4.1 Phenomenological Framework

The interactions of pseudoscalar ALP (a), the pNGB of a spontaneously broken global axial $U(1)$ symmetry by a complex scalar field $\Phi = (f_a + \rho)e^{ia/f_a}/\sqrt{2}$, with the SM particles can primarily be obtained by dimension-5 effective operators at the low energy. In this work, we consider the following ALP Lagrangian [215, 433, 439, 443]:

$$\mathcal{L}_{\text{eff}} = \mathcal{L}_{\text{ALP}} + \mathcal{L}_{\text{ALP-SM}} + \mathcal{L}_{\text{ALP-DM}}, \tag{4.1}$$

where

$$\mathcal{L}_{\text{ALP}} = \frac{1}{2}\partial_\mu a \partial^\mu a - \frac{1}{2}m_a^2 a^2 \tag{4.2}$$

$$\mathcal{L}_{\text{ALP-SM}} = -\frac{C_{aB}}{4} a B_{\mu\nu}\widetilde{B}^{\mu\nu} - \frac{C_{aW}}{4} a W_{\mu\nu}\widetilde{W}^{\mu\nu}. \tag{4.3}$$

Here $B_{\mu\nu}$ and $W_{\mu\nu}$ are field strength tensors corresponding to $U(1)_Y$ and $SU(2)_L$ gauge groups, respectively, while the dual field strength tensors are defined as $\widetilde{B}^{\mu\nu} = \frac{1}{2}\epsilon^{\mu\nu\alpha\beta}B_{\alpha\beta}$ and so on. The coupling constants, C_{ai} $(= \alpha_i/\pi f_a)$ for $i = B, W$, are the Wilson coefficients. As argued previously, unlike the QCD axion, the ALP mass (m_a) in Eq. 4.2 is a free parameter, which can arise from either non-perturbative dynamics or explicit breaking of the underlying symmetry. As evident from Eq. 4.3, we primarily focus on the ALP interaction with SM electroweak gauge bosons, while neglecting any direct couplings to SM

fermions and gluons. This setup can be naturally realized, analogous to the KSVZ axion model [164, 165], which is elaborated in appendix C.1. The absence of ALP-fermion couplings also prevents flavor-changing processes, which are strongly constrained by rare decay searches [418, 429, 431, 433].

After electroweak symmetry breaking, the Lagrangian that governs the ALP gauge boson couplings can be described (following Eq. 4.3) as

$$\mathcal{L}_{\rm ALP-SM} = -\frac{g_{a\gamma\gamma}}{4} a F_{\mu\nu}\widetilde{F}^{\mu\nu} - \frac{g_{aZZ}}{4} a Z_{\mu\nu}\widetilde{Z}^{\mu\nu} - \frac{g_{aWW}}{4} a W^{+}_{\mu\nu}\widetilde{W}^{-\mu\nu} - \frac{g_{a\gamma Z}}{4} a F_{\mu\nu}\widetilde{Z}^{\mu\nu}, \quad (4.4)$$

where $F_{\mu\nu}$, $Z_{\mu\nu}$ and $W_{\mu\nu}$ are corresponding to the field strength tensors of photon, Z and W bosons, respectively, and the effective couplings involved in Eq. 4.4 follow the relations

$$g_{a\gamma\gamma} = C_{aB}\cos^2\theta_W + C_{aW}\sin^2\theta_W \quad (4.5)$$

$$g_{aZZ} = C_{aB}\cos^2\theta_W + C_{aW}\sin^2\theta_W \quad (4.6)$$

$$g_{a\gamma Z} = (C_{aW} - C_{aB})\cos\theta_W \sin\theta_W \quad (4.7)$$

$$g_{aWW} = C_{aW}, \quad (4.8)$$

with θ_W being the weak mixing angle. For our convenience, we assume $C_{aB} = C_{aW}$, which greatly simplifies our analysis with $g_{a\gamma\gamma} = g_{aZZ} = g_{aWW}$ and $g_{a\gamma Z} = 0$. From the experimental perspective, the ALP interaction with two photons is particularly significant for $m_a < M_W, M_Z$ (with M_W and M_Z being the masses of W and Z bosons, respectively), resulting the decay width of ALP as [433]

$$\Gamma_a = \frac{g^2_{a\gamma\gamma} m_a^3}{64\pi}, \quad \text{with } g_{a\gamma\gamma} = \frac{\alpha_{\rm EM}}{\pi f_a}, \quad (4.9)$$

where $\alpha_{\rm EM}$ denotes the fine-structure constant.

We now focus our attention to ALP-DM interaction. As stated earlier, we consider a Dirac fermion Ψ, charged under the same global $U(1)$ symmetry, to serve as the dark matter candidate. The DM mass term and its shift-symmetric interaction with ALPs can then be expressed as

$$\mathcal{L}_{\rm ALP-DM} = -m_\Psi \bar{\Psi}\Psi - \frac{c_\Psi}{2f_a}(\partial_\mu a)\bar{\Psi}\gamma^\mu\gamma_5\Psi, \quad (4.10)$$

where c_Ψ is a dimensionless coefficient, typically of $\mathcal{O}(1)$. The origin of such ALP-DM interaction, after the spontaneous breaking of $U(1)$, is discussed in appendix C.1. In this setup, a residual Z_2 after $U(1)$ breaking is present which naturally stabilizes the dark matter[1], ensuring that it is always produced in $\bar{\Psi}\Psi$ pairs [427]. Choosing specific mass hierarchies as: $m_a \gtrsim 2m_\Psi$ and $m_a < M_W, M_Z$, in the following sections, we explore the phenomenology of ALP-mediated DM interactions and their potential detection in collider searches.

[1] A Majorana fermion can be another choice of such fermion DM candidate, which can be stabilized by Z_2 symmetry [418, 428, 431].

4.2 Dark Matter Phenomenology

In this section, we investigate the framework discussed above, mainly emphasizing on the possibility of DM thermal freeze out. For reasonably low f_a, ALPs and the dark sector are expected to maintain thermal equilibrium with the SM sector while allowing DM to freeze-out through Ψ annihilations into SM particles (except SM fermions). Following Eqs. 4.4 and 4.10, it is evident that DM interacts with SM electroweak gauge bosons via ALP mediation. The DM mass being smaller than the SM gauges bosons (as specified by the chosen mass hierarchies), the dominant annihilation channel of DM freeze out turns out to be $\bar{\Psi}\Psi \to \gamma\gamma$ as in Fig. 4.1, while other possible annihilation channels, such as $\bar{\Psi}\Psi \to W^+W^-$, $\bar{\Psi}\Psi \to ZZ$, and $\bar{\Psi}\Psi \to aa$ remain kinematically forbidden. Such a typical DM mass range is motivated by constraints from both indirect detection and collider searches, which we will discuss in detail later.

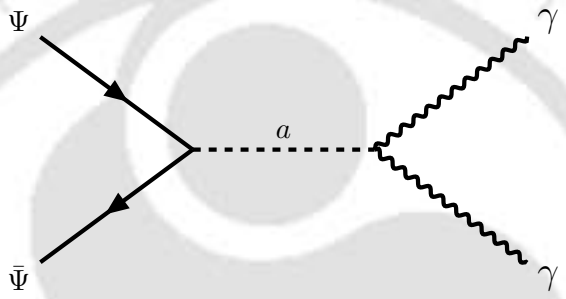

Figure 4.1: Feynman diagram indicating the annihilation of two Dirac fermion DM particles (Ψ) into two photons via ALP (a) mediation, responsible for DM freeze-out.

The evolution of DM can be analyzed by solving the Boltzmann equation in terms of the co-moving number density Y_Ψ ($= n_\Psi/\mathcal{S}$) and the dimensionless variable $x = m_\Psi/T$:

$$\frac{dY_\Psi}{dx} = -\frac{\mathcal{S}\langle\sigma_{\Psi\bar{\Psi}\to\gamma\gamma}v\rangle^{\rm sub}}{xH(x)}[Y_\Psi^2 - (Y_\Psi^{\rm eq})^2] - \frac{\langle\Gamma_a\rangle Y_a^{\rm eq}}{xH(x)}{\rm BR}(a\to\Psi\bar{\Psi})\left[\frac{Y_\Psi^2}{(Y_\Psi^{\rm eq})^2} - 1\right] \quad (4.11)$$

where m_i and $g_i = 1(2)$ (for scalar (fermion)) represent the mass and internal degrees of freedom of the species i. The thermally averaged cross-section for $\Psi\bar{\Psi} \to \gamma\gamma$ is denoted by $\langle\sigma_{\Psi\bar{\Psi}\to\gamma\gamma}v\rangle$, can be expressed as

$$\langle\sigma_{\Psi\bar{\Psi}\to\gamma\gamma}v\rangle = \frac{1}{8m_\Psi^4(m_\Psi/x)K_2^2(x)}\int_{4m_\Psi^2}^{\infty}\sigma_{\Psi\bar{\Psi}\to\gamma\gamma}(s-4m_\Psi^2)\sqrt{s}K_1\left(x\sqrt{s}/m_\Psi\right)ds, \quad (4.12)$$

where

$$\sigma_{\Psi\bar{\Psi}\to\gamma\gamma} = \frac{g_{a\gamma\gamma}^2 m_\Psi^2}{128\pi f_a^2}\frac{1}{\sqrt{1-4m_\Psi^2/s}}\frac{s^2}{(s-m_a^2)^2+m_a^2\Gamma_a^2}, \quad (4.13)$$

with s being the center-of-mass energy and $K_1(K_2)$ denotes the modifies Bessel's function of first (second) kind. Similarly, $\langle\Gamma_a\rangle$ in Eq. 4.11 represents the thermally averaged total decay width of ALP. For $m_\Psi < m_a/2$, ALP can dominantly decay into two DM particles, resulting

in an invisible decay width, given by

$$\Gamma(a \to \Psi\bar{\Psi}) = \frac{m_a m_\Psi^2}{8\pi f_a^2}\sqrt{1-\frac{4m_\Psi^2}{m_a^2}} \tag{4.14}$$

Hence, to eliminate the double-counting from the on-shell ALP contribution in the $\Psi\bar{\Psi} \to \gamma\gamma$ process, a subtraction must be applied, which results in the corrected thermally averaged cross-section (used in Eq. 4.11), expressed as [433]:

$$\langle\sigma_{\Psi\bar{\Psi}\to\gamma\gamma}v\rangle^{\rm sub} = \langle\sigma_{\Psi\bar{\Psi}\to\gamma\gamma}v\rangle - \frac{Y_a^{\rm eq}}{\mathcal{S}(Y_\Psi^{\rm eq})^2}\langle\Gamma_a\rangle\,{\rm BR}(a\to\Psi\bar{\Psi})\,{\rm BR}(a\to\gamma\gamma). \tag{4.15}$$

Although the decay channel (in Eq. 4.14) can significantly produce Ψ at $T \sim m_a$, however, at $T \lesssim m_a$, the ALP abundance is Boltzmann suppressed and hence, this decay channel becomes inefficient. Moreover, since we consider the case of a thermal DM, which tracks its equilibrium abundance ($Y_\Psi = Y_\Psi^{\rm eq}$) before freeze out, the second term on the r.h.s of Eq. 4.11 becomes negligible during that period.

On the other hand, the annihilation process $\Psi\bar{\Psi} \to \gamma\gamma$ produces a distinct gamma-ray line at $E_\gamma = m_\Psi$, which is subject to stringent constraints from gamma-ray line searches, including Fermi-LAT [444,445], MAGIC [446], HESS [447], EGRET, and COMPTEL [448,449]. As pointed out in [418, 431, 433], achieving the correct DM relic density via this process while evading indirect detection limits at the same time is therefore highly challenging. To ensure Ψ remains a viable freeze-out DM candidate with the observed relic abundance, $\Omega h^2 \approx 0.12$ [63], f_a typically needs to be at the $\mathcal{O}$(GeV) scale, which is further ruled out by collider searches [431].

Interestingly, a possible way to circumvent these constraints while achieving the correct relic abundance is to consider the resonance region, where $m_a/m_\Psi \approx 2$ [418,431,433]. This allows for a smaller SM-ALP coupling (corresponds to a larger f_a). Consequently, Eq. 4.12 exhibits a sharp peak around $s \approx m_a^2$ [418], indicating that the intermediate ALP is produced on-shell. It is convenient to use the narrow width approximation near the resonance region (with $\Gamma_a \ll m_a$), under which the ALP propagator can be effectively replaced by a Dirac delta function, simplifying the analysis as

$$\frac{1}{(s-m_a^2)^2+m_a^2\Gamma_a^2} \to \frac{\pi}{m_a\Gamma_a}\delta(s-m_a^2), \tag{4.16}$$

which leads to an approximated expression for $\langle\sigma_{\Psi\bar{\Psi}\to\gamma\gamma}v\rangle$ as

$$\langle\sigma_{\Psi\bar{\Psi}\to\gamma\gamma}v\rangle \approx \frac{\pi}{128}\frac{x g_{a\gamma\gamma}^2 r^5 K_1(x\,r)}{K_2(x)^2}. \tag{4.17}$$

This result follows the assumption that $\Gamma(a\to\Psi\bar{\Psi}) \gg \Gamma(a\to\gamma\gamma)$, such that the total ALP decay with can be approximated as $\Gamma_a \approx \Gamma(a\to\Psi\bar{\Psi})$. As evident from Eq. 4.17, near the resonance (while ensuring $m_a > 2m_\Psi$), the annihilation rate depends primarily on $g_{a\gamma\gamma}$ and the mass ratio $r = m_a/m_\Psi$, while the DM-ALP coupling does not explicitly appear [2].

[2]However, this is not the case when $m_a < 2m_\Psi$ ($r < 2$), as the decay $\Gamma(a\to\Psi\bar{\Psi})$ is forbidden when $r < 2$.

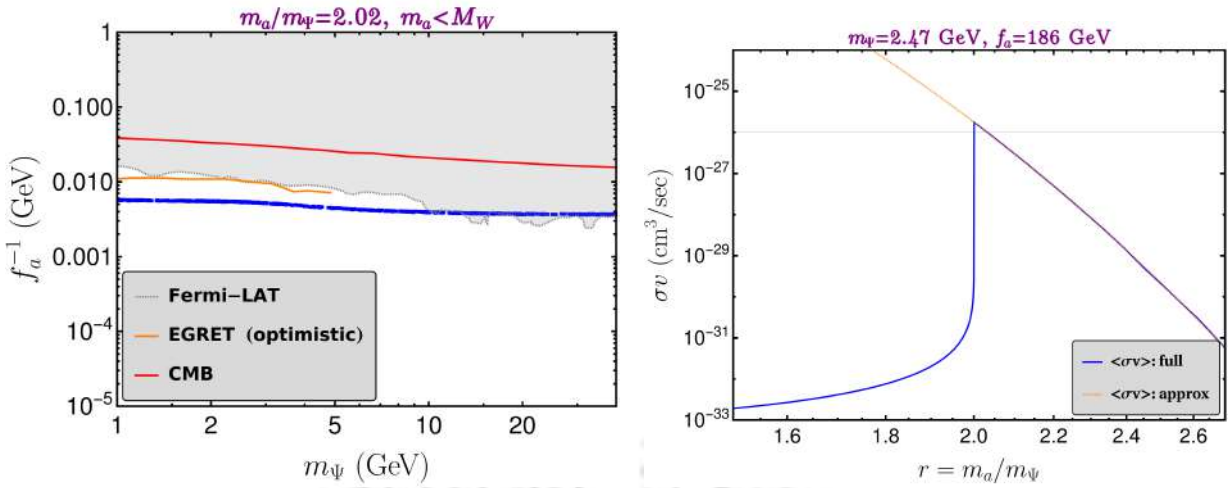

Figure 4.2: Left panel: Relic satisfied dark matter parameter space (shown in blue contour line), with mass ratio $r = m_a/m_\Psi = 2.02$. Also, constraints from CMB and indirect searches are shown, which are taken from [433]. **Right panel:** Variation of thermally averaged cross section $\langle\sigma v\rangle$ against r employing Eqs. 4.12-4.13 (solid blue), while use of the approximated expression of Eq. 4.17 is exhibited by dashed orange line (valid near resonance only). Here, $x = 20$ is assumed, which is the typical DM mass to temperature ratio during DM freeze-out. The black grid line refers to $\langle\sigma v\rangle \sim \mathcal{O}(10^{-26})$ cm^3/s, needed for satisfying the correct relic abundance.

We then set the mass ratio r to a benchmark value 2.02 and performed a parameter scan over f_a (related to $g_{a\gamma\gamma}$ via Eq. 4.9) and m_Ψ to obtain a viable DM parameter space, using `MicrOmegas` [450]. Our analysis primarily focuses on the DM mass range 1 GeV $\lesssim m_\Psi < M_W/2$, motivated from the collider prospects. The result is shown in Fig. 4.2 (left panel), where the blue line represents the relic density satisfied contour, while the red regions indicate constraints from indirect detection. We find that for the choice of $r = 2.02$, $m_\Psi \lesssim 10$ GeV, along with $f_a \lesssim \mathcal{O}(250)$ GeV ($g_{a\gamma\gamma} \gtrsim 10^{-5}$ GeV^{-1}) can successfully reproduce the correct relic density via thermal freeze-out while remaining consistent with indirect detection bounds. This result also agrees with the careful estimates given in [433]. In the right panel of Fig. 4.2, we show the thermally averaged cross section for a benchmark point within the allowed parameter space ($m_\Psi = 2.47$ GeV, $f_a = 186$ GeV), against the mass ratio r. As shown by the solid blue and dashed orange curves, obtaining the correct relic abundance through thermal freeze-out requires staying close to the resonance region, *i.e.* with r close to 2.02 justifying the choice of the benchmark value for r in left panel figure In this region, the cross section reaches $\langle\sigma v\rangle \sim \mathcal{O}(10^{-26})$ cm^3/s, which is needed to reproduce the observed dark matter density. It is pertinent to state that in the case of QCD axion mediation (instead of ALP), such smaller value of f_a is ruled out by Supernova, which places a stringent bound on KSVZ axion as $f_a \gtrsim 4 \times 10^8$ GeV [213].

4.3 Collider analysis

High-energy electron-positron colliders provide a unique opportunity for comprehensive DM searches through missing energy associated with a visible particle. The channel that we focus here for ALP search is the mono-photon plus missing energy final state signature. In collider experiments, DM particles do not interact with the detector, rendering them invisible to direct observation. Consequently, they escape detection, appearing as 'missing

energy' in the recorded measurements. This 'missing energy' serves as an indirect observation of DM production at the colliders [451–466] [3] The final state signal of our interest is associate ALP production with photon followed by the decay of ALP to DM pair as shown in Fig. 4.3 [4].This type of associate mono-photon production in contrast to ISR-photon often referred as *natural mono-photon*, which proves to be beneficial for improving signal-background estimation, as we discuss below. The non-interfering SM background consists of two main contributions. One comes from a W boson-mediated t-channel neutrino pair production, where a photon is radiated either from the initial state or from the W boson (left plot of Fig. 4.4). The other arises from Z-mediated s-channel neutrino pair production, with a photon emitted from the initial state (right plot of Fig. 4.4). In this analysis, we consider $\sqrt{s} = 1$ TeV ILC with an integrated luminosity of $\mathfrak{L}_{\text{int}} = 5\,\text{ab}^{-1}$ to perform a cut-based analysis. The DM phenomenology allowed benchmark point (BP) used in our study corresponds to a ALP mass $m_a = 5\,\text{GeV}$ and a decay constant $f_a = 186\,\text{GeV}$. This choice of f_a results in an effective scale $\Lambda_{\text{eff}} = 4\pi f_a = 2.3\,\text{TeV}$, ensuring the validity of the EFT approximation ($\sqrt{s} < \Lambda_{\text{eff}}$) in our analysis.

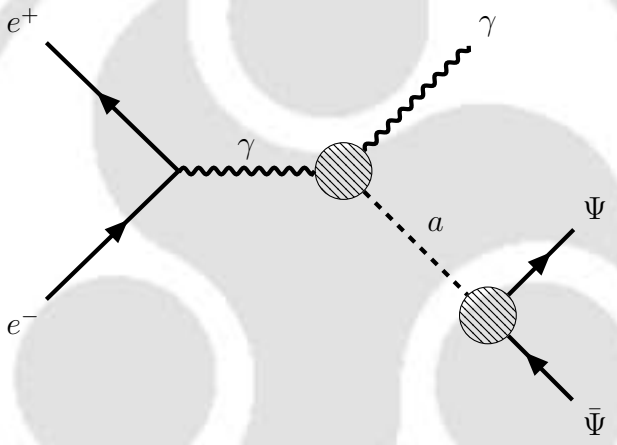

Figure 4.3: Feynman diagrams that induce mono-γ + missing energy final state within EFT framework.

We generate signal and background events in `Madgraph` [467], then showered and analyzed through `Pythia` [468] and the detector simulation is done by `Delphes` [469]. The `UFO` file that is feeded to `Madgraph` is generated through `FeynRules` [470]. During event generation, we constrain the phase space by requiring the photon to have a transverse momentum of $p_T^\gamma > 10\,\text{GeV}$ and a pseudorapidity within $|\eta_\gamma| \leq 2.5$. Additionally, we consider only events featuring a single photon while ensuring no leptons or jets are present in the final state. The key variables for cut-based analysis relevant to the mono-γ signal are defined as follows:

- **Missing energy (E_{miss}):** The energy carried away by missing particle is known as missing energy which is defined from the knowlege of $\sqrt{s}$ as

$$E_{\text{miss}} = \sqrt{s} - \sum_i E_i, \tag{4.18}$$

[3] This should be contrasted with missing transverse momentum or colloquially missing transverse energy ($\not{E}_T$) accessible at hadron colliders, in absence of the information about the sub process center-of-mass energy of the colliding partons.

[4] A Z-mediated s-channel contribution could also be possible if $C_{aB} \neq C_{aW}$.

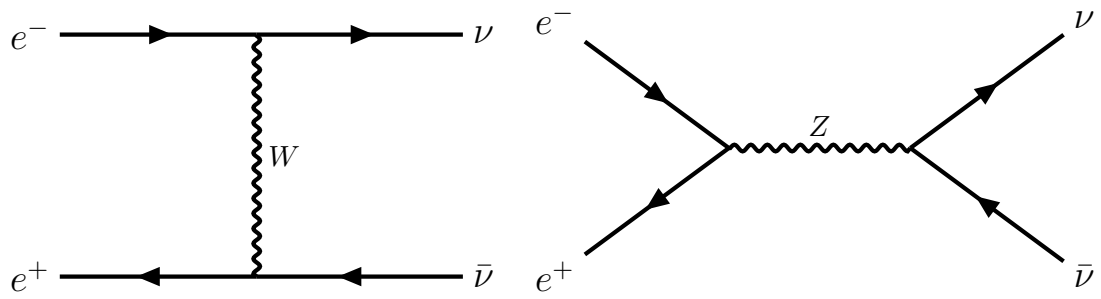

Figure 4.4: Feynman diagrams of non interfering SM backgrounds contributing to mono-γ+ missing energy ($\not{E}$) final state at the e^+e^- colliders. Left: W mediated t-channel diagram where a photon can arise both from the initial states and from the W-boson, contributing to the resulting final state. Right: Z mediated s-channel diagram where a photon can be radiated from initial states;

where i runs over all the visible particles in the final state.

- **Pseudorapidity (η_γ):** The definition of η_γ is given by

$$\eta_\gamma = \frac{1}{2}\log\left[\frac{E_\gamma + p_z}{E_\gamma - p_z}\right], \tag{4.19}$$

where E_γ and p_z are the energy and z component of 4-momenta of the ISR photon.

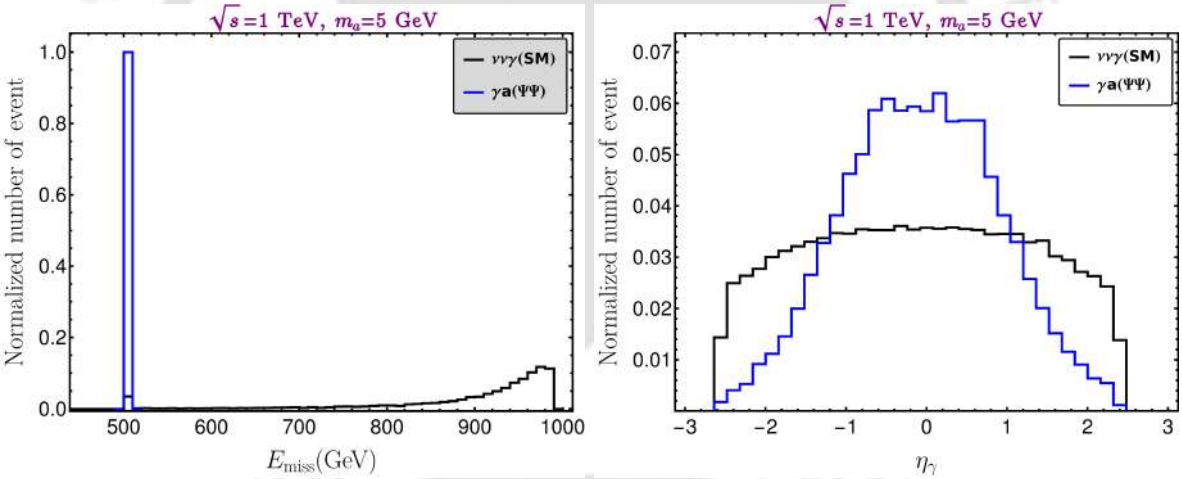

Figure 4.5: Normalized event distribution of kinematic variables at the ILC with $\sqrt{s} = 1$ TeV and $m_a = 5$ GeV. Left: missing energy ($E_{\rm miss}$), right: pseudorapidity (η_γ). Here, the mass ratio $r = m_a/m_\Psi = 2.02$ is considered.

The missing energy distribution of the SM background exhibits a distinctive double-peak structure, as shown in the left plot of Fig. 4.5. The first peak, occurring around 1000 GeV, is primarily arise to the dominant W-mediated t-channel process. Meanwhile, a secondary, sub-dominant peak appears near 500 GeV, resulting from the Z-mediated s-channel process. The position of the secondary peak at the tail of the distribution can be determined using the following expression

$$E_{\rm miss} = \frac{\sqrt{s}}{2}\left(1 + \frac{m_Z^2}{s}\right), \tag{4.20}$$

where m_Z is the Z boson mass. On the other hand, it is quite understandable that the signal

distribution peaks at 500 GeV[5]. Therefore, upper cut on $E_{\rm miss}$ eliminates 97% background keeping the signal intact. Furthermore, applying an absolute pseudorapidity (distribution shown in right plot of Fig. 4.5) cut of $|\eta_\gamma|> 1$ reduces the background by approximately 33%, while the signal is reduced by only about 12%. Linear electron-positron colliders possess partially polarized electron and positron beam which in advantageous in reducing SM backgrounds. Within the SM, left-handed leptons have stronger couplings strength than the right-handed leptons. Thus, right polarized electron and left-polarized positron beam reduce the SM backgrounds. Based on the ILC snowmass report [471], we choose $\{P_{e^+} : P_{e^-}\} = \{-20\% : +80\%\}$ combination that offers a five-fold suppression of the SM while amplifying the signal by 16% as apparent from Table 4.1.

Cuts	$\{P_{e^+}, P_{e^-}\} = \{0\%, 0\%\}$			$\{P_{e^+}, P_{e^-}\} = \{-20\%, +80\%\}$		
	$\Psi\bar{\Psi}\gamma$	$\nu\bar{\nu}\gamma$	Significance	$\Psi\bar{\Psi}\gamma$	$\nu\bar{\nu}\gamma$	Significance
Basic cuts	1750	12440000	0.50	2050	2389000	1.32
$E_{\rm miss} < 510$ GeV	1750	435400	2.63	2050	83615	6.95
$\lvert\eta_\gamma\rvert> 1$ GeV	1545	292589	2.86	1810	56189	7.64

Table 4.1: Cutflow for signal and SM background events for mono-γ signal at the ILC with $\sqrt{s} = 1$ TeV and $\mathfrak{L}_{\rm int}$ = 5 ab^{-1} for unpolarized ($\{P_{e^+} : P_{e^-}\} = \{0\% : 0\%\}$) and polarized ($\{P_{e^+} : P_{e^-}\} = \{-20\% : +80\%\}$) cases.

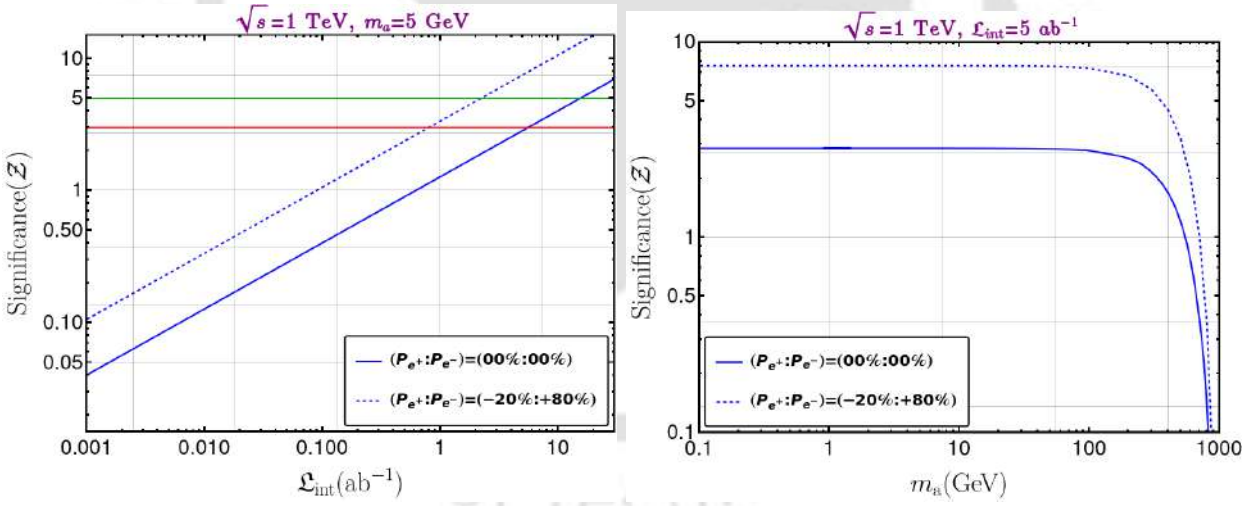

Figure 4.6: Left: variation of significance ($\mathcal{Z}$) with luminosity ($\mathfrak{L}_{\rm int}$) for a fixed $m_a = 5$ GeV for both unpolarized and polarized beams. Red (Green) line indicates 3σ (5σ) significance; right: variation of $\mathcal{Z}$ with the ALP mass (m_a) for a fixed $\mathfrak{L}_{\rm int} = 5$ ab^{-1} for both unpolarized and polarized beams. Here, the mass ratio $r = 2.02$ is considered.

The signal significance ($\mathcal{Z}$) is defined as [472]

$$\mathcal{Z} = \sqrt{2\left[(S+B)\log\left(1+\frac{S}{B}\right) - S\right]}, \tag{4.21}$$

[5]In the case of the off-shell decay of the ALP into a DM pair, the event distribution of $E_{\rm miss}$ exhibits a falling nature, peaking around 500 GeV and gradually decreasing at higher energies.

where S and B are the signal and background events, respectively. For the condition $B \gg S$, this expression reduced to $\mathcal{Z} = S/\sqrt{B}$. After the cuts mentioned in Table 4.1, $\mathcal{Z}$ is approximately 2.85σ for unpolarized beams with $\sqrt{s} = 1$ TeV and $\mathfrak{L}_{\rm int} = 5$ ab^{-1}. With the beam polarization, the $\mathcal{Z}$ is enhanced to 7.64σ. In the left of Fig. 4.6, we show the variation of $\mathcal{Z}$ with $\mathfrak{L}_{\rm int}$ for both polarized and unpolarized beams. We find that a significance of 3σ (5σ) can be achieved with an integrated luminosity of $\mathfrak{L}_{\rm int} = 5.5\ (15.5)$ ab^{-1} for unpolarized beams, whereas, for polarized beams, the same level of significance can be reached with a significantly lower luminosity of $\mathfrak{L}_{\rm int} = 0.8\ (2.2)$ ab^{-1}. In the right panel of Fig. 4.6, we present the variation of $\mathcal{Z}$ as a function of m_a for a fixed $\mathfrak{L}_{\rm int}$. We notice that $\mathcal{Z}$ remains approximately constant up to $m_a = 100$ GeV, as the cross-section does not change significantly in this range. However, beyond $m_a = 100$ GeV, $\mathcal{Z}$ starts to decrease due to phase-space suppression.

It is important to reiterate that the signal observability as achieved here, relies on a few key factors, first the ALP-photon interaction, which makes the photon appearing out of the production vertex, and thus distinguishable from the initial state radiation photon as in the SM background via $E_{\rm miss}$ and $|\eta_\gamma|$ variables; second is the partial polarizability of the initial beams which reduces the SM background significantly, and enhancing the signal. Both of these can be achieved at the future electron-positron machine, while it is difficult to achieve the same at the present LHC or in its high luminosity projection.

4.4 Estimation of $g_{a\gamma\gamma}$

The key parameter that allows us for collider detection of ALP is the ALP-photon coupling $g_{a\gamma\gamma}$. In this section, we present the estimation in accuracy measurement of $g_{a\gamma\gamma}$ coupling following the cut-based analysis discussed above. To achieve this, we adopt the conventional binned χ^2 method which is defined as follows:

$$\chi^2 = \sum_j^{\rm bins} \left(\frac{N_j^{\tt obs} - N_j^{\tt theo}(g_i)}{\Delta N_j} \right)^2 , \tag{4.22}$$

where $N_j^{\tt obs}$ denotes the number of simulated events in the $j^{\tt th}$ bin, and $N_j^{\tt theo}(g_i)$ represents the corresponding number of events predicted theoretically in the presence of NP, which depends on the coupling parameter(s) g_i. The summation extends over all bins of the chosen observable—the differential scattering cross-section defined in Eq. C.9—which is employed in the analysis. The statistical uncertainty in each bin, ΔN_j, is taken to be $\sqrt{N_j^{\tt obs}}$, under the assumption that the event counts follow a Poisson distribution. Our objective is to estimate the precision with which $g_{a\gamma\gamma}$ coupling can be estimated at the e^+e^- colliders. We set the input of $g_{a\gamma\gamma} = 1.33 \times 10^{-5}$ GeV^{-1} with $m_a = 5$ GeV in order to consistent with DM phenomenology. The variation of the χ^2 function with respect to the NP coupling is illustrated in Fig. 4.7. After employing cut on missing energy ($E_{\rm miss} < 510$ GeV) and dividing the differential cross-section distribution into 10 bins. Therefore, the number of degrees of freedom is 9, which corresponds to a chi-squared value of $\chi^2 = 8.34$ for a 68% confidence level (C.L.). For unpolarized beam, the accuracy of $g_{a\gamma\gamma}$ coupling is approximately 2.4%. If we consider $\{P_{e^+} : P_{e^-}\} = \{-20\% : +80\%\}$ polarization combination, non-interfering SM

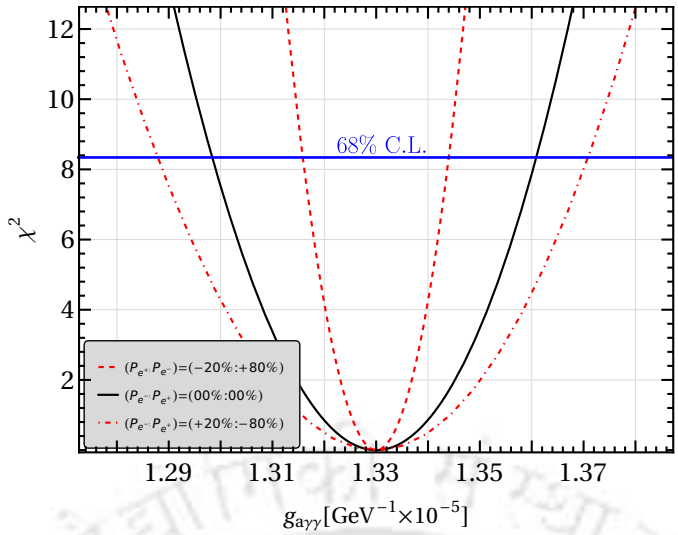

Figure 4.7: Optimal χ^2 variation with $g_{a\gamma\gamma}$ couplings at the ILC with $\sqrt{s} = 1$ TeV, $\mathfrak{L}_{\text{int}} = 500$ fb^{-1}, and three different beam polarization written in the insect with $m_a = 5$ GeV.

background is reduced substantially while the signal increases, the accuracy is enhanced to the 1.1%. The 'optimal' accuracy is obtained when the numerical bin-by-bin event distribution reaches close to that of the analytical distribution. This requires higher number of events and more luminosity. However, in the present context the betterment would be marginal, given the huge SM background left even after employing selection cuts.

4.5 Conclusions

In this work, we have examined the role of ALPs as a portal between a Dirac fermion DM and the SM sector, and investigated the prospects of probing such ALP-mediated DM at electron-positron colliders. This framework involves a derivative interaction between the DM and ALP, along with low-energy effective interactions of the ALP with SM electroweak gauge bosons. Focusing on the mass hierarchy $m_a \lesssim 2m_\Psi$ and $m_a < M_W, M_Z$, we demonstrated that for relatively lower values of the ALPs decay constant f_a, thermal DM production can be viable, with the dominant annihilation channel being $\Psi\Psi \to \gamma\gamma$, mediated by the ALP. We have showed that this annihilation channel can yield the correct DM relic abundance, while evading the strong indirect detection constraints, only in the near-resonance region where $m_a \approx 2m_\Psi$. Taking a benchmark ratio between the DM mass and ALP mass, $r = m_a/m_\Psi = 2.02$, we performed a detailed DM phenomenological analysis and found that DM masses $m_\Psi \gtrsim \mathcal{O}(10\ \text{GeV})$ can successfully reproduce the observed relic density. In this setup, the invisible decay channel $a \to \Psi\Psi$ becomes kinematically allowed and actually dominates over the diphoton decay mode, making it a dominant channel at the colliders giving rise to missing energy signature.

Following the DM phenomenology, we have conducted a signal-background analysis considering the invisible decay of the ALP at the International Linear Collider (ILC). The study is performed at a center-of-mass (CM) energy of 1 TeV with an integrated luminosity of 5 ab^{-1}, considering initial beam polarization. The final state under investigation is

characterized by a mono-photon plus missing energy. In this context, missing energy and pseudorapidity emerge as crucial kinematic variables, effectively suppressing substantial non-interfering SM neutrino background. This is possible due to the very specific ALP-photon interaction, which makes the mono photon signal largely segregable from that of the SM contamination. We must note here that most of the SM-DM effective interactions fail to provide this discrimination and hence should be noted carefully. For the beam polarization combination $\{P_{e^+} : P_{e^-}\} = \{-20\% : +80\%\}$ at 1 TeV CM energy, we have obtained exclusion (3σ) and discovery (5σ) limits for integrated luminosities of 1 ab^{-1} and 3 ab^{-1}, respectively. Furthermore, we have employed the standard χ^2 analysis to estimate the sensitivity to the ALP-photon couplings under the specified collider configuration. With the aforementioned beam polarization, the accuracy in determining the coupling can reach approximately 1%.

Chapter 5

Summary and conclusion

This thesis explores a compendium of works based on the phenomenology of two very well-known pNGBs, the Majorons and the ALPs, to elegantly connect some of the major BSM scenarios, $e.g.$, the dark matter, the existing matter-antimatter asymmetry of the Universe and the origin of tiny neutrino masses. Since exact global symmetries are quite rare in nature, such pNGBs with small yet non-zero masses appear naturally as an outcome of the spontaneous breaking of approximate global symmetries. One of the major motivations for studying pNGBs stems from the QCD axion, a pNGB of global axial $U(1)_{\rm PQ}$ symmetry, proposed as a solution of the strong CP problem, a long-standing puzzle of the SM. Although QCD axions are not the main theme of this thesis, we explored a wider class of axions, the ALPs. On the other hand, the Majoron emerges from the breaking of lepton number symmetry, which, in spite of being an accidental symmetry in the SM, is however broken at the quantum level. Being naturally light, pNGBs are promising candidates for various experimental searches and are further constrained by several astrophysical and cosmological observations. Their feebly interacting nature makes them long-lived particles or even viable DM candidates. Additionally, these light scalars can be instrumental in generating the matter-antimatter asymmetry of the Universe through scenarios like spontaneous leptogenesis, as well as in acting as a portal between a dark sector and the SM sector. With these motivations, this thesis explores the phenomenology of GeV and sub-GeV scale pNGBs across a few scenarios.

In Chapter 1, we begin with a brief outline of the SM of particle physics, followed by a summary of the thermal history of the expanding Universe and few of the shortcomings of the SM, which are also connected to the early Universe cosmology. Next, we introduce the Goldstone bosons and extend the discussion to pNGBs, arising from explicitly broken global symmetries, to which the rest of the thesis revolves around. We further provide an elongated discussions on two of the pNGBs of our interest, the Majorons and the ALPs, and try to motivate why they are relevant in exploring the new physics. In particular, for ALPs, we elaborately discuss the *misalignment mechanism*, through which axions and ALPs can serve as non-thermal DM via oscillations in the early Universe. We conclude this chapter with a summary of the motivations behind the works presented in the thesis.

In Chapter 2, we try to realize Majorons as freeze-in dark matter (FIMP) within the min-

imal setup of the type-I seesaw mechanism, which seemed to be impossible due to its production channels being heavily suppressed by the active-sterile neutrino mixing. Therefore, in most of the earlier works on FIMP-type Majoron, an explicit global $U(1)_L$ breaking Higgs portal interaction is introduced, that restricts the dark matter Majoron mass at an unique value of ~ 3 MeV. In the first part of this chapter, we aim to overcome such fine-tuned situation and broaden the allowed DM mass range while keeping the minimality and naturalness intact. By invoking an additional explicit global $U(1)_L$ breaking term at the dimension-5 level, which involves only RHNs and $U(1)_L$ breaking complex scalar fields, we achieve the desired amount of Majoron production for a broader Majoron mass range owing to the newly opened production channel via annihilation of RHNs. Focusing on the keV-GeV Majoron mass range, we obtain an adequate region of parameter space with Majoron being a viable FIMP Dark matter, abide by the lifetime of the Universe. As Majorons can decay into neutrinos (photons) at the tree (loop) level, the mass regime of our interest keV-GeV is also fascinating to be probed at various indirect searches such as monochromatic neutrino lines, X-ray and gamma-ray lines, etc. which we extensively discussed in this part. Then, in the next part, we adopt the same Majoron dark matter (DM) production channel and connect it to resonant leptogenesis. In this framework, the near-degeneracy of RHNs naturally arises from the model's construction (with the help of an additionally imposed Z_2 symmetry), and the small mass splitting between the RHNs arises from the same dimension-5 explicit $U(1)_L$ breaking terms which are responsible for DM production. Interestingly, contrary to the usual resonant leptogenesis, which is achieved by $\mathcal{O}$(TeV) scale RHNs, here, we realize the resonant leptogenesis with a relatively higher RHN masses ($\gtrsim 10^6$ GeV), correlated with the Majoron DM in the sub-GeV range. This links the generation of dark matter to the baryon asymmetry of the Universe.

In Chapter 3, we delve into the phenomenology of ALPs, where two of the important aspects of BSM, the dark matter and baryon asymmetry of the Universe, are addressed. In the first part of this chapter, following a discussion of misalignment mechanism for dark matter ALPs, we scrutinize the cosmic evolution of such dark matter ALPs in the presence of an additional explicit global symmetry-breaking term involving SM Higgs doublet. As a result, ALP obtains an additional contribution to its mass as the Higgs field gets a *vev* during electroweak phase transition. This leads to an alteration of the oscillation frequencies during EWSB and consequently modifies the relic density in contrast to the standard misalignment mechanism. Such a modification turns out to be remarkable for the ALP-photon coupling vs ALP mass parameter space which is heavily constrained by astrophysics, various lab experiments, and cosmology as we obtain a comprehensive amount of allowed parameter space compared to the standard misalignment scenario. In the other part of this chapter, we turn our attention from DM to the generation of BAU via spontaneous leptogenesis, where the lepton asymmetry is generated by incorporating dynamic CPT-violating effects, led by derivative interaction of ALP with the $(B-L)$ current along with a $(B-L)$ breaking interaction remains in thermal equilibrium. Conventionally, the Weinberg operator is used as the $(B-L)$ breaking interaction, which is connected to neutrino mass and therefore, confines the leptogenesis at a very high temperature ($\gtrsim \mathcal{O}(10^{13})$ GeV). Aiming to bringing down the scale of spontaneous leptogenesis, we introduce an additional Weinberg-like dimension-5

operator, assisted by an IHD. Being unconstrained by the neutrino mass, it enables a much lower decoupling temperature of $(B-L)$ violating interactions, thereby reducing the scale of spontaneous leptogenesis and allowing a lower reheating temperature. We also explore the situation where ALP possesses an initial velocity, which enables a further reduction in the scale of leptogenesis, accommodating lighter ALPs in the keV-GeV regime that can be probed in collider and beam-dump experiments.

In Chapter 4, we explored a pivotal role of ALP as a mediator between a Dirac fermionic DM and the SM sector. To realize it, we consider the ALP-SM effective interactions at low energy and additionally include an ALP-DM interaction, respecting the ALP shift-symmetry. Considering a hierarchy where the decay of an ALP into two DM particles is kinematically allowed, we find that with substantially lower values of ALP decay constant, DM freeze-out is possible via annihilations into two photons, where both ALPs and DM can be considered initially in thermal equilibrium. However, the requirement of correct DM relic density and escaping the stringent indirect detection bounds at the same time turns out to be only possible in the near resonance region. The interesting consequence of this setup comes from the invisible decay of the ALP into two DM particles, which can lead to a promising missing energy signature in the collider. Therefore, we analyze such invisible decay of ALPs at electron-positron collider, focusing on mono-photon + missing energy final states considering initial beam polarization. It turns out that the ALP-photon coupling, which is important to reproduce the DM relic density, can also play a crucial role in segregating the signal and SM background via the missing energy variable. We further perform a χ^2 analysis, which shows that the ALP-photon coupling can be measured with about 1% precision under this setup.

To put in a nutshell, this thesis focuses on the phenomenology of two very well-known pNGBs, the Majoron and ALPs, addressing some of the key issues of particle physics and cosmology. Therefore, in an expected way, explicit symmetry breaking interactions (especially at higher orders) have played a major role across this thesis. To be specific, we demonstrated that such explicit breaking terms not only provide Goldstone bosons a light mass, but also make a substantial contribution in solving the key issues in several ways. For example, in chapter 2, dimension-5 explicit breaking terms open up new production channels for Majoron DM, and moreover, help to achieve a high-scale resonant leptogenesis by inducing a mass difference between the RHNs. In a similar way, in chapter 3, a dimension-6 $U(1)$ breaking operator results in an enlarged ALP DM parameter space and furthermore, the introduction of a dimension-5 lepton number violating operator helps in achieving a low-scale spontaneous leptogenesis scenario. Therefore, such explicit breaking terms can help in solving the SM shortcomings while maintaining the particle physics models minimal in terms of the additional fields. Finally, in chapter 4, we explore a direct way to probe the ALP-photon interaction in e^+e^- collider (correlated with a DM scenario) utilizing low-energy ALP effective field theory.

To conclude this thesis, we outline some of the possible aspects for future exploration, inspired by the works presented here. So far, Majoron DM has been connected to a high-scale resonant leptogenesis. However, an usual low-scale resonant leptogenesis (for RHNs with masses of $\mathcal{O}$(TeV) or less), correlated with Majoron DM would be more compelling

possibility from detection point of view. Additionally, connecting ALPs (or even QCD axions) with cosmological phase transition could be an exciting possibility, which might generate detectable gravitational waves, offering novel insights of early Universe dynamics. In analogy with the ALP–photon coupling, the Majoron-neutrino interaction, characterized by lepton number violation, can be explored in colliders, which can provide indirect insights into Majoron models. Furthermore, both Majorons and ALPs can leave distinct cosmological imprints, such as affecting the effective number of neutrino species, $N_{\rm eff}$, which is further linked to issues such as the Hubble tension. Thus, the light and feeble-interacting nature of the pNGBs make them highly attractive not only from theoretical standpoint but also from experimental perspectives. With more and more data from colliders, beam-dump, helioscopes as well as gravitational wave detectors, and future neutrino and dark matter search experiments to come, our understandings of the Universe and the role of pNGBs within it will be more transparent.

Appendices

Appendix A

Appendix related to chapter 2

A.1 Appendix related to scenario B

A.1.1 CP violating couplings

In this appendix, we discuss what happens if the CP symmetry is not conserved, in other words, unequal couplings of Φ and Φ^* in the Yukawa interaction of Eq. 2.41 are present. For example, one can make the Yukawa interaction of Eq. 2.41 non-uniform between Φ and Φ^* by considering an additional parameter α as

$$y_{\alpha 2}\overline{\ell_{L\alpha}}\widetilde{H}\mathcal{N}_2\frac{(\Phi+\alpha\Phi^*)}{\Lambda} \supset iy_{\alpha 2}\overline{\ell_{L\alpha}}\widetilde{H}\mathcal{N}_2\frac{(1-\alpha)}{\sqrt{2}\Lambda}\chi, \tag{A.1}$$

which induces additional Majoron production channel such as $\ell_L H \to N\chi$. However, the presence of the Yukawa coupling $y_{\alpha 2} \lesssim \mathcal{O}(1)$ in front along with $(1-\alpha) < 1$ suggests that this contribution would remain comparable or less compared to main production channel of Majoron $N_i N_i \to \chi\chi$.

On the other hand, the presence of α also enables Majoron to decay (hence, may cause instability) into two light neutrinos via active-sterile mixing. The corresponding decay width can be approximated as

$$\Gamma_{\chi\to\nu\nu} \approx \left[\frac{(1-\alpha)\, m_\nu}{\Lambda}\right]^2 \frac{m_\chi}{8\pi}, \tag{A.2}$$

which turns out to be suppressed compared to the similar decay of Majoron (already used to constrain the parameter space) as in Eq. 2.11, due to the additional suppression resulting from the appearance of $(1-\alpha)^2$ in numerator and Λ ($> v_\phi$) in the denominator. Hence, in nutshell, the CP symmetry considered for Φ seems useful in restricting Majorons not to communicate with the N_2 (via Yukawa interaction of dimension-5) and the SM lepton sector (first two terms of Eq. 2.41 as well).

A.1.2 Constraints on the parameter space satisfying both Majoron DM and resonant leptogenesis

It is interesting to explore the constraints from monochromatic neutrino search experiments, X-ray and gamma-rays observation on the parameter spaces in Fig. 2.14, which simultaneously satisfies correct relic density for Majoron DM and resonant leptogenesis. Following

the discussions as in subsection 2.2.4, here we show the sensitivity of the neutrino and γ-line searches on the parameter spaces we obtained in Fig. 2.14.

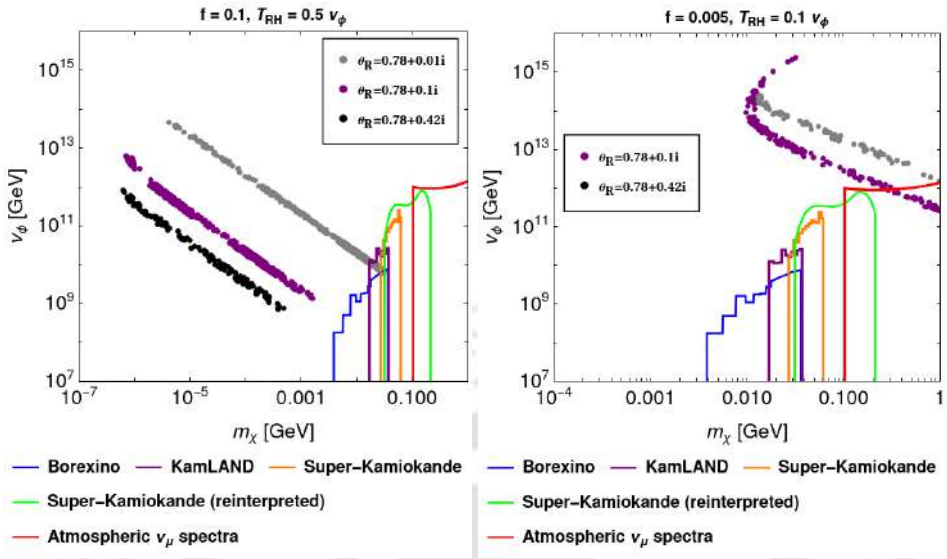

Figure A.1: Constraints from monochromatic various neutrino search experiments (as indicated in the figure) on DM and resonant leptogenesis satisfied parameter space in $m_\chi - v_\phi$ plane.

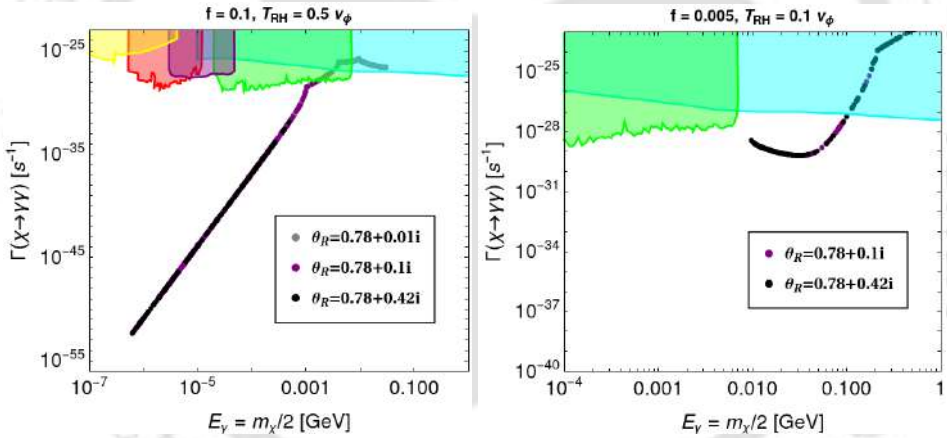

Figure A.2: γ-ray line emission constraints for DM and resonant leptogenesis satisfied parameter space in $(E_\gamma) - \Gamma_{\chi\to\gamma\gamma}$ plane. The colored regions indicate the range of different X-ray and γ-ray observations, e.g., COMPTEL/EGRET (cyan), INTEGRAL (green), HEAO (purple), XMM (red), Chandra (Yellow).

Similar to the correlation plot in Fig. 2.14, in Figs. A.1 and A.2, we consider the same values of θ_R for two benchmark choices of f and $T_{\rm RH}/v_\phi$. For $f = 0.1$ and $T_{\rm RH}/v_\phi = 0.5$, the left panel of Fig. A.1 demonstrates that neutrino-search experiments are sensitive for $m_\chi \gtrsim 20$ MeV for the gray colored parameter space only ($\theta_R = 0.78 + 0.01i$), while the region for other two choices of θ_R remains unconstrained. Similarly, the left panel of Fig. A.2 indicates that the parameter space involving $m_\chi \gtrsim \mathcal{O}(1)$ MeV falls within the exclusion limit of γ-ray emission lines for the choice of $\theta_R = 0.78{+}0.01i$ (gray) and $\theta_R = 0.78{+}0.1i$ (purple). However, for the line corresponding to $\theta_R = 0.78{+}0.42i$ (black) remains unconstrained from these observations. On the other hand, from the right panel of Fig. A.1 (for $f = 0.005$ and $T_{\rm RH}/v_\phi = 0.1$), one can observe that the region with $\theta_R = 0.78{+}0.1i$ (purple) falls within the sensitiveness of the neutrino experiments for $m_\chi \gtrsim 0.3$ MeV, and hence disallowed, while the

gray region ($\theta_R = 0.78 + 0.01i$) is almost unconstrained due to higher values of v_ϕ. Similarly, the right panel of Fig. A.2 illustrates that the parameter space involving $m_\chi \gtrsim \mathcal{O}(100)$ MeV is excluded by γ-ray observations for both choices of $\theta_R = 0.78 + 0.1i$ (purple) and $0.78 + 0.42i$ (black).

Appendix B

Appendix related to chapter 3

B.1 Appendix related to scenario A

B.1.1 Origin of dimension-6 operator

Here, we present a possible origin of dimension-6 global $U(1)$ symmetry breaking operator of our kind using the fact that any global symmetry is expected to be explicitly broken by gravity at $M_{\rm Pl}$ [248–251, 253]. For this purpose, we consider the following Lagrangian (relevant part only)

$$-\mathcal{L} \supset \mu\Phi^2 e^{i\alpha}\zeta + \frac{|H|^4\zeta^\dagger}{M_{\rm Pl}} + H.c.. \tag{B.1}$$

Here, Φ is our $U(1)$ symmetry breaking complex scalar field having charge $+1$ under $U(1)$ while ζ is a heavy (mass M_ζ) complex SM singlet scalar field carrying charge -2 such that the first term respects the $U(1)$ symmetry. The dimensionful coupling μ can naturally be of order $M_{\rm Pl}$. The second term being a dimension-5 operator can be thought of a soft symmetry breaking one resulting due to the explicit breaking of the $U(1)$ by gravity at $M_{\rm Pl}$. Considering the hierarchy of mass scales as: $M_\zeta < \mu = M_{\rm Pl}$, integrating out the heavy field ζ at energies below M_ζ results into the following dimension-6 term [473]

$$\frac{1}{M_\zeta^2}|H|^4\Phi^2 e^{i\alpha} + H.c.. \tag{B.2}$$

Identifying M_ζ with the scale Λ, we obtain the operator considered in our analysis. Note that such a construction would not allow any other dimension-6 operator such as $\frac{|H|^2}{\Lambda^2}\Phi^4 e^{i\alpha} + H.c.$ which could otherwise be present.

B.1.2 Phenomenology in presence of two dimension-6 operators

For completeness purpose, we will briefly discuss here how the phenomenology changes if we include the other possible dimension-6 operator ($i.e.$ without restricting to the possible origin of such operator as outlined in Appendix-B.1.1)

$$y\frac{|H|^2}{\Lambda^2}\Phi^4 e^{i\alpha} + H.c., \tag{B.3}$$

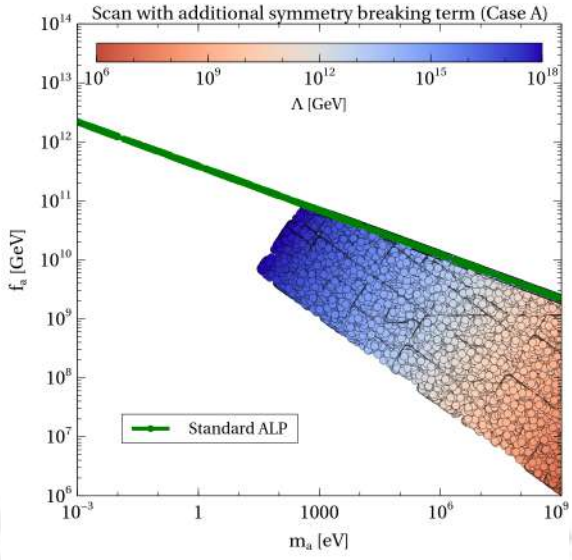

Figure B.1: DM parameter space satisfying correct DM relic density comparison between case A ($T^0_{\rm osc} \leq T_{\rm EW}$) and standard case in ($m_a - f_a$) plane in presence of two dimension-6 $U(1)$ breaking terms. Here, the variation of Λ is shown in the color bar and $y = 10^{-4}$ is employed.

where y is a dimensionless coupling. With both the explicit breaking terms present (via Eqs. 3.10 and B.3) and considering $\alpha = \pi$, ALP will acquire a bigger mass (in comparison to Eq. 3.14) after EWSB, without altering the potential minimum ($\theta_{\rm min} = 0$), as follows

$$m_a^2 = m_{a0}^2 + \frac{v^4}{\Lambda^2} + \frac{4y f_a^2 v^2}{\Lambda^2}. \tag{B.4}$$

Apart from inducing a sizeable contribution to the final mass of ALP, the new term (Eq. B.3) also allows a dominant production of ALPs through decay (and annihilation) of the Higgs field after EWSB. As a result, a possible freeze-in production of ALPs remains viable in addition to the production through misalignment mechanism. Such a possibility although prevails with the other dimension-6 operator (we comment on this in the conclusion section), here with the additional one via Eq. B.3, the freeze-in of ALP may proceed with larger coupling strength (between two ALPs and the Higgs field) proportional to $v f_a^2/\Lambda^2$, in contrary to the other case (with Eq. 3.10 only), where f_a was replaced by the Higgs *vev* v ($f_a \gg v$). Hence, freeze-in can be significantly enhanced by inclusion of the operator in Eq. B.3. Additionally, it may lead to the possibility of ALP thermalisation if $v f_a^2/\Lambda^2$ happens to be of order $\mathcal{O}(10^{-6})$ or more. To alleviate such possibilities, we find that restricting y by $y \lesssim \mathcal{O}(10^{-4})$, ALP can favourably be produced through misalignment mechanism only.

Therefore, considering the presence of both the dimension-6 operators with $y \lesssim \mathcal{O}(10^{-4})$, we showcase the relic allowed parameter space in Fig. B.1. Here $m_{a0} > \mathcal{O}(10^{-13})$ GeV is taken so that the conventional ALP oscillation starts prior to EWSB. As the operator of Eq. B.3 adds a substantial contribution to ALP mass via Eq. B.4, a lower value of f_a is required to achieve the correct relic density as evident from Eq. 3.21, which is also observed in Fig. B.1. We notice that with the choice of $y = 10^{-4}$, the relic allowed parameter space is shifted beyond $m_a \gtrsim \mathcal{O}(100)$ eV, where the leftmost boundary is dictated by the choice of $\Lambda < M_{\rm Pl}$. Hence it turns out that after imposing all the relevant cosmological and astrophysical bounds

(as outlined in section 3.2.3), only a tiny fraction of the parameter space remains viable to achieve the correct relic density through misalignment mechanism in this case.

B.1.3 Transition of ALP mass across EWSB

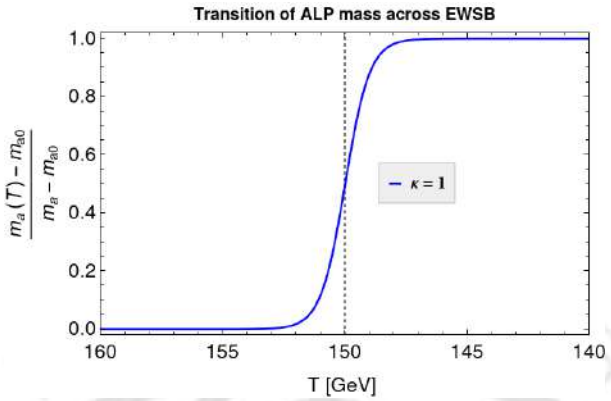

Figure B.2: Transition of ALP mass across $T_{\rm EW} = 150$ GeV with $\kappa = 1$. The dashed gray gridline corresponds to $T = T_{\rm EW}$.

In connecting the evolution of the ALP field θ across $T_{\rm EW}$, an apparent discontinuity is felt due to the sudden change in the mass of ALP: from m_{a0} at $T < T_{\rm EW}$ to m_a at $T = T_{\rm EW}$ (representative of a step function at $T_{\rm EW}$). To retain the continuity of the ALP field while passing through the EWPT, we propose to make the transition of m_{a0} to m_a a smooth one by introducing logistic function for the mass $m_a(T)$ [474] defined as

$$m_a(T) = m_{a0} + \frac{m_a(T) - m_{a0}}{1 + e^{-2\kappa(T_{\rm EW}-T)}}, \tag{B.5}$$

across $T = T_{\rm EW}$. Here, κ is a parameter which controls the abruptness involved in the transition (a large κ indicates a more sharper transition). Since the EWPT happens within a finite range of temperature ΔT, such an approximation is justified provided the the change of ALP mass extends over that period ΔT. A schematic presentation of such an approximation is exhibited in Fig. B.2 with $\kappa = 1$ is employed. This is for the illustration purpose in case one tries to track the evolution of the θ field via Eq. 3.17. While evaluating the energy density of the ALP field, we use the sudden approximation in line with Eq. 3.18.

B.2 Appendix related to scenario B

B.2.1 Relationship among chemical potentials in presence of IHD

Here, we proceed to evaluate first the effective chemical potential μ_{B-L} contributing toward the equilibrium number density of $B - L$ charges $n^{\rm eq}_{B-L}$ in presence of the inert Higgs doublet (IHD) in section B.2.1. Although the basic prescription can be found in [364, 384], the inclusion of IHD would alter the final result.

During the evolution of the Universe, fundamental particles participating in an interaction (say, $i + j + ... \leftrightarrow a + b + ..$) remains in chemical equilibrium as long as the respective interaction rate becomes comparable to the Hubble expansion rate of the Universe. When in

equilibrium, the associated chemical potentials of the participating particles would follow a relation

$$\mu_i + \mu_j + ... + \mu_a + \mu_b + ... = 0. \tag{B.6}$$

As a consequence, one can have inter-relations among chemical potentials of different particles leading to an estimate for μ_{B-L} as discussed below.

- The gauge interactions come into equilibrium at very early Universe where the electroweak symmetry remain unbroken. In this unbroken phase, the gauge bosons remain massless leading to vanishing chemical potentials, $\mu_B = \mu_W = \mu_g = 0$. As a consequence, the components of the electroweak and color multiplets will have the same chemical potentials i.e. $\mu_q \equiv \mu_{u_L} = \mu_{d_L}$, $\mu_l \equiv \mu_{\nu_L} = \mu_{e_L}$, and $\mu_H \equiv \mu_{H^+} = \mu_{H^0}$. Similarly, the chemical potential of the additional IHD also follows $\mu_\Phi \equiv \mu_{\Phi^+} = \mu_{\Phi^0}$.
- IHD being a scalar, has self interactions (consistent with its Z_2 odd property for being a dark matter candidate) as well as portal interactions with the Standard Model (SM) Higgs doublet [121, 393, 394]. One such term in these portal interactions is $\lambda(\Phi^\dagger H)^2$ whose chemical equilibration leads to $\mu_\Phi = \mu_H$. As a consequence, the hypercharge neutrality condition takes the form

  $$\mu_q + 2\mu_u - \mu_d - \mu_l - \mu_E + \frac{4}{N_f}\mu_H = 0, \tag{B.7}$$

  where $\mu_{u,d(E)}$ are the chemical potential of the SM singlet right handed quarks (leptons). Here N_f (=3 in SM) represents the number of generations of the quarks and leptons.
- Since we include a low reheating temperature ($T_{\rm RH} \ll 10^{12}$ GeV) in the study, all N_f generations of Yukawa interactions are considered to be in equilibrium[1]. This leads to the following relations

  $$\mu_u = \mu_q + \mu_H, \qquad \mu_d = \mu_q - \mu_H, \qquad \mu_E = \mu_l - \mu_H. \tag{B.8}$$

- At $T \lesssim 10^{12}$ GeV, electroweak (EW) sphalerons enter in thermal equilibrium [388], enforcing $3\mu_q + \mu_l = 0$. This is going to be modified in presence of CPT violating interactions as discussed below.

In our framework, the CPT violating interaction of the form $\frac{c_X}{f_a}\partial_\mu a J^\mu_X$ (in a time dependent and homogeneous ALP background) induces [384] an additional effective chemical potential $\bar{\mu}_{\rm ws}$ to the chemical potential relation describing the EW-sphaleron process, originated from chiral anomaly, given by

$$3\mu_q + \mu_l = -\bar{\mu}_{\rm ws}. \tag{B.9}$$

Furthermore, the same CPT violation also modifies the chemical potential relation associ-

[1]For an extended reheating phase, see [321, 322] for details.

ated to the $B-L$ violating operator $\ell_L\ell_L\Phi\Phi/\Lambda$ (when in equilibrium) as [384]:

$$\mu_l + \mu_\phi = \mu_l + \mu_H = -\bar{\mu}_\ell. \tag{B.10}$$

Given all the SM leptons and baryons are in thermal and chemical equilibria, $n^{\rm eq}_{B-L}$ can then be calculated from $n^{\rm eq}_{B-L} = \mu_{B-L}T^2/6$, where μ_{B-L} takes the form

$$\mu_{B-L} = \mu_B - \mu_L = (2\mu_q + \mu_u + \mu_d)N_f - (2\mu_l + \mu_E)N_f \tag{B.11}$$

$$= N_f\left(-\frac{4}{3}\bar{\mu}_{\rm ws} + \frac{13}{3}\bar{\mu}_\ell + \frac{16}{3}\mu_H\right), \tag{B.12}$$

obtained by employing Eqs. (B.8)-(B.10). Finally, rewriting μ_H in terms of $\bar{\mu}_{\rm ws}$ and $\bar{\mu}_\ell$ through Eq. (B.7), we obtain the equilibrium μ_{B-L} in terms of $\bar{\mu}_{\rm ws}$ and $\bar{\mu}_\ell$ as

$$\mu_{B-L} = -\frac{4N_f(1+N_f)}{3+5N_f}\bar{\mu}_{\rm ws} + \frac{N_f(11N_f-13)}{(3+5N_f)}\bar{\mu}_\ell. \tag{B.13}$$

However, as shown in [384], with proper rotations on the quarks and leptons, we can transform the basis to $\{\bar{\mu}_{\rm ws}, \bar{\mu}_\ell\} \to \{\delta_{\rm ws}, 0\}$ with $\delta_{\rm ws} = \dot{\theta}$, the non-zero ALP velocity [364]. In the new basis, μ_{B-L} can be re-written as

$$\mu_{B-L} = \frac{4N_f(1+N_f)}{3+5N_f}\delta_{\rm ws}. \tag{B.14}$$

B.2.2 Construction of the Boltzmann equation

The modified Boltzmann equation relevant for the $B-L$ asymmetry evolution is constructed here. To study the evolution of the produced $B-L$ asymmetry across the decoupling of $B-L$ violating interaction (associated to $\ell_L\ell_L\Phi\Phi/\Lambda$), a Boltzmann equation for n_{B-L} can be constructed having the following form,

$$\dot{n}_{B-L} + 3\mathcal{H}n_{B-L} = \frac{\gamma_{\not L}}{T}\sum_{i,j=3}(\mu_{l_i} + \mu_{l_j} + 2\mu_H) = 18\frac{\gamma_{\not L}}{T}(\mu_l + \mu_H), \tag{B.15}$$

assuming flavour-universal interaction rate density $\gamma_{\not L}$ for different leptons. In the r.h.s of the Boltzmann equation, μ_l and μ_H can be expressed in terms of n_B and n_L as

$$\mu_l = \frac{24(1+N_f)n_L - 3N_f n_B}{2N_f(6+5N_f)T^2}, \tag{B.16}$$

$$\mu_H = \frac{12n_L - 9n_B}{2(6+5N_f)T^2}. \tag{B.17}$$

The n_B and n_L can be further related to the chemical potential of the weak sphaleron δ_{ws} and n_{B-L} by employing Eqs. (B.7)-(B.10) and can be denoted as

$$n_B = \frac{T^2}{6}4N_f\mu_q = \frac{12(1+N_f)n_{B-L} - \delta_{\rm ws}T^2N_f(6+5N_f)}{39+33N_f}; \tag{B.18}$$

$$n_L = \frac{T^2}{6}N_f(2\mu_l + \mu_E) = -\frac{3(9+7N_f)n_{B-L} + \delta_{\rm ws}T^2N_f(6+5N_f)}{39+33N_f}. \tag{B.19}$$

Finally, substituting Eqs. (B.18) and (B.19) in both the Eqs. (B.16) and (B.17), we obtain the final form of the Boltzmann equation as

$$\dot{n}_{B-L} + 3\mathcal{H}n_{B-L} = -18\frac{6(3+5N_f)}{N_f(13+11N_f)}\frac{\gamma_{\not L}}{T^3}\left[n_{B-L} + \frac{4N_f(1+N_f)}{6(3+5N_f)}\delta_{\rm ws}T^2\right], \tag{B.20}$$

$$= -\Gamma^{\Phi}_{\not L}(n_{B-L} - n^{\rm eq}_{B-L}), \tag{B.21}$$

where $\Gamma^{\Phi}_{\not L}$ is given by,

$$\Gamma^{\Phi}_{\not L} = 18\frac{6(3+5N_f)}{N_f(13+11N_f)}\frac{\gamma_{\not L}}{T^3}. \tag{B.22}$$

Note that with $N_f = 3$, Eqs. (B.14) and (B.22) become $\mu_{B-L} = -\frac{8}{3}\dot{\theta}$ and $\Gamma^{\Phi}_{\not L} = \frac{324}{23}\frac{\gamma_{\not L}}{T^3} \simeq \frac{324}{23}\frac{6T^3}{8\pi^3\Lambda^2}$ respectively, which we used in our analysis.

Appendix C

Appendix related to chapter 4

C.1 UV Completion of ALP-DM Coupling Without ALP-SM Fermion Interactions

Here, we outline a minimal UV-complete model where ALP couples to a Dirac fermionic DM, while remaining decoupled from the SM fermions. To do so, we consider a global axial $U(1)$ symmetry that is spontaneously broken at a scale f_a by the *vev* of a complex scalar field Φ, which can be parameterized as

$$\Phi = \frac{1}{\sqrt{2}}(f_a + \rho)e^{ia/f_a} \tag{C.1}$$

where ρ is the massive radial degree of freedom and a is the ALP, which emerges as the pNGB of the broken symmetry. We also consider a Dirac fermionic DM candidate Ψ and heavy vector like fermions (VLF) Q, which are charged under $U(1)$ symmetry and transform as

$$\Phi \to e^{i\alpha}\Phi, \quad \Psi \to e^{i(\alpha/2)\gamma_5}\Psi, \quad Q \to e^{i(\alpha/2)\gamma_5}Q. \tag{C.2}$$

Here, we further consider the VLFs (Q) to be charged under the SM electroweak symmetry as well. Importantly, the SM fermions are assumed to be singlets under $U(1)$, and thus do not couple directly to the ALP. Therefore, the relevant UV Lagrangian for the $U(1)$ sector is

$$\mathcal{L} \supset |\partial_\mu \Phi|^2 - V(\Phi) + \overline{\Psi} i\partial\!\!\!/ \Psi + \bar{Q} i\partial\!\!\!/ Q + (y_\Psi \Phi \overline{\Psi}_L \Psi_R + y_Q \Phi \overline{Q}_L Q_R + H.c.) \tag{C.3}$$

where, $y_Q(\sim \mathcal{O}(1)) \gg y_\Psi$ is assumed. After the spontaneous symmetry breaking, $\langle\Phi\rangle = f_a/\sqrt{2}$, the Lagrangian provides

$$\mathcal{L} \supset -m_\Psi \overline{\Psi}_L \Psi_R e^{ia/f_a}, \tag{C.4}$$

where, $m_\Psi = y_\Psi f_a/\sqrt{2}$. The e^{ia/f_a} in Eq. C.4 can be removed via a field redefinition such as

$$\Psi \to \Psi e^{i\gamma_5 a/(2f_a)}. \tag{C.5}$$

Such field redefinition in turn generates the standard ALP-DM interaction once we invoke Eq. C.5 into the DM kinetic term in Eq. C.3, which yields

$$\mathcal{L} = -\frac{1}{2f_a}\partial_\mu a \overline{\Psi}\gamma^\mu\gamma_5\Psi, \tag{C.6}$$

where the shift-symmetry of ALP is maintained. This is the standard derivative coupling expected for pseudo-Goldstone bosons. Also, by expanding the e^{ia/f_a} in Eq. C.4, one can get an alternate ALP-DM interaction term as

$$\mathcal{L} = -i\frac{m_\Psi}{f_a} a \overline{\Psi}\gamma_5\Psi, \tag{C.7}$$

which is, however, not a shift symmetric term for ALP. Similarly, the heavy exotic quarks will also obtain a mass as $m_Q = y_Q f_a/\sqrt{2}$. However, as Q fields are also charged under the SM electroweak symmetry, a similar field redefinition on Q such as in Eq. C.5 generates effective ALP couplings to the SM electroweak gauge bosons through the axial anomaly. Therefore, at energies well below f_a, the effective interactions of ALPs can be generated as written in Eq. 4.3 where these exotic quarks appear as the intermediate states. On the other hand, ALP-SM fermion couplings do not appear in the scenario as the SM fermion fields do not couple to Φ and carry no $U(1)$ charge. This setup, resembling the KSVZ model [164,165] in the context of QCD axion, allows for ALP-mediated dark matter interactions and anomaly induced couplings relevant for astrophysical and cosmological probes, while maintaining consistence with flavor and collider bounds.

C.2 Differential cross-section

Associate productions of ALPs are an important mechanism for phenomenological studies. The relevant Feynman diagram is shown in Fig. 4.3. The amplitude of the process $e^+(p_2)e^-(p_1) \to \gamma(k_2)a(k_1)$ is given by

$$\mathcal{M} = \frac{e_0 g_{a\gamma\gamma}}{4s}\bar{v}(p_2)\gamma^\mu u(p_1)\epsilon_{\mu\nu\rho\sigma}k^\rho q^\sigma \epsilon^{*\nu}(k) \tag{C.8}$$

with $q = (p_1 + p_2)$ and $k = (q - k_1)$. e_0 denotes the $U(1)_{\rm EM}$ charge and $\epsilon_{\mu\nu\rho\sigma}$ is the anti-symmetric tensor. The differential cross section for ALPs produced in association with a γ is given by

$$\frac{d\sigma(e^+e^- \to \gamma a)}{d\Omega} = \frac{\alpha}{64}g^2_{a\gamma\gamma}\left(1 - \frac{m_a^2}{s}\right)^3\left(1 + \cos^2\theta\right), \tag{C.9}$$

where $\alpha = e_0^2/4\pi$ is the fine structure constant.

Bibliography

[1] E. S. Abers and B. W. Lee, "Gauge Theories," *Phys. Rept.* **9** (1973) 1–141.

[2] J. E. Kim, P. Langacker, M. Levine, and H. H. Williams, "A Theoretical and Experimental Review of the Weak Neutral Current: A Determination of Its Structure and Limits on Deviations from the Minimal SU(2)-L x U(1) Electroweak Theory," *Rev. Mod. Phys.* **53** (1981) 211.

[3] P. Aurenche, "The Standard model of particle physics," in *Cinquieme Seminaire Rhodanien, Symetries en Physique*. 7, 1997. arXiv:hep-ph/9712342.

[4] M. K. Gaillard, P. D. Grannis, and F. J. Sciulli, "The Standard model of particle physics," *Rev. Mod. Phys.* **71** (1999) S96–S111, arXiv:hep-ph/9812285.

[5] M. Herrero, "The Standard model," *NATO Sci. Ser. C* **534** (1999) 1–59, arXiv:hep-ph/9812242.

[6] G. ALTARELLI, "The Standard model of particle physics," arXiv:hep-ph/0510281.

[7] J. Iliopoulos, "Introduction to the Standard Model of the Electro-Weak Interactions," in *8th CERN–Latin-American School of High-Energy Physics*. 5, 2013. arXiv:1305.6779 [hep-ph].

[8] **ATLAS** Collaboration, M. Aaboud *et al.*, "Measurements of Higgs boson properties in the diphoton decay channel with 36 fb^{-1} of pp collision data at $\sqrt{s} = 13$ TeV with the ATLAS detector," *Phys. Rev.* **D98** (2018) 052005, arXiv:1802.04146 [hep-ex].

[9] **CMS** Collaboration, A. M. Sirunyan *et al.*, "Combined measurements of Higgs boson couplings in proton–proton collisions at $\sqrt{s} = 13$ TeV," *Eur. Phys. J.* **C79** (2019) no. 5, 421, arXiv:1809.10733 [hep-ex].

[10] **Particle Data Group** Collaboration, P. A. Zyla *et al.*, "Review of Particle Physics," *PTEP* **2020** (2020) no. 8, 083C01.

[11] F. Englert and R. Brout, "Broken Symmetry and the Mass of Gauge Vector Mesons," *Phys. Rev. Lett.* **13** (1964) 321–323.

[12] P. W. Higgs, "Broken Symmetries and the Masses of Gauge Bosons," *Phys. Rev. Lett.* **13** (1964) 508–509.

[13] G. S. Guralnik, C. R. Hagen, and T. W. B. Kibble, "Global Conservation Laws and Massless Particles," *Phys. Rev. Lett.* **13** (1964) 585–587.

[14] N. Cabibbo, "Unitary Symmetry and Leptonic Decays," *Phys. Rev. Lett.* **10** (1963) 531–533.

[15] M. Kobayashi and T. Maskawa, "CP Violation in the Renormalizable Theory of Weak Interaction," *Prog. Theor. Phys.* **49** (1973) 652–657.

[16] **Particle Data Group** Collaboration, R. L. Workman *et al.*, "Review of Particle Physics," *PTEP* **2022** (2022) 083C01.

[17] **UA1** Collaboration, G. Arnison *et al.*, "Experimental Observation of Isolated Large Transverse Energy Electrons with Associated Missing Energy at $\sqrt{s} = 540$ GeV," *Phys. Lett. B* **122** (1983) 103–116.

[18] **UA2** Collaboration, M. Banner *et al.*, "Observation of Single Isolated Electrons of High Transverse Momentum in Events with Missing Transverse Energy at the CERN anti-p p Collider," *Phys. Lett. B* **122** (1983) 476–485.

[19] **UA1** Collaboration, G. Arnison *et al.*, "Experimental Observation of Lepton Pairs of Invariant Mass Around 95-GeV/c**2 at the CERN SPS Collider," *Phys. Lett. B* **126** (1983) 398–410.

[20] **UA2** Collaboration, P. Bagnaia *et al.*, "Evidence for $Z^0 \to e^+e^-$ at the CERN $\bar{p}p$ Collider," *Phys. Lett. B* **129** (1983) 130–140.

[21] S. Myers and E. Picasso, "The Design, construction and commissioning of the CERN Large Electron Positron collider," *Contemp. Phys.* **31** (1990) 387–403.

[22] D. Brandt, H. Burkhardt, M. Lamont, S. Myers, and J. Wenninger, "Accelerator physics at LEP," *Rept. Prog. Phys.* **63** (2000) 939–1000.

[23] **ALEPH, DELPHI, L3, OPAL, SLD, LEP Electroweak Working Group, SLD Electroweak Group, SLD Heavy Flavour Group** Collaboration, S. Schael *et al.*, "Precision electroweak measurements on the Z resonance," *Phys. Rept.* **427** (2006) 257–454, arXiv:hep-ex/0509008.

[24] **Particle Data Group** Collaboration, P. A. Zyla *et al.*, "Review of Particle Physics," *PTEP* **2020** (2020) no. 8, 083C01.

[25] **Tevatron Electroweak Working Group** Collaboration, "Combination of CDF and D0 Results on the Width of the W boson," arXiv:1003.2826 [hep-ex].

[26] **ALEPH, DELPHI, L3, OPAL, LEP Electroweak** Collaboration, S. Schael *et al.*, "Electroweak Measurements in Electron-Positron Collisions at W-Boson-Pair Energies at LEP," *Phys. Rept.* **532** (2013) 119–244, arXiv:1302.3415 [hep-ex].

[27] **ATLAS, CDF, CMS, D0** Collaboration, "First combination of Tevatron and LHC measurements of the top-quark mass," arXiv:1403.4427 [hep-ex].

[28] **CDF, D0** Collaboration, "Combination of CDF and D0 Results on the Mass of the Top Quark," arXiv:0903.2503 [hep-ex].

[29] **Tevatron Electroweak Working Group, CDF, D0** Collaboration, T. A. Aaltonen, "Combination of CDF and DO Results on the Mass of the Top Quark Using up to 8.7 fb^{-1} at the Tevatron," arXiv:1305.3929 [hep-ex].

[30] **ATLAS** Collaboration, G. Aad *et al.*, "Observation of a new particle in the search for the Standard Model Higgs boson with the ATLAS detector at the LHC," *Phys. Lett. B* **716** (2012) 1–29, arXiv:1207.7214 [hep-ex].

[31] **CMS** Collaboration, S. Chatrchyan *et al.*, "Observation of a New Boson at a Mass of 125 GeV with the CMS Experiment at the LHC," *Phys. Lett. B* **716** (2012) 30–61, arXiv:1207.7235 [hep-ex].

[32] **CMS** Collaboration, S. Chatrchyan *et al.*, "Observation of a New Boson with Mass Near 125 GeV in pp Collisions at $\sqrt{s} = 7$ and 8 TeV," *JHEP* **06** (2013) 081, arXiv:1303.4571 [hep-ex].

[33] T. van Ritbergen and R. G. Stuart, "Complete two loop quantum electrodynamic contributions to the muon lifetime in the Fermi model," *Phys. Rev. Lett.* **82** (1999) 488–491, arXiv:hep-ph/9808283.

[34] **CMS** Collaboration, A. M. Sirunyan *et al.*, "Combined measurements of Higgs boson couplings in proton–proton collisions at $\sqrt{s} = 13$ TeV," *Eur. Phys. J. C* **79** (2019) no. 5, 421, arXiv:1809.10733 [hep-ex].

[35] K. Begeman, A. Broeils, and R. Sanders, "Extended rotation curves of spiral galaxies: Dark haloes and modified dynamics," *Mon. Not. Roy. Astron. Soc.* **249** (1991) 523.

[36] D. Clowe, M. Bradac, A. H. Gonzalez, M. Markevitch, S. W. Randall, C. Jones, and D. Zaritsky, "A direct empirical proof of the existence of dark matter," *Astrophys. J. Lett.* **648** (2006) L109–L113, arXiv:astro-ph/0608407.

[37] W. H. Julian, "On the Effect of Interstellar Material on Stellar Non-Circular Velocities in Disk Galaxies," *Astrophys. J.* **148** (1967) 175.

[38] **SDSS** Collaboration, M. Tegmark *et al.*, "Cosmological parameters from SDSS and WMAP," *Phys. Rev. D* **69** (2004) 103501, arXiv:astro-ph/0310723.

[39] **Super-Kamiokande** Collaboration, Y. Fukuda *et al.*, "Evidence for oscillation of atmospheric neutrinos," *Phys. Rev. Lett.* **81** (1998) 1562–1567, arXiv:hep-ex/9807003.

[40] **SNO** Collaboration, Q. R. Ahmad *et al.*, "Measurement of the rate of $\nu_e + d \to p + p + e^-$ interactions produced by ^{8}B solar neutrinos at the Sudbury Neutrino Observatory," *Phys. Rev. Lett.* **87** (2001) 071301, arXiv:nucl-ex/0106015.

[41] A. Riotto and M. Trodden, "Recent progress in baryogenesis," *Ann. Rev. Nucl. Part. Sci.* **49** (1999) 35–75, arXiv:hep-ph/9901362.

[42] M. Dine and A. Kusenko, "The Origin of the matter - antimatter asymmetry," *Rev. Mod. Phys.* **76** (2003) 1, arXiv:hep-ph/0303065.

[43] M. Fukugita and T. Yanagida, "Baryogenesis Without Grand Unification," *Phys. Lett. B* **174** (1986) 45–47.

[44] W. Buchmuller, P. Di Bari, and M. Plumacher, "Leptogenesis for pedestrians," *Annals Phys.* **315** (2005) 305–351, arXiv:hep-ph/0401240.

[45] A. Anisimov, S. Blanchet, and P. Di Bari, "Viability of Dirac phase leptogenesis," *JCAP* **04** (2008) 033, arXiv:0707.3024 [hep-ph].

[46] S. Davidson, E. Nardi, and Y. Nir, "Leptogenesis," *Phys. Rept.* **466** (2008) 105–177, arXiv:0802.2962 [hep-ph].

[47] W. Buchmuller, R. Peccei, and T. Yanagida, "Leptogenesis as the origin of matter," *Ann. Rev. Nucl. Part. Sci.* **55** (2005) 311–355, arXiv:hep-ph/0502169.

[48] E. W. Kolb and M. S. Turner, *The Early Universe*, vol. 69. Taylor and Francis, 5, 2019.

[49] S. Dodelson, *Modern Cosmology*. Academic Press, Amsterdam, 2003.

[50] **WMAP** Collaboration, E. Komatsu *et al.*, "Seven-Year Wilkinson Microwave Anisotropy Probe (WMAP) Observations: Cosmological Interpretation," *Astrophys. J. Suppl.* **192** (2011) 18, arXiv:1001.4538 [astro-ph.CO].

[51] **Particle Data Group** Collaboration, K. Nakamura *et al.*, "Review of particle physics," *J. Phys. G* **37** (2010) 075021.

[52] C. Grupen, *Astroparticle physics*. 2005.

[53] R. D. Peccei and H. R. Quinn, "CP Conservation in the Presence of Instantons," *Phys. Rev. Lett.* **38** (1977) 1440–1443.

[54] R. D. Peccei and H. R. Quinn, "Constraints Imposed by CP Conservation in the Presence of Instantons," *Phys. Rev. D* **16** (1977) 1791–1797.

[55] S. Weinberg, "A New Light Boson?," *Phys. Rev. Lett.* **40** (1978) 223–226.

[56] F. Wilczek, "Problem of Strong P and T Invariance in the Presence of Instantons," *Phys. Rev. Lett.* **40** (1978) 279–282.

[57] G. 't Hooft, "Naturalness, chiral symmetry, and spontaneous chiral symmetry breaking," *NATO Sci. Ser. B* **59** (1980) 135–157.

[58] J. A. Casas, J. R. Espinosa, and M. Quiros, "Improved Higgs mass stability bound in the standard model and implications for supersymmetry," *Phys. Lett. B* **342** (1995) 171–179, arXiv:hep-ph/9409458.

[59] G. Isidori, G. Ridolfi, and A. Strumia, "On the metastability of the standard model vacuum," *Nucl. Phys.* **B609** (2001) 387–409, arXiv:hep-ph/0104016 [hep-ph].

[60] R. H. Brandenberger, "Introduction to Early Universe Cosmology," *PoS* **ICFI2010** (2010) 001, arXiv:1103.2271 [astro-ph.CO].

[61] D. Baumann, *Cosmology*. Cambridge University Press, 2022.

[62] A. G. Riess, W. Yuan, L. M. Macri, D. Scolnic, D. Brout, S. Casertano, D. O. Jones, Y. Murakami, G. S. Anand, L. Breuval, *et al.*, "A comprehensive measurement of the local value of the hubble constant with 1 km s- 1 mpc- 1 uncertainty from the hubble space telescope and the sh0es team," *The Astrophysical journal letters* **934** (2022) no. 1, L7.

[63] **Planck** Collaboration, N. Aghanim *et al.*, "Planck 2018 results. VI. Cosmological parameters," *Astron. Astrophys.* **641** (2020) A6, arXiv:1807.06209 [astro-ph.CO]. [Erratum: Astron.Astrophys. 652, C4 (2021)].

[64] E. Di Valentino, O. Mena, S. Pan, L. Visinelli, W. Yang, A. Melchiorri, D. F. Mota, A. G. Riess, and J. Silk, "In the realm of the Hubble tension—a review of solutions," *Class. Quant. Grav.* **38** (2021) no. 15, 153001, arXiv:2103.01183 [astro-ph.CO].

[65] B. Wallisch, *Review of Modern Cosmology*, pp. 9–47. Springer International Publishing, Cham, 2019. https://doi.org/10.1007/978-$\widetilde{b}$3-$\widetilde{b}$030-$\widetilde{b}$31098-$\widetilde{b}1_2$.

[66] **Planck** Collaboration, N. Aghanim *et al.*, "Planck 2018 results. VI. Cosmological parameters," *Astron. Astrophys.* **641** (2020) A6, arXiv:1807.06209 [astro-ph.CO].

[67] F. Zwicky, "Die Rotverschiebung von extragalaktischen Nebeln," *Helv. Phys. Acta* **6** (1933) 110–127. [Gen. Rel. Grav.41,207(2009)].

[68] V. C. Rubin and W. K. Ford, Jr., "Rotation of the Andromeda Nebula from a Spectroscopic Survey of Emission Regions," *Astrophys. J.* **159** (1970) 379–403.

[69] A. Bergmann, V. Petrosian, and R. Lynds, "Gravitational lens models of arcs in clusters,"*ApJ* **350** (03, 1990) .

[70] **Planck** Collaboration, N. Aghanim *et al.*, "Planck 2018 results. I. Overview and the cosmological legacy of Planck," *Astron. Astrophys.* **641** (2020) A1, arXiv:1807.06205 [astro-ph.CO].

[71] A. A. Penzias and R. W. Wilson, "A Measurement of excess antenna temperature at 4080-Mc/s," *Astrophys. J.* **142** (1965) 419–421.

[72] G. Steigman and M. S. Turner, "Cosmological Constraints on the Properties of Weakly Interacting Massive Particles," *Nucl. Phys. B* **253** (1985) 375–386.

[73] K. A. Olive, "TASI lectures on dark matter," in *Theoretical Advanced Study Institute in Elementary Particle Physics (TASI 2002): Particle Physics and Cosmology: The Quest for Physics Beyond the Standard Model(s)*. 1, 2003. arXiv:astro-ph/0301505.

[74] D. Hooper, "Particle Dark Matter," in *Theoretical Advanced Study Institute in Elementary Particle Physics: The Dawn of the LHC Era*. 1, 2009. arXiv:0901.4090 [hep-ph].

[75] K. Garrett and G. Duda, "Dark Matter: A Primer," *Adv. Astron.* **2011** (2011) 968283, arXiv:1006.2483 [hep-ph].

[76] G. B. Gelmini, "The Hunt for Dark Matter," in *Theoretical Advanced Study Institute in Elementary Particle Physics: Journeys Through the Precision Frontier: Amplitudes for Colliders*. 2, 2015. arXiv:1502.01320 [hep-ph].

[77] M. Lisanti, "Lectures on Dark Matter Physics," in *Theoretical Advanced Study Institute in Elementary Particle Physics: New Frontiers in Fields and Strings*. 3, 2016. arXiv:1603.03797 [hep-ph].

[78] M. Bauer and T. Plehn, *Yet Another Introduction to Dark Matter: The Particle Physics Approach*, vol. 959 of *Lecture Notes in Physics*. Springer, 2019. arXiv:1705.01987 [hep-ph].

[79] P. Gondolo and G. Gelmini, "Cosmic abundances of stable particles: Improved analysis," *Nucl. Phys. B* **360** (1991) 145–179.

[80] J. Edsjo and P. Gondolo, "Neutralino relic density including coannihilations," *Phys. Rev. D* **56** (1997) 1879–1894, arXiv:hep-ph/9704361.

[81] F. Couchot, S. Henrot-Versillé, O. Perdereau, S. Plaszczynski, B. Rouillé d'Orfeuil, M. Spinelli, and M. Tristram, "Cosmological constraints on the neutrino mass including systematic uncertainties," *Astron. Astrophys.* **606** (2017) A104, arXiv:1703.10829 [astro-ph.CO].

[82] S. Giagu, "WIMP Dark Matter Searches With the ATLAS Detector at the LHC," *Front. in Phys.* **7** (2019) 75.

[83] **LUX** Collaboration, D. S. Akerib *et al.*, "Results from a search for dark matter in the complete LUX exposure," *Phys. Rev. Lett.* **118** (2017) no. 2, 021303, arXiv:1608.07648 [astro-ph.CO].

[84] E. Aprile *et al.*, "Dark Matter Search Results from a One Tonne×Year Exposure of XENON1T," arXiv:1805.12562 [astro-ph.CO].

[85] **PandaX-II** Collaboration, A. Tan *et al.*, "Dark Matter Results from First 98.7 Days of Data from the PandaX-II Experiment," *Phys. Rev. Lett.* **117** (2016) no. 12, 121303, arXiv:1607.07400 [hep-ex].

[86] **PandaX-II** Collaboration, X. Cui *et al.*, "Dark Matter Results From 54-Ton-Day Exposure of PandaX-II Experiment," arXiv:1708.06917 [astro-ph.CO].

[87] **LZ** Collaboration, J. Aalbers *et al.*, "Dark Matter Search Results from 4.2 Tonne-Years of Exposure of the LUX-ZEPLIN (LZ) Experiment," arXiv:2410.17036 [hep-ex].

[88] K. Kohri, A. Mazumdar, N. Sahu, and P. Stephens, "Probing Unified Origin of Dark Matter and Baryon Asymmetry at PAMELA/Fermi," *Phys. Rev.* **D80** (2009) 061302, arXiv:0907.0622 [hep-ph].

[89] B. Eiteneuer, A. Goudelis, and J. Heisig, "The inert doublet model in the light of Fermi-LAT gamma-ray data – a global fit analysis," arXiv:1705.01458 [hep-ph].

[90] **Fermi-LAT, MAGIC** Collaboration, M. L. Ahnen *et al.*, "Limits to dark matter annihilation cross-section from a combined analysis of MAGIC and Fermi-LAT observations of dwarf satellite galaxies," *JCAP* **1602** (2016) no. 02, 039, arXiv:1601.06590 [astro-ph.HE].

[91] L. J. Hall, K. Jedamzik, J. March-Russell, and S. M. West, "Freeze-In Production of FIMP Dark Matter," *JHEP* **03** (2010) 080, arXiv:0911.1120 [hep-ph].

[92] F. Elahi, C. Kolda, and J. Unwin, "UltraViolet Freeze-in," *JHEP* **03** (2015) 048, arXiv:1410.6157 [hep-ph].

[93] J. Preskill, M. B. Wise, and F. Wilczek, "Cosmology of the Invisible Axion," *Phys. Lett. B* **120** (1983) 127–132.

[94] L. F. Abbott and P. Sikivie, "A Cosmological Bound on the Invisible Axion," *Phys. Lett. B* **120** (1983) 133–136.

[95] M. Dine and W. Fischler, "The Not So Harmless Axion," *Phys. Lett. B* **120** (1983) 137–141.

[96] M. S. Turner, "Coherent Scalar Field Oscillations in an Expanding Universe," *Phys. Rev. D* **28** (1983) 1243.

[97] P. Arias, D. Cadamuro, M. Goodsell, J. Jaeckel, J. Redondo, and A. Ringwald, "WISPy Cold Dark Matter," *JCAP* **06** (2012) 013, arXiv:1201.5902 [hep-ph].

[98] **KamLAND** Collaboration, S. Abe *et al.*, "Precision Measurement of Neutrino Oscillation Parameters with KamLAND," *Phys. Rev. Lett.* **100** (2008) 221803, arXiv:0801.4589 [hep-ex].

[99] **Super-Kamiokande** Collaboration, Y. Fukuda *et al.*, "Evidence for oscillation of atmospheric neutrinos," *Phys. Rev. Lett.* **81** (1998) 1562–1567, arXiv:hep-ex/9807003.

[100] **K2K** Collaboration, M. H. Ahn *et al.*, "Indications of neutrino oscillation in a 250 km long baseline experiment," *Phys. Rev. Lett.* **90** (2003) 041801, arXiv:hep-ex/0212007.

[101] Z. Maki, M. Nakagawa, and S. Sakata, "Remarks on the unified model of elementary particles," *Prog. Theor. Phys.* **28** (1962) 870–880.

[102] P. F. de Salas, D. V. Forero, S. Gariazzo, P. Martínez-Miravé, O. Mena, C. A. Ternes, M. Tórtola, and J. W. F. Valle, "2020 global reassessment of the neutrino oscillation picture," *JHEP* **02** (2021) 071, arXiv:2006.11237 [hep-ph].

[103] S. Weinberg, "Baryon and Lepton Nonconserving Processes," *Phys. Rev. Lett.* **43** (1979) 1566–1570.

[104] P. Minkowski, "$\mu \to e\gamma$ at a Rate of One Out of 10^9 Muon Decays?," *Phys. Lett. B* **67** (1977) 421–428.

[105] T. Yanagida, "Horizontal gauge symmetry and masses of neutrinos," *Conf. Proc. C* **7902131** (1979) 95–99.

[106] T. Yanagida, "Horizontal Symmetry and Mass of the Top Quark," *Phys. Rev. D* **20** (1979) 2986.

[107] M. Gell-Mann, P. Ramond, and R. Slansky, "Complex Spinors and Unified Theories," *Conf. Proc. C* **790927** (1979) 315–321, arXiv:1306.4669 [hep-th].

[108] R. N. Mohapatra and G. Senjanovic, "Neutrino Mass and Spontaneous Parity Nonconservation," *Phys. Rev. Lett.* **44** (1980) 912.

[109] J. Schechter and J. W. F. Valle, "Neutrino Masses in SU(2) x U(1) Theories," *Phys. Rev. D* **22** (1980) 2227.

[110] J. Schechter and J. W. F. Valle, "Neutrino Decay and Spontaneous Violation of Lepton Number," *Phys. Rev. D* **25** (1982) 774.

[111] R. N. Mohapatra and G. Senjanovic, "Neutrino Masses and Mixings in Gauge Models with Spontaneous Parity Violation," *Phys. Rev.* **D23** (1981) 165.

[112] G. Lazarides, Q. Shafi, and C. Wetterich, "Proton Lifetime and Fermion Masses in an SO(10) Model," *Nucl. Phys.* **B181** (1981) 287–300.

[113] C. Wetterich, "Neutrino Masses and the Scale of B-L Violation," *Nucl. Phys.* **B187** (1981) 343–375.

[114] B. Brahmachari and R. N. Mohapatra, "Unified explanation of the solar and atmospheric neutrino puzzles in a minimal supersymmetric SO(10) model," *Phys. Rev.* **D58** (1998) 015001, arXiv:hep-ph/9710371 [hep-ph].

[115] R. Foot, H. Lew, X. G. He, and G. C. Joshi, "Seesaw Neutrino Masses Induced by a Triplet of Leptons," *Z. Phys.* **C44** (1989) 441.

[116] R. N. Mohapatra and J. W. F. Valle, "Neutrino mass and baryon-number nonconservation in superstring models,"*Phys. Rev. D* **34** (Sep, 1986) 1642–1645. https://link.aps.org/doi/10.1103/PhysRevD.34.1642.

[117] R. N. Mohapatra, "Mechanism for Understanding Small Neutrino Mass in Superstring Theories," *Phys. Rev. Lett.* **56** (1986) 561–563.

[118] A. Zee, "A Theory of Lepton Number Violation, Neutrino Majorana Mass, and Oscillation," *Phys. Lett. B* **93** (1980) 389. [Erratum: Phys.Lett.B 95, 461 (1980)].

[119] K. S. Babu, "Model of 'Calculable' Majorana Neutrino Masses," *Phys. Lett. B* **203** (1988) 132–136.

[120] A. Zee, "Quantum Numbers of Majorana Neutrino Masses," *Nucl. Phys. B* **264** (1986) 99–110.

[121] E. Ma, "Verifiable radiative seesaw mechanism of neutrino mass and dark matter," *Phys. Rev. D* **73** (2006) 077301, arXiv:hep-ph/0601225.

[122] T. Yanagida, "Horizontal Symmetry and Masses of Neutrinos," *Progress of Theoretical Physics* **64** (09, 1980) 1103–1105, https://academic.oup.com/ptp/article-pdf/64/3/1103/5394376/64-3-1103.pdf. https://doi.org/10.1143/PTP.64.1103.

[123] S. F. King, "Large mixing angle MSW and atmospheric neutrinos from single right-handed neutrino dominance and U(1) family symmetry," *Nucl. Phys. B* **576** (2000) 85–105, arXiv:hep-ph/9912492.

[124] J. A. Casas and A. Ibarra, "Oscillating neutrinos and muon —> e, gamma," *Nucl. Phys.* **B618** (2001) 171–204, arXiv:hep-ph/0103065 [hep-ph].

[125] G. Steigman, "Observational tests of antimatter cosmologies," *Ann. Rev. Astron. Astrophys.* **14** (1976) 339–372.

[126] B. D. Fields, K. A. Olive, T.-H. Yeh, and C. Young, "Big-Bang Nucleosynthesis after Planck," *JCAP* **03** (2020) 010, arXiv:1912.01132 [astro-ph.CO]. [Erratum: JCAP 11, E02 (2020)].

[127] **Particle Data Group** Collaboration, R. L. Workman *et al.*, "Review of Particle Physics," *PTEP* **2022** (2022) 083C01.

[128] A. D. Sakharov, "Violation of CP Invariance, C asymmetry, and baryon asymmetry of the universe," *Pisma Zh. Eksp. Teor. Fiz.* **5** (1967) 32–35.

[129] V. A. Kuzmin, V. A. Rubakov, and M. E. Shaposhnikov, "On the Anomalous Electroweak Baryon Number Nonconservation in the Early Universe," *Phys. Lett.* **155B** (1985) 36.

[130] A. G. Cohen, D. B. Kaplan, and A. E. Nelson, "Progress in electroweak baryogenesis," *Annual Review of Nuclear and Particle Science* **43** (1993) no. 1, 27–70.

[131] S. Dimopoulos and L. Susskind, "On the Baryon Number of the Universe," *Phys. Rev. D* **18** (1978) 4500–4509.

[132] M. Yoshimura, "Unified Gauge Theories and the Baryon Number of the Universe," *Phys. Rev. Lett.* **41** (1978) 281–284. [Erratum: Phys.Rev.Lett. 42, 746 (1979)].

[133] S. Weinberg, "Cosmological Production of Baryons," *Phys. Rev. Lett.* **42** (1979) 850–853.

[134] I. Affleck and M. Dine, "A New Mechanism for Baryogenesis," *Nucl. Phys. B* **249** (1985) 361–380.

[135] M. A. Luty, "Baryogenesis via leptogenesis," *Phys. Rev. D* **45** (1992) 455–465.

[136] A. Pilaftsis, "CP violation and baryogenesis due to heavy Majorana neutrinos," *Phys. Rev. D* **56** (1997) 5431–5451, arXiv:hep-ph/9707235.

[137] **LZ** Collaboration, J. Aalbers *et al.*, "First Dark Matter Search Results from the LUX-ZEPLIN (LZ) Experiment," *Phys. Rev. Lett.* **131** (2023) no. 4, 041002, arXiv:2207.03764 [hep-ex].

[138] S. Davidson and A. Ibarra, "A Lower bound on the right-handed neutrino mass from leptogenesis," *Phys. Lett.* **B535** (2002) 25–32, arXiv:hep-ph/0202239 [hep-ph].

[139] M. E. Peskin and D. V. Schroeder, *An Introduction to quantum field theory*. Addison-Wesley, Reading, USA, 1995.

[140] P. B. Pal, *An Introductory Course of Particle Physics*. CRC Press, 7, 2014.

[141] M. Lusignoli, A. Masiero, and M. Roncadelli, "Spontaneous versus explicit breaking of a continuous global symmetry," *Phys. Lett. B* **252** (1990) 247–250.

[142] R. Kallosh, A. D. Linde, D. A. Linde, and L. Susskind, "Gravity and global symmetries," *Phys. Rev. D* **52** (1995) 912–935, arXiv:hep-th/9502069.

[143] M. Kamionkowski and J. March-Russell, "Planck scale physics and the Peccei-Quinn mechanism," *Phys. Lett. B* **282** (1992) 137–141, arXiv:hep-th/9202003.

[144] S. L. Adler and D. G. Boulware, "Anomalous commutators and the triangle diagram," *Phys. Rev.* **184** (1969) 1740–1744.

[145] Y. Chikashige, R. N. Mohapatra, and R. D. Peccei, "Are There Real Goldstone Bosons Associated with Broken Lepton Number?," *Phys. Lett. B* **98** (1981) 265–268.

[146] I. Z. Rothstein, K. S. Babu, and D. Seckel, "Planck scale symmetry breaking and majoron physics," *Nucl. Phys. B* **403** (1993) 725–748, arXiv:hep-ph/9301213.

[147] V. Berezinsky and J. W. F. Valle, "The KeV majoron as a dark matter particle," *Phys. Lett. B* **318** (1993) 360–366, arXiv:hep-ph/9309214.

[148] C. Garcia-Cely and J. Heeck, "Neutrino Lines from Majoron Dark Matter," *JHEP* **05** (2017) 102, arXiv:1701.07209 [hep-ph].

[149] R. D. Peccei, "The Strong CP problem and axions," *Lect. Notes Phys.* **741** (2008) 3–17, arXiv:hep-ph/0607268.

[150] R. J. Crewther, P. Di Vecchia, G. Veneziano, and E. Witten, "Chiral Estimate of the Electric Dipole Moment of the Neutron in Quantum Chromodynamics," *Phys. Lett. B* **88** (1979) 123. [Erratum: Phys.Lett.B 91, 487 (1980)].

[151] C. A. Baker *et al.*, "An Improved experimental limit on the electric dipole moment of the neutron," *Phys. Rev. Lett.* **97** (2006) 131801, arXiv:hep-ex/0602020.

[152] M. Pospelov and A. Ritz, "Electric dipole moments as probes of new physics," *Annals Phys.* **318** (2005) 119–169, arXiv:hep-ph/0504231.

[153] C. Abel *et al.*, "Measurement of the Permanent Electric Dipole Moment of the Neutron," *Phys. Rev. Lett.* **124** (2020) no. 8, 081803, arXiv:2001.11966 [hep-ex].

[154] C. Vafa and E. Witten, "Parity Conservation in QCD," *Phys. Rev. Lett.* **53** (1984) 535.

[155] D. J. Gross, R. D. Pisarski, and L. G. Yaffe, "QCD and Instantons at Finite Temperature," *Rev. Mod. Phys.* **53** (1981) 43.

[156] A. Bazavov *et al.*, "The chiral and deconfinement aspects of the QCD transition," *Phys. Rev. D* **85** (2012) 054503, arXiv:1111.1710 [hep-lat].

[157] L. Di Luzio, M. Giannotti, E. Nardi, and L. Visinelli, "The landscape of QCD axion models," *Phys. Rept.* **870** (2020) 1–117, arXiv:2003.01100 [hep-ph].

[158] M. S. Turner, "Cosmic and Local Mass Density of Invisible Axions," *Phys. Rev. D* **33** (1986) 889–896.

[159] **Particle Data Group** Collaboration, S. Navas *et al.*, "Review of particle physics," *Phys. Rev. D* **110** (2024) no. 3, 030001.

[160] T. W. Donnelly, S. J. Freedman, R. S. Lytel, R. D. Peccei, and M. Schwartz, "Do Axions Exist?," *Phys. Rev. D* **18** (1978) 1607.

[161] Y. Asano, E. Kikutani, S. Kurokawa, T. Miyachi, M. Miyajima, Y. Nagashima, T. Shinkawa, S. Sugimoto, and Y. Yoshimura, "Search for a Rare Decay Mode K+ —> pi+ Neutrino anti-neutrino and Axion," *Phys. Lett. B* **107** (1981) 159.

[162] A. R. Zhitnitsky, "On Possible Suppression of the Axion Hadron Interactions. (In Russian)," *Sov. J. Nucl. Phys.* **31** (1980) 260.

[163] M. Dine, W. Fischler, and M. Srednicki, "A Simple Solution to the Strong CP Problem with a Harmless Axion," *Phys. Lett. B* **104** (1981) 199–202.

[164] J. E. Kim, "Weak Interaction Singlet and Strong CP Invariance," *Phys. Rev. Lett.* **43** (1979) 103.

[165] M. A. Shifman, A. I. Vainshtein, and V. I. Zakharov, "Can Confinement Ensure Natural CP Invariance of Strong Interactions?," *Nucl. Phys. B* **166** (1980) 493–506.

[166] A. Ringwald, "Exploring the Role of Axions and Other WISPs in the Dark Universe," *Phys. Dark Univ.* **1** (2012) 116–135, arXiv:1210.5081 [hep-ph].

[167] A. Davidson and K. C. Wali, "MINIMAL FLAVOR UNIFICATION VIA MULTIGENERATIONAL PECCEI-QUINN SYMMETRY," *Phys. Rev. Lett.* **48** (1982) 11.

[168] F. Wilczek, "Axions and Family Symmetry Breaking," *Phys. Rev. Lett.* **49** (1982) 1549–1552.

[169] L. Calibbi, F. Goertz, D. Redigolo, R. Ziegler, and J. Zupan, "Minimal axion model from flavor," *Phys. Rev. D* **95** (2017) no. 9, 095009, arXiv:1612.08040 [hep-ph].

[170] F. Arias-Aragon and L. Merlo, "The Minimal Flavour Violating Axion," *JHEP* **10** (2017) 168, arXiv:1709.07039 [hep-ph]. [Erratum: JHEP 11, 152 (2019)].

[171] L. Di Luzio, A. W. M. Guerrera, X. P. Díaz, and S. Rigolin, "On the IR/UV flavour connection in non-universal axion models," *JHEP* **06** (2023) 046, arXiv:2304.04643 [hep-ph].

[172] B. Bellazzini, A. Mariotti, D. Redigolo, F. Sala, and J. Serra, "R-axion at colliders," *Phys. Rev. Lett.* **119** (2017) no. 14, 141804, arXiv:1702.02152 [hep-ph].

[173] P. Svrcek and E. Witten, "Axions In String Theory," *JHEP* **06** (2006) 051, arXiv:hep-th/0605206.

[174] K.-S. Choi, I.-W. Kim, and J. E. Kim, "String compactification, QCD axion and axion-photon-photon coupling," *JHEP* **03** (2007) 116, arXiv:hep-ph/0612107.

[175] A. Arvanitaki, S. Dimopoulos, S. Dubovsky, N. Kaloper, and J. March-Russell, "String Axiverse," *Phys. Rev. D* **81** (2010) 123530, arXiv:0905.4720 [hep-th].

[176] M. Cicoli, M. Goodsell, and A. Ringwald, "The type IIB string axiverse and its low-energy phenomenology," *JHEP* **10** (2012) 146, arXiv:1206.0819 [hep-th].

[177] M. Demirtas, C. Long, L. McAllister, and M. Stillman, "The Kreuzer-Skarke Axiverse," *JHEP* **04** (2020) 138, arXiv:1808.01282 [hep-th].

[178] A. Pargner, *Phenomenology of Axion Dark Matter*. PhD thesis, KIT, Karlsruhe, IKP, 2, 2019.

[179] R. L. Davis, "Cosmic Axions from Cosmic Strings," *Phys. Lett. B* **180** (1986) 225–230.

[180] D. Harari and P. Sikivie, "On the Evolution of Global Strings in the Early Universe," *Phys. Lett. B* **195** (1987) 361–365.

[181] A. Vaquero, J. Redondo, and J. Stadler, "Early seeds of axion miniclusters," *JCAP* **04** (2019) 012, arXiv:1809.09241 [astro-ph.CO].

[182] M. Dine, N. Fernandez, A. Ghalsasi, and H. H. Patel, "Comments on axions, domain walls, and cosmic strings," *JCAP* **11** (2021) 041, arXiv:2012.13065 [hep-ph].

[183] R. T. Co, L. J. Hall, and K. Harigaya, "Axion Kinetic Misalignment Mechanism," *Phys. Rev. Lett.* **124** (2020) no. 25, 251802, arXiv:1910.14152 [hep-ph].

[184] C.-F. Chang and Y. Cui, "New Perspectives on Axion Misalignment Mechanism," *Phys. Rev. D* **102** (2020) no. 1, 015003, arXiv:1911.11885 [hep-ph].

[185] M. Dine, L. Randall, and S. D. Thomas, "Baryogenesis from flat directions of the supersymmetric standard model," *Nucl. Phys. B* **458** (1996) 291–326, arXiv:hep-ph/9507453.

[186] I. G. Irastorza and J. Redondo, "New experimental approaches in the search for axion-like particles," *Prog. Part. Nucl. Phys.* **102** (2018) 89–159, arXiv:1801.08127 [hep-ph].

[187] C. O'Hare, "cajohare/axionlimits: Axionlimits." https://cajohare.github.io/AxionLimits/, July, 2020.

[188] Y. K. Semertzidis and S. Youn, "Axion dark matter: How to see it?," *Sci. Adv.* **8** (2022) no. 8, abm9928, arXiv:2104.14831 [hep-ph].

[189] **CAST** Collaboration, S. Andriamonje *et al.*, "An Improved limit on the axion-photon coupling from the CAST experiment," *JCAP* **04** (2007) 010, arXiv:hep-ex/0702006.

[190] **CAST** Collaboration, V. Anastassopoulos *et al.*, "New CAST Limit on the Axion-Photon Interaction," *Nature Phys.* **13** (2017) 584–590, arXiv:1705.02290 [hep-ex].

[191] **IAXO** Collaboration, A. Abeln *et al.*, "Conceptual design of BabyIAXO, the intermediate stage towards the International Axion Observatory," *JHEP* **05** (2021) 137, arXiv:2010.12076 [physics.ins-det].

[192] P. Sikivie, "Experimental Tests of the Invisible Axion," *Phys. Rev. Lett.* **51** (1983) 1415–1417. [Erratum: Phys.Rev.Lett. 52, 695 (1984)].

[193] **ADMX** Collaboration, S. J. Asztalos *et al.*, "A SQUID-based microwave cavity search for dark-matter axions," *Phys. Rev. Lett.* **104** (2010) 041301, arXiv:0910.5914 [astro-ph.CO].

[194] **ADMX** Collaboration, T. Braine *et al.*, "Extended Search for the Invisible Axion with the Axion Dark Matter Experiment," *Phys. Rev. Lett.* **124** (2020) no. 10, 101303, arXiv:1910.08638 [hep-ex].

[195] S. Beurthey *et al.*, "MADMAX Status Report," arXiv:2003.10894 [physics.ins-det].

[196] F. Bajjali *et al.*, "First results from BRASS-p broadband searches for hidden photon dark matter," *JCAP* **08** (2023) 077, arXiv:2306.05934 [hep-ex].

[197] **DMRadio** Collaboration, L. Brouwer *et al.*, "Projected sensitivity of DMRadio-m3: A search for the QCD axion below 1 μeV," *Phys. Rev. D* **106** (2022) no. 10, 103008, arXiv:2204.13781 [hep-ex].

[198] Z. Zhang, D. Horns, and O. Ghosh, "Search for dark matter with an LC circuit," *Phys. Rev. D* **106** (2022) no. 2, 023003, arXiv:2111.04541 [hep-ex].

[199] A. A. Anselm, "Arion ↔ Photon Oscillations in a Steady Magnetic Field. (In Russian)," *Yad. Fiz.* **42** (1985) 1480–1483.

[200] K. Van Bibber, N. R. Dagdeviren, S. E. Koonin, A. Kerman, and H. N. Nelson, "Proposed experiment to produce and detect light pseudoscalars," *Phys. Rev. Lett.* **59** (1987) 759–762.

[201] K. Ehret *et al.*, "New ALPS Results on Hidden-Sector Lightweights," *Phys. Lett. B* **689** (2010) 149–155, arXiv:1004.1313 [hep-ex].

[202] **OSQAR** Collaboration, R. Ballou *et al.*, "New exclusion limits on scalar and pseudoscalar axionlike particles from light shining through a wall," *Phys. Rev. D* **92** (2015) no. 9, 092002, arXiv:1506.08082 [hep-ex].

[203] M. D. Ortiz *et al.*, "Design of the ALPS II optical system," *Phys. Dark Univ.* **35** (2022) 100968, arXiv:2009.14294 [physics.optics].

[204] F. Della Valle, A. Ejlli, U. Gastaldi, G. Messineo, E. Milotti, R. Pengo, G. Ruoso, and G. Zavattini, "The PVLAS experiment: measuring vacuum magnetic birefringence and dichroism with a birefringent Fabry–Perot cavity," *Eur. Phys. J. C* **76** (2016) no. 1, 24, arXiv:1510.08052 [physics.optics].

[205] K. K. Rogers and H. V. Peiris, "Strong Bound on Canonical Ultralight Axion Dark Matter from the Lyman-Alpha Forest," *Phys. Rev. Lett.* **126** (2021) no. 7, 071302, arXiv:2007.12705 [astro-ph.CO].

[206] D. Wouters and P. Brun, "Constraints on Axion-like Particles from X-Ray Observations of the Hydra Galaxy Cluster," *Astrophys. J.* **772** (2013) 44, arXiv:1304.0989 [astro-ph.HE].

[207] M. C. D. Marsh, H. R. Russell, A. C. Fabian, B. P. McNamara, P. Nulsen, and C. S. Reynolds, "A New Bound on Axion-Like Particles," *JCAP* **12** (2017) 036, arXiv:1703.07354 [hep-ph].

[208] C. S. Reynolds, M. C. D. Marsh, H. R. Russell, A. C. Fabian, R. Smith, F. Tombesi, and S. Veilleux, "Astrophysical limits on very light axion-like particles from Chandra grating spectroscopy of NGC 1275," *Astrophys. J.* **890** (2020) 59, arXiv:1907.05475 [hep-ph].

[209] J. S. Reynés, J. H. Matthews, C. S. Reynolds, H. R. Russell, R. N. Smith, and M. C. D. Marsh, "New constraints on light axion-like particles using Chandra transmission grating spectroscopy of the powerful cluster-hosted quasar H1821+643," *Mon. Not. Roy. Astron. Soc.* **510** (2021) no. 1, 1264–1277, arXiv:2109.03261 [astro-ph.HE].

[210] A. Ayala, I. Domínguez, M. Giannotti, A. Mirizzi, and O. Straniero, "Revisiting the bound on axion-photon coupling from Globular Clusters," *Phys. Rev. Lett.* **113** (2014) no. 19, 191302, arXiv:1406.6053 [astro-ph.SR].

[211] D. Cadamuro and J. Redondo, "Cosmological bounds on pseudo Nambu-Goldstone bosons," *JCAP* **02** (2012) 032, arXiv:1110.2895 [hep-ph].

[212] P. F. Depta, M. Hufnagel, and K. Schmidt-Hoberg, "Robust cosmological constraints on axion-like particles," *JCAP* **05** (2020) 009, arXiv:2002.08370 [hep-ph].

[213] G. G. Raffelt, "Astrophysical axion bounds," *Lect. Notes Phys.* **741** (2008) 51–71, arXiv:hep-ph/0611350.

[214] K. Mimasu and V. Sanz, "ALPs at Colliders," *JHEP* **06** (2015) 173, arXiv:1409.4792 [hep-ph].

[215] M. Bauer, M. Neubert, and A. Thamm, "Collider Probes of Axion-Like Particles," *JHEP* **12** (2017) 044, arXiv:1708.00443 [hep-ph].

[216] B. Döbrich, J. Jaeckel, F. Kahlhoefer, A. Ringwald, and K. Schmidt-Hoberg, "ALPtraum: ALP production in proton beam dump experiments," *JHEP* **02** (2016) 018, arXiv:1512.03069 [hep-ph].

[217] A. Lella, E. Ravensburg, P. Carenza, and M. C. D. Marsh, "Supernova limits on QCD axionlike particles," *Phys. Rev. D* **110** (2024) no. 4, 043019, arXiv:2405.00153 [hep-ph].

[218] P. S. B. Dev, R. N. Mohapatra, and Y. Zhang, "Revisiting supernova constraints on a light CP-even scalar," *JCAP* **08** (2020) 003, arXiv:2005.00490 [hep-ph]. [Erratum: JCAP 11, E01 (2020)].

[219] Y. Li and Z. Liu, "Supernova constraints on lepton flavor violating ALPs," arXiv:2501.12075 [hep-ph].

[220] F. Bazzocchi, M. Lattanzi, S. Riemer-Sørensen, and J. W. F. Valle, "X-ray photons from late-decaying majoron dark matter," *JCAP* **08** (2008) 013, arXiv:0805.2372 [astro-ph].

[221] P.-H. Gu, E. Ma, and U. Sarkar, "Pseudo-Majoron as Dark Matter," *Phys. Lett. B* **690** (2010) 145–148, arXiv:1004.1919 [hep-ph].

[222] M. Frigerio, T. Hambye, and E. Masso, "Sub-GeV dark matter as pseudo-Goldstone from the seesaw scale," *Phys. Rev. X* **1** (2011) 021026, arXiv:1107.4564 [hep-ph].

[223] B. Shakya and J. D. Wells, "Exotic Sterile Neutrinos and Pseudo-Goldstone Phenomenology," *JHEP* **02** (2019) 174, arXiv:1801.02640 [hep-ph].

[224] M. Lattanzi, S. Riemer-Sorensen, M. Tortola, and J. W. F. Valle, "Updated CMB and x- and γ-ray constraints on Majoron dark matter," *Phys. Rev. D* **88** (2013) no. 6, 063528, arXiv:1303.4685 [astro-ph.HE].

[225] F. S. Queiroz and K. Sinha, "The Poker Face of the Majoron Dark Matter Model: LUX to keV Line," *Phys. Lett. B* **735** (2014) 69–74, arXiv:1404.1400 [hep-ph].

[226] J. M. Cline, K. Kainulainen, P. Scott, and C. Weniger, "Update on scalar singlet dark matter," *Phys. Rev. D* **88** (2013) 055025, arXiv:1306.4710 [hep-ph]. [Erratum: Phys.Rev.D 92, 039906 (2015)].

[227] C. Gross, O. Lebedev, and T. Toma, "Cancellation Mechanism for Dark-Matter–Nucleon Interaction," *Phys. Rev. Lett.* **119** (2017) no. 19, 191801, arXiv:1708.02253 [hep-ph].

[228] D. Azevedo, M. Duch, B. Grzadkowski, D. Huang, M. Iglicki, and R. Santos, "One-loop contribution to dark-matter-nucleon scattering in the pseudo-scalar dark matter model," *JHEP* **01** (2019) 138, arXiv:1810.06105 [hep-ph].

[229] K. Ishiwata and T. Toma, "Probing pseudo Nambu-Goldstone boson dark matter at loop level," *JHEP* **12** (2018) 089, arXiv:1810.08139 [hep-ph].

[230] K. Huitu, N. Koivunen, O. Lebedev, S. Mondal, and T. Toma, "Probing pseudo-Goldstone dark matter at the LHC," *Phys. Rev. D* **100** (2019) no. 1, 015009, arXiv:1812.05952 [hep-ph].

[231] C. Arina, A. Beniwal, C. Degrande, J. Heisig, and A. Scaffidi, "Global fit of pseudo-Nambu-Goldstone Dark Matter," *JHEP* **04** (2020) 015, arXiv:1912.04008 [hep-ph].

[232] M. Escudero and S. J. Witte, "The hubble tension as a hint of leptogenesis and neutrino mass generation," *Eur. Phys. J. C* **81** (2021) no. 6, 515, arXiv:2103.03249 [hep-ph].

[233] T. Brune and H. Päs, "Massive Majorons and constraints on the Majoron-neutrino coupling," *Phys. Rev. D* **99** (2019) no. 9, 096005, arXiv:1808.08158 [hep-ph].

[234] Y. Abe, Y. Hamada, T. Ohata, K. Suzuki, and K. Yoshioka, "TeV-scale Majorogenesis," *JHEP* **07** (2020) no. 07, 105, arXiv:2004.00599 [hep-ph].

[235] Y. Abe, T. Toma, and K. Yoshioka, "Non-thermal Production of PNGB Dark Matter and Inflation," *JHEP* **03** (2021) 130, arXiv:2012.10286 [hep-ph].

[236] S. F. King, "Constructing the large mixing angle MNS matrix in seesaw models with right-handed neutrino dominance," *JHEP* **09** (2002) 011, arXiv:hep-ph/0204360.

[237] A. Pilaftsis and T. E. J. Underwood, "Resonant leptogenesis," *Nucl. Phys.* **B692** (2004) 303–345, arXiv:hep-ph/0309342 [hep-ph].

[238] A. Ibarra and G. G. Ross, "Neutrino phenomenology: The Case of two right-handed neutrinos," *Phys. Lett.* **B591** (2004) 285–296, arXiv:hep-ph/0312138 [hep-ph].

[239] S. K. Manna and A. Sil, "Majorons revisited: Light dark matter as a FIMP," *Phys. Rev. D* **108** (2023) no. 7, 075026, arXiv:2212.08404 [hep-ph].

[240] **Borexino** Collaboration, G. Bellini *et al.*, "Study of solar and other unknown anti-neutrino fluxes with Borexino at LNGS," *Phys. Lett. B* **696** (2011) 191–196, arXiv:1010.0029 [hep-ex].

[241] **KamLAND** Collaboration, A. Gando *et al.*, "A study of extraterrestrial antineutrino sources with the KamLAND detector," *Astrophys. J.* **745** (2012) 193, arXiv:1105.3516 [astro-ph.HE].

[242] **Super-Kamiokande** Collaboration, Y. Gando *et al.*, "Search for anti-nu(e) from the sun at Super-Kamiokande I," *Phys. Rev. Lett.* **90** (2003) 171302, arXiv:hep-ex/0212067.

[243] A. Boyarsky, D. Malyshev, A. Neronov, and O. Ruchayskiy, "Constraining DM properties with SPI," *Mon. Not. Roy. Astron. Soc.* **387** (2008) 1345, arXiv:0710.4922 [astro-ph].

[244] H. Yuksel and M. D. Kistler, "Circumscribing late dark matter decays model independently," *Phys. Rev. D* **78** (2008) 023502, arXiv:0711.2906 [astro-ph].

[245] **Fermi-LAT** Collaboration, M. Ackermann *et al.*, "Updated search for spectral lines from Galactic dark matter interactions with pass 8 data from the Fermi Large Area Telescope," *Phys. Rev. D* **91** (2015) no. 12, 122002, arXiv:1506.00013 [astro-ph.HE].

[246] R. Holman, S. D. H. Hsu, T. W. Kephart, E. W. Kolb, R. Watkins, and L. M. Widrow, "Solutions to the strong CP problem in a world with gravity," *Phys. Lett. B* **282** (1992) 132–136, arXiv:hep-ph/9203206.

[247] S. Ghigna, M. Lusignoli, and M. Roncadelli, "Instability of the invisible axion," *Phys. Lett. B* **283** (1992) 278–281.

[248] S. B. Giddings and A. Strominger, "Loss of Incoherence and Determination of Coupling Constants in Quantum Gravity," *Nucl. Phys. B* **307** (1988) 854–866.

[249] S. R. Coleman, "Why There Is Nothing Rather Than Something: A Theory of the Cosmological Constant," *Nucl. Phys. B* **310** (1988) 643–668.

[250] S.-J. Rey, "The Axion Dynamics in Wormhole Background," *Phys. Rev. D* **39** (1989) 3185.

[251] L. F. Abbott and M. B. Wise, "Wormholes and Global Symmetries," *Nucl. Phys. B* **325** (1989) 687–704.

[252] R. Barbieri, J. R. Ellis, and M. K. Gaillard, "Neutrino Masses and Oscillations in SU(5)," *Phys. Lett. B* **90** (1980) 249–252.

[253] E. K. Akhmedov, Z. G. Berezhiani, and G. Senjanovic, "Planck scale physics and neutrino masses," *Phys. Rev. Lett.* **69** (1992) 3013–3016, arXiv:hep-ph/9205230.

[254] R. Foot, A. Kobakhidze, K. L. McDonald, and R. R. Volkas, "Poincaré protection for a natural electroweak scale," *Phys. Rev. D* **89** (2014) no. 11, 115018, arXiv:1310.0223 [hep-ph].

[255] R. Coy and M. A. Schmidt, "Freeze-in and freeze-out of sterile neutrino dark matter," arXiv:2204.08795 [hep-ph].

[256] M. Escudero, N. Rius, and V. Sanz, "Sterile neutrino portal to Dark Matter I: The $U(1)_{B-L}$ case," *JHEP* **02** (2017) 045, arXiv:1606.01258 [hep-ph].

[257] C. A. Argüelles, D. Delgado, A. Friedlander, A. Kheirandish, I. Safa, A. C. Vincent, and H. White, "Dark Matter decay to neutrinos," arXiv:2210.01303 [hep-ph].

[258] S. Alvi, T. Brinckmann, M. Gerbino, M. Lattanzi, and L. Pagano, "Do you smell something decaying? Updated linear constraints on decaying dark matter scenarios," arXiv:2205.05636 [astro-ph.CO].

[259] P. Draper, I. G. Garcia, and M. Reece, "Snowmass White Paper: Implications of Quantum Gravity for Particle Physics," in *Snowmass 2021*. 3, 2022. arXiv:2203.07624 [hep-ph].

[260] C. Cordova, K. Ohmori, and T. Rudelius, "Generalized symmetry breaking scales and weak gravity conjectures," *JHEP* **11** (2022) 154, arXiv:2202.05866 [hep-th].

[261] M. Chianese, B. Fu, and S. F. King, "Minimal Seesaw extension for Neutrino Mass and Mixing, Leptogenesis and Dark Matter: FIMPzillas through the Right-Handed Neutrino Portal," *JCAP* **03** (2020) 030, arXiv:1910.12916 [hep-ph].

[262] M. R. Haque, D. Maity, and P. Saha, "Two-phase reheating: CMB constraints on inflation and dark matter phenomenology," *Phys. Rev. D* **102** (2020) no. 8, 083534, arXiv:2009.02794 [hep-th].

[263] I. Esteban, M. C. Gonzalez-Garcia, M. Maltoni, T. Schwetz, and A. Zhou, "The fate of hints: updated global analysis of three-flavor neutrino oscillations," *JHEP* **09** (2020) 178, arXiv:2007.14792 [hep-ph].

[264] I. Esteban, M. C. Gonzalez-Garcia, M. Maltoni, I. Martinez-Soler, and T. Schwetz, "Updated fit to three neutrino mixing: exploring the accelerator-reactor complementarity," *JHEP* **01** (2017) 087, arXiv:1611.01514 [hep-ph].

[265] S. Bhattacharya, R. Roshan, A. Sil, and D. Vatsyayan, "Symmetry origin of Baryon Asymmetry, Dark Matter and Neutrino Mass," arXiv:2105.06189 [hep-ph].

[266] A. Datta, R. Roshan, and A. Sil, "Imprint of the seesaw mechanism on feebly interacting dark matter and the baryon asymmetry," arXiv:2104.02030 [hep-ph].

[267] **Planck** Collaboration, N. Aghanim *et al.*, "Planck 2018 results. V. CMB power spectra and likelihoods," *Astron. Astrophys.* **641** (2020) A5, arXiv:1907.12875 [astro-ph.CO].

[268] **Planck** Collaboration, N. Aghanim *et al.*, "Planck 2018 results. VIII. Gravitational lensing," *Astron. Astrophys.* **641** (2020) A8, arXiv:1807.06210 [astro-ph.CO].

[269] M. Escudero, J. Lopez-Pavon, N. Rius, and S. Sandner, "Relaxing Cosmological Neutrino Mass Bounds with Unstable Neutrinos," *JHEP* **12** (2020) 119, arXiv:2007.04994 [hep-ph].

[270] L. Heurtier and Y. Zhang, "Supernova Constraints on Massive (Pseudo)Scalar Coupling to Neutrinos," *JCAP* **02** (2017) 042, arXiv:1609.05882 [hep-ph].

[271] Y. Farzan, "Bounds on the coupling of the Majoron to light neutrinos from supernova cooling," *Phys. Rev. D* **67** (2003) 073015, arXiv:hep-ph/0211375.

[272] K. Akita, S. H. Im, and M. Masud, "Probing non-standard neutrino interactions with a light boson from next galactic and diffuse supernova neutrinos," *JHEP* **12** (2022) 050, arXiv:2206.06852 [hep-ph].

[273] D. F. G. Fiorillo, G. G. Raffelt, and E. Vitagliano, "Strong Supernova 1987A Constraints on Bosons Decaying to Neutrinos," arXiv:2209.11773 [hep-ph].

[274] **Kamiokande-II** Collaboration, K. Hirata *et al.*, "Observation of a Neutrino Burst from the Supernova SN 1987a," *Phys. Rev. Lett.* **58** (1987) 1490–1493.

[275] R. M. Bionta *et al.*, "Observation of a Neutrino Burst in Coincidence with Supernova SN 1987a in the Large Magellanic Cloud," *Phys. Rev. Lett.* **58** (1987) 1494.

[276] **Super-Kamiokande** Collaboration, H. Zhang *et al.*, "Supernova Relic Neutrino Search with Neutron Tagging at Super-Kamiokande-IV," *Astropart. Phys.* **60** (2015) 41–46, arXiv:1311.3738 [hep-ex].

[277] **IceCube** Collaboration, R. Abbasi *et al.*, "Search for dark matter from the Galactic halo with the IceCube Neutrino Telescope," *Phys. Rev. D* **84** (2011) 022004, arXiv:1101.3349 [astro-ph.HE].

[278] J. Heeck and H. H. Patel, "Majoron at two loops," *Phys. Rev. D* **100** (2019) no. 9, 095015, arXiv:1909.02029 [hep-ph].

[279] A. Boyarsky, A. Neronov, O. Ruchayskiy, and M. Shaposhnikov, "Constraints on sterile neutrino as a dark matter candidate from the diffuse x-ray background," *Mon. Not. Roy. Astron. Soc.* **370** (2006) 213–218, arXiv:astro-ph/0512509.

[280] A. Boyarsky, D. Iakubovskyi, O. Ruchayskiy, and V. Savchenko, "Constraints on decaying Dark Matter from XMM-Newton observations of M31," *Mon. Not. Roy. Astron. Soc.* **387** (2008) 1361, arXiv:0709.2301 [astro-ph].

[281] M. Viel, G. D. Becker, J. S. Bolton, and M. G. Haehnelt, "Warm dark matter as a solution to the small scale crisis: New constraints from high redshift Lyman-α forest data," *Phys. Rev. D* **88** (2013) 043502, arXiv:1306.2314 [astro-ph.CO].

[282] V. K. Narayanan, D. N. Spergel, R. Dave, and C.-P. Ma, "Constraints on the mass of warm dark matter particles and the shape of the linear power spectrum from the Lyα forest," *Astrophys. J. Lett.* **543** (2000) L103–L106, arXiv:astro-ph/0005095.

[283] M. Viel, J. Lesgourgues, M. G. Haehnelt, S. Matarrese, and A. Riotto, "Constraining warm dark matter candidates including sterile neutrinos and light gravitinos with WMAP and the Lyman-alpha forest," *Phys. Rev. D* **71** (2005) 063534, arXiv:astro-ph/0501562.

[284] J. Baur, N. Palanque-Delabrouille, C. Yèche, C. Magneville, and M. Viel, "Lyman-alpha Forests cool Warm Dark Matter," *JCAP* **08** (2016) 012, arXiv:1512.01981 [astro-ph.CO].

[285] V. Iršič *et al.*, "New Constraints on the free-streaming of warm dark matter from intermediate and small scale Lyman-α forest data," *Phys. Rev. D* **96** (2017) no. 2, 023522, arXiv:1702.01764 [astro-ph.CO].

[286] N. Palanque-Delabrouille, C. Yèche, N. Schöneberg, J. Lesgourgues, M. Walther, S. Chabanier, and E. Armengaud, "Hints, neutrino bounds and WDM constraints from SDSS DR14 Lyman-α and Planck full-survey data," *JCAP* **04** (2020) 038, arXiv:1911.09073 [astro-ph.CO].

[287] A. Garzilli, A. Magalich, O. Ruchayskiy, and A. Boyarsky, "How to constrain warm dark matter with the Lyman-α forest," *Mon. Not. Roy. Astron. Soc.* **502** (2021) no. 2, 2356–2363, arXiv:1912.09397 [astro-ph.CO].

[288] J. Heeck and D. Teresi, "Cold keV dark matter from decays and scatterings," *Phys. Rev. D* **96** (2017) no. 3, 035018, arXiv:1706.09909 [hep-ph].

[289] K. J. Bae, A. Kamada, S. P. Liew, and K. Yanagi, "Light axinos from freeze-in: production processes, phase space distributions, and Ly-α forest constraints," *JCAP* **01** (2018) 054, arXiv:1707.06418 [hep-ph].

[290] A. Kamada and K. Yanagi, "Constraining FIMP from the structure formation of the Universe: analytic mapping from m_{WDM}," *JCAP* **11** (2019) 029, arXiv:1907.04558 [hep-ph].

[291] G. Ballesteros, M. A. G. Garcia, and M. Pierre, "How warm are non-thermal relics? Lyman-α bounds on out-of-equilibrium dark matter," *JCAP* **03** (2021) 101, arXiv:2011.13458 [hep-ph].

[292] F. D'Eramo and A. Lenoci, "Lower mass bounds on FIMP dark matter produced via freeze-in," *JCAP* **10** (2021) 045, arXiv:2012.01446 [hep-ph].

[293] Q. Decant, J. Heisig, D. C. Hooper, and L. Lopez-Honorez, "Lyman-α constraints on freeze-in and superWIMPs," *JCAP* **03** (2022) 041, arXiv:2111.09321 [astro-ph.CO].

[294] S. F. King, S. K. Manna, R. Roshan, and A. Sil, "Leptogenesis with Majoron Dark Matter," arXiv:2412.14121 [hep-ph].

[295] B. Barman, D. Borah, and R. Roshan, "Effective Theory of Freeze-in Dark Matter," *JCAP* **11** (2020) 021, arXiv:2007.08768 [hep-ph].

[296] B. Barman, D. Borah, and R. Roshan, "Non-thermal leptogenesis and UV freeze-in of dark matter: impact of inflationary reheating," arXiv:2103.01675 [hep-ph].

[297] S. F. King, R. Roshan, X. Wang, G. White, and M. Yamazaki, "Quantum gravity effects on fermionic dark matter and gravitational waves," *JCAP* **05** (2024) 071, arXiv:2311.12487 [hep-ph].

[298] K. Akita and M. Niibo, "Updated constraints and future prospects on majoron dark matter," *JHEP* **07** (2023) 132, arXiv:2304.04430 [hep-ph].

[299] G. Lazarides and Q. Shafi, "Origin of matter in the inflationary cosmology," *Phys. Lett. B* **258** (1991) 305–309.

[300] H. Murayama, H. Suzuki, T. Yanagida, and J. Yokoyama, "Chaotic inflation and baryogenesis by right-handed sneutrinos," *Phys. Rev. Lett.* **70** (1993) 1912–1915.

[301] E. W. Kolb, A. D. Linde, and A. Riotto, "GUT baryogenesis after preheating," *Phys. Rev. Lett.* **77** (1996) 4290–4293, arXiv:hep-ph/9606260.

[302] G. F. Giudice, M. Peloso, A. Riotto, and I. Tkachev, "Production of massive fermions at preheating and leptogenesis," *JHEP* **08** (1999) 014, arXiv:hep-ph/9905242.

[303] T. Asaka, K. Hamaguchi, M. Kawasaki, and T. Yanagida, "Leptogenesis in inflaton decay," *Phys. Lett. B* **464** (1999) 12–18, arXiv:hep-ph/9906366.

[304] T. Asaka, K. Hamaguchi, M. Kawasaki, and T. Yanagida, "Leptogenesis in inflationary universe," *Phys. Rev. D* **61** (2000) 083512, arXiv:hep-ph/9907559.

[305] K. Hamaguchi, H. Murayama, and T. Yanagida, "Leptogenesis from N dominated early universe," *Phys. Rev. D* **65** (2002) 043512, arXiv:hep-ph/0109030.

[306] B. Barman, D. Borah, S. J. Das, and R. Roshan, "Non-thermal origin of asymmetric dark matter from inflaton and primordial black holes," *JCAP* **03** (2022) no. 03, 031, arXiv:2111.08034 [hep-ph].

[307] B. Barman, D. Borah, S. Das Jyoti, and R. Roshan, "Cogenesis of Baryon Asymmetry and Gravitational Dark Matter from PBH," arXiv:2204.10339 [hep-ph].

[308] G. Lazarides, R. Maji, R. Roshan, and Q. Shafi, "A predictive SO(10) model," *JCAP* **12** (2022) 009, arXiv:2210.03710 [hep-ph].

[309] B. Barman, A. Datta, and M. R. Haque, "Is leptogenesis during gravitational reheating flavourful?," arXiv:2410.16381 [hep-ph].

[310] B. Barman, A. Basu, D. Borah, A. Chakraborty, and R. Roshan, "Testing cogenesis during reheating with primordial gravitational waves," arXiv:2410.19048 [hep-ph].

[311] M. Flanz, E. A. Paschos, U. Sarkar, and J. Weiss, "Baryogenesis through mixing of heavy Majorana neutrinos," *Phys. Lett. B* **389** (1996) 693–699, arXiv:hep-ph/9607310.

[312] S. Iso, N. Okada, and Y. Orikasa, "Resonant Leptogenesis in the Minimal B-L Extended Standard Model at TeV," *Phys. Rev.* **D83** (2011) 093011, arXiv:1011.4769 [hep-ph].

[313] X. Qi and H. Sun, "Interplay between dark matter and leptogenesis in a common framework," *JHEP* **09** (2023) 118, arXiv:2208.13345 [hep-ph].

[314] A. Das and Y. Orikasa, "Resonant leptogenesis in minimal $U(1)_X$ extensions of the Standard Model," arXiv:2407.05644 [hep-ph].

[315] M. Plumacher, "Baryogenesis and lepton number violation," *Z. Phys. C* **74** (1997) 549–559, arXiv:hep-ph/9604229.

[316] A. Abada, S. Davidson, F.-X. Josse-Michaux, M. Losada, and A. Riotto, "Flavor issues in leptogenesis," *JCAP* **04** (2006) 004, arXiv:hep-ph/0601083.

[317] E. Nardi, Y. Nir, E. Roulet, and J. Racker, "The Importance of flavor in leptogenesis," *JHEP* **01** (2006) 164, arXiv:hep-ph/0601084.

[318] S. Blanchet and P. Di Bari, "Flavor effects on leptogenesis predictions," *JCAP* **03** (2007) 018, arXiv:hep-ph/0607330.

[319] P. S. B. Dev, P. Di Bari, B. Garbrecht, S. Lavignac, P. Millington, and D. Teresi, "Flavor effects in leptogenesis," *Int. J. Mod. Phys. A* **33** (2018) 1842001, arXiv:1711.02861 [hep-ph].

[320] A. Datta, R. Roshan, and A. Sil, "Scalar triplet flavor leptogenesis with dark matter," *Phys. Rev. D* **105** (2022) no. 9, 095032, arXiv:2110.03914 [hep-ph].

[321] A. Datta, R. Roshan, and A. Sil, "Effects of Reheating on Charged Lepton Yukawa Equilibration and Leptogenesis," arXiv:2206.10650 [hep-ph].

[322] A. Datta, R. Roshan, and A. Sil, "Flavor Leptogenesis During Reheating Era," arXiv:2301.10791 [hep-ph].

[323] A. Datta and A. Sil, "Probing Leptogenesis through Gravitational Waves," arXiv:2410.01900 [hep-ph].

[324] S. K. Manna and A. Sil, "Effects of electroweak symmetry breaking on axionlike particles as dark matter," *Phys. Rev. D* **109** (2024) no. 9, 095036, arXiv:2311.05125 [hep-ph].

[325] K. S. Jeong, K. Matsukawa, S. Nakagawa, and F. Takahashi, "Cosmological effects of Peccei-Quinn symmetry breaking on QCD axion dark matter," *JCAP* **03** (2022) no. 03, 026, arXiv:2201.00681 [hep-ph].

[326] H.-J. Li, "Axion dark matter with explicit Peccei-Quinn symmetry breaking in the axiverse," arXiv:2307.09245 [hep-ph].

[327] A. Chatrchyan, C. Eröncel, M. Koschnitzke, and G. Servant, "ALP dark matter with non-periodic potentials: parametric resonance, halo formation and gravitational signatures," arXiv:2305.03756 [hep-ph].

[328] R. T. Co, L. J. Hall, and K. Harigaya, "Predictions for Axion Couplings from ALP Cogenesis," *JHEP* **01** (2021) 172, arXiv:2006.04809 [hep-ph].

[329] C. Eröncel, R. Sato, G. Servant, and P. Sørensen, "ALP dark matter from kinetic fragmentation: opening up the parameter window," *JCAP* **10** (2022) 053, arXiv:2206.14259 [hep-ph].

[330] W. Chao, M. Jin, H.-J. Li, and Y.-Q. Peng, "Axion-like Dark Matter from the Type-II Seesaw Mechanism," arXiv:2210.13233 [hep-ph].

[331] S. H. Im and K. S. Jeong, "Freeze-in Axion-like Dark Matter," *Phys. Lett. B* **799** (2019) 135044, arXiv:1907.07383 [hep-ph].

[332] P. S. B. Dev, F. Ferrer, Y. Zhang, and Y. Zhang, "Gravitational Waves from First-Order Phase Transition in a Simple Axion-Like Particle Model," *JCAP* **11** (2019) 006, arXiv:1905.00891 [hep-ph].

[333] V. K. Oikonomou, "Effects of the axion through the Higgs portal on primordial gravitational waves during the electroweak breaking," *Phys. Rev. D* **107** (2023) no. 6, 064071, arXiv:2303.05889 [hep-ph].

[334] T. Higaki, K. S. Jeong, N. Kitajima, and F. Takahashi, "Quality of the Peccei-Quinn symmetry in the Aligned QCD Axion and Cosmological Implications," *JHEP* **06** (2016) 150, arXiv:1603.02090 [hep-ph].

[335] N. Arkani-Hamed, L. Motl, A. Nicolis, and C. Vafa, "The String landscape, black holes and gravity as the weakest force," *JHEP* **06** (2007) 060, arXiv:hep-th/0601001.

[336] S. M. Barr and D. Seckel, "Planck scale corrections to axion models," *Phys. Rev. D* **46** (1992) 539–549.

[337] D. J. E. Marsh, "Axion Cosmology," *Phys. Rept.* **643** (2016) 1–79, arXiv:1510.07633 [astro-ph.CO].

[338] J. Jaeckel and A. Ringwald, "The Low-Energy Frontier of Particle Physics," *Ann. Rev. Nucl. Part. Sci.* **60** (2010) 405–437, arXiv:1002.0329 [hep-ph].

[339] M. S. Turner, "Windows on the Axion," *Phys. Rept.* **197** (1990) 67–97.

[340] P. Gondolo and G. G. Raffelt, "Solar neutrino limit on axions and keV-mass bosons," *Phys. Rev. D* **79** (2009) 107301, arXiv:0807.2926 [astro-ph].

[341] S. De Panfilis, A. C. Melissinos, B. E. Moskowitz, J. T. Rogers, Y. K. Semertzidis, W. Wuensch, H. J. Halama, A. G. Prodell, W. B. Fowler, and F. A. Nezrick, "Limits on the Abundance and Coupling of Cosmic Axions at 4.5-Microev $<$ m(a) $<$ 5.0-Microev," *Phys. Rev. Lett.* **59** (1987) 839.

[342] W. Wuensch, S. De Panfilis-Wuensch, Y. K. Semertzidis, J. T. Rogers, A. C. Melissinos, H. J. Halama, B. E. Moskowitz, A. G. Prodell, W. B. Fowler, and F. A. Nezrick, "Results of a Laboratory Search for Cosmic Axions and Other Weakly Coupled Light Particles," *Phys. Rev. D* **40** (1989) 3153.

[343] C. Hagmann, P. Sikivie, N. S. Sullivan, and D. B. Tanner, "Results from a search for cosmic axions," *Phys. Rev. D* **42** (1990) 1297–1300.

[344] **ADMX** Collaboration, S. J. Asztalos *et al.*, "An Improved RF cavity search for halo axions," *Phys. Rev. D* **69** (2004) 011101, arXiv:astro-ph/0310042.

[345] M. Regis, M. Taoso, D. Vaz, J. Brinchmann, S. L. Zoutendijk, N. F. Bouché, and M. Steinmetz, "Searching for light in the darkness: Bounds on ALP dark matter with the optical MUSE-faint survey," *Phys. Lett. B* **814** (2021) 136075, arXiv:2009.01310 [astro-ph.CO].

[346] J. Redondo and A. Ringwald, "Light shining through walls," *Contemp. Phys.* **52** (2011) 211–236, arXiv:1011.3741 [hep-ph].

[347] **ALPS** Collaboration, K.-S. Isleif, "The Any Light Particle Search Experiment at DESY," *Moscow Univ. Phys. Bull.* **77** (2022) no. 2, 120–125, arXiv:2202.07306 [hep-ex].

[348] C. Balázs *et al.*, "Cosmological constraints on decaying axion-like particles: a global analysis," *JCAP* **12** (2022) 027, arXiv:2205.13549 [astro-ph.CO].

[349] E. Masso and R. Toldra, "On a light spinless particle coupled to photons," *Phys. Rev. D* **52** (1995) 1755–1763, arXiv:hep-ph/9503293.

[350] J. M. Overduin and P. S. Wesson, "Dark matter and background light," *Phys. Rept.* **402** (2004) 267–406, arXiv:astro-ph/0407207.

[351] C. O'hare, "cajohare/AxionLimits: AxionLimits," 2020.

[352] J. Hamann, S. Hannestad, G. G. Raffelt, and Y. Y. Y. Wong, "Isocurvature forecast in the anthropic axion window," *JCAP* **06** (2009) 022, arXiv:0904.0647 [hep-ph].

[353] M. Beltran, J. Garcia-Bellido, and J. Lesgourgues, "Isocurvature bounds on axions revisited," *Phys. Rev. D* **75** (2007) 103507, arXiv:hep-ph/0606107.

[354] M. Kawasaki, E. Sonomoto, and T. T. Yanagida, "Cosmologically allowed regions for the axion decay constant F_a," *Phys. Lett. B* **782** (2018) 181–184, arXiv:1801.07409 [hep-ph].

[355] **Planck** Collaboration, P. A. R. Ade *et al.*, "Planck 2015 results. XX. Constraints on inflation," *Astron. Astrophys.* **594** (2016) A20, arXiv:1502.02114 [astro-ph.CO].

[356] C. A. J. O'Hare, "Cosmology of axion dark matter," *PoS* **COSMICWISPers** (2024) 040, arXiv:2403.17697 [hep-ph].

[357] A. G. Cohen and D. B. Kaplan, "Thermodynamic Generation of the Baryon Asymmetry," *Phys. Lett. B* **199** (1987) 251–258.

[358] A. G. Cohen and D. B. Kaplan, "SPONTANEOUS BARYOGENESIS," *Nucl. Phys. B* **308** (1988) 913–928.

[359] M.-z. Li, X.-l. Wang, B. Feng, and X.-m. Zhang, "Quintessence and spontaneous leptogenesis," *Phys. Rev. D* **65** (2002) 103511, arXiv:hep-ph/0112069.

[360] M. Yamaguchi, "Generation of cosmological large lepton asymmetry from a rolling scalar field," *Phys. Rev. D* **68** (2003) 063507, arXiv:hep-ph/0211163.

[361] A. Kusenko, K. Schmitz, and T. T. Yanagida, "Leptogenesis via Axion Oscillations after Inflation," *Phys. Rev. Lett.* **115** (2015) no. 1, 011302, arXiv:1412.2043 [hep-ph].

[362] M. Ibe and K. Kaneta, "Spontaneous thermal Leptogenesis via Majoron oscillation," *Phys. Rev. D* **92** (2015) no. 3, 035019, arXiv:1504.04125 [hep-ph].

[363] F. Takahashi and M. Yamada, "Spontaneous Baryogenesis from Asymmetric Inflaton," *Phys. Lett. B* **756** (2016) 216–220, arXiv:1510.07822 [hep-ph].

[364] K. J. Bae, J. Kost, and C. S. Shin, "Deformation of Axion Potentials: Implications for Spontaneous Baryogenesis, Dark Matter, and Isocurvature Perturbations," *Phys. Rev. D* **99** (2019) no. 4, 043502, arXiv:1811.10655 [hep-ph].

[365] V. Domcke, Y. Ema, K. Mukaida, and M. Yamada, "Spontaneous Baryogenesis from Axions with Generic Couplings," *JHEP* **08** (2020) 096, arXiv:2006.03148 [hep-ph].

[366] M. Berbig, "Diraxiogenesis," *JHEP* **01** (2024) 061, arXiv:2307.14121 [hep-ph].

[367] W. Chao and Y.-Q. Peng, "Majorana Majoron and the Baryon Asymmetry of the Universe," arXiv:2311.06469 [hep-ph].

[368] E. J. Chun and T. H. Jung, "Leptogenesis driven by a Majoron," *Phys. Rev. D* **109** (2024) no. 9, 095004, arXiv:2311.09005 [hep-ph].

[369] A. De Simone and T. Kobayashi, "Cosmological Aspects of Spontaneous Baryogenesis," *JCAP* **08** (2016) 052, arXiv:1605.00670 [hep-ph].

[370] J. W. Foster, S. Kumar, B. R. Safdi, and Y. Soreq, "Dark Grand Unification in the axiverse: decaying axion dark matter and spontaneous baryogenesis," *JHEP* **12** (2022) 119, arXiv:2208.10504 [hep-ph].

[371] A. Datta, S. K. Manna, and A. Sil, "Spontaneous leptogenesis with sub-GeV axionlike particles," *Phys. Rev. D* **110** (2024) no. 9, 095035, arXiv:2405.07003 [hep-ph].

[372] **CLEO** Collaboration, R. Balest *et al.*, "Upsilon (1s) —> gamma + noninteracting particles," *Phys. Rev. D* **51** (1995) 2053–2060.

[373] **BaBar** Collaboration, P. del Amo Sanchez *et al.*, "Search for Production of Invisible Final States in Single-Photon Decays of $\Upsilon(1S)$," *Phys. Rev. Lett.* **107** (2011) 021804, arXiv:1007.4646 [hep-ex].

[374] E. M. Riordan *et al.*, "A Search for Short Lived Axions in an Electron Beam Dump Experiment," *Phys. Rev. Lett.* **59** (1987) 755.

[375] J. D. Bjorken, S. Ecklund, W. R. Nelson, A. Abashian, C. Church, B. Lu, L. W. Mo, T. A. Nunamaker, and P. Rassmann, "Search for Neutral Metastable Penetrating Particles Produced in the SLAC Beam Dump," *Phys. Rev. D* **38** (1988) 3375.

[376] **FASER** Collaboration, A. Ariga *et al.*, "FASER's physics reach for long-lived particles," *Phys. Rev. D* **99** (2019) no. 9, 095011, arXiv:1811.12522 [hep-ph].

[377] R. T. Co and K. Harigaya, "Axiogenesis," *Phys. Rev. Lett.* **124** (2020) no. 11, 111602, arXiv:1910.02080 [hep-ph].

[378] K. Harigaya and I. R. Wang, "Axiogenesis from $SU(2)_R$ phase transition," *JHEP* **10** (2021) 022, arXiv:2107.09679 [hep-ph]. [Erratum: JHEP 12, 193 (2021)].

[379] R. T. Co, T. Gherghetta, and K. Harigaya, "Axiogenesis with a heavy QCD axion," *JHEP* **10** (2022) 121, arXiv:2206.00678 [hep-ph].

[380] R. T. Co, N. Fernandez, A. Ghalsasi, L. J. Hall, and K. Harigaya, "Lepto-Axiogenesis," *JHEP* **03** (2021) 017, arXiv:2006.05687 [hep-ph].

[381] J. Kawamura and S. Raby, "Lepto-axiogenesis in minimal SUSY KSVZ model," *JHEP* **04** (2022) 116, arXiv:2109.08605 [hep-ph].

[382] P. Barnes, R. T. Co, K. Harigaya, and A. Pierce, "Lepto-axiogenesis and the scale of supersymmetry," *JHEP* **05** (2023) 114, arXiv:2208.07878 [hep-ph].

[383] P. Barnes, R. T. Co, K. Harigaya, and A. Pierce, "Lepto-axiogenesis with light right-handed neutrinos," arXiv:2402.10263 [hep-ph].

[384] B. Shi and S. Raby, "Basis invariant description of chemical equilibrium with implications for a recent axionic leptogenesis model," *Phys. Rev. D* **92** (2015) no. 8, 085008, arXiv:1507.08392 [hep-ph].

[385] S. Y. Khlebnikov and M. E. Shaposhnikov, "The Statistical Theory of Anomalous Fermion Number Nonconservation," *Nucl. Phys. B* **308** (1988) 885–912.

[386] P. B. Arnold and L. D. McLerran, "The Sphaleron Strikes Back," *Phys. Rev. D* **37** (1988) 1020.

[387] J. A. Harvey and M. S. Turner, "Cosmological baryon and lepton number in the presence of electroweak fermion number violation," *Phys. Rev. D* **42** (1990) 3344–3349.

[388] L. Bento, "Sphaleron relaxation temperatures," *JCAP* **11** (2003) 002, arXiv:hep-ph/0304263.

[389] G. F. Giudice, E. W. Kolb, and A. Riotto, "Largest temperature of the radiation era and its cosmological implications," *Phys. Rev.* **D64** (2001) 023508, arXiv:hep-ph/0005123 [hep-ph].

[390] M. Kawasaki, K. Kohri, and N. Sugiyama, "MeV scale reheating temperature and thermalization of neutrino background," *Phys. Rev. D* **62** (2000) 023506, arXiv:astro-ph/0002127.

[391] J. Martin and C. Ringeval, "First CMB Constraints on the Inflationary Reheating Temperature," *Phys. Rev. D* **82** (2010) 023511, arXiv:1004.5525 [astro-ph.CO].

[392] L. Dai, M. Kamionkowski, and J. Wang, "Reheating constraints to inflationary models," *Phys. Rev. Lett.* **113** (2014) 041302, arXiv:1404.6704 [astro-ph.CO].

[393] R. Barbieri, L. J. Hall, and V. S. Rychkov, "Improved naturalness with a heavy Higgs: An Alternative road to LHC physics," *Phys. Rev.* **D74** (2006) 015007, arXiv:hep-ph/0603188 [hep-ph].

[394] L. Lopez Honorez, E. Nezri, J. F. Oliver, and M. H. G. Tytgat, "The Inert Doublet Model: An Archetype for Dark Matter," *JCAP* **0702** (2007) 028, arXiv:hep-ph/0612275 [hep-ph].

[395] L. Lopez Honorez and C. E. Yaguna, "The inert doublet model of dark matter revisited," *JHEP* **09** (2010) 046, arXiv:1003.3125 [hep-ph].

[396] D. Borah and J. M. Cline, "Inert Doublet Dark Matter with Strong Electroweak Phase Transition," *Phys. Rev.* **D86** (2012) 055001, arXiv:1204.4722 [hep-ph].

[397] M. Gustafsson, S. Rydbeck, L. Lopez-Honorez, and E. Lundstrom, "Status of the Inert Doublet Model and the Role of multileptons at the LHC," *Phys. Rev.* **D86** (2012) 075019, arXiv:1206.6316 [hep-ph].

[398] A. Biswas, D. Majumdar, A. Sil, and P. Bhattacharjee, "Two Component Dark Matter : A Possible Explanation of 130 GeV $\gamma-$ Ray Line from the Galactic Centre," *JCAP* **1312** (2013) 049, arXiv:1301.3668 [hep-ph].

[399] A. Arhrib, Y.-L. S. Tsai, Q. Yuan, and T.-C. Yuan, "An Updated Analysis of Inert Higgs Doublet Model in light of the Recent Results from LUX, PLANCK, AMS-02 and LHC," *JCAP* **1406** (2014) 030, arXiv:1310.0358 [hep-ph].

[400] V. Keus, S. F. King, S. Moretti, and D. Sokolowska, "Dark Matter with Two Inert Doublets plus One Higgs Doublet," *JHEP* **11** (2014) 016, arXiv:1407.7859 [hep-ph].

[401] A. Ilnicka, M. Krawczyk, and T. Robens, "Inert Doublet Model in light of LHC Run I and astrophysical data," *Phys. Rev.* **D93** (2016) no. 5, 055026, arXiv:1508.01671 [hep-ph].

[402] A. Belyaev, G. Cacciapaglia, I. P. Ivanov, F. Rojas-Abatte, and M. Thomas, "Anatomy of the Inert Two Higgs Doublet Model in the light of the LHC and non-LHC Dark Matter Searches," *Phys. Rev.* **D97** (2018) no. 3, 035011, arXiv:1612.00511 [hep-ph].

[403] S. Choubey and A. Kumar, "Inflation and Dark Matter in the Inert Doublet Model," *JHEP* **11** (2017) 080, arXiv:1707.06587 [hep-ph].

[404] J. Kalinowski, W. Kotlarski, T. Robens, D. Sokolowska, and A. F. Zarnecki, "Benchmarking the Inert Doublet Model for e^+e^- colliders," *JHEP* **12** (2018) 081, arXiv:1809.07712 [hep-ph].

[405] A. Bhardwaj, P. Konar, T. Mandal, and S. Sadhukhan, "Probing Inert Doublet Model using jet substructure with multivariate analysis," arXiv:1905.04195 [hep-ph].

[406] S. Bhattacharya, P. Ghosh, A. K. Saha, and A. Sil, "Two component dark matter with inert Higgs doublet: neutrino mass, high scale validity and collider searches," arXiv:1905.12583 [hep-ph].

[407] D. Borah, R. Roshan, and A. Sil, "Minimal two-component scalar doublet dark matter with radiative neutrino mass," *Phys. Rev. D* **100** (2019) no. 5, 055027, arXiv:1904.04837 [hep-ph].

[408] A. Dutta Banik, R. Roshan, and A. Sil, "Neutrino mass and asymmetric dark matter: study with inert Higgs doublet and high scale validity," *JCAP* **03** (2021) 037, arXiv:2011.04371 [hep-ph].

[409] S. Chakraborty, T. H. Jung, and T. Okui, "Composite neutrinos and the QCD axion: Baryogenesis, dark matter, small Dirac neutrino masses, and vanishing neutron electric dipole moment," *Phys. Rev. D* **105** (2022) no. 1, 015024, arXiv:2108.04293 [hep-ph].

[410] B. Barman, N. Bernal, N. Ramberg, and L. Visinelli, "QCD Axion Kinetic Misalignment without Prejudice," *Universe* **8** (2022) no. 12, 634, arXiv:2111.03677 [hep-ph].

[411] T. Hasegawa, N. Hiroshima, K. Kohri, R. S. L. Hansen, T. Tram, and S. Hannestad, "MeV-scale reheating temperature and thermalization of oscillating neutrinos by

radiative and hadronic decays of massive particles," *JCAP* **12** (2019) 012, arXiv:1908.10189 [hep-ph].

[412] H. Georgi, D. B. Kaplan, and L. Randall, "Manifesting the Invisible Axion at Low-energies," *Phys. Lett. B* **169** (1986) 73–78.

[413] P. Carenza, O. Straniero, B. Döbrich, M. Giannotti, G. Lucente, and A. Mirizzi, "Constraints on the coupling with photons of heavy axion-like-particles from Globular Clusters," *Phys. Lett. B* **809** (2020) 135709, arXiv:2004.08399 [hep-ph].

[414] J. Jaeckel, P. C. Malta, and J. Redondo, "Decay photons from the axionlike particles burst of type II supernovae," *Phys. Rev. D* **98** (2018) no. 5, 055032, arXiv:1702.02964 [hep-ph].

[415] G. Lucente, P. Carenza, T. Fischer, M. Giannotti, and A. Mirizzi, "Heavy axion-like particles and core-collapse supernovae: constraints and impact on the explosion mechanism," *JCAP* **12** (2020) 008, arXiv:2008.04918 [hep-ph].

[416] A. Caputo, H.-T. Janka, G. Raffelt, and E. Vitagliano, "Low-Energy Supernovae Severely Constrain Radiative Particle Decays," *Phys. Rev. Lett.* **128** (2022) no. 22, 221103, arXiv:2201.09890 [astro-ph.HE].

[417] S. Hoof and L. Schulz, "Updated constraints on axion-like particles from temporal information in supernova SN1987A gamma-ray data," *JCAP* **03** (2023) 054, arXiv:2212.09764 [hep-ph].

[418] M. J. Dolan, T. Ferber, C. Hearty, F. Kahlhoefer, and K. Schmidt-Hoberg, "Revised constraints and Belle II sensitivity for visible and invisible axion-like particles," *JHEP* **12** (2017) 094, arXiv:1709.00009 [hep-ph]. [Erratum: JHEP 03, 190 (2021)].

[419] **L3** Collaboration, M. Acciarri *et al.*, "Search for anomalous Z –> gamma gamma gamma events at LEP," *Phys. Lett. B* **345** (1995) 609–616.

[420] **OPAL** Collaboration, G. Abbiendi *et al.*, "Multiphoton production in e+ e- collisions at s**(1/2) = 181-GeV to 209-GeV," *Eur. Phys. J. C* **26** (2003) 331–344, arXiv:hep-ex/0210016.

[421] S. Knapen, T. Lin, H. K. Lou, and T. Melia, "Searching for Axionlike Particles with Ultraperipheral Heavy-Ion Collisions," *Phys. Rev. Lett.* **118** (2017) no. 17, 171801, arXiv:1607.06083 [hep-ph].

[422] **Belle-II** Collaboration, F. Abudinén *et al.*, "Search for Axion-Like Particles produced in e^+e^- collisions at Belle II," *Phys. Rev. Lett.* **125** (2020) no. 16, 161806, arXiv:2007.13071 [hep-ex].

[423] D. Aloni, C. Fanelli, Y. Soreq, and M. Williams, "Photoproduction of Axionlike Particles," *Phys. Rev. Lett.* **123** (2019) no. 7, 071801, arXiv:1903.03586 [hep-ph].

[424] J. Jaeckel and M. Spannowsky, "Probing MeV to 90 GeV axion-like particles with LEP and LHC," *Phys. Lett. B* **753** (2016) 482–487, arXiv:1509.00476 [hep-ph].

[425] M. J. Dolan, F. Kahlhoefer, C. McCabe, and K. Schmidt-Hoberg, "A taste of dark matter: Flavour constraints on pseudoscalar mediators," *JHEP* **03** (2015) 171, arXiv:1412.5174 [hep-ph]. [Erratum: JHEP 07, 103 (2015)].

[426] X. Cid Vidal, A. Mariotti, D. Redigolo, F. Sala, and K. Tobioka, "New Axion Searches at Flavor Factories," *JHEP* **01** (2019) 113, arXiv:1810.09452 [hep-ph]. [Erratum: JHEP 06, 141 (2020)].

[427] A. Bharucha, F. Brümmer, N. Desai, and S. Mutzel, "Axion-like particles as mediators for dark matter: beyond freeze-out," *JHEP* **02** (2023) 141, arXiv:2209.03932 [hep-ph].

[428] D. K. Ghosh, A. Ghoshal, and S. Jeesun, "Axion-like particle (ALP) portal freeze-in dark matter confronting ALP search experiments," *JHEP* **01** (2024) 026, arXiv:2305.09188 [hep-ph].

[429] P. J. Fitzpatrick, Y. Hochberg, E. Kuflik, R. Ovadia, and Y. Soreq, "Dark matter through the axion-gluon portal," *Phys. Rev. D* **108** (2023) no. 7, 075003, arXiv:2306.03128 [hep-ph].

[430] J. A. Dror, S. Gori, and P. Munbodh, "QCD axion-mediated dark matter," *JHEP* **09** (2023) 128, arXiv:2306.03145 [hep-ph].

[431] F. Acanfora, R. Franceschini, A. Mastroddi, and D. Redigolo, "Fusing photons into nothing, a new search for invisible ALPs and Dark Matter at Belle II," *JHEP* **11** (2024) 156, arXiv:2307.06369 [hep-ph].

[432] G. Armando, P. Panci, J. Weiss, and R. Ziegler, "Leptonic ALP portal to the dark sector," *Phys. Rev. D* **109** (2024) no. 5, 055029, arXiv:2310.05827 [hep-ph].

[433] S. Allen, A. Blackburn, O. Cardenas, Z. Messenger, N. H. Nguyen, and B. Shuve, "Electroweak axion portal to dark matter," *Phys. Rev. D* **110** (2024) no. 9, 095010, arXiv:2405.02403 [hep-ph].

[434] "The International Linear Collider Technical Design Report - Volume 1: Executive Summary," arXiv:1306.6327 [physics.acc-ph].

[435] **ILC International Development Team** Collaboration, A. Aryshev *et al.*, "The International Linear Collider: Report to Snowmass 2021," arXiv:2203.07622 [physics.acc-ph].

[436] C.-X. Yue, H.-Y. Zhang, and H. Wang, "Production of axion-like particles via vector boson fusion at future electron-positron colliders," *Eur. Phys. J. C* **82** (2022) no. 1, 88, arXiv:2112.11604 [hep-ph].

[437] C.-X. Yue, H. Wang, and Y.-Q. Wang, "Detecting the coupling of axion-like particles with fermions at the ILC," *Phys. Lett. B* **848** (2024) 138368, arXiv:2311.16768 [hep-ph].

[438] L. Calibbi, Z. Huang, S. Qin, Y. Yang, and X. Yin, "Testing axion couplings to leptons in Z decays at future e+e- colliders," *Phys. Rev. D* **108** (2023) no. 1, 015002, arXiv:2212.02818 [hep-ph].

[439] M. Bauer, M. Heiles, M. Neubert, and A. Thamm, "Axion-Like Particles at Future Colliders," *Eur. Phys. J. C* **79** (2019) no. 1, 74, arXiv:1808.10323 [hep-ph].

[440] H.-Y. Zhang, C.-X. Yue, Y.-C. Guo, and S. Yang, "Searching for axionlike particles at future electron-positron colliders," *Phys. Rev. D* **104** (2021) no. 9, 096008, arXiv:2103.05218 [hep-ph].

[441] C.-X. Yue, S. Yang, H. Wang, and N. Zhang, "Prospects for detecting axionlike particles via the decay $Z \to a f f$ at future Z factories," *Phys. Rev. D* **105** (2022) no. 11, 115027, arXiv:2204.04702 [hep-ph].

[442] C.-T. Lu, "Lighting electroweak-violating ALP-lepton interactions at e^+e^- and ep colliders," *Phys. Rev. D* **108** (2023) no. 11, 115029, arXiv:2210.15648 [hep-ph].

[443] I. Brivio, M. B. Gavela, L. Merlo, K. Mimasu, J. M. No, R. del Rey, and V. Sanz, "ALPs Effective Field Theory and Collider Signatures," *Eur. Phys. J. C* **77** (2017) no. 8, 572, arXiv:1701.05379 [hep-ph].

[444] **Fermi-LAT** Collaboration, A. Albert, G. A. Gomez-Vargas, M. Grefe, C. Munoz, C. Weniger, E. D. Bloom, E. Charles, M. N. Mazziotta, and A. Morselli, "Search for 100 MeV to 10 GeV γ-ray lines in the Fermi-LAT data and implications for gravitino dark matter in $\mu\nu$SSM," *JCAP* **10** (2014) 023, arXiv:1406.3430 [astro-ph.HE].

[445] J. W. Foster, Y. Park, B. R. Safdi, Y. Soreq, and W. L. Xu, "Search for dark matter lines at the Galactic Center with 14 years of Fermi data," *Phys. Rev. D* **107** (2023) no. 10, 103047, arXiv:2212.07435 [hep-ph].

[446] **MAGIC** Collaboration, H. Abe *et al.*, "Search for Gamma-Ray Spectral Lines from Dark Matter Annihilation up to 100 TeV toward the Galactic Center with MAGIC," *Phys. Rev. Lett.* **130** (2023) no. 6, 061002, arXiv:2212.10527 [astro-ph.HE].

[447] **HESS** Collaboration, H. Abdallah *et al.*, "Search for γ-Ray Line Signals from Dark Matter Annihilations in the Inner Galactic Halo from 10 Years of Observations with H.E.S.S.," *Phys. Rev. Lett.* **120** (2018) no. 20, 201101, arXiv:1805.05741 [astro-ph.HE].

[448] A. R. Pullen, R.-R. Chary, and M. Kamionkowski, "Search with EGRET for a Gamma Ray Line from the Galactic Center," *Phys. Rev. D* **76** (2007) 063006, arXiv:astro-ph/0610295. [Erratum: Phys.Rev.D 83, 029904 (2011)].

[449] K. K. Boddy and J. Kumar, "Indirect Detection of Dark Matter Using MeV-Range Gamma-Ray Telescopes," *Phys. Rev. D* **92** (2015) no. 2, 023533, arXiv:1504.04024 [astro-ph.CO].

[450] G. Bélanger, F. Boudjema, A. Goudelis, A. Pukhov, and B. Zaldivar, "micrOMEGAs5.0 : Freeze-in," *Comput. Phys. Commun.* **231** (2018) 173–186, arXiv:1801.03509 [hep-ph].

[451] P. J. Fox, R. Harnik, J. Kopp, and Y. Tsai, "LEP Shines Light on Dark Matter," *Phys. Rev. D* **84** (2011) 014028, arXiv:1103.0240 [hep-ph].

[452] Z.-H. Yu, Q.-S. Yan, and P.-F. Yin, "Detecting interactions between dark matter and photons at high energy e^+e^- colliders," *Phys. Rev. D* **88** (2013) no. 7, 075015, arXiv:1307.5740 [hep-ph].

[453] R. Essig, J. Mardon, M. Papucci, T. Volansky, and Y.-M. Zhong, "Constraining Light Dark Matter with Low-Energy e^+e^- Colliders," *JHEP* **11** (2013) 167, arXiv:1309.5084 [hep-ph].

[454] K. Kadota and J. Silk, "Constraints on Light Magnetic Dipole Dark Matter from the ILC and SN 1987A," *Phys. Rev. D* **89** (2014) no. 10, 103528, arXiv:1402.7295 [hep-ph].

[455] Z.-H. Yu, X.-J. Bi, Q.-S. Yan, and P.-F. Yin, "Dark matter searches in the mono-Z channel at high energy e^+e^- colliders," *Phys. Rev. D* **90** (2014) no. 5, 055010, arXiv:1404.6990 [hep-ph].

[456] A. Freitas and S. Westhoff, "Leptophilic Dark Matter in Lepton Interactions at LEP and ILC," *JHEP* **10** (2014) 116, arXiv:1408.1959 [hep-ph].

[457] S. Dutta, D. Sachdeva, and B. Rawat, "Signals of Leptophilic Dark Matter at the ILC," *Eur. Phys. J. C* **77** (2017) no. 9, 639, arXiv:1704.03994 [hep-ph].

[458] D. Choudhury and D. Sachdeva, "Model independent analysis of MeV scale dark matter. II. Implications from e^-e^+ colliders and direct detection," *Phys. Rev. D* **100** (2019) no. 7, 075007, arXiv:1906.06364 [hep-ph].

[459] S.-I. Horigome, T. Katayose, S. Matsumoto, and I. Saha, "Leptophilic fermion WIMP: Role of future lepton colliders," *Phys. Rev. D* **104** (2021) no. 5, 055001, arXiv:2102.08645 [hep-ph].

[460] B. Barman, S. Bhattacharya, S. Girmohanta, and S. Jahedi, "Effective Leptophilic WIMPs at the e^+e^- collider," *JHEP* **04** (2022) 146, arXiv:2109.10936 [hep-ph].

[461] S. Kundu, A. Guha, P. K. Das, and P. S. B. Dev, "EFT analysis of leptophilic dark matter at future electron-positron colliders in the mono-photon and mono-Z channels," *Phys. Rev. D* **107** (2023) no. 1, 015003, arXiv:2110.06903 [hep-ph].

[462] S. Bhattacharya, P. Ghosh, J. Lahiri, and B. Mukhopadhyaya, "Mono-X signal and two component dark matter: New distinction criteria," *Phys. Rev. D* **108** (2023) no. 11, L111703, arXiv:2211.10749 [hep-ph].

[463] S.-F. Ge, K. Ma, X.-D. Ma, and J. Sheng, "Associated production of neutrino and dark fermion at future lepton colliders," *JHEP* **11** (2023) 190, arXiv:2306.00657 [hep-ph].

[464] B. Barman, S. Bhattacharya, S. Jahedi, D. Pradhan, and A. Sarkar, "Lepton Collider as a window to Reheating," arXiv:2406.11963 [hep-ph].

[465] D. Borah, N. Das, S. Jahedi, and B. Thacker, "Collider and CMB complementarity of leptophilic dark matter with light Dirac neutrinos," *JHEP* **01** (2025) 074, arXiv:2408.14548 [hep-ph].

[466] B. Barman, S. Bhattacharya, S. Jahedi, D. Pradhan, and A. Sarkar, "Lepton Collider as a window to Reheating: II," arXiv:2410.18198 [hep-ph].

[467] J. Alwall, R. Frederix, S. Frixione, V. Hirschi, F. Maltoni, O. Mattelaer, H. S. Shao, T. Stelzer, P. Torrielli, and M. Zaro, "The automated computation of tree-level and next-to-leading order differential cross sections, and their matching to parton shower simulations," *JHEP* **07** (2014) 079, arXiv:1405.0301 [hep-ph].

[468] T. Sjöstrand, S. Ask, J. R. Christiansen, R. Corke, N. Desai, P. Ilten, S. Mrenna, S. Prestel, C. O. Rasmussen, and P. Z. Skands, "An introduction to PYTHIA 8.2," *Comput. Phys. Commun.* **191** (2015) 159–177, arXiv:1410.3012 [hep-ph].

[469] **DELPHES 3** Collaboration, J. de Favereau, C. Delaere, P. Demin, A. Giammanco, V. Lemaître, A. Mertens, and M. Selvaggi, "DELPHES 3, A modular framework for fast simulation of a generic collider experiment," *JHEP* **02** (2014) 057, arXiv:1307.6346 [hep-ex].

[470] N. D. Christensen and C. Duhr, "FeynRules - Feynman rules made easy," *Comput. Phys. Commun.* **180** (2009) 1614–1641, arXiv:0806.4194 [hep-ph].

[471] **CMB-HD** Collaboration, S. Aiola *et al.*, "Snowmass2021 CMB-HD White Paper," arXiv:2203.05728 [astro-ph.CO].

[472] G. Cowan, K. Cranmer, E. Gross, and O. Vitells, "Asymptotic formulae for likelihood-based tests of new physics," *Eur. Phys. J. C* **71** (2011) 1554, arXiv:1007.1727 [physics.data-an]. [Erratum: Eur.Phys.J.C 73, 2501 (2013)].

[473] Q. Bonnefoy, "Heavy fields and the axion quality problem," *Phys. Rev. D* **108** (2023) no. 3, 035023, arXiv:2212.00102 [hep-ph].

[474] P. Di Bari, D. Marfatia, and Y.-L. Zhou, "Gravitational waves from neutrino mass and dark matter genesis," *Phys. Rev. D* **102** (2020) no. 9, 095017, arXiv:2001.07637 [hep-ph].